
SEDIMENT TRANSPORT MODELING REPORT

PATRICK BAYOU

Prepared for

U.S. Environmental Protection Agency
Region 6
Dallas, Texas

Patrick Bayou Joint Defense Group
Houston, Texas

Prepared by

Anchor QEA, LLC
305 W. Grand Avenue, Ste 300
Montvale, New Jersey 07645

September 2011

TABLE OF CONTENTS

EXECUTIVE SUMMARY	ES-1
1 INTRODUCTION	1
1.1 Overview of Patrick Bayou Configuration and Hydrology	1
1.2 Definitions of Sediment Transport Terms	3
1.3 Study Objectives.....	4
1.4 Overview of Technical Approach	5
1.5 Report Organization.....	8
2 DEVELOPMENT, CALIBRATION, AND VALIDATION OF MODELING FRAMEWORK	9
2.1 General Description of Modeling Framework.....	9
2.2 Watershed Model.....	10
2.2.1 General Model Description.....	10
2.2.2 Model Inputs and Parameters	11
2.2.3 Calibration Approach and Results.....	14
2.3 Hydrodynamic Model.....	16
2.3.1 General Description	17
2.3.2 Numerical Grid and Geometry	17
2.3.3 Boundary Conditions	18
2.3.4 Calibration Approach and Results.....	23
2.4 Sediment Transport Model	24
2.4.1 Model Structure and Capabilities	24
2.4.2 Sediment Properties	29
2.4.3 Bed Properties.....	32
2.4.4 Boundary Conditions	36
2.4.5 Sediment Transport Model Calibration	40
2.4.6 Sediment Transport Model Validation.....	44
3 DIAGNOSTIC AND PROGNOSTIC MODELING ANALYSES.....	50
3.1 Evaluation of July-December 2007 Period	50
3.2 Sediment Bed Stability during High-Flow Events	52
3.2.1 Diagnostic Evaluation of High-Flow Events.....	52

3.2.2	Sensitivity Analysis	54
3.3	Effects of External Sediment Loads on Mixing-Zone Layer Composition.....	57
3.3.1	Diagnostic Evaluation of 14-Year Simulation.....	57
3.3.2	Uncertainty Analysis.....	58
4	SUMMARY AND SYNTHESIS OF RESULTS.....	64
4.1	Summary of Model Reliability	64
4.2	Integration and Synthesis of Results.....	64
4.3	Conceptual Site Model for Sediment Transport	68
5	REFERENCES	70

List of Tables

Table 2-1	Curve Number Ranges for Different Land-Use and Soil Categories.....	13
Table 2-2	Statistical Analysis of Watershed Model Results for October 2006 Period.....	16
Table 2-3	Mean and Range of Outfall Flow Rates During 1998-2006 for Outfalls Upstream of Model Inflow Boundary.....	21
Table 2-4	Results of Error Analysis for Hydrodynamic Model Calibration Period.....	24
Table 2-5	Approximations and Assumptions Used in Hydrodynamic and Sediment Transport Models	26
Table 2-6	Model Inputs and Data Sources	29
Table 2-7	Characteristics of Sediment Particle Size Classes.....	31
Table 2-8	Vertical Variation in Erosion Rate Parameters	36
Table 2-9	Comparison of Predicted and Measured NSR for 14-Year Simulation.....	43
Table 2-10	Predicted Decay Rate Coefficients at Core Locations During 14-Year Period	46
Table 3-1	Return Periods and Flow Rates for High-Flow Events	53
Table 3-2	Bounding Limits For Uncertainty Simulations	60

List of Figures

Figure 1-1	Overview of Patrick Bayou Study Area
Figure 2-1	Overview of Patrick Bayou Modeling Framework
Figure 2-2	Watershed Sub-basin Delineation
Figure 2-3	Location of Precipitation Gauges in Harris County Used in the Watershed Model
Figure 2-4	Land Use Categories for the Watershed Sub-basins
Figure 2-5	Hydrologic Soil Groups for the Watershed Sub-basins
Figure 2-6	October 2006 Storm-Event Sampling Locations
Figure 2-7	Comparisons of Measured and Predicted Flow Rates at Stations PB075 and EF005 Between October 12 and 28, 2006
Figure 2-8	Numerical Grid and Projected Bathymetry

Figure 2-9	Cumulative Frequency Distribution of Flow Rate During Days With No Precipitation at Stations PB075, EF005, and PB020 Used to Estimate Base Flow
Figure 2-10	Locations of NOAA Tidal Gauge Stations at Battleship Texas State Park and Morgans Point
Figure 2-11	Comparison of Water Surface Elevations Measured at Morgans Point and Battleship Texas State Park Gauging Stations Between April and July 2007
Figure 2-12	Time History of Flow Rate and Stage Height During October 2006 Calibration Period
Figure 2-13	Locations of Outfalls and Storm Drains
Figure 2-14	Monthly Average Flow Rates in QxyChem Outfalls 001, 002, and 003 Between 1997 and 2006
Figure 2-15	Monthly Average Flow Rates in QxyChem Outfalls 001, 002, and 003 Between 1993 and 2006 for Model Input
Figure 2-16	Comparisons of Measured and Predicted Stage Height and Current Speed at Station PB020 During October 2006 Calibration Period
Figure 2-17	Spatial Distribution of Evolved Bed Composition Used as Initial Conditions for Model Simulations: Class 1 Sediment
Figure 2-18	Spatial Distribution of Evolved Bed Composition Used as Initial Conditions for Model Simulations: Class 2 Sediment
Figure 2-19	Spatial Distribution of Evolved Bed Composition Used as Initial Conditions for Model Simulations: Class 3 Sediment
Figure 2-20	Spatial Distribution of Evolved Bed Composition Used as Initial Conditions for Model Simulations: Class 4 Sediment
Figure 2-21	Erosion Rate (Sedflume) Core Locations
Figure 2-22	Comparison of Erosion Rate Ratio for Sedflume Cores Collected in Patrick Bayou
Figure 2-23	Sediment Rating Curve for Station PB075
Figure 2-24	Sediment Rating Curve for Station EF005
Figure 2-25	Location of Galveston Bay National Estuary Program Sampling Stations Near Patrick Bayou
Figure 2-26	Comparison of Cumulative Frequency Distributions for Historical TSS Concentration Data Collected at Two HSC Stations

Figure 2-27	Comparisons of Measured and Predicted TSS Concentrations at Station PB012 During October 2006 Calibration Period
Figure 2-28	Radioisotope Core Sampling Locations and Mass Balance Zone Delineation
Figure 2-29	Comparison of Measured and Predicted NSR for 14-year Simulation
Figure 2-30	Spatial Distribution of Predicted Net Sedimentation Rate in Patrick Bayou for 14-year Period (1993-2006)
Figure 2-31	Areal Distribution of Predicted Net Sedimentation Rates for 14-year Simulation (1993-2006)
Figure 2-32a	Schematic of Idealized Deposition and Mixing-zone Layer Model
Figure 2-32b	Time History of Exponential Decreasing Chemical Concentration for Idealized Mixing-zone Layer Model
Figure 2-33	Predicted Bed Elevation Change and Mixing-zone Layer Bed Content at Station PB003
Figure 2-34	Predicted Bed Elevation Change and Mixing-zone Layer Bed Content at Station PB022
Figure 2-35	Predicted Bed Elevation Change and Mixing-zone Layer Bed Content at Station PB036
Figure 2-36	Predicted Bed Elevation Change and Mixing-zone Layer Bed Content at Station PB048
Figure 2-37	Predicted Bed Elevation Change and Mixing-zone Layer Bed Content at Station PB057
Figure 2-38	Relationship Between Predicted Net Sedimentation Rate and Bed-source Sediment Content in Mixing-zone Layer at End of 14-year Period
Figure 3-1	Locations of Sediment Marker Horizon Stations
Figure 3-2	Predicted Bed Shear Stress at Marker Horizon Stations PB003, PB018, PB023, and PB035: July-December 2007
Figure 3-3	Predicted Bed Shear Stress at Marker Horizon Stations PB048, PB057, and PB062: July-December 2007
Figure 3-4	Spatial Distribution of Predicted Net Erosion Depth During 2-yr High-flow Event
Figure 3-5	Spatial Distribution of Predicted Net Erosion Depth During 10-yr High-flow Event

Figure 3-6	Spatial Distribution of Predicted Net Erosion Depth During 100-yr High-flow Event
Figure 3-7	Predicted Sediment Mass Balance During 100-yr High-flow Event
Figure 3-8	High-resolution Numerical Grid and Projected Bathymetry for Sensitivity Simulations
Figure 3-9	Spatial Distribution of Predicted Net Erosion Depth During 100-yr High-flow Sensitivity Simulation: Lower-bound Erosion Parameters
Figure 3-10	Spatial Distribution of Predicted Net Erosion Depth During 100-yr High-flow Sensitivity Simulation: Upper-bound Erosion Parameters
Figure 3-11	Spatial Distribution of Predicted Net Erosion Depth During 100-yr High-flow Sensitivity Simulation: Lower-bound Upstream Sediment Load
Figure 3-12	Spatial Distribution of Predicted Net Erosion Depth During 100-yr High-flow Sensitivity Simulation: Upper-Bound Upstream Sediment Load
Figure 3-13	Spatial Distribution of Predicted Net Erosion Depth During 100-yr High-flow Sensitivity Simulation: Lower-bound Effective Bed Roughness Height
Figure 3-14	Spatial Distribution of Predicted Net Erosion Depth During 100-yr High-flow Sensitivity Simulation: Upper-bound Effective Bed Roughness Height
Figure 3-15	Spatial Distribution of Predicted Net Erosion Depth During 100-yr High-flow Sensitivity Simulation: High-resolution Grid
Figure 3-16	Cumulative Frequency Distributions of Bed Elevation Change During 100-year Flood Simulation for Original and High-resolution Grids
Figure 3-17	Comparison of Normalized Net Erosion Area and Net Erosion Mass for Base-case and Sensitivity Simulations During 100-yr High-flow Event
Figure 3-18	Predicted Sediment Mass Balance for 14-year Simulation Period (1993-2006)
Figure 3-19	Relative Proportions of Bed- and External-source Sediment for 14-year Simulation Period (1993-2006)
Figure 3-20	Spatial Distribution of Predicted Half-time of Bed-source Sediment in Mixing Zone Layer (0-10 cm) Sediment. Predicted Half-times are Average Values for 14-year Simulation Period (1993-2006)
Figure 3-21	Areal distribution of Predicted Half-time of Bed-source Sediment in Mixing Zone Layer (0-10 cm)
Figure 3-22	Relationship Between Predicted Net Sedimentation Rate and Half-time of Bed Source Sediment in Mixing-zone Layer

Figure 3-23	Comparison of Predicted Net Sedimentation Rates at the End of 7- and 14-year Simulation Periods
Figure 3-24	Time Histories of Predicted Bed Elevation Change at Station PB003 for Base-case and Uncertainty Simulations
Figure 3-25	Time Histories of Predicted Bed Elevation Change at Station PB006 for Base-case and Uncertainty Simulations
Figure 3-26	Time Histories of Predicted Bed Elevation Change at Station PB016 for Base-case and Uncertainty Simulations
Figure 3-27	Time Histories of Predicted Bed Elevation Change at Station PB022 for Base-case and Uncertainty Simulations
Figure 3-28	Time Histories of predicted bed elevation change at Station PB025 for Base-case and Uncertainty Simulations
Figure 3-29	Time Histories of Predicted Bed Elevation Change at Station PB036 for Base-case and Uncertainty Simulations
Figure 3-30	Time Histories of Predicted Bed Elevation Change at Station PB048 for Base-case and Uncertainty Simulations
Figure 3-31	Time Histories of Predicted Bed Elevation Change at Station PB052 for Base-case and Uncertainty Simulations
Figure 3-32	Time Histories of Predicted Bed Elevation Change at Station PB057 for Base-case and Uncertainty Simulations
Figure 3-33	Comparison of Laterally-averaged Net Sedimentation Rates at End of 7-year Period for Uncertainty Simulations
Figure 3-34	Comparison of Normalized Net Sedimentation Rates at Stations PB022 and PB048 for Uncertainty Simulations
Figure 3-35	Comparison of Normalized Net Sedimentation Rates at Stations PB006 and PB016 for Uncertainty Simulations
Figure 3-36	Comparison of Normalized Net Sedimentation Rates at Stations PB025 and PB052 for Uncertainty Simulations
Figure 3-37	Comparison of Normalized Trapping Efficiency and Net Deposition for Uncertainty Simulations
Figure 3-38	Spatial Distribution of Predicted Net Sedimentation Rate at End of 7-year Period: Base-case Simulation

-
- Figure 3-39 Spatial Distribution of Predicted Net Sedimentation Rate at End of 7-year Period: Lower-bound Simulation
- Figure 3-40 Spatial Distribution of Predicted Net Sedimentation Rate at End of 7-year Period: Upper-bound Simulation
- Figure 3-41 Comparison of Areal Distributions of Predicted Half-time of Bed-source Sediment in Mixing-zone Layer (0-10 cm) for Base-case and Bounding Simulations
- Figure 3-42 Cumulative Frequency Distributions of Bed Elevation Change During 3-year Period (1993-1995) for Original and High-resolution Grids
- Figure 3-43 Spatial Distribution of Predicted Net Sedimentation Rate in Patrick Bayou for 3-year Period (1993-1995): Original Grid
- Figure 3-44 Spatial Distribution of Predicted Net Sedimentation Rate in Patrick Bayou for 3-year Period (1993-1995): High-resolution Grid
- Figure 3-45 Spatial Distribution of Predicted Net Erosion Depth in Patrick Bayou for 3-year Period (1993-1995): Original Grid
- Figure 3-46 Spatial Distribution of Predicted Net Erosion Depth in Patrick Bayou for 3-year Period (1993-1995): High-resolution Grid
- Figure 3-47 Spatial Distributions of Laterally-averaged Net Sedimentation Rates at End of 3-year Period (1993-1995) for Original and High-Resolution Grids
- Figure 3-48 Comparison of Measured and Predicted NSR Values for 3-year Period (1993-1995) for Original and High-resolution Grids

List of Appendices

- Appendix A Details of Sediment Transport Model Theory and Formulation
- Appendix B Analysis of Erosion Rate (Sedflume) Data
- Appendix C Boundary Conditions for 14-Year Simulation

LIST OF ACRONYMS AND ABBREVIATIONS

AOC	Administrative Order on Consent
cfs	Cubic Feet Per Second
CN	Curve Number
COPC	Contaminants of Potential Concern
CSM	Conceptual Site Model
EFDC	Environmental Fluid Dynamics Code
ENC	Electronic Navigation Chart
EPA	U.S. Environmental Protection Agency
FFS	Focused Feasibility Study
FS	Feasibility Study
GOM	Gulf of Mexico
GSD	Grain Size Distribution
HCOEM	Harris County Homeland Security and Emergency Management
HGAC	Houston Galveston Area Council
HSC	Houston Ship Channel
JDG	Patrick Bayou Joint Defense Group
LDW	Lower Duwamish Waterway
MSL	Mean Sea Level
MT	Metric Ton
NOAA	National Oceanic and Atmospheric Administration
NRCS	Natural Resources Conservation Service
NS	Nash-Sutcliffe
NSR	Net Sedimentation Rate
Pa	Pascal
PAH	Polycyclic Aromatic Hydrocarbon
PCB	Polychlorinated Biphenyl
ppt	Part Per Thousand
QEA	Quantitative Environmental Analysis, LLC
RI/FS	Remedial Investigation/Feasibility Study
RMS	Root-mean-square
SCS	Soil Conservation Service
Site	Patrick Bayou Superfund Site
STATSGO	State Soil Geographic
TSS	Total Suspended Sediment
USDA	U.S. Department of Agriculture
USGS	U.S. Geological Survey
WSE	Water Surface Elevation

EXECUTIVE SUMMARY

This Sediment Transport Modeling Report was developed by Anchor QEA on behalf of the Patrick Bayou Joint Defense Group (JDG). The JDG is signatory to the Administrative Settlement Agreement and Order on Consent (AOC) with U.S. Environmental Protection Agency (EPA) Region 6, dated January 31, 2006. The AOC concerns the performance of a Remedial Investigation/Feasibility Study (RI/FS) at the Patrick Bayou Superfund Site (Site).

The Site was added to EPA's National Priority List on September 5, 2002. Patrick Bayou is one of several small bayous connected to the Houston Ship Channel (HSC), which is located within the lower portion of the San Jacinto River Basin. The transport and fate of particle-associated contaminants of potential concern (COPCs) in Patrick Bayou are affected by a range of physical and chemical processes. Generally, sediment transport processes (i.e., net sedimentation, erosion, bed stability) have a significant effect on the transport and fate of these types of chemicals. Accordingly, this study is focused on a quantitative evaluation of the physical transport of sediment. FS will use the results of these analyses, along with relevant chemical information, to examine the importance of sediment transport processes relative to potential remedial alternatives for the Site.

A goal of this study was to develop an improved understanding of sediment transport processes in the Site. Results of the empirical and modeling analyses were used to develop the following conceptual site model (CSM) for sediment transport in Patrick Bayou:

- As a whole, Patrick Bayou is net depositional over annual time scales, with approximately 55% to 60% of the sediment load entering the Site from the surrounding watershed being deposited within the Site.
- Net sedimentation rates (NSR) are spatially variable in Patrick Bayou, with values ranging from less than 0.1 cm/yr to over 2 cm/year.

- Bed erosion is typically an episodic process that is most pronounced during high-flow events. During the 100-year high-flow event (i.e., event with 1% chance of occurring in a given year), net erosion occurs in approximately 65% of the total bed area and the majority of the net erosion is less than 6 cm. During the 2-year high-flow event (i.e., event with 50% chance of occurring in a given year), net erosion occurs in about 45% of the total bed area and erosion depths are less than 2 cm. Generally, erosion at the Site, even during high-flow events, only affects surface-layer sediments and is limited to bed depths that represent relatively recent deposition.
- The results indicate that for about 70% of the Site, the concentration of a COPC in the mixing-zone layer will decrease by one-half of its current concentration in less than 10 years in areas assuming “clean” sediment input.

1 INTRODUCTION

This Sediment Transport Modeling Report was developed by Anchor QEA on behalf of the Patrick Bayou Joint Defense Group (JDG). The JDG is signatory to the Administrative Settlement Agreement and Order on Consent (AOC) with U.S. Environmental Protection Agency (EPA) Region 6, dated January 31, 2006. The AOC concerns the performance of a Remedial Investigation/Feasibility Study (RI/FS) at the Patrick Bayou Superfund Site (Site).

Patrick Bayou was added to the EPA's National Priority List on September 5, 2002. Patrick Bayou is one of several small bayous connected to the Houston Ship Channel (HSC), which is located within the lower portion of the San Jacinto River Basin. The Site is located in southeast Harris County, north of Deer Park, Texas (Figure 1-1). The Site originates south of State Highway 225 in the City of Deer Park and flows approximately 2.5 miles in a northerly direction, discharging into the south side of the HSC, approximately 2.3 miles upstream of the confluence of the HSC and San Jacinto River. The Site and its salient features are described in more detail in the Preliminary Site Characterization Report (Anchor Environmental 2006).

The transport and fate of particle-associated contaminants of potential concern (COPCs) in Patrick Bayou are affected by a range of physical and chemical processes. Generally, sediment transport processes (i.e., net sedimentation, erosion, bed stability) have a significant effect on the transport and fate of these types of chemicals. Accordingly, this study is focused on a quantitative evaluation of the physical transport of sediment; chemical fate and transport was not simulated during this study. The FS will use the results of these analyses, along with relevant chemical information, to examine the importance of sediment transport processes relative to potential remedial alternatives for the Site. The FS will include an evaluation of natural recovery potential, and estimated natural recovery rates, using the results of the sediment transport modeling.

1.1 Overview of Patrick Bayou Configuration and Hydrology

Patrick Bayou is part of an estuarine system and estuaries tend to act as sediment traps for incoming sediment because current velocities generally decrease as freshwater flow enters the estuary and, hence, the carrying capacity of the inflowing waters is reduced. The spatial

distribution and rate of sediment deposition in the estuarine system that includes Patrick Bayou (i.e., HSC and Galveston Bay) is dependent on the physical characteristics of the estuary, including bathymetry and morphology, tidal range, storm surges, wind-generated circulation, freshwater inflow, and sediment loading.

Erosion in an estuary may be separated into two main categories. First, tidal currents may cause a thin surficial layer of fluff to be resuspended into the water column during peak flow conditions for lunar tides and wind-driven storm events. Fluff refers to a surficial layer of flocculent material that is primarily composed of organic detritus, clay, and silt. The resuspended fluff is subsequently re-deposited onto the bed during slack water conditions between ebb and flood tides. Generally, the fluff layer is relatively thin (i.e., less than 1 cm), contains a relatively small amount of material (i.e., has a low bulk density), and is not part of the consolidated sediment bed. Second, storm events may increase current velocities or generate wind waves, which may increase near-bed velocities sufficiently to cause erosion at the surface of the consolidated bed. The eroded sediment may be transported to other areas in the estuary and be re-deposited, or it may be transported out of the estuary and into the adjacent coastal waters.

The Patrick Bayou watershed drains an area of about 2,800 acres and it contains a mixture of urban, industrial and rural land. The upper portion of the bayou consists of a gunnite-lined channel for rapid transport of storm water. Downstream of the gunnite-lined side and earthen bottom channel, the bayou extends for a distance of about 7,500 feet until it connects with the HSC. Within this region, which is the focus of the modeling study described in this report, the bayou consists of sub-tidal and inter-tidal areas with most of the sediment bed being composed of cohesive (muddy) sediment. Water depths in the bayou vary over the course of a tidal cycle, with typical water depths ranging from 2 to 9 feet.

Circulation in Patrick Bayou is affected by diurnal tides with a typical tidal range of 2 feet. During conditions of low freshwater flow, inter-tidal areas will drain during ebb tide and mudflats will be exposed at various locations. Storm surges during significant storm events also affect water levels and circulation. Despite the presence of salinity in the bayou during low-flow conditions, the water column is not significantly stratified (i.e., typical vertical

variation in salinity of 1-3 parts per thousand [ppt] between surface and bottom) mainly because of relatively shallow water depths in the bayou.

1.2 Definitions of Sediment Transport Terms

Various technical terms related to sediment transport processes are used throughout this report. For convenience, brief definitions of these terms are provided here:

- **Annual time scales:** Refers to time periods of one to 10 years, with average or “typical” conditions being the focus of the sediment transport processes that are examined or discussed. Temporal variability in the processes exists but conclusions or observations generally relate to long-term average conditions.
- **Depositional environment:** An area in which the sediment bed is net depositional (i.e., bed elevation increasing) over annual time scales. The bed may experience episodic erosion as a result of high-flow events.
- **Erosional environment:** An area in which the sediment bed is net erosional (i.e., bed elevation decreasing) over annual time scales. The bed may experience net deposition over time scales of less than a year.
- **Dynamic equilibrium:** The condition in which the sediment bed is neither net erosional nor net depositional, with minimal changes in bed elevation occurring over annual time scales. The bed may experience episodic erosion as a result of high-flow events or net deposition over short time scales.
- **Episodic erosion:** Bed scour that occurs during an episodic high-flow event. The occurrence of episodic erosion at a particular location does not necessarily mean that an erosional environment exists at that location; a depositional or dynamic equilibrium environment can experience episodic erosion. During these events, current velocities are sufficiently fast to erode the bed at some locations. Generally, episodic erosion occurs over periods of hours to days.
- **Net depositional:** The condition in which a portion of the sediment bed, or a reach of the river or waterway, experiences more deposition (i.e., settling of sediment from the water column onto the bed) than erosion (i.e., scour from the bed to the water column) over periods of about 1 year or longer (i.e., annual time scales). The net sedimentation rate is the rate at which net deposition occurs.

Episodic erosion can occur during periods of net deposition. For example, a net depositional area may experience episodic erosion, but more sediment is deposited on the bed over one or more years than is eroded during a small number of high-flow events (i.e., freshwater inflow with a return period of 2 years or greater) during that same period. This scenario was shown to occur in Patrick Bayou from the modeling results presented in this report.

1.3 Study Objectives

The primary goal of the sediment transport modeling study is to develop a reliable management tool that can be used to understand site-specific conditions and to evaluate the efficacy of different remedial alternatives. Specific objectives of this study are to:

- Develop a numerical model that can be used as a quantitative tool to evaluate short-term and long-term sediment transport processes and trends in Patrick Bayou.
- Develop a conceptual site model (CSM) for sediment transport within the Site.
- Provide information to support the FS and inform remedial decision-making.

Sediment transport and sediment stability information are crucial components of a CSM for sediment transport for Patrick Bayou. In general, CSMs for sediment transport are narrative or graphical representations of processes that influence the transport and fate of physical media (e.g., water, soil, sediment) within a study area of interest. Conceptual site models may incorporate both spatial and temporal elements.

Only sediment transport modeling was conducted during this study; a chemical transport and fate model was not developed. However, several issues concerning the potential effects of sediment transport on chemical transport and fate were addressed through application of the sediment transport model. Multi-year simulations were conducted to predict long-term changes in bed elevation (i.e., net sedimentation rate), as well as changes in surface-layer sediment composition. These results will be used in the FS to estimate the rate of natural recovery in Patrick Bayou attributable to sediment transport processes for various management strategies. Specific questions that are addressed using the sediment transport model for long-term, multi-year periods include:

- What areas in Patrick Bayou are net depositional, net erosional, or in dynamic equilibrium?

- How does the composition of the surface-layer sediment change over time as external sediment loads become incorporated into the sediment bed?
- What is the effect of high-flow events on episodic scour in otherwise net depositional areas?
- What is the potential depth of scour during high-flow events in areas that are net depositional, net erosional, or in dynamic equilibrium?

In addition, the potential for re-exposing buried sediments during high-flow events was evaluated with the model. The FS will examine whether the predicted scour depths have the potential for re-exposing buried sediments with COPC concentrations at levels of concern, and whether specific remedial actions are warranted to address bed scour during high-flow events. For episodic high-flow events, questions of interest include:

- What areas in Patrick Bayou are depositional and what areas experience erosion during a high-flow event?
- In the areas that experience erosion during high-flow events, what is the potential depth of scour?
- What is the potential for re-exposing buried sediments?

The following model outputs were used to achieve the goals of this study:

- Areas of net deposition and net erosion, areas that experience erosion during a high-flow event, and areas that are in dynamic equilibrium
- Spatial and temporal changes in bed elevation and composition
- Water-column concentrations of suspended sediment (temporally and spatially variable)
- Changes in composition of existing surface-layer sediment as a result of external sediment loads
- Fate of sediment that is eroded from the bed

1.4 Overview of Technical Approach

The modeling framework for this study consisted of three models that are linked together: 1) watershed (hydrology); 2) hydrodynamics; and 3) sediment transport. The development,

calibration and application of the modeling framework for Patrick Bayou involved the following basic steps:

- Collection, compilation, and analysis of data related to watershed hydrology, hydrodynamics and sediment transport
- Development and calibration of the watershed model
- Development and calibration of the hydrodynamic model
- Development, calibration and validation of the sediment transport model
- Use of the calibrated model as a tool to address study questions related to sediment transport

An overview of the technical approach used to implement these five steps is provided below.

The first step in developing a modeling framework for Patrick Bayou was collection, compilation and analysis of data for the three models. For the watershed model, these data included: watershed delineation; type of land cover; watershed topography; precipitation; and measurements of freshwater inflow to the bayou. Data needed for the hydrodynamic model included: geometry and bathymetry of the bayou and HSC; tidal elevation; salinity; and current velocity. Data requirements for the sediment transport model included: bulk bed properties (e.g., grain size distribution, dry density); erosion properties of bayou sediment; sediment loading from external sources; suspended sediment concentration; and net sedimentation rate. These data were used to develop a wide range of inputs to the modeling framework, including initial conditions, boundary conditions, forcing functions, spatial properties within the watershed and bayou, and model parameters.

Development and calibration of the watershed model was the first step in creating the modeling framework for the bayou. The watershed model was used to predict freshwater inflow to Patrick Bayou due to runoff from the surrounding watershed during rain events. This information was used as input to the hydrodynamic model. Flow rate data collected at three locations in the bayou during October 2006 were used to calibrate the watershed model.

The hydrodynamic model was used to predict water surface elevation (water depth), current velocity and salinity in the bayou and HSC. A three-dimensional model was used so that

vertical variations in current velocity and salinity can be predicted. Use of a three-dimensional model is also necessary for simulating density-driven currents in this estuarine system. The hydrodynamic model was calibrated using water surface elevation and current velocity data collected in the bayou during October 2006. The following hydrodynamic information was transferred to the sediment transport model: water depth, current velocity and bed shear stress.

The sediment transport model predicts suspended sediment concentration, deposition and erosion fluxes, and bed elevation change. The model can also be used to track the transport and fate of sediment from different sources (e.g., original bed, external sediment loads). A two-step process was used to calibrate the sediment transport model by adjusting two model inputs: 1) settling speed of cohesive (clay/silt) sediment; and 2) incoming sediment load during low-flow conditions. First, the model was calibrated using suspended sediment concentration data collected during several high-flow events that occurred in October 2006 by adjusting the settling speed of cohesive sediment. Second, net sedimentation rate data from the bayou were used to calibrate the model over multi-year periods by adjusting the incoming sediment load during low-flow conditions. The model was validated using empirical estimates of the rate of attenuation of chemical concentrations in the assumed mixing-zone (0-10 cm) layer of the sediment bed.

Successful calibration and validation of the model produces a reliable tool to answer the study questions posed in Section 1.3. The model was used to simulate sediment transport during high-flow events, including an event with a return period of 100 years. A primary result of this analysis was predictions of the location and depth of bed scour in the bayou after a high-flow event. The effect of external sediment loads on the composition of surface-layer bed sediment was evaluated using the results of a 14-year simulation. These results may be used to estimate the rates of natural attenuation in the mixing-zone layer due to deposition of sediment from external sources. The mixing-zone layer is the surface-layer of the sediment bed where active physical mixing occurs due to biological burrowing (bioturbation) and hydrodynamic forces. To evaluate uncertainty in model predictions associated with uncertainty in model inputs, sensitivity and uncertainty analyses were conducted as part of the high-flow event and external sediment load analyses.

1.5 Report Organization

The main body of this report presents an overview and general description of the modeling framework and technical approach. The report focuses on presenting and interpreting model results, and synthesizing those results with other studies and empirical evidence from Patrick Bayou. The primary goal of the main body of this report is to address the questions posed in Section 1.3. This report is organized into these main sections:

- Executive Summary
- Section 1: Introduction
- Section 2: Development, Calibration, and Validation of Modeling Framework
- Section 3: Results of Diagnostic Modeling Analyses
- Section 4: Summary and Synthesis of Results
- Section 5: References

The main body of this report is supported by these appendices:

- Appendix A: Details of Sediment Transport Theory and Formulation
- Appendix B: Analysis of Erosion Rate (Sedflume) Data
- Appendix C: Boundary Conditions for 14-Year Simulation

2 DEVELOPMENT, CALIBRATION, AND VALIDATION OF MODELING FRAMEWORK

This section presents an overview of the structure and capabilities of the Patrick Bayou modeling framework, which consists of three linked models: watershed, hydrodynamic, and the sediment transport models. Development, calibration and validation of the models are presented below, with a summary of the model reliability concluding this section.

2.1 General Description of Modeling Framework

The mathematical modeling framework that was applied to Patrick Bayou consists of watershed, hydrodynamic and sediment transport models that are linked together (Figure 2-1). The watershed model was used to predict the freshwater inflows to the study area due to precipitation in the surrounding watershed. The freshwater inflows predicted by the watershed model are then used as inputs to the hydrodynamic model, which simulates the movement of water in the bayou. The hydrodynamic model accounts for the effects of the following factors on water movement in Patrick Bayou: freshwater inflow from the surrounding watershed; tides in the HSC; and estuarine circulation resulting from density differences between seawater and freshwater. The hydrodynamic model is used to simulate temporal and spatial changes in water depth, current velocity, and bed shear stress. This information is transferred from the hydrodynamic model to the sediment transport model, where it is used to simulate the erosion, deposition, and transport of sediment in the bayou. The sediment transport model is used to simulate temporal and spatial changes in: suspended sediment concentrations in the water column; bed elevation changes (i.e., bed scour depth, net sedimentation rate); and changes in sediment bed composition (i.e., relative amounts of clay, silt, and sand from different sources).

The modeling framework provides a deterministic approach for simulating sediment transport within Patrick Bayou. The sediment transport model simulates the movement of sediment by suspended load (i.e., primarily clay, silt, fine sand). Bed-load transport of sediment (i.e., near-bed movement of coarse sand and gravel) is not simulated in this study because this mode of sediment transport is minimal in the bayou. The hydrodynamic and sediment transport models are constrained by governing equations that are based on the conservation of mass and momentum. Mechanistic formulations and algorithms are used in the sediment transport model to simulate deposition and erosion of cohesive and non-

cohesive sediment. The formulations and algorithms used to simulate deposition and erosion are based on empirical information and data from a wide range of laboratory and field studies (see Appendix A for a detailed discussion of the theory and equations used in the sediment transport model). In addition, site-specific data are used to determine various parameters used in the sediment transport model, which provides additional constraints on the model.

2.2 Watershed Model

This sub-section describes the development and calibration of the watershed model. The primary objective of the watershed model is to predict direct runoff from the watershed surrounding Patrick Bayou based on rainfall and land-use characteristics of the watershed.

2.2.1 General Model Description

One of the primary variables used to predict runoff from land surfaces is the runoff curve number. This variable is an empirically derived parameter used in hydrology for predicting direct runoff or infiltration from excess rainfall (U.S. Department of Agriculture [USDA] 1986). The curve number method was developed by the USDA Natural Resources Conservation Service (NRCS), which was formerly called the Soil Conservation Service (SCS); this number is still popularly known as a "SCS runoff curve number". The runoff curve number was developed from an empirical analysis of runoff from small catchments and hill-slope plots monitored by the USDA. It is a widely used and efficient method for determining the approximate amount of direct runoff from a rainfall event in a particular area. The runoff curve number is dependent on the following characteristics of a watershed basin: hydrologic soil group, land use, treatment, and hydrologic condition. The runoff depth is calculated using:

$$Q = 2 (P - I_a) / (P - I_a + S) \quad (2-1)$$

where:

Q = runoff depth (inches)

P = amount of rainfall (inches)

S	=	potential maximum retention after runoff begins (inches)
I _a	=	initial abstraction (inches)

The initial abstraction is the amount of water retained by the ground before runoff begins, such as by infiltration or rainfall interception by vegetation. Through studies of many small agricultural watersheds by the USDA, I_a was determined to be proportional to S (i.e., I_a = C_a S), with the proportionality constant (C_a) ranging between 0 and 0.8. It is thus treated as a calibration parameter. Substituting the initial abstraction into Equation 2-1 produces a relationship of runoff (Q) as a function of rainfall (P) and retention (S). Discharge volume from a watershed, or sub-basin, is calculated by multiplying the runoff depth (Q) by the watershed area. The discharge volume is converted to a flow rate, which is the final product of the watershed model that is transferred to the hydrodynamic model, by dividing discharge volume by the model timestep.

The SCS developed the concept of the dimensionless curve number (CN), which is related to S as follows:

$$S = (1000 / CN) - 10 \quad (2-2)$$

The dimensionless CN ranges from 30 to 100; lower numbers indicate low runoff potential while larger numbers are for increasing runoff potential. The SCS has classified over 8,500 soil series into four hydrologic groups according to their infiltration characteristics. The hydrologic groups have been designated as A, B, C, and D (SCS 1972). Group A is composed of soils considered to have low runoff potential. These soils have a high infiltration rate even when thoroughly wetted. Group B soils have a moderate infiltration rate when thoroughly wetted. Group C soils are those which have slow infiltration rates when thoroughly wetted, and group D soils are those which are considered to have a high potential for runoff, since they have very slow infiltration rates when thoroughly wetted.

2.2.2 Model Inputs and Parameters

The watershed model requires the following data and information for input: amount of rainfall; land cover in the watershed; soil types in the watershed; hydrologic condition data;

curve numbers for the watershed; and sub-basin area. Using these inputs, the model predicts time-dependent runoff for each sub-basin in the study area. Model inputs for the Patrick Bayou watershed model consist of several spatial and temporal data-sets. Temporal data include rainfall, which is the primary forcing function for the model. Spatially-variable data-sets include: land cover; rainfall gauge locations; topographic digital raster images; and soil data. All spatial data were obtained from the Texas Natural Resource Information Service (see <http://www.tnris.state.tx.us/>).

The Patrick Bayou watershed was manually delineated into three sub-basins to route runoff from the watershed to the bayou inflow locations, which are located at three stations used during the October 2006 field survey. The U.S. Geological Survey (USGS) digital-raster-graphic image of the surrounding watershed, which was obtained during 1999 to 2000, contained contour elevation data that were used to estimate the boundaries of each sub-basin. Figure 2-2 shows the results of the sub-basin delineations for inflows located at stations PB075 (sub-basin 1), EF005 (sub-basin 2), and PB012 (sub-basin 3). The total area of the Patrick Bayou watershed is 2,775 acres, with sub-basins 1, 2, and 3 representing 69%, 11%, and 20% of the total watershed area, respectively.

Rainfall data were obtained from the Harris County Homeland Security and Emergency Management (HCOEM). HCOEM maintains nearly 900 gauges throughout Harris County that measure climate conditions. Four gauges were identified near the study area with rainfall data available during the model calibration period (Figure 2-3). The identification numbers for these four gauges are: 2230 (Toll Road East); 240 (B100 Armand Bayou at Beltway 8); 270 (B112 Willow Spring at Fairmont Parkway); and 640 (F216 Little Cedar Bayou at Sens Road). During initial development and testing of the watershed model, it was determined that averaging rainfall measured at the four stations (i.e., arithmetic average) provided the best estimate of precipitation in the watershed. The precipitation gauges also recorded rainfall on a sub-hourly basis with an inconsistent period between measurements. Therefore, the data were converted to hourly rainfall values for input to the watershed model. The volume of rainfall that flowed through each sub-basin was a function of the average rainfall from the four stations multiplied by the area of each sub-basin.

Land-use data, collected during 2002, were obtained from the Houston Galveston Area Council (HGAC). The data were divided into eight categories: high-intensity development; residential/light development; cultivated land; grassland; woody land; open water; wetland; and bare/transitional land. Based on observations of the digital ortho-photo quadrangles (i.e., satellite photographs) of the watershed, these categories were modified to better represent the land cover in the watershed. High-intensity development was divided into commercial development south of Highway 225 (Pasadena Freeway) and industrial development north of Highway 225. The spatial distribution of land-use categories for the watershed sub-basins is shown on Figure 2-4.

The spatial distribution of soil categories was determined through the State Soil Geographic (STATSGO) data-set, which was collected in 1994. STATSGO is a national data-set, developed and supported by the NRCS (NRCS 1994). The soil groups for the watershed sub-basins are presented on Figure 2-5. The study area is primarily composed of soil group D, which has a high potential for runoff. The STATSGO soils data were combined with the land-use data to provide information necessary for establishing the curve numbers within a sub-basin. Table 2-1 lists curve number ranges for each land-use and soil category (Maidment 1993).

Table 2-1
Curve Number Ranges for Different Land-Use and Soil Categories

Type of Land Cover	Curve Number Range: Hydrologic Soil Group B	Curve Number Range: Hydrologic Soil Group D
Commercial Development	89 – 98	89 – 98
Industrial Development	81 – 98	81 – 98
Residential/Light Development	68 – 85	84 – 92
Cultivated Land	70 – 81	80 – 91
Grassland	61 – 84	80 – 94
Woody Land	55 – 71	77 – 88
Open Water	100	100
Wetland	98	98
Bare/Transitional Land *	86 – 98	94 - 98

* Estimated

2.2.3 Calibration Approach and Results

The watershed model was calibrated using data collected during the October 2006 survey. During this field study, current velocity and water surface elevation were measured at different locations in the bayou (see Figure 2-6). The current velocity and water surface elevation data were used to estimate flow rates at stations PB075 and EF00. These flow rate estimates were used for calibration of the watershed model.

Using the average rainfall data from the four rainfall gauges as a forcing function for the model during October 2006, the watershed model predicted the excess rainfall for each sub-basin within the watershed. Model calibration was achieved by adjusting the following model inputs to optimize the agreement between predicted and estimated flow rate at the three stations: 1) initial abstraction (I_a); 2) rainfall-event duration; and 3) curve numbers. The adjustment of CN values was done on a basin-wide basis, with the CN values being constrained to the realistic range of values for a given land-use category. The rainfall-event duration represented the length of time a given land area would remain saturated and runoff occurred.

Different methods are available for quantifying the performance of a watershed model (ASCE 1993). Two relatively simple, yet important, measures of model performance are: 1) Nash-Sutcliffe model-efficiency coefficient (Nash and Sutcliffe 1970); and 2) deviation of runoff flow. The Nash-Sutcliffe coefficient (NS), which is used to assess the predictive power of a watershed model, is defined as:

$$NS = 1 - \frac{\sum_{i=1}^n (X_{oi} - X_{si})^2}{\sum_{i=1}^n (X_{oi} - X_m)^2} \quad (2-3)$$

where:

X_{oi} = observed discharge at time i
 X_m = mean observed discharge
 X_{si} = modeled discharge at time i

Nash-Sutcliffe coefficients can range from $-\infty$ to 1. A NS coefficient value of 1 corresponds to perfect agreement between predicted and observed flow rate (i.e., zero error). A NS coefficient value of 0 indicates that the model predictions are as accurate as the mean of the observed data. A NS coefficient value less than zero occurs when the mean value of the data is a better predictor than the model. Essentially, model accuracy increases as the NS coefficient approaches a value of one. The deviation of runoff volume (D_v) is defined as:

$$D_v = \frac{V^* - V}{V} \cdot 100 \quad (2-4)$$

where:

V^* = predicted runoff flow rate

V = measured runoff flow rate

This equation is similar to the percent difference between measured and predicted values.

While use of the NS coefficient is widely accepted as a general indicator of model performance, this approach has some weaknesses. In particular, it can be dependent on the timing differences between predicted and measured values. For example, the timing of a rainfall event may cause the model to predict the peak discharge during a storm at a different time than measured peak discharge because the model does not account for routing and temporary storage within the watershed. For this reason, a range of model metrics (e.g., correlation coefficient (R^2), NS coefficient, flow deviation) were considered when evaluating model performance.

Results of the model calibration are shown on Figure 2-7, with a statistical analysis of model-data comparisons presented in Table 2-2. Base-flow was subtracted from the flow rate data to yield rainfall runoff values for the model calibration. Base-flow was calculated as the mean sub-basin discharge during periods of zero precipitation. Model predictive capability was optimized during calibration, which produced the following input values for the calibrated model: 1) initial abstraction proportionality constant equal to 0.5 (i.e., $I_a = 0.5$ S); 2) maximum CN values for a given soil and land-use category (i.e., maximum values in

Table 2-1); and 3) rainfall-event duration of 72 hours. The correlation coefficient (R^2) in Table 2-2 is defined as correlation between predicted and measured flow rates, with a value of one representing perfect agreement between predicted and measured values.

Table 2-2
Statistical Analysis of Watershed Model Results for October 2006 Period

Watershed Sub-Basin	Correlation Coefficient (R^2)	NS Coefficient	Deviation of Runoff Volume (%)
PB075	0.86	0.86	-19
EF005	0.41	0.32	-38

The model-data comparisons shown on Figure 2-7 indicate that the model predictions are qualitatively consistent with observed flow rates at stations PB075 and EF005. Statistically, the best prediction of runoff occurs in sub-basin PB075. The statistical results for sub-basin EF005 suggests that this sub-basin, which is the smallest of the three sub-basins, is more sensitive to rainfall than the model predicts. This limitation in the model could be caused by the following: 1) land-cover changes since the generation of the land cover data-set; 2) mis-classification of the hydrologic soil group in the EF005 sub-basin; or 3) an artifact of the transformation of the sub-hourly precipitation data to hourly inputs. Despite these uncertainties, the model performs adequately for the purposes of this study.

2.3 Hydrodynamic Model

This sub-section presents the development and calibration of the hydrodynamic model for Patrick Bayou. The hydrodynamic modeling analysis provides predictions of current velocities, water depth, and bed shear stresses in the study area for a wide range of inflow and tidal conditions, with this information being transferred to the sediment transport model. The hydrodynamic model was calibrated using data collected during October 2006. The calibrated model was used to simulate hydrodynamics in the bayou and HSC for a 14-year period (1993 through 2006).

2.3.1 General Description

The hydrodynamic model that was applied in this study is the Environmental Fluid Dynamics Code (EFDC), which is supported by EPA. EFDC is a three-dimensional hydrodynamic model capable of simulating time-variable flow in rivers, lakes, reservoirs, estuaries, and coastal areas. The model solves the conservation of mass, momentum and salt equations, which are the fundamental equations governing the movement of water in an estuary. The effects of density-driven processes on circulation in an estuary, such as Patrick Bayou, are incorporated into EFDC. In addition, the model includes a sophisticated turbulence closure algorithm that simulates the effects of vertical turbulence on estuarine circulation. A characteristic of EFDC that is of importance for this study is the wetting-drying feature, which makes it possible to realistically simulate the flooding and drying of inter-tidal areas caused by tidal action in Patrick Bayou. The model has been applied to a wide range of environmental studies in large number of rivers, estuaries and coastal ocean areas. A complete description of the model is given in Hamrick (1992).

2.3.2 Numerical Grid and Geometry

The study area within Patrick Bayou that is included in the model domain extends from the bayou confluence with the HSC to station PB075, which is about 1.4 miles upstream of the confluence. Upstream of station PB075, the sides of the channel are gunnite-lined and the bed is composed of hard-packed sediment which experiences minimal erosion and deposition. Thus, this channelized region was excluded from the model domain because it behaves as a simple conduit for water and sediment from the sub-basin 1 of the watershed to the bayou. The model domain includes a four-mile portion of the HSC, which extends from the National Oceanic and Atmospheric Administration (NOAA) gauging station at Battleship Texas State Park (downstream boundary) to a location about two miles upstream of the bayou confluence. Inclusion of the HSC in the model domain increases the predictive capability and reliability of the hydrodynamic and sediment transport models.

The shoreline delineation in Patrick Bayou was verified using geo-referenced aerial photographs taken in 2007. The model domain in the bayou was laterally extended from the shoreline to a topographic elevation of +5 feet with respect to mean sea level (MSL). This extension beyond the shoreline makes it possible to realistically simulate flow in the bayou

during rare high-flow events when inundated areas go beyond normal inter-tidal areas in the bayou. Delineation of the shoreline and the navigation channel in HSC was based on information from NOAA Electronic Navigation Chart (ENC) data-base.

A boundary-fitted curvilinear numerical grid was generated to delineate the geometry of the model domain (Figure 2-8). The numerical grid contains about 900 grid cells in the horizontal plane and 10 layers in the vertical direction, which resulted in a total of about 9,000 grid cells. Patrick Bayou is delineated using 50 grid cells in the along-channel direction and 8 grid cells in cross-channel direction. Average dimensions for a grid cell within the bayou are 42 feet long and 17 feet wide.

Bathymetry data in Patrick Bayou were obtained from a field survey conducted during June 2005. Bathymetry in the navigation channel of the HSC were determined from the NOAA nautical chart (Houston Ship Channel, 11325, 11329) published in April 2000. The bathymetry in the bench areas of the HSC was estimated based on NOAA ENC data. Bathymetry data from all sources were incorporated to generate a continuous surface that represents the bed elevation in the model domain; an interpolation process was used to create the bed elevation surface. The spatial distribution of bathymetry, as projected onto the numerical grid, within the bayou and HSC is shown on Figure 2-8.

2.3.3 *Boundary Conditions*

Inputs for three boundary conditions need to be specified for the hydrodynamic model: 1) freshwater inflow at the upstream boundaries of the bayou; 2) salinity at the upstream and downstream HSC boundaries; and 3) water surface elevation at the upstream and downstream HSC boundaries. As discussed in Section 2.2, freshwater inflows for the hydrodynamic model were determined using the results of the watershed model. Salinity and water surface elevation at the upstream and downstream boundaries in the HSC were specified using site-specific data.

The watershed model only predicts freshwater inflow to Patrick Bayou during rainfall events; the model does not predict base-flow discharge (i.e., freshwater inflow during periods with no precipitation). Base-flow discharge was estimated using flow rate data collected at

stations PB075 and EF005 during October through December, 2006. Only data collected during the days of no precipitation were used in the base-flow analysis. Furthermore, flow rate data collected within a 48-hour period following a rainfall were excluded. Cumulative frequency distributions of base-flow data collected during the 2006 field study at stations PB075 and EF005 are presented on Figure 2-9. For station PB075 (i.e., Main inflow), base-flow discharge ranges from about 1 to 100 cubic feet per second (cfs), with an average value of 28 cfs. For station EF005 (i.e., East Fork), base-flow discharge is about a factor-of-ten less than the Main inflow, with an average value of 2 cfs and a range of about 0.1 to 10 cfs.

Salinity at the upstream and downstream boundaries of the model in the HSC is specified during the portions of the tidal cycle when flow is entering the model domain (i.e., ebb tide at the downstream boundary and flood tide at the upstream boundary). Based on salinity data used in an earlier hydrodynamic modeling study (Berger et al. 1995), average salinity near Morgan's Point ranges from 10 to 20 ppt. It is assumed that minimal differences in salinity exist between the upstream and downstream boundaries in HSC, so a salinity of 16 ppt was specified during incoming flow at both boundary locations. In addition, minimal vertical stratification typically occurs in the HSC, so the salinity boundary condition (16 ppt) was assumed to be constant in the vertical direction.

Boundary conditions for water surface elevation (WSE) in the HSC need to incorporate the following processes: 1) diurnal tides generated in the Gulf of Mexico (GOM); 2) low-frequency storm events (e.g., hurricane storm surges); and 3) long-period waves propagating up and down the HSC. Thus, it was necessary to use WSE data collected at NOAA tidal gauge stations located near the study area so the combined effects of diurnal tides and low-frequency storm events were properly incorporated into the model boundary conditions. The closest NOAA tidal gauge station is located at Battleship Texas State Park, which coincides with location of the downstream model boundary (Figure 2-10). Verified WSE data at the Battleship Texas State Park station are available for October 2006, but data are not available for the entire 14-year period from 1993 through 2006. Thus, it was necessary use WSE data collected at the Morgans Point station (Figure 2-10) for the 14-year simulation (1993 through 2006). Because the Battleship Texas State Park and Morgans Point stations are located about eight miles apart, it was necessary to compare contemporaneous WSE data collected at the two stations to determine if significant differences in WSE amplitude and

phase exist. Comparisons of WSE data obtained at the two stations for the four-month period from April through July 2007 are shown on Figure 2-11. These comparisons show that no significant differences exist in WSE amplitude and phase between the two stations. Thus, verified WSE data from the Battleship Texas State Park station were used as model input at the downstream HSC boundary for the October 2006 simulation period, while WSE data from the Morgans Point station were used for the 14-year simulation (1993 through 2006).

The hydrograph for total freshwater inflow to Patrick Bayou for October 2006, which includes base-flow discharge, is shown on the top panel of Figure 2-12. The maximum total peak inflow of 5,900 cfs occurred on October 16 (return period of about 10 years), with discharge from the Main inflow, East Fork, and direct runoff contributing 66%, 11%, and 23%, respectively, to the maximum total inflow. The average total inflow to the bayou was 240 cfs during October 2006. As shown on Figure 2-12, high-flow events in the bayou are flashy and typically occur over timescales of 6 to 24 hours. Hydrographs for freshwater inflow for the 14-year period from 1993 through 2006 are presented in Appendix-C. The average total freshwater inflow from the watershed (i.e., excluding inflow from the OxyChem outfalls) for this 14-year period is 40 cfs, with discharge from the Main inflow, East Fork, and direct runoff contributing 85%, 8%, and 7%, respectively, to the total inflow from the watershed.

In addition to freshwater inflow from the surrounding watershed, water is discharged into Patrick Bayou from various outfalls and storm drains. The locations of the process outfalls and storm drains in the vicinity of the Patrick Bayou study area are shown in Figure 2-13. The current location of the inflow (upstream) boundary of the model domain (i.e., numerical grid) is shown as a thick red line on this figure. Figure 2-13 shows several outfalls and storm drains located upstream of the model domain, as well as outfalls and storm drains located within the model domain. Anchor QEA personnel obtained information and data on outfalls and storm drains from: Greg Holleman (City of Deer Park wastewater treatment plant [WWTP]); Richard Tisch (Praxair); Jeffrey Adamski (Glenn Springs Holdings); Norman Mollard (Lubrizol); and Jeff Stevenson (Shell).

The outfalls that are located upstream of the inflow boundary on the Main channel of the model are: City of Deer Park WWTP outfall; Lubrizol outfall; Praxair outfall; Rohm & Haas outfall; and Shell outfall. In addition, four storm drains are located upstream of the inflow boundary. Table 2-3 shows the average monthly flow rate at these outfalls, from data collected between January 1998 and October 2006. The average base flow in the Main channel is 28 cfs, based on flow rate data collected at station PB075 (i.e., at upstream boundary of the model). The sum of the average monthly flows for the four outfalls is approximately 7.3 cfs, which is about 26% of the average base flow. Thus, the discharge from outfalls located upstream of the model inflow boundary is included in the measured flow rate at station PB075, which means that the flow from these outfalls does not have to be explicitly specified for model input.

Table 2-3
Mean and Range of Outfall Flow Rates During 1998-2006 for Outfalls Upstream of Model Inflow Boundary

Outfall	Average Monthly Flow Rate (cfs)	Flow Rate Range (cfs)
City of Deer Park WWTP	5.0	3.0 – 8.7
Lubrizol	1.4	1.0 – 2.0
Praxair	0.1	0.05 – 0.9
Shell Chemical 001	0.8	0.0 – 10
Shell Refinery 001	1.4	0.6 – 1.9
Total	8.7	4.7 – 23.5

Three OxyChem outfalls are located downstream of the inflow boundary and flow directly into Patrick Bayou: outfalls 001, 002, and 003 (see Figure 2-13). Monthly-average flow rate data for the three outfalls were provided by Jeffrey Adamski of Glenn Springs Holdings for the period between 1997 and 2006 (see Figure 2-14). No outfall flow data are available prior to 1997. All three outfalls are a combination of process and stormwater runoff flow. The primary source of water for the three outfalls is the Houston Ship Channel water, which is supplemented with rainwater during storm events as well as minor continuous amounts of industrial water (i.e., clarified Trinity River water) or softened water from on-site softeners. Outfall 001 has become a rainwater-only outfall due to closure activities conducted after 2005. Average discharge from outfall 002 discharge decreased significantly (i.e., from about

101 cfs to about 28 cfs) after the former chlor-alkali facility was shut down in late 2001 through early 2002.

In addition, storm drain outfalls located downstream of the inflow boundary include R003, R004, and R009, which are along the western shore of Patrick Bayou (Figure 2-13).

Inflow from the three OxyChem outfalls were specified for model input using discharge data collected during the period from 1997 through 2006 (see Figure 2-14). Monthly-average flow rate values were used for model input, with the inflow from a particular outfall held at a constant value for an entire month (i.e., no variation on a daily or hourly basis). The 14-year period (i.e., 1993 through 2006) used for model calibration includes a 4-year period prior to 1997 during which discharge data are not available for outfalls 001, 002 and 003. Thus, outfall discharges were estimated for the pre-1997 period. The average flow rates for outfalls 001 and 002 during the 6-year period of 1997 through 2002 were used to specify model inputs for outfalls 001 and 002 during the pre-1997 period. This 6-year period (1997 to 2002) was assumed to be representative of the pre-1997 period for outfalls 001 and 002 because discharge from outfalls 001 and 002 were significantly lower during the post-2002 period. No significant temporal trend in discharge from outfall 003 was evident in the data (Figure 2-14), so the average flow rate for outfall 003 during the period from 1997 through 2006 was assumed to be representative of the pre-1997 period (Figure 2-15).

The watershed model was used to predict direct runoff during rain events from the area immediately adjacent to Patrick Bayou. These results from the watershed model were input to the revised version of the hydrodynamic model at the three storm drain locations (i.e., R003, R004, and R009) along the western shore. The total direct runoff predicted by the watershed model was evenly divided between the three storm drain locations.

The effects of low-frequency storm events on WSE in the HSC, and consequently Patrick Bayou, are evident during October 2006 (top panel, Figure 2-12). Due to Tropical Storm Norman, a storm surge occurred during October 15 and 16, 2006, with a significant influx of water from the GOM and Galveston Bay propagating into the HSC and the bayou. On October 26 and 27, 2006, a large outflow of water from the HSC and the bayou occurred due to offshore winds blowing water out of the Galveston Bay system and into the GOM

(i.e., Galveston Bay set-down). These storm events, which occur at irregular intervals, have important effects on hydrodynamic and sediment transport processes in Patrick Bayou.

The long-period (tidal) waves propagating up and down the HSC are progressive waves due to the geometry of the system. Thus, it is valid to assume that there are no differences in WSE amplitude at the two boundaries in HSC. However, because the upstream and downstream boundaries are separated by a distance of approximately 3.7 miles, a difference will exist in the phase of the progressive wave at these two boundary locations. To estimate the phase difference between the upstream and downstream boundaries, an idealized progressive wave model of the HSC was developed and used to determine that the phase difference between the two boundaries is about 10 minutes. Numerical experiments with the hydrodynamic model demonstrated that the phase shift is necessary for realistic simulations in the HSC. Use of the 10-minute phase shift between the upstream and downstream boundaries produces model predictions of net tidally-averaged flow (i.e., residual flow) moving from upstream to downstream in the HSC, which is qualitatively correct.

2.3.4 Calibration Approach and Results

Assessment of the predictive capability of the hydrodynamic model was achieved through comparisons of predicted and measured WSE and current velocity in the bayou during October 2006. The model parameter that was adjusted to achieve the optimum agreement between predicted and observed water surface elevation and current velocity was the effective bed roughness (z_0) in the hydrodynamic model, which represents the total roughness due to form drag and skin friction (see Appendix A.1). Generally, z_0 ranges from about 0.1 to 10 centimeters (cm).

Calibration for the hydrodynamic model of Patrick Bayou was conducted using WSE and depth-averaged current velocity data collected at station PB020 (see Figure 2-6) during October 2006. Freshwater inflows and WSE in the HSC during the calibration period are shown on Figure 2-12. During October 2006, total freshwater inflow to the bayou had a maximum peak value of about 5,900 cfs, which corresponds to a high-flow event with a

return period of approximately 10 years. The ratio between the peak flow rate during this high-flow event (5,900 cfs) and average inflow from the watershed (40 cfs) is about 150.

A value of 1 cm for total effective bed roughness produced the best agreement between observed and predicted WSE and depth-averaged current velocity at station PB020 during the October 2006 calibration period (Figure 2-16). The hydrodynamic model simulates changes in WSE in the bayou during the storm surge that occurred on October 15-16, 2006 and also during the Galveston Bay set-down event that occurred on October 27, 2006. During high freshwater inflow events, the predicted WSE and current velocity at station PB020 are in good agreement with the observed data. During periods of low freshwater inflow, predicted and observed current velocities are in good agreement, but WSE is under-predicted by about 0.5 feet compared with the observed data. The average absolute and root-mean-square (RMS) errors for WSE and current velocity during the calibration period are listed in Table 2-4. Overall the results from the calibration indicate the hydrodynamic model is able to adequately simulate WSE and current velocity in Patrick Bayou for a wide range of freshwater inflow and tidal conditions.

Table 2-4
Results of Error Analysis for Hydrodynamic Model Calibration Period

Model Output	Average Absolute Error	RMS Error
Water surface elevation (m)	0.50	0.55
Current velocity (cm/s)	8.2	15

2.4 Sediment Transport Model

2.4.1 Model Structure and Capabilities

Sediments of particle sizes ranging from clay to sand are transported within Patrick Bayou primarily as suspended load. Suspended load transport corresponds to the movement of sediment, primarily clay, silt, and fine sand, suspended in the water column. Bed-load transport is the movement of sand and gravel in a thin layer (i.e., about 1 millimeter [mm] to 1 cm thick) just above the sediment surface.

The sediment transport model used in this study, referred to as SEDZLJ, is capable of simulating erosion and deposition of sediment within cohesive (i.e., muddy) and non-cohesive (i.e., sandy) bed areas (Ziegler et al. 2000; Jones and Lick 2001; QEA 2008). The sediment transport model has the following characteristics and capabilities: 1) three-dimensional transport of suspended sediment in the water column; 2) use of Sedflume core data to specify erosion rate parameters; 3) specification of spatially variable bed properties; and 4) inclusion of a sediment bed model that tracks temporal changes in bed composition (i.e., sediment particle size, sediment source). For this study, bed-load transport was not simulated because of the negligible bed-load that occurs in a cohesive sediment bed, such as exists in Patrick Bayou. A detailed description of the formulations used in and structure of the sediment transport model is provided in Appendix A.

The hydrodynamic model within EFDC is linked to the sediment transport model, which is incorporated into EFDC, via a coupling file, which transfers hydrodynamic transport information (e.g., current velocity, water depth) from the hydrodynamic model to the sediment transport model. For a particular period, the hydrodynamic model is used to simulate circulation within the study area. During the hydrodynamic simulation, the relevant transport information is output to the coupling file every 15 minutes during the simulation. This frequency of output is necessary to accurately represent the effects of tidal estuarine circulation on sediment transport. The coupling file is used as input to the model during a sediment transport simulation. This process significantly reduces the time required to complete a sediment transport simulation because: 1) a larger timestep can be used than if the hydrodynamic and sediment transport models are running in parallel; and 2) the computational burden is lower because the hydrodynamic calculations do not have to be repeated every time a sediment transport simulation is repeated for a specific time period. For example, the timesteps used in the hydrodynamic and sediment transport models are one and four seconds, respectively. Use of the coupling-file approach reduces the simulation times by nearly a factor-of-eight, with respect to a simulation that has the hydrodynamic and sediment transport models running in parallel. Thus, long-term, multi-year simulations are only possible using the coupling-file approach.

The coupling between the hydrodynamic and sediment transport models produces a limitation on the predictive capabilities of the modeling framework. This coupling is one-way with no feedback between the two models; output from the hydrodynamic model feeds into the sediment transport model. Changes in bed elevation predicted by the sediment transport model are not incorporated into the hydrodynamic model (i.e., bathymetry in the hydrodynamic model is assumed to remain constant with time). While this limitation may appear to reduce the reliability of the model predictions, successful calibration and validation of the model indicate that this limitation in the modeling framework does not have a significant effect on the predictive capabilities of the sediment transport model in Patrick Bayou.

A summary of the primary assumptions and approximations used in the hydrodynamic and sediment transport models is presented in Table 2-5. Justification for each assumption and approximation is also given in that table.

Table 2-5
Approximations and Assumptions Used in Hydrodynamic and Sediment Transport Models

Model	Approximation or Assumption	Justification
Hydrodynamic	Effect of temperature gradients on water density is assumed to be negligible	Unlike lakes and reservoirs, significant thermal stratification does not occur in a tidal system like Patrick Bayou.
Hydrodynamic	Effect of local winds on currents in the Bayou is assumed to be negligible	The bayou geometry, with relatively small open fetches, minimizes the effects of wind-driven currents in Patrick Bayou. The effects of large-scale winds on the HSC-Galveston Bay system, and the Bayou, is incorporated into the tidal elevation data specified at the boundaries of the hydrodynamics model in the HSC.
Hydrodynamic	Vertical variations in water column variables are approximated using 10 layers	Simulating estuarine hydrodynamics using 10 vertical layers has been demonstrated to produce satisfactory results in numerous modeling studies.
Sediment transport	Effect of form drag on bed shear stress is negligible in cohesive bed areas	Generally, bed forms are not a significant feature of cohesive sediment beds.

Model	Approximation or Assumption	Justification
Sediment transport	Sediment bed in Patrick Bayou is assumed to be cohesive	Sediment samples collected in the bayou are primarily composed of cohesive sediment, with isolated, localized areas of non-cohesive sediment also being present.
Sediment transport	No erosion is allowed to occur in the sediment bed of the Houston Ship Channel	Erosion rate data are not available for the HSC, and neither are bed-type data. Thus, specifying bed property parameters for that area is highly uncertain.
Sediment transport	Bed-load transport is assumed to be negligible.	The morphology and bed composition (i.e., primarily cohesive) of Patrick Bayou indicate that minimal bed-load transport occurs in the bayou.
Sediment transport	Predicted spatial distribution of bed composition (i.e., evolved bed) is assumed to be best estimate of initial conditions	Based on extensive model testing and diagnostic simulations, it was determined that the model was the most reliable method for specifying initial conditions (see Section 2.4.3 for discussion).
Sediment transport	Distribution of sediment particle sizes is assumed to be represented by 4 size classes	Sufficient composition data for external sediment loads are not available to warrant use of additional size classes. Previous studies have developed reliable models using 2, 3, or 4 size classes (e.g., QEA 2008).
Sediment transport	Vertical variations in erosion properties are represented using 5 layers, with 0-20 cm represented by four 5-cm layers	Vertical variations in erosion properties were specified based on the vertical distribution of Sedflume data (see Appendix B).
Sediment transport	Bed properties below 25-cm depth are assumed to be equal to 20-25 cm layer values	Erosion rate data are not available below 25-cm depth, so data collected in the 20-25 cm layer are the best estimate for values below 25 cm. Typically, consolidation effects cause erosion rates to decrease with depth in the bed. Thus, this assumption produces conservative model predictions.
Sediment transport	Effects of flocculation on cohesive settling speed are not explicitly simulated	A previous modeling study of an estuarine system (QEA 2008) successfully used this approximation.
Sediment transport	Effects of consolidation on the erosion properties of deposited cohesive sediment	The effects of consolidation on cohesive erosion properties are implicitly incorporated into the Sedflume data (i.e.,

Model	Approximation or Assumption	Justification
	are not explicitly simulated	erosion rates generally decrease with increasing depth in the bed). An explicit consolidation model primarily addresses the issue of the erosion properties of freshly deposited material (i.e., fluff layer). The objectives of this study are focused on the evolution of the consolidated bed, so inclusion of the fluff layer in the model was not needed to meet study objectives.
Sediment transport	Erosion properties of bayou sediment were assumed to be approximately spatially constant in the horizontal plane.	Sufficient Sedflume data were not available to use standard interpolation methods to develop a horizontal distribution of erosion properties. The potential effect of this approximation on model predictions was evaluated during a sensitivity analysis.
Sediment transport	Erosion rates measured by Sedflume are assumed to be representative of in-situ bed erosion	Use of Sedflume data in other modeling studies has been shown to produce reliable results.
Sediment transport	Dry density is assumed to be spatially constant within cohesive and non-cohesive bed areas	Sufficient data are not available to reliably develop spatial distributions of dry density in the cohesive and non-cohesive bed areas (which have different dry density values).
Hydrodynamic and sediment transport	No feedback between hydrodynamic and sediment transport models (i.e., changes in bed elevation due to erosion and deposition are not incorporated into the hydrodynamic model)	Direct coupling of the models (i.e., incorporation of feedback) would make conducting long-term, multi-year simulations infeasible.

Inputs for the sediment transport model are separated into three broad categories:

1) sediment properties; 2) bed properties; and 3) boundary conditions. Sediment properties correspond to the physical properties of sediment particles (i.e., effective particle diameter, settling speed). Bed properties range from bulk bed characteristics (e.g., dry density, grain size distribution) to erosion rates. Determining boundary conditions for the model corresponds to the specification of sediment loads at different inflow locations. A summary

of model inputs is presented in Table 2-6, which includes the data sources and an estimate of the level of uncertainty for each input.

Table 2-6
Model Inputs and Data Sources

Model Input	Data Source	Level of Uncertainty
Bathymetry and geometry	Field survey conducted during June 2005; NOAA nautical charts	Measurement uncertainty in vertical bed elevation is: ± 0.5 ft in Patrick Bayou
Freshwater inflow rate	Watershed model predictions which depend on rainfall data collected at 4 stations	Level of uncertainty in predicted inflow rate is about $\pm 25\%$
Tidal elevation in HSC	NOAA gauging stations at Battleship Texas State Park and Morgans Point	Accuracy of tidal elevation measurements is ± 0.3 cm
Sediment bed: erosion parameters	Sedflume study conducted during June 2007; 12 cores	Level of uncertainty of Sedflume data for a specific core cannot be assessed. Potential uncertainties due to spatial variability were addressed through a sensitivity analysis.
Sediment bed: dry density	Samples collected from 12 cores during June 2007 field study	95% confidence interval, with respect to average value, is 0.70-0.84 grams per cubic centimeter (g/cm^3)
Sediment bed: effective bed roughness (D_{90})	9 samples from cores collected during October 2006 field study	95% confidence interval, with respect to average value, is 180-270 micrometers (μm)
Upstream sediment load: magnitude	Field study conducted during October 2006	Annual sediment load estimates have approximately factor-of-two level of uncertainty.

2.4.2 Sediment Properties

For estuaries such as Patrick Bayou, suspended sediment particles typically have a range of sizes, with particle diameters ranging from less than 1 μm clays to coarse sands on the order of 1,000 μm (van Rijn 1993). Simulation of the entire particle size spectrum is impractical for

several reasons: simulation times and array-storage requirements increase with each particle-size class that is added; limitations in grain size distribution data for the sediment bed make it difficult to specify initial conditions for the entire spectrum; and sparse data for the composition of the external sediment load make it problematic for specifying this boundary condition for the entire spectrum. Therefore, particles were separated into four classes: 1) clay and silt with particle diameters less than 62 μm ; 2) fine sand (62 to 250 μm); 3) medium and coarse sand (250 to 2,000 μm); and 4) gravel (greater than 2,000 μm). Use of these four size classes provides an adequate approximation of the grain size distribution of bed sediment observed in Patrick Bayou for achieving the objectives of this study; each class represents a major component of the bayou sediment bed. Based on experience from previous modeling studies (e.g., QEA 2008), the four size classes used in Patrick Bayou simulations provide a realistic range of sediment particle sizes (from clay to gravel) that are present in the graded bed of the bayou. Inclusion of this wide range of particle sizes in the model is necessary for simulation of bed armoring processes during an erosion event. From a practical point of view, simulating the transport of four sediment size classes makes it possible to conduct long-term, multi-year simulations in a practical amount of time. Finally, the results of the model calibration and validation exercises (discussed below) indicate that use of four sediment size classes is sufficient for producing a modeling framework with adequate accuracy and reliability for the application and use of the sediment transport model as specified in this report.

For convenience, the four sediment classes have been labeled as noted in Table 2-7. Each sediment size class is represented as an effective particle diameter. The effective particle diameter for class 1 was treated as an adjustable calibration parameter, see Section 2.4.5. Effective particle diameters for classes 2 through 4 were estimated using the following approach (QEA 2008). This method provides an objective method for estimating the effective particle diameters for classes 2 through 4. Grain size distribution (GSD) data are available for the surface layer of sediment cores (i.e., top 2.1 cm) collected from the bayou during October 2006. For sand and gravel particles, the GSD data were reported as the fractional composition for these seven particle size ranges: 1) 72 – 106 μm ; 2) 106 – 250 μm ; 3) 250 – 425 μm ; 4) 425 – 850 μm ; 5) 850 – 2,000 μm ; 6) 2,000 – 4,750 μm ; and 7) > 4,750 μm . The effective diameter of each size range corresponds to the geometric mean of that range. For example, the geometric mean of the 106 – 250 μm size range is 163 μm . The GSD data

provide information on the relative amounts of sand in each of the seven size ranges. The effective diameters of classes 2, 3, and 4 (i.e., d_2 , d_3 , d_4) for a particular core sample were estimated from the GSD data using (QEA 2008):

$$d_2 = (f_{r1}G_{r1} + f_{r2}G_{r2}) / (f_{r1} + f_{r2}) \quad (2-5)$$

$$d_3 = (f_{r3}G_{r3} + f_{r4}G_{r4} + f_{r5}G_{r5}) / (f_{r3} + f_{r4} + f_{r5}) \quad (2-6)$$

$$d_4 = (f_{r6}G_{r6} + f_{r7}G_{r7}) / (f_{r6} + f_{r7}) \quad (2-7)$$

where:

f_{rk} = fractional composition of size range k

G_{rk} = geometric mean (effective diameter) of size range k

Using Equations 2-5 through 2-7 to analyze the GSD data for surface-layer sediment (i.e., top 2.1 cm) produced median values of effective diameters for classes 2, 3 and 4 of 130, 630, and 3,210 μm , respectively. These median values are assumed to be the effective particle diameters for classes 2, 3, and 4 in the sediment transport model. The settling speeds corresponding to the effective diameters of classes 2, 3, and 4 are 770, 6,400, and 21,000 meters per day (m/day), respectively. The effective settling speeds for the four sediment size classes have a large range, from about 1 m/day for class 1 to about 21,000 m/day for class 4 (Table 2-7). This wide range (i.e., factor of 20,000) has a significant effect on the transport characteristics of the different sediment classes. Note that the effective particle diameter for class 1 was treated as a calibration parameter, as discussed in Section 2.4.5.

Table 2-7
Characteristics of Sediment Particle Size Classes

Sediment Size Class	Particle Size Range (μm)	Effective Particle Diameter (μm)	Effective Settling Speed (m/day)
1: clay and silt	< 62	7	1.3
2: fine sand	62 – 250	130	770
3: medium, coarse sand	250 – 2,000	630	6,400
4: gravel	> 2,000	3,210	21,000

2.4.3 Bed Properties

The sediment bed in Patrick Bayou may be separated into two distinct types: 1) cohesive (i.e., muddy bed composed of a mixture of clay, silt, sand and organic matter); and 2) non-cohesive (i.e., sandy bed composed of sand and gravel, with small amounts of clay and silt). Sediment samples collected in Patrick Bayou indicate that the bed is primarily composed of cohesive sediment, with non-cohesive sediment occurring in isolated, localized areas in the bayou. Thus, it was assumed in the sediment transport model that the entire sediment bed is cohesive in the bayou. The bed in the HSC was assumed to be non-erosional due to lack of bed property data in the HSC. However, the model simulated deposition in the HSC.

The sediment transport model requires specification of the following bed property inputs within Patrick Bayou: 1) dry (bulk) density; 2) initial sediment bed composition (i.e., relative amounts of sediment size classes 1, 2, 3, and 4); 3) effective bed roughness; and 4) erosion rate properties. The dry density in this study was assumed to be spatially constant throughout the bayou, with a value of 0.77 g/cm³. This value corresponds to the average of 12 cores collected during the Sedflume study of June 2007 (see discussion below).

The spatial distribution of bed composition needs to be specified as an initial condition for the sediment transport model. The proportional content of the four sediment size classes (i.e., classes 1, 2, 3 and 4) in the bed must be specified at each grid cell at the beginning of a simulation. Initial conditions for bed composition were determined using the following procedure. Grain size distribution data from surface-layer (top 2.1 cm) samples collected in Patrick Bayou during October 2006 were used to calculate average values of bed composition in the bayou. As a first approximation, the average values of bed content for classes 1, 2, 3, and 4 (i.e., 50%, 33%, 9%, and 8%, respectively) were applied to the entire study area. This initial specification of bed content distribution is an approximation to the heterogeneous distribution that exists in the bayou. The spatial distribution of bed content that exists in the bayou is the result of hydrodynamic and sediment transport processes within the bayou. Thus, it was assumed that the sediment transport model provides a rational and mechanistic method for estimating the spatial distribution of bed content.

Using the specification of bed content discussed above (i.e., average values) as initial conditions for the model, a 14-year simulation was conducted and the sediment bed was

allowed to “evolve” during that period. Changes in bed composition occurred over that 14-year period as a result of erosion, deposition, and transport of sediment over a wide range of flow and tidal conditions. The predicted spatial distribution of bed content at the end of the 14-year simulation provides an improved estimate of conditions in Patrick Bayou, see Figures 2-17 through 2-20. Comparisons of predicted and observed bed composition were conducted during model validation (see Section 2.4.6). Those comparisons indicate that the model adequately predicts bed composition in the bayou, which supports the use of this approach for estimating initial bed composition conditions. The spatial distributions of sediment composition from the “evolved” bed were used as initial bed compositions for the simulations discussed in Sections 2 and 3.

Grain size distribution data for surface-layer sediment were analyzed to determine effective bed roughness (i.e., D_{90}) values for use in calculating skin friction shear stress, see Appendix A.1. Information on data sources for D_{90} values are presented in Table 2-6. The average D_{90} of nine sediment samples collected in the bayou was 230 μm . It was assumed that the average D_{90} value is representative of effective bed roughness throughout the bayou (i.e., D_{90} is spatially constant and time invariant).

As discussed in Appendix A.3, the gross erosion rate of cohesive sediment is dependent on skin friction shear stress as follows (Jones and Lick 2001):

$$\begin{aligned} E_{\text{gross}} &= A \tau_{\text{sf}}^n && \text{for } \tau_{\text{sf}} > \tau_{\text{cr}} \\ &= 0 && \text{for } \tau_{\text{sf}} \leq \tau_{\text{cr}} \end{aligned} \quad (2-8)$$

where:

- E_{gross} = erosion rate (centimeters per second [cm/s])
- τ_{sf} = skin friction shear stress (Pa)
- τ_{cr} = critical shear stress (Pa), which is the shear stress at which a small, but measurable, rate of erosion occurs (generally less than 2 millimeters per hour [mm/hr])

The erosion parameters, A , n and τ_{cr} , are site-specific and may be spatially variable, both horizontally and vertically.

A Sedflume study was conducted during June 2007 to obtain data on the erosion properties of Patrick Bayou sediments. The locations of 12 Sedflume cores collected and tested during the Sedflume study are shown on Figure 2-21. A description of the study and analysis of Sedflume core data are presented in Appendix B. The primary purpose of the Sedflume core data analysis was to determine values of A , n and τ_{cr} in Equation 2-8 for use in specifying model inputs. Of particular interest in the data analysis is spatial variability, both horizontally and vertically, of the erosion rate parameters.

In the vertical direction, Sedflume core data were obtained from five discrete layers with the following depth intervals: 0-6, 6-11, 11-16, 16-21, and 21-26 cm (see Appendix B). These depth intervals were chosen because the shear stress series used in the Sedflume tests were cycled over these depth intervals. As discussed in Appendix A.3, the sediment bed is separated into five layers, with the top layer being 6-cm thick and the deeper layers being 5-cm thick. The thicknesses of the bed layers were selected based on the Sedflume core data; this structure of the bed model layering is consistent with the discrete layers in the cores from which erosion rate data were obtained. The erosion rate parameters in Equation 2-8 (i.e., A , n , τ_{cr}), which is used to calculate gross erosion rate (E_{gross}), vary with depth in the bed, with specific values of A , n , and τ_{cr} for each of the five bed layers.

In addition to vertical variation, horizontal variability in the erosion rate parameters may be incorporated into the model. To evaluate horizontal and vertical variability of erosion properties in Patrick Bayou, a procedure was developed to quantify differences in the erodibility of Sedflume core samples. This procedure is presented in Appendix B. The results of the erodibility analysis are presented on Figure 2-22, which compares values of the average erosion rate ratio (R_{avg}) for all of the Sedflume core samples. The erosion rate ratios shown on this figure are compared to the average erodibility of all the cores in the 0-6 cm interval. When the R_{avg} value is less/greater than one, the erodibility of the Sedflume core sample is less/greater than the average erodibility for all samples in the 0-6 cm interval. With respect to horizontal variability of the erodibility of sediment in Patrick Bayou, the following insights are derived from this analysis: 1) minimum erodibility occurs in core

SF-6; 2) maximum erodibility occurs in core SF-11; 3) horizontal variability in erodibility is lowest in the top (0-6 cm) layer, with spatial variability tending to increase with depth in the sediment bed; and 4) no spatial patterns are evident in the horizontal plane. With respect to vertical variability of sediment erodibility, the following characteristics are observed:

1) sediments downstream of approximately PB042 (see Figure 2-22) tend to have significant decreases in erodibility with increasing depth in the bed due to consolidation effects; and 2) sediments upstream of approximately PB042 tend to exhibit variable erodibility in the vertical direction, with some cores having increasing erodibility with increasing depth (e.g., core SF-11).

Sedflume data from 12 cores are not sufficient to use standard interpolation methods to develop a reliable horizontal distribution of erosion properties. In addition, no spatial patterns in the erosion rate ratio of surface-layer sediment are evident on Figure 2-22. Thus, developing a credible spatial distribution of erosion parameters in the horizontal plane may be problematic. Thus, it was assumed that the erosion parameters (i.e., A and n) for a given depth interval are spatially constant in the horizontal plane. The potential effects of this assumption on model predictions were evaluated during a sensitivity analysis (see Section 3.2.2).

The erosion parameter values for each layer in the bed were specified using the average parameters for a given depth interval. For a log-linear relationship (i.e., Equation 2-8), the average exponent (n) value for a depth interval is the arithmetic average of the n values for the cores within the interval. The average proportionality constant (A_{ave}) is determined by calculating the log-average value:

$$\log(A_{ave}) = (1/K) \sum \log(A_k) \quad (2-9)$$

where:

K = the number of cores (i.e., 12)

By assuming that the erosion parameters are spatially constant in the horizontal plane, the erosion parameters only vary in the vertical direction. The potential effects of this

approximation on model predictions are evaluated during the sensitivity analysis (see Section 3.2). The erosion parameters for the five layers in the bed model are listed in Table 2-8, where E_{gross} and skin friction shear stress have units of cm/s and Pa, respectively.

Table 2-8
Vertical Variation in Erosion Rate Parameters

Depth Interval	Proportionality Constant: A	Exponent: n	Critical Shear Stress (Pa)
0 – 6 cm	0.0046	2.5	0.21
6 – 11 cm	0.0016	2.7	0.38
11 – 16 cm	0.0017	2.7	0.35
16 – 21 cm	0.0010	3.1	0.49
21 – 26 cm	0.0009	3.1	0.49

2.4.4 Boundary Conditions

Incoming sediment loads to the bayou need to be specified at these model boundaries:

1) Main inflow; 2) East Fork inflow; 3) direct runoff to the bayou from the surrounding watershed; 4) OxyChem outfalls; 5) upstream HSC boundary (during ebb tide); and 6) downstream HSC boundary (during flood tide). Both the magnitude and composition (i.e., relative amounts of classes 1, 2, 3, and 4) of the incoming sediment loads must be specified.

Total suspended sediment (TSS) concentration data were collected at sampling stations in the Main inflow (station PB075) and East Fork (station EF005) during the October 2006 study. Flow rate data were collected concurrently at these two stations, making it possible to construct sediment rating curves (i.e., TSS concentration as a function of flow rate), see Figures 2-23 and 2-24. In general, different relationships between TSS concentration and flow rate occur during low- and high-flow conditions. Transition flow rates for the two flow regimes are 80 and 20 cfs for the Main inflow and East Fork, respectively. At the Main inflow, minimal correlation between TSS concentration and flow rate exists for both the low- and high-flow regimes (Figure 2-23). Thus, a valid approximation for the Main inflow is to use the average TSS concentrations for each flow regime (i.e., 24 milligrams per liter [mg/L] for flow rates less than 80 cfs and 58 mg/L for flow rates greater than 80 cfs). At the East Fork, there is minimal correlation between TSS concentration and flow rate in the low-

flow regime, so the average TSS concentration for the flow regime (32 mg/L) was specified when flow rates were 20 cfs or less. For the high-flow regime in the East Fork, TSS concentration shows a reasonable correlation with flow rate. Therefore, TSS concentration at the East Fork boundary during high-flow conditions (i.e., greater than 20 cfs) is specified using:

$$C_{TSS} = 5.4 Q^{0.49} \quad (2-10)$$

where:

C_{TSS} = TSS concentration (mg/L)

Q = flow rate (cfs)

These boundary loadings produce average annual sediment loads from the Main inflow and East Fork of 930 and 120 metric tons per year (MT/year), respectively, for the 14-year period from 1993 through 2006. As noted above, significant scatter in the data results in relatively low correlation between TSS concentration and flow rate, which translates to uncertainty in the magnitude of the incoming sediment load to the bayou. Potential effects of sediment load uncertainty on model predictions are evaluated during the sensitivity and uncertainty analyses, see Sections 3.2 and 3.4.

Sediment load composition data are not available for the Main inflow and East Fork. It was assumed that the incoming load is composed of 100% class 1 sediment (i.e., clay and silt) during low-flow conditions. This assumption is reasonable because minimal sand will be transported into the bayou from its two primary tributaries during low-flow conditions. The relative amounts of the four sediment classes in the incoming sediment load during high-flow conditions were estimated using the following method. Because class 4 was assumed to be immobile (i.e., not transported as suspended load), the content of this sediment class was set to zero. Thus, the total incoming load (L_{tot}) is:

$$L_{tot} = L_1 + L_2 + L_3 \quad (2-11)$$

where:

L_{k} = incoming load of class k sediment

The total mass of net deposited sediment, on an annual average basis, (D_{tot}) is:

$$D_{\text{tot}} = D_1 + D_2 + D_3 \quad (2-12)$$

where:

D_{k} = net deposition mass of class k sediment

The trapping efficiency of Patrick Bayou is defined as the fraction of the incoming load that is deposited in the bayou, so that:

$$D_{\text{tot}} = TE_{\text{total}} L_{\text{tot}} \quad (2-13)$$

$$D_k = TE_k L_k \quad (2-14)$$

where:

TE_{total} = total trapping efficiency of the bayou

TE_k = trapping efficiency of class k sediment

The content of class k sediment in the incoming load ($F_{\text{IL},k}$) is given by:

$$F_{\text{IL},k} = L_k / L_{\text{tot}} \quad (2-15)$$

and: :

$$F_{\text{IL},1} + F_{\text{IL},2} + F_{\text{IL},3} = 1 \quad (2-16)$$

where:

$F_{\text{IL},k}$ = content of class k sediment in incoming sediment load

The average content of class k sediment in the sediment bed ($F_{\text{B},k}$) is given by:

$$F_{\text{B},k} = D_k / D_{\text{total}} \quad (2-17)$$

Using Equations 2-13 and 2-14 in Equation 2-17 produces:

$$F_{IL,k} = (TE_{total}/TE_k) F_{B,k} \quad (2-18)$$

For the three classes transported as suspended load, the average composition of the sediment bed in the bayou ($F_{B,k}$) is 54%, 36%, and 10% for classes 1, 2, and 3, respectively. Therefore, substituting these values into Equation 2-18 and using Equation 2-16 yields:

$$F_{IL,1} = 0.54 (TE_{total}/TE_1) \quad (2-19)$$

$$F_{IL,3} = 0.10 (TE_{total}/TE_3) \quad (2-20)$$

$$F_{IL,2} = 1 - F_{IL,1} - F_{IL,3} \quad (2-21)$$

As a first-approximation, it was assumed that: 1) TE_{total} is 40%; 2) TE_1 is 28% (clay/silt); and 3) TE_3 is 100% (medium/coarse sand). These assumptions were based on professional judgment and past experience from sediment transport modeling studies on other sites. Using these approximate trapping efficiency values in Equations 2-19, 2-20 and 2-21 results in the composition of the incoming sediment load during high-flow conditions being 76%, 20%, 4%, and 0% for sediment classes 1, 2, 3, and 4, respectively.

Sediment loads from direct runoff to Patrick Bayou needed to be specified at three point source locations distributed along the bayou. In addition, sediment loads from the three OxyChem outfalls had to be specified. No or minimal TSS concentration data were available to specify loading from direct runoff or the OxyChem outfalls. Thus, sediment loads for the three OxyChem outfalls and direct runoff were adjusted during model calibration due to a lack of data for the magnitude and composition of these loads, see Section 2.4.5.

Incoming sediment loads at the two HSC boundaries were specified using TSS concentration data collected by the Galveston Bay National Estuary Program during the period from 1972 through 2005. Sampling locations used by Galveston Bay National Estuary Program are shown on Figure 2-25. Stations 11271 and 11264 are closest to the upstream and downstream HSC boundaries, respectively. Minimal correlation exists between local precipitation or tributary flow rate and TSS concentration measured at these two stations. Thus, similar to the bayou tributary inflows, average TSS concentrations at the HSC stations (i.e., about 25 mg/L) were used to specify incoming load at the HSC boundaries. Cumulative

frequency distributions for the TSS concentration data collected at stations 11271 and 11264 are presented on Figure 2-26. The two distributions are similar, which indicates that there is no significant difference between TSS concentrations at these two HSC locations over long time periods. Therefore, TSS concentrations at the HSC upstream and downstream boundaries during inflow conditions (i.e., flood tide at the downstream boundary and ebb tide at the upstream boundary) were specified as 25 mg/L. Sediment load composition are not available in the HSC, so it was assumed that the incoming sediment load at the HSC boundaries was composed of 100% class 1 (clay/silt) sediment.

2.4.5 *Sediment Transport Model Calibration*

Calibration of the sediment transport model involved adjusting selected model inputs such that the agreement between model predictions and data is optimized. The model was calibrated using data that are representative of two different timescales: 1) short-term, high-flow events; and 2) long-term, multi-year periods. For short-term, high-flow events, TSS concentration data obtained during the October 2006 study were used for model calibration. For long-term, multi-year periods, net sedimentation rate (NSR) values were estimated using radioisotope data from several sediment cores collected in Patrick Bayou during October 2006. Thus, the calibration process was a two-step process, with the first step involving simulation of a short-term, high-flow event and the second step using a 14-year (1993 through 2006) simulation. A wide range of tidal and flow conditions occurred during the 14-year period, including one high-flow event with a return period of about 10 years (October 2006 storm).

Three model inputs were adjusted during the calibration process: 1) effective particle diameter of class 1 sediment; 2) magnitude of incoming sediment load to the bayou during low-flow conditions; and 3) magnitude of sediment load from direct runoff and the OxyChem outfalls. The effective particle diameter of class 1 sediment affects the settling speed of that particle-size class. This model input was adjusted to optimize model-data agreement during the first step of the calibration process, which was the October 2006 simulation. After the first calibration step was completed, the initial 14-year simulation was conducted using the approach discussed in Section 2.4.4 to specify the incoming sediment load to the bayou. The results of this initial simulation indicated that the model under-

predicted NSR in Patrick Bayou by about a factor-of-four. It was determined that the cause of this under-prediction was an underestimation of the incoming sediment load to the bayou during low-flow conditions. Sediment loading to the bayou during low-flow conditions is uncertain because of significant variability in: 1) TSS concentrations in the Main inflow and East Fork (see Figures 2-23 and 2-24); and 2) discharge in the Main inflow and East Fork during periods with no precipitation (i.e., base-flow conditions). Thus, the sediment load during low-flow conditions was treated as an adjustable parameter for the second step of the calibration process (i.e., predicting NSR during the 14-year simulation).

The first step in the calibration process was to simulate the high-flow events that occurred during October 2006. Flow rate and TSS concentration data were collected at the Main inflow (station PB075) and East Fork (station EF005) during this one-month period; these data were used to specify boundary condition inputs during the calibration simulation. In addition, TSS concentration data were collected at station PB012 (see Figure 2-6) during October 2006, which is located about 1,200 ft upstream of the confluence of Patrick Bayou and the HSC. Those data were used as a calibration target for the October 2006 simulation. As discussed above, the effective particle diameter of class 1 sediment (clay/silt) was adjusted to optimize model-data agreement during this step in the calibration process. The optimum effective particle diameter for class 1 sediment was 7 μm , which corresponds to a settling speed of 3.6 m/day. This settling speed is within the realistic range for class 1 sediment, which typically ranges between about 1 and 20 m/day. Comparisons of predicted and measured TSS concentrations at station PB012 during October 2006 are shown on Figure 2-27. The high-flow events during October 14-16 are simulated reasonably well, with the model predicting the peak TSS concentrations with acceptable accuracy. The peak TSS concentration (about 400 mg/L) during the high-flow event that occurred on October 26-27 is under-predicted by the sediment transport model. It is unclear whether or not this one data point is an anomaly because the peak incoming flow rate during the October 26-27 high-flow event is about 50% lower than the October 16 peak flow rate, and the peak TSS concentration during the October 16 event was about 250 mg/L. However, the October 2006 simulation results indicate that, generally, the sediment transport model adequately predicts TSS concentration in Patrick Bayou during high-flow events. The model tends to under-predict TSS concentration during low-flow conditions, which is probably due to not

including the presence of suspended biological and clay particles with relatively low settling speed (i.e., 0.1 m/day or less) in the model.

The second step in the calibration process was to evaluate the ability of the sediment transport model to predict NSR in Patrick Bayou. Overall, this capability of the model is of primary importance for meeting the study objectives stated in Section 1.3. The 14-year period from 1993 through 2006 was used for the multi-year simulation. This period was chosen because adequate precipitation data for input to the watershed model were not available prior to 1993. Boundary condition inputs for the 14-year simulation are discussed and presented in Appendix C. Note that this 14-year period contains a wide range of flow and tidal conditions, including a 10-year high-flow event that occurred during 2006.

Net sedimentation rates in Patrick Bayou were estimated using radioisotope data from sediment cores collected from five locations in the bayou during October 2006 and 10 locations during November 2008. The ^{210}Pb age-dating analysis was useful for estimating NSRs that are representative of the period from about 1980 to the present, which is consistent with multi-year period (1993 through 2006) used for the calibration simulation. Of the 15 cores examined during the ^{210}Pb age-dating analysis, only the cores collected at stations PB022 and PB048 during the October 2006 study (Anchor Environmental 2007a) and at stations PB006, PB016, PB025 and PB052 during the November 2008 study (Anchor QEA 2009) produced NSR values, see Figure 2-28. The estimated NSR values at these six stations are listed in Table 2-7. The other nine cores were “unreadable”, which means that the variability of the vertical profiles of ^{210}Pb activity was too high to reliably estimate NSR in those cores.

As noted above, the initial 14-year simulation used the sediment loading approach discussed in Section 2.4.4, which resulted in an under-prediction of NSR at stations PB022 and PB048 by about a factor-of-four. Numerical experiments using the sediment transport model demonstrated that predicted NSR at these two locations in the bayou are linearly correlated to the total average annual sediment load from the bayou tributaries. Thus, increasing this load by a factor-of-four was needed to achieve adequate agreement between predicted and measured NSR values at stations PB022 and PB048. The original approach to specifying sediment loads in the Main inflow and East Fork assumed a total base-flow of 30 cfs

(i.e., total for both tributaries), where base-flow is flow rate during periods of no precipitation. This total base-flow value corresponds to the average of base-flow data collected in these two tributaries. As discussed in Section 2.3.3, total base-flow is variable and uncertain, with a range from less than 1 cfs to 120 cfs. Therefore, the incoming sediment load was increased by increasing the total base-flow from 30 to 120 cfs, with the base-flow in the Main inflow and East Fork being 112 and 8 cfs, respectively. These base-flow values correspond to the maximum measured flow rates during days with no precipitation at stations PB075 and EF005 (Figure 2-9). The sediment loads from the OxyChem outfalls and direct runoff were adjusted during model calibration. The best results were obtained with: 1) direct runoff sediment load set to zero; and 2) class 1 (clay/silt) concentration set at 10 mg/L in the three OxyChem outfalls.

Predicted and estimated NSR values at the six core locations are compared in Figure 2-29 and Table 2-9. The model over-predicts NSR values at stations PB006 and PB016, while under-predicting the NSR value at station PB052. Good agreement between predicted and estimated NSR values was achieved at stations PB022, PB025 and PB048. Overall, the results of the model calibration are acceptable for the objectives of this study.

Table 2-9
Comparison of Predicted and Measured NSR for 14-Year Simulation

Core Location	Measured NSR (cm/yr)	Predicted NSR (cm/yr)	Relative Error Between Predicted and Measured NSR (%)
Station PB006	0.30	0.81	+170
Station PB016	0.15	0.94	+530
Station PB022	0.82	0.91	+11
Station PB025	0.25	0.25	0
Station PB048	1.7	1.6	-6
Station PB052	2.5	0.9	-64

The spatial distribution of average NSR for the 14-year period (1993 through 2006) as predicted by the sediment transport model is presented on Figure 2-30. These results show that significant spatial variability in NSR exists in Patrick Bayou, ranging from areas in dynamic equilibrium (i.e., NSR less than about 0.1 cm/yr) and areas with relatively net

sedimentation (i.e., NSR greater than 1.5 cm/yr). Most of the bayou is net depositional over the 14-year period, with the exception of some areas located between stations PB025 and PB036, and another area immediately downstream of station PB012. Generally, NSR tends to decrease moving from the Main inflow and East Fork toward the HSC. However, NSR tends to increase in the vicinity of the confluence of the bayou with the HSC (i.e., downstream of station PB012) due to the influence of sediment loading from the HSC. The areal extent of four ranges of NSR values (i.e., 0-0.25, 0.25-0.75, 0.75-1.5, >1.5 cm/yr) for the entire bayou bed area is shown on Figure 2-31. About 65% to 70% of the entire bayou area was predicted to have NSR values greater than 0.75 cm/yr.

2.4.6 Sediment Transport Model Validation

Validation of the sediment transport model involved the comparison of model predictions to an independent data-set (i.e., data not used to calibrate the model) without adjustment of calibration parameters. Radioisotope and chemical concentration data were obtained from cores collected at stations PB003, PB022, PB036, PB048 and PB057 during the October 2006 study (see Figure 2-28 for core locations). Analyses of the vertical profiles of mercury, total PCBs and total polycyclic aromatic hydrocarbons (PAHs) were conducted. The results of these analyses produced estimates of the rates of natural attenuation in surface-layer sediment at each core location (Anchor Environmental 2007a). This information on rates of natural attenuation in surface-layer sediment was used to validate the model as follows.

Temporal change in chemical concentration in the mixing-zone layer due to deposition may be approximated by an idealized model as shown on Figure 2-32. This idealized model assumes continuous deposition with no erosion and, thus, chemical concentration will decrease at an exponential rate, which is expressed mathematically as (Thomann and Mueller 1997):

$$C_b(t) = C_{b,o} \text{ EXP}[-\lambda (t - t_o)] + C_w (1 - \text{EXP}[-\lambda (t - t_o)]) \quad (2-22)$$

where:

C_b = chemical concentration in the mixing-zone layer

$C_{b,o}$ = initial bed concentration at time t_o

C_w	=	chemical concentration on sediment particles being deposited
t	=	time
λ	=	decay rate coefficient with units of inverse time (e.g., year ⁻¹)

The decay rate coefficient depends on ratio of sedimentation rate (Γ) and mixing-zone layer thickness (T):

$$\lambda = \Gamma/T \quad (2-23)$$

As the value of the decay rate coefficient increases, the rate at which C_b declines will increase. As time progresses, bed concentration asymptotically approaches the concentration of depositing particles (C_w).

The effect of deposition of sediment from external sources (i.e., sediment loading from Main inflow, East Fork, direct runoff) on changes in sediment composition of the mixing-zone layer was used to estimate the rate of chemical attenuation in the Patrick Bayou sediment bed. The mixing-zone layer corresponds to the surface layer in the sediment bed that is affected by bioturbation and other physical mixing processes, which tend to homogenize the physical and chemical properties of this surface layer. The model was used to predict these rates by tracking sediment from two sources: 1) external loads (i.e., Main inflow, East Fork, direct runoff); and 2) original bed sediment (i.e., bed sediment at the beginning of the 14-year simulation). For this simulation, it was assumed that the mixing-zone layer was 10 cm thick. Sediment from the two sources was separated into four size classes (i.e., classes 1, 2, 3, and 4), with the sediment transport characteristics of the four size classes being the same for each source. For example, the erosion, deposition, and transport of class 1 sediment are treated the same way for sediment originating from the bed and external sources. Thus, the model simulated the erosion, deposition, and transport of eight sediment classes during the 14-year period.

At the beginning of the 14-year simulation, the composition of mixing-zone (0-10 cm) layer is 100% bed-source sediment, with no sediment from the external source. As the 14-year simulation progresses, external-source sediment is transported into the bayou and is deposited in the mixing-zone layer, which reduces the relative amount of bed-source

sediment in that layer. The model tracks spatial and temporal changes in the relative amounts of sediment from the two sources over the course of the 14-year period that result from erosion, deposition, and transport processes in Patrick Bayou.

Predicted changes in bed elevation and bed-source content in the mixing-zone layer at the five core locations during the 14-year period (1993 through 2006) are shown on Figures 2-33 through 2-37. To evaluate the validity of the hypothesis that bed-source content in the mixing-zone layer decreases at an exponential rate, values of the predicted decay rate coefficient (λ_{bed}), which represents the average value for the 14-year period based on beginning and ending values of bed-source content, at the five core locations were determined using:

$$\lambda_{bed} = -\ln(C_{bed,14}/C_{bed,o}) / 14 \quad (2-24)$$

where:

- $C_{bed,14}$ = the predicted bed-source content in the mixing-zone layer at the end of the 14-year period
- $C_{bed,o}$ = the initial bed-source content (i.e., 100 %)

Values of λ_{bed} , NSR (Γ), and Γ/T , based on sediment transport model predictions, for each core location are listed in Table 2-10.

Table 2-10
Predicted Decay Rate Coefficients at Core Locations During 14-Year Period

Core Location	Relative Decrease of Bed-Source Content During 14-Year Period (%)	Net Sedimentation Rate (cm/yr)	Γ/T (yr ⁻¹)	Predicted Decay Rate Coefficient, λ_{bed} (yr ⁻¹)
PB003	90	1.6	0.16	0.16
PB022	72	0.93	0.093	0.091
PB036	28	-0.09	NA	NA
PB048	89	1.6	0.16	0.16
PB057	87	1.4	0.14	0.15

NA = not applicable

The predicted decay rate coefficients (λ_{bed}) listed in Table 2-10 were used in Equation 2-22, with C_w set to zero, to predict the theoretical exponential decrease in bed-source content in the mixing-zone layer based on the idealized model discussed above (i.e., continuous deposition). The theoretical exponential decreases in bed-source content at the five core locations are compared to changes in bed-source content as predicted by the sediment transport model on the bottom panels of Figures 2-33 through 2-37. In addition, the exponential decay rates in mixing-zone layer sediment for mercury, total PCBs and total PAHs, which were estimated from analyses of vertical concentration profiles of those chemicals, are compared to predicted bed-source content changes at core locations PB022, PB048, and PB057 (Anchor Environmental 2007a). .

At station PB003, the model predicts a relatively high NSR (1.6 cm/yr) and the bed-source content decreases at approximately an exponential rate (Figure 2-33). The sediment core analysis did not produce a readable ^{210}Pb profile, nor were decay rate coefficients for the three chemicals able to be estimated. The apparent inconsistency between predicted and observed behavior of material in the mixing-zone layer at this location may be caused by complex interactions between the bayou and HSC in the vicinity of this core location.

At station PB022, deposition occurs at a relatively continuous rate, with erosion during high-flow events having a minor effect on bed elevation change (Figure 2-34). This characteristic produces an approximately exponential decrease in bed-source content during the 14-year period. This behavior is consistent with the ability to estimate NSR at this core location from the ^{210}Pb vertical profile; unreadable ^{210}Pb profiles typically occur at locations that are dynamic, with discontinuous deposition and erosion during high-flow events. In addition, the predicted rate of change in bed-source content is in good agreement with the exponential decrease in surface-layer concentrations of mercury, total PCBs and total PAHs (see bottom panel of Figure 2-36). In conjunction with the low error in predicted NSR (i.e., 13%, see Table 2-9), these results indicate that the model is adequately simulating sediment transport processes at this location.

At station PB036, predicted bed elevation changes are more dynamic than at station PB022, with net erosion (about 1 cm) occurring over the 14-year period (Figure 2-35). The

predicted variability in bed elevation at station PB036 is consistent with the inability to interpret the vertical profile of ^{210}Pb activity in the core collected at this location. In addition, the prediction of approximately dynamic equilibrium conditions at this location is consistent with the observation of relatively low sediment accumulation in this region of Patrick Bayou. Although net erosion occurs at this location, bed-source content in the mixing-zone layer does decrease during the 14-year period. The decrease in bed-source content is caused by the deposition of sediment from external sources during low-flow periods, even though bed scour occurs during high-flow events.

At station PB048, the model predicts approximately continuous net sedimentation, at a relatively high rate (1.6 cm/yr), with minimal bed scour occurring during high-flow events (Figure 2-36). Similar to station PB022, the model predicts an exponential decrease of bed-source content in the mixing-zone layer but at a higher rate of decrease due to the higher NSR at station PB048. As shown on the bottom panel of Figure 2-36, the predicted exponential decrease in bed-source content is in good agreement with observed exponential decreases in surface-layer concentrations of mercury, total PCBs and total PAHs at this location.

At station PB057, the model predicts a relatively high NSR (1.4 cm/yr) but the deposition is not as continuous as at stations PB022 and PB048 (Figure 2-37). Similar to model results at stations PB022 and PB048, the predicted exponential decrease in bed-source content is in good agreement with the attenuation rate of the three chemical concentrations in surface-layer sediment. At this location, the vertical profile of ^{210}Pb activity was not interpretable, which is inconsistent with the relatively high NSR and exponential decay of bed-source content predicted by the model. The cause of this inconsistency is unclear.

The validation results presented above provide additional support of the predictive capability of the model. These results indicate that the model is able to: 1) capture spatial differences in depositional conditions throughout the bayou; and 2) adequately predict the rate of decrease of bed-source content in the mixing-zone layer. Both of these capabilities are of importance for using the model to evaluate the efficacy of various remedial alternatives within Patrick Bayou.

Additional analysis of the rate of decrease of bed-source content in the mixing-zone layer was conducted to better understand its relationship to NSR. The relationship between predicted bed-source content decrease over the 14-year period and NSR is shown on Figure 2-38. The solid circles on this figure represent predicted NSR and bed-source content values at the end of the 14-yr period for all grid cells that were net depositional. Also shown on that figure is the idealized relationship between bed-source content decline rate and NSR (shown as a red line on Figure 2-38), which is based on Equations 2-22 and 2-23. These results indicate that the model results tend to follow the same general trend as the idealized formulation.

3 DIAGNOSTIC AND PROGNOSTIC MODELING ANALYSES

This section describes diagnostic and prognostic modeling analyses that were performed using the calibrated and validated modeling framework described in Section 2. The model was used as a diagnostic tool to investigate the July through December 2007 period when the marker horizon study was conducted. Predictive simulations (i.e., prognostic mode) were conducted to evaluate the potential effects of high-flow events on bed stability in Patrick Bayou. In addition, a sensitivity analysis was carried out to evaluate the effects of variation in model inputs on model predictions for a 100-year high-flow event. Additional analysis of the 14-year simulation results was conducted to develop insights about natural attenuation processes in the mixing-zone layer in the bayou, including an uncertainty analysis to quantify the effects of uncertainty in model inputs and parameters on model predictions.

3.1 Evaluation of July-December 2007 Period

In July 2007, a marker-horizon study was conducted to develop an improved understanding of sediment transport processes in Patrick Bayou. The methodology used in the marker-horizon study was developed by the USGS and it is discussed in detail in the 2007 Work Plan (Anchor Environmental 2007b). This approach uses simultaneous measures of elevation from temporary benchmarks using a sedimentation-erosion table and estimates vertical accretion from marker horizons within sediment cores that are collected using a cryogenic coring apparatus. The measurements in the cores are made with a level of resolution sufficient to distinguish between the influence of surface and sub-surface processes on bed elevation. The method for measuring vertical accretion involved periodically recording the rate of accumulation of sediment above a thin layer marker horizon (i.e., white feldspar) that is laid upon the bottom sediments. Seven locations within the bayou where marker-horizon material was placed on the sediment bed during July 2007 are shown on Figure 3-1.

A field survey was conducted six months after the marker-horizon material was placed on the sediment bed to determine conditions at the seven locations. Sediment cores were collected at all of the marker-horizon locations during January 2008. It was determined through visual inspection of the marker-horizon cores that the marker material was no longer evident at any of the locations. A review of meteorological records during the six-month period from July through December 2007 showed that several rainstorms occurred in

the vicinity of Patrick Bayou soon after the horizon-marker material was deployed during the week of July 9. The model was used to evaluate the potential effects of these storms on hydrodynamics and sediment transport in the bayou to determine if these storms were responsible for washing away the horizon-marker material before the material was fully incorporated into the sediment bed.

The model was used to predict temporal changes in skin friction shear stress at the seven marker-horizon locations from July through December 2007. The approach for calculating skin friction shear stress is described in Appendix A. The effective bed roughness (i.e., D_{90} value) was set at 230 μm , which is the same value used in the sediment transport model.

Time histories of predicted bed shear stress at the seven marker-horizon locations for the six-month period (July-December 2007) are presented on Figures 3-2 and 3-3. Typically, critical shear stress for erosion of fine-grained, cohesive sediment is about 0.1 Pa. A reasonable assumption for the marker-horizon material that was placed on the sediment bed of the bayou is that it behaves similar to cohesive sediment with respect to erosion. Thus, it was assumed that erosion of the marker-horizon material may have occurred during the six-month period if the bed shear stress exceeded 0.1 Pa. The horizontal dotted lines on Figures 3-2 and 3-3 are set at a value of 0.1 Pa. The critical shear stresses for surface (0-6 cm) layer sediment, based on erosion rate testing of Sedflume cores in the vicinity of the seven marker-horizon locations (see Table B-1), range between 0.09 and 0.23 Pa.

The model predicted that the bed shear stress equaled or exceeded 0.1 Pa at six out of the seven marker-horizon locations during the high-flow event that occurred on August 16-17, which was less than 6 weeks after the marker-horizon material was distributed in the bayou. Given the relatively short time between placement of the marker-horizon material and the occurrence of the mid-August storm, it is likely that the marker-horizon material was not fully incorporated into the sediment bed. Thus, it is highly probable that the marker-horizon material was resuspended during the mid-August storm at the six locations where the bed shear stress was 0.1 Pa or greater (i.e., stations PB003, PB018, PB023, PB036, PB048, PB057). At station PB062, relatively low bed shear stress values were predicted by the model for the entire six-month period. This location is near the mouth of the East Fork. At this location, the numerical grid resolution is relatively coarse, consisting of two grid cells at this

inflow boundary. The relatively coarse grid resolution in the vicinity of East Fork inflow makes it possible that model predictions are uncertain in the vicinity of station PB062, and that low bed shear stress values predicted by the model are not representative of actual conditions at this location.

3.2 Sediment Bed Stability During High-Flow Events

The calibrated and validated model was used to simulate sediment transport processes in Patrick Bayou during high-flow events. The results of these simulations were used to address specific questions about the effects of high-flow events on bed stability. A range of high-flow conditions, from 2- to 100-year events, were investigated, with the objective being to answer the following questions:

- What areas in the bayou are depositional and what areas experience erosion during a high-flow event?
- In the areas that experience erosion, what is the potential depth of net erosion?

In addition, a sensitivity analysis was conducted to evaluate the effects of uncertainty in model inputs on model results.

3.2.1 Diagnostic Evaluation of High-Flow Events

Three high-flow events were evaluated during the bed stability analysis; the three events have return periods of 2, 10, and 100 years. For this analysis, return period refers to the probability of an extreme precipitation event occurring in any given year. For example, the return periods of 2-, 10-, and 100-year events are 50%, 10%, and 1%, respectively. The magnitude for the high-flow events were obtained from the Harris County Flood Control District, with these events representing the district's calculation for specific design storms. In this analysis, a 24-hour design storm was selected as being representative of the study area. Rainfall magnitudes for the 2-, 10-, and 100-year events are 4.5, 7.8, and 13.5 inches, respectively. For a given precipitation event, the 24-hour design storm (which produced the appropriate amount of rainfall) was used as input to the watershed model. Output from the watershed model for a specific precipitation event was transferred to the hydrodynamic model (i.e., freshwater inflow at the Main inflow and East Fork boundaries). Table 3-1

shows the peak flow rates (i.e., total inflow to Patrick Bayou) for each extreme precipitation event as predicted by the watershed model.

Table 3-1
Return Periods and Flow Rates for High-Flow Events

Return Period of High-Flow Event (years)	Total Peak Flow Rate (cfs)
2	3,000
10	6,000
100	10,000

Simulating sediment transport in Patrick Bayou during a high-flow event requires specifying time-variable inflow at the two tributaries to the bayou (i.e., high-flow hydrograph). For this analysis, the hydrograph that occurred during the high-flow event on October 26-27, 2006 was chosen to be representative for the bayou. This storm event had peak inflow rate of approximately 4,000 cfs and it lasted about 24 hours. The hydrograph for a specific high-flow event (i.e., 2-, 10-, or 100-year events) was developed by linearly adjusting the October 26-27 hydrograph so that the peak flow rate corresponded to the appropriate values for that event. For example, the hydrograph for the 100-year event was generated by increasing the flow rates for the October 26-27 by about 250%.

All other forcing function and bed initial conditions were similar to the setup for the calibration simulation. Temporal variations in tidal elevation at the model boundaries along the HSC were based on data from the NOAA gauge station Battleship Texas State Park. Sediment loading was based on the TSS rating curve developed for PB075 and EF005.

Spatial distributions of predicted net erosion depths during the 2-, 10-, and 100-year high-flow events are shown on Figures 3-4, 3-5, and 3-6, respectively. During the 2-year high-flow event, net erosion is predicted to occur in about 44% of the total bed area of the bayou, with bed scour primarily in the sub-tidal zone (Figure 3-4). Erosion depths are less than 2 cm, with maximum net erosion depth of 1.7 cm occurring near station PB036. During the 10-year high-flow event, most of the net erosion depths are predicted to be less than 2 cm, but there are some areas with erosion depths predicted to range between 2 and 5 cm (maximum

scour depth of 4.5 cm). Net erosion is predicted to occur in about 52% of the total bed area of the bayou for the 10-year event. During the 100-year high-flow event, net erosion is predicted to occur in approximately 65% of the total bed area. The majority of the predicted net erosion is less than 6 cm, with a small area between stations PB006 and PB016 experiencing predicted net erosion depths between 8 and 10 cm. Maximum net erosion within this area is predicted to be 9.4 cm.

A sediment mass balance was constructed for Patrick Bayou during the 100-year high-flow event, see Figure 3-7. The bayou was separated into four zones to evaluate potential spatial differences within the bayou, see Figure 2-28 for a delineation of these zones. Overall, Patrick Bayou is predicted to be net erosional during the 100-year high-flow event.

3.2.2 *Sensitivity Analysis*

Results of the model calibration and validation process indicate that the modeling framework is a reliable tool for evaluating sediment stability during high-flow events. However, uncertainty exists in the model predictions because of uncertainty in model inputs. Thus, the effects of input uncertainty on model predictions were evaluated through a sensitivity analysis.

The 100-year high-flow event was used to evaluate the effects of varying the following model inputs: 1) erosion rate parameters; 2) external sediment load; and 3) effective bed roughness. The input values were varied between lower- and upper-bound limits. Thus, six sensitivity simulations were conducted, with the 100-year high-flow event simulation being repeated with the appropriate changes to model inputs. The effects of each sensitivity simulation were evaluated through comparison to base-case simulation results (i.e., 100-year high-flow event simulation discussed above). In addition, the sensitivity of model predictions to the resolution of the numerical grid was evaluated. The numerical grid originally developed for the hydrodynamic and sediment transport models has about 1,000 grid cells in the horizontal plane (Figure 2-8). For the sensitivity analysis, a high-resolution numerical grid was created which has about 3,800 grid cells in the horizontal plane (Figure 3-8). Both numerical grids have 10 layers in the vertical plane. Simulation times are about

four to five times longer for the high-resolution grid than for the original grid, which prevents use of the high-resolution grid for multi-year simulations.

Erosion rate parameters for the lower- and upper-bound cases were based on the erosion parameters for Sedflume cores SF-6 and SF-11, respectively. These two cores were chosen because core SF-6 erodibility was consistently lower than the average difference ratio (R_{avg}) for all five depth layers, while core SF-11 erodibility was consistently higher than the average (see Figure 2-22). For the lower-bound erosion rate simulation, the erosion parameters for core SF-6 were applied to the entire bayou, which tends to decrease predicted scour depths relative to the base-case simulation. For the upper-bound erosion rate simulation, the erosion parameters for core SF-11 were applied to the entire bayou, which tends to increase predicted scour depths relative to the base-case simulation.

For the external sediment load and effective bed roughness sensitivity simulations, lower- and upper-bound parameters were varied by a factor-of-two with respect to the base-case simulation. For the external sediment load sensitivity simulation, the incoming load was decreased by 50% and increased by 100% for the lower- and upper-bound cases, respectively. Decreasing (lower-bound simulation) sediment load tends to increase predicted bed scour depths and increasing (upper-bound simulation) sediment load tends to decrease bed scour depths. The external sediment load for the base-case simulation was 190 MT. The external sediment loads for the lower- and upper-bound simulations were 95 and 380 MT, respectively.

Decreasing (lower-bound simulation) effective bed roughness causes a decrease in bed shear stress, which tends to decrease predicted bed scour depths. Increasing (upper-bound simulation) effective bed roughness causes an increase in bed shear stress, which tends to increase bed scour depths. The effective bed roughness in the sediment transport model is determined by the D_{90} value for the bed, which was 115 and 460 μm for the lower- and upper-bound simulations, respectively.

Spatial distributions of predicted net erosion depth during the 100-year high-flow event for the seven sensitivity simulations are presented on Figures 3-9 through 3-15. These results show that the model behaves as expected: erosion depths increase/decrease for upper/lower

bound erosion parameters, decreased/increased sediment load, and increased/decreased effective bed roughness. For the original grid resolution, the maximum predicted net erosion depth varies between 4.1 cm for the lower-bound erosion rate parameters to 42 cm for the upper-bound erosion rate parameters. The model was most sensitive to the erosion rate parameters, with relatively minor sensitivity to upstream sediment load and effective bed roughness height.

Generally, the predicted erosion depths for the original and high-resolution grid simulations are similar, except in a small area between stations PB006 and PB016. The maximum scour depth predicted by the high-resolution grid model in that area was 72 cm (Figure 3-15). Cumulative frequency distributions of bed elevation change for the original and high-resolution grids are compared on Figure 3-16. That comparison shows that, generally, the two numerical grids produce similar results for the 100-year high-flow event. Only six grid cells in the high-resolution grid have predicted scour depths of more than 10 cm.

The overall effects of the sensitivity analysis are compared on Figure 3-17. This figure uses two metrics to compare the sensitivity simulations to the base-case simulation: 1) total area of net erosion (23.5 acres predicted for base-case simulation); and 2) total mass of eroded sediment (1,420 MT predicted for base-case simulation). The predicted area and mass of erosion for each sensitivity simulation were normalized with respect to the values for the base-case simulation. The results shown on Figure 3-17 indicate that the predicted net erosion area is less sensitive to variation in the three sensitivity parameters than the predicted erosion mass. Model predictions are relatively insensitive to variation in the external sediment load, and moderately sensitive to effective bed roughness. The model is most sensitive to the lower- and upper-bound values of the erosion rate parameters. The normalized net erosion areas for the lower- and upper-bound erosion rate parameters are predicted to be less than the base-case value, which appears counter-intuitive. The reason that the net erosion area for the upper-bound erosion rate parameters is less than the base-case area is that about 3.6 times more sediment mass was predicted to erode for the upper-bound erosion rate parameters. Model predictions indicate that a portion of this eroded mass was re-deposited in areas of the bayou that were net erosional for the original grid but were transformed to net depositional for the high-resolution grid. Finally, the net erosion areas

and erosion masses for the original and high-resolution grids are similar (i.e., these two metric are relatively insensitive to the resolution of the numerical grid).

3.3 Effects of External Sediment Loads on Mixing-Zone Layer Composition

This section presents additional analysis of the 14-year simulation used for model calibration and validation. In Section 2.4.6, the effects of external sediment loads on the composition of the mixing-zone (0-10 cm) layer were evaluated during the 14-year simulation period. Two sources of sediment were considered: 1) external loads; and 2) original bed sediment (i.e., sediment at the beginning of the 14-year simulation). The effects of the external loads on the sediment composition from the two sources in the mixing-zone layer of the sediment bed over the 14-year period were predicted by the sediment transport model. Similar to the modeling analysis for high-flow events, uncertainty exists in the results of the 14-year simulation. The effects of input uncertainty on model predictions were evaluated through an uncertainty analysis.

3.3.1 Diagnostic Evaluation of 14-Year Simulation

A sediment mass balance for the 14-year simulation is shown on Figure 3-18. The four zones used in the mass balance for the 100-year high-flow event were used for the 14-year period. Trapping efficiency (i.e., percentage of incoming sediment load that is deposited within a zone) varies between zones because of differences in the hydrodynamic and sediment transport characteristics of those zones. Overall, the model predicts that about 55% to 60% of the external sediment load is deposited within Patrick Bayou. The relative effects of the two sediment sources (i.e., external load and original bed) on the sediment mass balance are compared on Figure 3-19. These results indicate that: 1) the suspended sediment transport in the bayou is dominated by the external load; and 2) less than 10% of the sediment load transported from the bayou to the HSC is composed of sediment from the original bed.

As discussed in Section 2.4.6, the bed-source content of the mixing-zone (0-10 cm) layer decreases with time at an approximately exponential rate, primarily because of the deposition of external-source sediment. The rate of decrease of bed-source content in the mixing-zone layer is spatially variable within Patrick Bayou as a result of variations in the net sedimentation rate. Half-time (i.e., time needed for a 50% reduction in bed-source

content in the mixing-zone layer) is a convenient measure of the rate of decrease of bed-source content. Half-time ($T_{1/2}$) is calculated using:

$$T_{1/2} = -\ln(0.5) / \lambda_{\text{bed}} \quad (3-1)$$

where:

λ_{bed} = the predicted decay rate coefficient as defined in Equation 2-16

$\ln(0.5)$ = the natural logarithm of 0.5 (-0.693)

Values of $C_{\text{bed},14}$ (i.e., predicted bed-source content in the mixing-zone layer at the end of the 14-year period) were used to calculate λ_{bed} (using Equation 2-16) and, subsequently, $T_{1/2}$ (using Equation 3-1) in each grid cell within Patrick Bayou.

The spatial distribution of predicted half-time of bed-source sediment in the mixing-zone layer (0-10 cm) is shown on Figure 3-20. Predicted half-times are average values for the 14-year simulation period (i.e., 1993 through 2006). Model predictions indicate that approximately 30% of the total bed area in Patrick Bayou has a half-time of less than 5 years and about 40% to 45% of the total bed area has a half-time of between 5 and 10 years (Figure 3-21). About 10% of Patrick Bayou bed area was predicted to have a half-time of 30 years or more.

Because a relationship exists between bed-source content at the end of the 14-year period and NSR (see Figure 2-38), it was expected that a relationship exists between half-time and NSR, and that relationship is presented on Figure 3-22. Also shown on that figure is the idealized relationship between half-time and NSR (shown as a red line on Figure 3-22). These results indicate that half-times of 30 years or greater occur in areas with predicted NSR values of 0.3 cm/yr or less. Half-times of 5 years or less occur when predicted NSR values are greater than about 1 cm/yr.

3.3.2 *Uncertainty Analysis*

The calibrated sediment transport model is a reliable tool for evaluating the effects of external sediment loads on surface-layer bed composition over multi-year periods. However,

uncertainty exists in the results of the 14-year simulation because of uncertainty in model inputs or parameters. The effects of input uncertainty and resolution of the numerical grid on model predictions were evaluated through an uncertainty analysis.

Based on a similar uncertainty analysis conducted for a sediment transport model of the Lower Duwamish Waterway, which is an estuary near Seattle, Washington (QEA 2008), the effects of three inputs on model uncertainty were chosen for this analysis: 1) external sediment load; 2) settling speed of the class 1 (fine silt/clay) sediment; and 3) effective bed roughness (D_{90}). Lower- and upper-bound limits of these there inputs were specified as follows:

- *Upstream sediment load*: \pm a factor-of-two with respect to base-case simulation
- *Class 1 settling speed*: \pm a factor-of-two with respect to base-case simulation
- *Effective bed roughness*: \pm a factor-of-two with respect to base-case simulation

The effective diameter of class 1 for the base-case simulation was 7 μm , which corresponds to a settling speed of 2.6 meters/day. Thus, the class 1 settling speeds for the lower- and upper-bound simulations were 1.3 and 5.2 m/day, respectively. Lower- and upper-bound values of the effective bed roughness were similar to values used in the sensitivity analysis for 100-year high-flow event (i.e., D_{90} values 115 and 460 μm).

To evaluate the effects of possible interactions between the three inputs, a factorial analysis was conducted, which resulted in eight simulations to account for all of the possible combinations of the bounding limits of the three inputs. The parameter sets used in the eight uncertainty simulations are provided in Table 3-2, where “lower” refers to lower-bound value and “upper” refers to upper-bound value.

Table 3-2
Bounding Limits For Uncertainty Simulations

Simulation Number	Upstream Sediment Load Bound	Effective Bed Roughness Bound	Class 1 Settling Speed Bound
1	Lower	Lower	Lower
2	Lower	Lower	Upper
3	Lower	Upper	Lower
4	Lower	Upper	Upper
5	Upper	Lower	Lower
6	Upper	Lower	Upper
7	Upper	Upper	Lower
8	Upper	Upper	Upper

Because of the relatively long computational time for a 14-year simulation, using the entire 14-year period to evaluate model uncertainty was not feasible. To solve the problem of long computational times, the first seven years of the 14-year period was chosen for the uncertainty analysis. Numerical experiments demonstrated that the simulation for the 7-year period (i.e., 1993 through 1999) produced results that were comparable to the 14-year period. Comparisons of the predicted NSR values at the end of the 7- and 14-year periods are shown on Figure 3-23. Thus, the 7-year period chosen for the uncertainty analysis is an acceptable surrogate for the 14-year period. The results of each 7-year uncertainty simulation were compared to results of the first seven years of the 14-year base-case simulation.

Time histories of predicted bed elevation change at the nine sediment core locations used in the model validation (see Figure 2-28) are presented on Figures 3-24 through 3-32. These results indicate that at core locations where there is relatively continuous deposition (i.e., stations PB022, PB048, and PB057) the model is most sensitive to external sediment load, moderately sensitive to class 1 settling speed, and relatively insensitive to the effective bed roughness. The combination of input parameters that generally causes the highest net sedimentation corresponds to simulation 6, which had upper-bound external load, upper-bound settling speed, and lower-bound effective bed roughness. The combination of input parameters that generally causes the lowest net sedimentation corresponds to simulation 3,

which had lower-bound external load, lower-bound settling speed, and upper-bound effective bed roughness.

The effects of model input uncertainty on large-scale net sedimentation in the bayou are illustrated on Figure 3-33. This figure presents the spatial distribution, along the longitudinal axis of the bayou, of the laterally-averaged (i.e., cross channel) NSR. Even though variability in NSR exists in the lateral direction, examining the spatial variation in laterally-averaged NSR is informative for understanding large-scale variations in sedimentation patterns and for comparing the results of the uncertainty simulations. Longitudinal variation in net sedimentation rate for the 7-year period is shown on this figure, with the NSRs representing laterally-averaged (i.e., cross-channel averaging) values. Three general observations can be made from the results shown on Figure 3-33: 1) NSR values tend to decrease as distance from the upstream boundary increases (but there is significant variability in NSR at smaller spatial scales than represented on Figure 3-33); 2) NSR increases within 0.2 miles of the confluence with the HSC as a result of interactions between the bayou and HSC; and 3) the model is more sensitive to input uncertainty in the region upstream of PB042 (i.e., 4,200 feet upstream of the HSC confluence) than in the region downstream of that location.

The results presented on Figure 3-24 through 3-33 show the effects of the full range of input uncertainty on model predictions. However, not all of the combinations of model inputs used in the eight uncertainty simulations may produce results that are realistic; some uncertainty simulations may produce results that are inconsistent with site-specific data and, therefore, would be judged to be outside the range of acceptable calibration. To determine which uncertainty simulations produce realistic results, predicted NSR values for the base-case and uncertainty simulations were compared to observed values at stations PB006, PB016, PB022, PB025, PB048 and PB052, which were used for model calibration (see Figures 3-34, 3-35 and 3-36). The predicted NSR values on these figures have been normalized to the observed values at the six locations, see Table 2-9 for the observed NSR values.

The normalized sedimentation rates for the base case are slightly over-predicted at PB022. The model-data comparison at PB048 is much better. At station PB022, changes in external

sediment load have the most effect on predicted NSR. At station PB048, predicted NSR is significantly affected by uncertainty in the external sediment load and class 1 settling speed.

A review of these results indicates that the parameter combinations for uncertainty simulations 4 and 5 produce results that correspond to realistic lower- and upper-bound parameter sets, respectively. Uncertainty simulations 4 and 5 produce results that are not at the extremes of the uncertainty results, so these parameter sets will not significantly under- or over-predict NSR values in the bayou.

Comparisons of overall trapping efficiency and net deposition mass for the base-case and uncertainty simulations are shown on Figure 3-37. Both output parameters are normalized with respect to values for the base-case simulation (i.e., 79% trapping efficiency and net deposition mass of 16,600 MT). Overall uncertainty in trapping efficiency ranges from about 70% to 120% of the base-case value, with the realistic lower- and upper-bound values corresponding to 110% and 80% of the base-case value, respectively. Overall uncertainty in the net deposition mass ranges from 30% to 230% of the base-case value, with the realistic lower- and upper-bound values corresponding to 64% and 150% of the base-case value, respectively.

Spatial distribution of predicted NSR for the 7-year simulations for the base-case, lower-bound and upper-bound scenarios are shown on Figures 3-38 through 3-40, respectively. As expected, NSR values are generally lower for the lower-bound simulation and generally higher for the upper-bound simulation. For the lower-bound simulation, the model predicts the existence of two relatively large areas of net erosion (Figure 3-39).

Differences in the areal extent of predicted half-times of bed-source content between the bounding and base-case simulations are quantified on Figure 3-41. Half-times of 10 years or less range from 35% to 94% of the bayou bed area for the lower- and upper-bound simulations, respectively, as compared to 80% of the bayou for the base-case simulation. Half-times of 30 years or greater range from 19% to 0% of bayou area for the lower- and upper-bound simulations, respectively, as compared to 4% for the base-case simulation.

The effects of numerical grid resolution on predicted bed elevation change were evaluated by comparing results between the original and high-resolution grids during the first 3 years of the 14-year calibration period. The relatively long computational times required for the high-resolution grid dictated the use of a 3-year period for this analysis. Cumulative frequency distributions of predicted NSR values for the original and high-resolution grids are compared on Figure 3-42. This comparison shows that the overall distributions of predicted NSR are similar for both grids. Spatial distributions predicted NSR values for the original and high-resolution grids are shown on Figures 3-43 and 3-44, respectively. Generally, the two grids tend to predict similar spatial distributions of NSR. The high-resolution grid predicts slightly higher NSRs in the region between station PB048 and the Main inflow. Spatial distributions of predicted net erosion depth for the original and high-resolution grids during the 3-year period are shown on Figures 3-45 and 3-46, respectively. The general locations of net erosional areas are similar for the two grids. In the vicinity of station PB036, the high-resolution grid predicted deeper net erosion in a few isolated grid cells than the original grid. The net erosional area located downstream of station PB016 was predicted to be a slightly larger by the high-resolution grid than original grid. The spatial distributions of laterally-averaged NSRs for the original and high-resolution grids are compared on Figure 3-47. Note that negative NSR values on this figure correspond to net erosional areas. Overall, the general spatial trends in laterally-averaged NSR are comparable for the two grids. Measured and predicted (original and high-resolution grids) NSR values at the six core locations used for model calibration are compared on Figure 3-48. In summary, these results indicate that the original and high-resolution grids produce comparable results. Thus, use of the high-resolution grid would not produce a significant increase in model predictive capability.

4 SUMMARY AND SYNTHESIS OF RESULTS

4.1 Summary of Model Reliability

The results of the model calibration and validation presented in Section 2, in conjunction with the sensitivity and uncertainty analyses discussed in Section 3, indicate that the predictive capability and reliability of the sediment transport model are sufficient for achieving the overall objectives of this study:

- Develop a numerical model that can be used as a quantitative tool to evaluate short-term and long-term sediment transport processes and trends in Patrick Bayou.
- Develop a CSM for sediment transport in the bayou.
- Provide information to support the Feasibility Study and inform remedial decision-making.

Calibration and validation of the modeling framework were used to evaluate the accuracy and reliability of the model. The 14-year simulation period used to calibrate and validate the model was a strong test of the model's capabilities because of the wide range of tidal and freshwater inflow conditions during that period. Results of the calibration and validation exercises indicate that the model simulates sediment transport processes in Patrick Bayou. Based on these results, the following conclusions concerning model reliability were developed:

- The modeling framework may be used to refine, confirm and validate the CSM for sediment transport.
- The analysis provides quantitative uncertainty estimates for model predictions.
- The model provides a framework to support the evaluation of physical processes and the effects of potential remedial actions in Patrick Bayou.
- The model is a reliable framework for supporting extrapolation to conditions where no erosion and/or NSR data are available within Patrick Bayou.

4.2 Integration and Synthesis of Results

The modeling analyses conducted during this study, in conjunction with empirical analyses (e.g., estimation of NSR values), have produced an improved understanding of sediment transport processes in Patrick Bayou. A large amount of information on the hydrodynamics

and sediment transport within the bayou, and the hydrology of the surrounding watershed, is presented in this report. The objective of this sub-section is to integrate and synthesize the results and findings from the major components of the study so that a clear and concise picture of sediment transport in Patrick Bayou may be developed.

Freshwater flow into the bayou is significantly affected by runoff from the surrounding watershed during precipitation events. The bayou watershed is relatively small with industrialized and urbanized areas and, thus, runoff during a rainstorm occurs rapidly. The hydrologic system may be described as flashy, with runoff to the bayou increasing rapidly once a precipitation event begins and, similarly, runoff decreasing quickly after rainfall ceases. This behavior has a significant effect on the bayou hydrodynamics, as well as the external sediment loading from the watershed to the bayou.

Freshwater flow into Patrick Bayou is specified from four sources for input to the hydrodynamic model: 1) Main inflow; 2) East Fork; 3) direct runoff (which is specified as a spatially-distributed input); and 4) three OxyChem outfalls. The average total freshwater inflow from watershed runoff is 40 cfs (i.e., excluding flow from OxyChem outfalls). Total discharge from the OxyChem outfalls is presently about 28 cfs. Peak total inflow rates during precipitation events with return periods of 2, 10, and 100 years are 3,000, 6,000, and 10,000 cfs, respectively. For total inflow rate, the ratio of the 100-year event to average conditions is about 150, which demonstrates the flashy nature of this system.

Patrick Bayou is hydrodynamically connected to the HSC, with observed salinity values ranging from 10 to 20 ppt in the HSC. Estuarine circulation does occur in the bayou, with gradients in water density, due to differences in salinity, affecting bayou currents to some extent. However, Patrick Bayou has minimal vertical stratification and two-layer flow, due to the morphology and bathymetry of the bayou.

During conditions of low freshwater inflow, circulation patterns are dominated by diurnal tidal currents within Patrick Bayou. Tidal range is relatively low (i.e., typically 1-2 feet), but significant areas of mudflats in the inter-tidal zone of the bayou may be exposed during ebb tide conditions. Salinity levels in the bayou are similar to that of the HSC, with minimal horizontal gradients throughout most of the bayou.

During precipitation events with high freshwater inflow, circulation in the bayou reacts relatively quickly due to the flashy nature of the surrounding watershed. High-flow events typically occur over hourly timescales, with sustained high freshwater inflow rarely lasting for more than 24 hours during a single event. These events can have significant effects on bayou hydrodynamics. Flood waters can inundate inter-tidal zones and floodplain areas above the normal inter-tidal high-water level in the bayou. Freshwater inflow, with a large portion of the total inflow coming from the Main inflow, dominates tidal currents in the bayou during a high-flow event. Most of the bayou will contain freshwater, with large volumes of freshwater inflow pushing most of the salty water out of the bayou. After a high-flow event is over, the salinity in the bayou slowly increases as tidal processes transport brackish water into the bayou from the HSC, with the return to low-flow salinity conditions typically occurring over a period of many days.

As mentioned above, diurnal tides and the relatively low tidal elevation ranges can affect estuarine circulation in Patrick Bayou. In addition, water surface elevation conditions due to non-tidal processes in the HSC and Galveston Bay can have a significant effect on bayou hydrodynamics. Two important non-tidal processes are: 1) storm surges during hurricanes; and 2) drawdown during offshore (northerly) wind storms.

The sediment bed in Patrick Bayou is primarily composed of cohesive (i.e., muddy) sediment, with isolated areas of non-cohesive (i.e., sandy) sediment. The bayou bed located upstream of the confluence of the East Fork (i.e., upstream of PB065) is cohesive, but it is a highly consolidated bed and in the model was considered to be “hard bottom”, with negligible erosion and deposition.

External sediment loads to the bayou originate from four primary sources: 1) Main inflow; 2) East Fork; 3) OxyChem outfalls and direct runoff; and 4) HSC (i.e., upstream HSC boundary during ebb tide and downstream HSC boundary during flood tide). Sediment loading from the HSC affects the lower portion of the bayou, typically within about 0.2 miles of the confluence, with decreasing effect on bed deposition with increasing distance from the HSC. The relative contributions of annual sediment loading from the freshwater inflows are 72%, 8%, and 20% for the Main inflow, East Fork and OxyChem outfalls/direct runoff,

respectively. A large portion of the annual sediment loading (i.e., 88%) occurs during low-flow conditions. The flashy behavior of the watershed during high-flow conditions results in a relatively small portion of the annual sediment load occurring during these events. On average, for decadal periods, about 58% of the external sediment load entering Patrick Bayou is deposited in the bayou.

Long-term average net sedimentation rates in the bayou are spatially variable. Generally, NSR values decrease when moving from the upstream portion of the bayou, near the freshwater inflows, toward the HSC, but there is significant variability in NSR at localized spatial scales. Most of the bayou is predicted to be net depositional over the 14-year period, with the exception of some areas located between stations PB025 and PB036, and another area immediately downstream of station PB012.

For multi-year periods, the relative amount of bed-source sediment in the mixing-zone layer (0-10 cm) tends to decrease at an exponential rate due to deposition of external-source sediment. The half-time of bed-source content in the mixing-zone layer is related to NSR, with half-time increasing as NSR decreases. For half-times of 10 years or less, the predicted NSR is 0.7 cm/yr or greater. Predicted net sedimentation rates between 0.2 and 0.7 cm/yr correspond to half-times between 10 and 30 years. For half-times of 30 years or greater, the predicted NSR is less than 0.2 cm/yr. Within Patrick Bayou, 73%, 18%, and 9% of the bayou bed area is predicted to have half-times of bed-source content of less than 10, 10-30, and greater than 30 years, respectively.

For a precipitation event with a return period of 100 years, the bayou is predicted to be net erosional. About 1,400 MT of bed-source sediment is predicted to be transported from the bayou to the HSC. This amount of sediment corresponds to about 65% of the average annual mass of net deposition in Patrick Bayou (i.e., 2,100 MT/yr). The maximum depth of bed scour predicted by the model is about 9 cm, with most of the eroded area in the bayou experiencing bed scour of 4 cm or less. Net erosion is predicted to occur over about 67% of the bayou area, with the rest of the bayou being net depositional during this high-flow event.

4.3 Conceptual Site Model for Sediment Transport

Sediment transport and stability information from this study and historical studies are important in the formulation of a CSM for Patrick Bayou. A CSM is a useful tool for understanding transport and fate processes. In general, a CSM is a narrative or graphical representation of processes that influence the transport and fate of physical media (e.g., water, soil, sediment) within a study area of interest. Conceptual site models may incorporate both spatial and temporal elements.

The results and conclusions concerning the evaluation of sediment transport and bed stability in the bayou are largely based on modeling analyses. While the models used in this study provide reliable results, the uncertainty associated with the results, and limitations in the models, must be acknowledged. The qualitative conclusions derived from these analyses have a relatively low level of uncertainty, whereas the quantitative results have a higher level of uncertainty. The results of sensitivity analyses demonstrate that quantitative model results have an uncertainty level of a factor-of-two or less that is attributable to uncertainty in model inputs. This level of uncertainty is acceptable for the intended uses of the sediment transport model.

A goal of this study was to develop an improved understanding of sediment transport processes in the bayou. Results of the empirical and modeling analyses were used to develop the following conceptual model for sediment transport in Patrick Bayou:

- As a whole, Patrick Bayou is net depositional over annual time scales, with approximately 55% to 60% of the sediment load entering the Site from the surrounding watershed being deposited within the Site.
- Net sedimentation rates are spatially variable in Patrick Bayou, with values ranging from less than 0.1 cm/yr to over 2 cm/yr.

- Bed erosion is typically an episodic process that is most pronounced during high-flow events. During the 100-year high-flow event (i.e., event with 1% chance of occurring in a given year), net erosion occurs in approximately 65% of the total bed area and the majority of the net erosion is less than 6 cm. During the 2-year high-flow event (i.e., event with 50% chance of occurring in a given year), net erosion occurs in about 45% of the total bed area and erosion depths are less than 2 cm. Generally, erosion at the Site, even during high-flow events, only affects surface-layer sediments and is limited to bed depths that represent relatively recent deposition.
- The results indicate that for about 70% of the Site, the concentration of a COPC in the mixing-zone layer will decrease by one-half of its current concentration in less than 10 years in areas assuming “clean” sediment input.

5 REFERENCES

- American Society of Civil Engineers (ASCE), 1993. Task Committee on Definition of Criteria for Evaluation of Watershed Models of the Watershed Management Committee, Irrigation and Drainage Division. *Journal of Irrigation and Drainage Engineering* 119(3):429-442.
- Anchor Enironmental, 2007a. Remedial Investigation Work Plan Remedial Investigation/ Feasibility Study, Patrick Bayou Superfund Site, Deer Park, Texas. Prepared for U.S. Environmental Protection Agency and the Patrick Bayou Joint Defense Group. Prepared by Anchor Environmental, L.L.C., 1011 DeSoto Street, Ocean Springs, Mississippi 39564, January 2007, 184 pp.
- Anchor Environmental, 2007b. *Draft Supplemental Work Plan: Additional Hydrodynamic Data Collection, Geotechnical Data Collection, Sediment Accretion Values, Porewater Sampling and Estimation of Distribution Coefficients*. Report prepared for the Patrick Bayou Joint Defense Group, April 2007.
- Anchor Environmental, 2006. *Preliminary Site Characterization Report. Patrick Bayou Superfund Site. Deer Park, Texas*. Prepared for USEPA and Patrick Bayou Joint Defense Group.
- Berger, R.C., R.T. McAdory, J.H. Schmidt, W.D. Martin and L.H. Hauck, 1995. Houston-Galveston Navigation Channels, Texas Project, Report 4. Three-Dimensional Numerical Modeling of Hydrodynamics and Salinity. Technical Report HL-92-7. USACE, Waterways Experiment Station.
- Cheng, N.S., 1997. Simplified settling velocity formula for sediment particle. *ASCE J Hydr Engr*. 123(2):149-152.
- Garcia, M. and G. Parker, 1991. Entrainment of bed sediment into suspension. *ASCE J Hydr Engr*, 117(4):414-435.
- Gessler, J., 1967. *The beginning of bedload movement of mixtures investigated as natural armoring in channels*. W.M. Keck Laboratory of Hydraulics and Water Resources, California Institute of Technology, Translation T-5.

- Guy, H.P., D.B. Simons, and E.V. Richardson, 1966. *Summary of alluvial channel data from flume experiments, 1956-1961*. U.S. Geological Survey Professional Paper 462-I. Washington, D.C.
- Hamrick, J.M., 1992. A Three-Dimensional Environmental Fluid Dynamics Computer Code: Theoretical and Computational Aspects. College of William and Mary, Virginia Institute of Marine Sciences. Special Report 317. 63 pp.
- Jepsen R, J. Roberts, and W. Lick, 1997. Effects of bulk density on sediment erosion rates. *Water Air Soil Pollution*, 99:21-31.
- Jones, C.A. and W. Lick, 2001. *SEDZLJ: A Sediment Transport Model*. Final report. University of California, Santa Barbara, California. May 29, 2001.
- Karim, M.F. and J.F. Kennedy, 1981. *Computer-based predictors for sediment discharge and friction factor of alluvial streams, IIHR report no. 242*. Univ. of Iowa, Iowa City, Iowa.
- Maidment, D.R., 1993. Hydrologic Effects of Land-Use Change. In *Handbook of Hydrology*. New York: McGraw-Hill, Inc., 13.1-13.50.
- Nash, J.E. and J.V. Sutcliffe, 1970. River flow forecasting through conceptual models, part 1- A discussion of principles. *Journal of Hydrology* 10(3):282-290.
- Natural Resources Conservation Service (NRCS), 1994. *State Soil Geographic (STATSGO) Data Base*. Misc. publication 1492. Fort Worth, TX.
- Parker, G., 2004. *1D Sediment Transport Morphodynamics, with Applications to Rivers and Turbidity Currents*. E-book located at:
http://cee.uiuc.edu/people/parkerg/morphodynamics_e-book.htm.
- Quantitative Environmental Analysis, LLC (QEA), 2008. *Lower Duwamish Waterway Sediment Transport Modeling Report, Draft Final*. Prepared for USEPA, Region 10 and Washington State Dept. of Ecology. June 2008.
- Rahuel, J.L., F.M. Holly, J.P. Chollet, P.J. Belleudy, and G. Yang, 1989. Modeling of riverbed evolution for bedload sediment mixtures. *ASCE J Hydr Engr*, 115(11):1521-1542.
- Roberts J., R. Jepsen, and W. Lick, 1998. Effects of particle size and bulk density on the erosion of quartz particles. *ASCE J Hydr Engr* 124(12):1261-1267.

-
- Thomann, R.V. and J.A. Mueller, 1997. *Principles of Surface Water Quality Modeling and Control*. Prentice Hall, New York. 656 pages.
- U.S. Department of Agriculture, Conservation Engineering Division, 1986. *Urban Hydrology for Small Watersheds, TR-55*. USDA, June 1986.
- U.S. Department of Agriculture – Soil Conservation Service (SCS), 1972. *SCS National Engineering Handbook on Hydrology*, Washington, D.C.
- Van den Berg, J.H. and A. van Gelder, 1993. Prediction of suspended bed material transport in flows over silt and very fine sand. *Water Resour. Res.*, 29(5):1392-1404.
- Van Rijn, L.C., 1993. *Principles of Sediment Transport in Rivers, Estuaries and Coastal Seas*. Aqua Publications. Delft, The Netherlands.
- Van Rijn, L.C., H. van Rossum, and P. Termes, 1990. Field verification of 2-D and 3-D suspended-sediment models. *ASCE J Hydr Engr*, 116(10):1270-1288.
- Van Rijn, L.C., 1984a. Sediment transport, part I: bed load transport. *ASCE J Hydr Engr*. 110(10):1431-1456.
- Van Rijn, L.C., 1984b. Sediment transport, part II: suspended load transport. *ASCE J Hydr Engr*. 110(11):1612-1638.
- Van Rijn, L.C., 1984c. Sediment transport, part III: bed forms and alluvial roughness. *ASCE J Hydr Engr*. 110(12):1732-1754.
- Voogt, L., L.C. van Rijn, and J.H. van den Berg, 1991. Sediment transport of fine sands at high velocities. *ASCE J Hydr Engr*, 117(7):869-890.
- Wright, S., and G. Parker, 2004. Flow resistance and suspended load in sand-bed rivers: simplified stratification model. *ASCE J. Hydr. Engr*. 130(8):796-805.
- Ziegler, C.K, P.H. Israelsson, and J.P. Connolly, 2000. Modeling sediment transport dynamics in Thompson Island Pool, Upper Hudson River. *Water Quality and Ecosystem Modeling* 1:193-222.
- Ziegler, C.K. and W. Lick, 1988. The transport of fine-grained sediments in shallow waters. *Environmental Geology and Water Sciences* 11:123-132.

APPENDIX A
DETAILS OF SEDIMENT TRANSPORT
MODEL THEORY AND FORMULATION

APPENDIX A

DETAILS OF SEDIMENT TRANSPORT MODEL

THEORY AND FORMULATION

This appendix presents discussion of the theory and formulations used in the sediment transport model to calculate erosion and deposition fluxes at the sediment-water interface. For bed scour, erosion fluxes in cohesive and non-cohesive bed areas are treated differently. In a grid cell specified as hard bottom, the erosion and deposition fluxes are set to zero, so no change in bed elevation is calculated during a simulation.

A.1 CALCULATION OF BED SHEAR STRESS

Erosion rate is dependent on bed shear stress, which is calculated using near-bed current velocity predicted by the hydrodynamic model. The bed shear stress calculated within the hydrodynamic model is the total bed shear stress, which represents the total drag on the water column by the sediment bed. The total bed shear stress (τ_{tot}) is the sum of shear stresses associated with skin friction (τ_{sf}) and form drag (τ_{fd}):

$$\tau_{\text{tot}} = \tau_{\text{sf}} + \tau_{\text{fd}} \quad (\text{A-1})$$

Skin friction represents the shear stress generated by sediment particles (i.e., small-scale physical features), whereas form drag corresponds to the drag generated by bedforms (e.g., ripples, dunes) and other large-scale physical features. When simulating the erosion of a cohesive bed, skin friction is considered the dominant component of the bed shear stress for most applications. The hydrodynamic and sediment bed conditions in Patrick Bayou are not favorable for developing physical features (e.g., wavy beds) that induce form drag. Thus, it is a reasonable approximation, and a standard approach, to use the skin friction component and neglect form drag for calculating bed shear stress for a cohesive bed. This approach is consistent with accepted sediment transport theory (Parker 2004). Skin friction shear stress is calculated using the quadratic stress law:

$$\tau_{\text{sf}} = \rho_w C_f u^2 \quad (\text{A-2})$$

where ρ_w is the density of water, C_f is the bottom friction coefficient, and u is the near-bed current velocity (i.e., predicted velocity in the bottom layer of the numerical grid). Use of the near-bed current velocity is standard practice for calculating bed shear stress in a three-dimensional model. The bottom friction coefficient is determined using (Parker 2004):

$$C_f = \kappa^2 \ln^{-2}(11 z_{ref} / k_s) \quad (A-3)$$

where z_{ref} is a reference height above the sediment bed, k_s is the effective bed roughness, and κ is von Karman's constant (0.4). The reference height (z_{ref}) is spatially and temporally variable because it is equal to half of the thickness of the bottom layer of the numerical grid. Because a stretched (sigma-layer) grid is used in the vertical direction, the thickness of the bottom layer of the vertical grid is equal to 10% of the local water depth, which varies due to changes in tidal elevation and river flow rate. Thus, the reference height properly incorporates temporal and spatial variations in water depth into the calculation of the bottom friction coefficient. The effective bed roughness is assumed to be proportional to the D_{90} of the surface sediment layer (Parker 2004, Wright and Parker 2004):

$$k_s = 2D_{90} \quad (A-4)$$

Grain size distribution data were used to specify D_{90} values for the surface layer of Patrick Bayou sediments (see Section 2.4.3).

The validity of the above approach for calculating the bottom friction coefficient is evaluated as follows. Bottom friction coefficients were calculated for Patrick Bayou over a range of water depths using an average D_{90} value of 230 μm (see Table A-1). The range of bottom friction coefficient values in Table A-1 is consistent with expected values for cohesive beds (van Rijn 1993). This approach provides an objective method for estimating the effective bed roughness, which will decrease the uncertainty associated with subjective estimates of roughness.

Table A-1
Bottom Friction Coefficient Values for a Range of Water Depths

Water Depth (m)	Bottom Coefficient: $D_{90} = 230 \text{ } \mu\text{m}$
1	0.0032
2	0.0026
3	0.0024
4	0.0022

For use in formulations presented below, a demonstrated accurate equation for bed-shear velocity (u^*) is defined as (van Rijn 1993):

$$u^* = (\tau_{sf} / \rho_w)^{0.5} \quad (\text{A-5})$$

Current velocity in turbulent flow, which exists in the bayou for all flow and tidal conditions, is the sum of two components: time-averaged mean velocity and turbulent fluctuations about the mean value. The bed-shear velocity (u^*) corresponds to the turbulent-fluctuation component of the current velocity. Thus, the skin friction shear stress is driven by the turbulent fluctuations in the flow, which randomly variable with time. Random variation in turbulence along the sediment bed is the primary reason that a probabilistic approach to calculating deposition and erosion fluxes is necessary; use of probability of deposition (see Equation A-6) and suspension (see Equation A-15) formulations have been incorporated into the model to account for these turbulence effects.

A.2 DEPOSITION PROCESSES

The deposition flux for size class k sediment (D_k) is expressed as (Ziegler et al. 2000):

$$D_k = P_{\text{dep},k} W_{s,k} C_k \quad (\text{A-6})$$

where $P_{\text{dep},k}$ is probability of deposition of class k , $W_{s,k}$ is settling speed of class k , and C_k is near-bed suspended sediment concentration of class k . Deposition flux has units of mass per unit area per time (e.g., $\text{g}/\text{cm}^2\text{-s}$). The near-bed concentration (C_k) is calculated using the

sediment transport model and is represented by the value in the vertical grid cell immediately above the bed.

Probability of deposition of cohesive sediment (i.e., class 1) is determined using the Krone formulation (van Rijn 1993):

$$P_{\text{dep},k} = 1 - (\tau_{\text{sf}}/\tau_{\text{cr,dep}}) \quad \text{for } \tau_{\text{sf}} < \tau_{\text{cr,dep}} \quad (\text{A-7})$$

$$= 0 \quad \text{for } \tau_{\text{sf}} > \tau_{\text{cr,dep}} \quad (\text{A-8})$$

where τ_{sf} is bed shear stress (skin friction) and $\tau_{\text{cr,dep}}$ is the critical bed shear stress for deposition. The relationship between probability of deposition and bed shear stress for class 1 is shown in Figure A-1.

For non-cohesive sediment that is suspendable (i.e., classes 2 and 3), the probability of deposition depends on bed shear stress and particle diameter, and is described by a Gaussian distribution (Gessler 1967, Ziegler et al. 2000):

$$P_{\text{dep},k} = (2\pi)^{-0.5} \int \text{EXP}(-0.5x^2) dx \quad (\text{A-9})$$

where the lower and upper limits of the integral are negative infinity and Y , respectively, and EXP corresponds to the exponential function with base e . The parameter Y is given by:

$$Y = 1.75 (\tau_{\text{c},k} / \tau_{\text{sf}} - 1) \quad (\text{A-10})$$

where $\tau_{\text{c},k}$ is critical shear stress for suspension of class k sediment, which is:

$$\tau_{\text{c},k} = \rho_w u_{*,\text{crs},k}^2 \quad (\text{A-11})$$

where $u_{*,\text{crs},k}$ is critical bed-shear velocity for initiation of suspension for class k :

$$u_{*,\text{crs},k} = 4 W_{s,k} / d_{*,k} \quad \text{for } 1 < d_{*,k} \leq 10 \quad (\text{A-12})$$

$$= 0.4 W_{s,k} \quad \text{for } d_{*,k} > 10$$

and:

$$d_{*,k} = d_k [(s-1)g/\nu^2]^{1/3} \quad (\text{A-13})$$

where d_k is particle diameter for class k , s is specific density of particle (i.e., 2.65), g is acceleration caused by gravity, and ν is kinematic viscosity of water. The non-dimensional particle parameter ($d_{*,k}$) is commonly used in a wide range of sediment transport formulations (van Rijn 1993). The probability of deposition for classes 2 and 3 as a function of bed shear stress and particle diameter is presented in Figure A-2.

Numerous field and laboratory experiments have demonstrated that a physically realistic representation of the settling speed of a discrete particle is related to the particle diameter, representing size class k , as follows (Cheng 1997):

$$W_{s,k} = (\nu/d_k) [(25 + 1.5 d_{*,k}^2)^{0.5} - 5]^{1.5} \quad (\text{A-14})$$

The dependence of settling speed on particle diameter is shown in Figure A-3. The effective particle diameters for the four sediment classes (d_k), which determine the settling speeds of each class through use of Equation A-14, were specified as follows. Effective particle diameter for class 1 (i.e., clay and silt) was treated as an adjustable calibration parameter. Specification of effective particle diameters for classes 2, 3 and 4 (i.e., fine sand, medium/coarse sand, and gravel) was based on an analysis of Patrick Bayou grain size distribution data.

A.3 EROSION PROCESSES: COHESIVE BED

Within sediment bed areas designated as cohesive, the following numerical algorithm is used to calculate the erosion flux of sediment from the bed to the water column, where it is transported as suspended sediment. The erosion flux for size class k sediment (E_k) from a cohesive bed is given by:

$$E_k = \rho_{\text{dry}} f_{AS,k} S_k P_{\text{sus},k} E_{\text{gross}} \quad (\text{A-15})$$

where E_{gross} is the gross erosion rate, $P_{\text{sus},k}$ probability of suspension for size class k , S_k is the particle-shielding factor for size class k , ρ_{dry} is dry density of bed sediment, and $f_{\text{AS},k}$ is the fraction of size class k sediment in the active-surface layer. Erosion flux has units of mass per unit area per time (e.g., $\text{g}/\text{cm}^2\text{-s}$).

Erosion of a sediment bed depends on a number of factors, including, but not limited to: shear stress, grain size distribution, dry (bulk) density, total organic carbon content, and gas content (Jepsen et al. 1997, Roberts et al. 1998). Factors such as TOC content, gas content and bioturbation are implicitly incorporated into the cohesive erosion algorithm through the use of site-specific erosion rate data (i.e., Sedflume core data). The rate at which sediment is removed from the consolidated sediment bed and transported to a thin near-bed layer that exists between the consolidated sediment bed and the water column is termed the gross erosion rate (E_{gross}). Some of the eroded sediment in the near-bed layer is re-deposited to the consolidated bed; the rate of re-deposition is referred to as the gross deposition rate (D_{gross}). The remainder of the eroded material in the near-bed layer is transported to the water column; this rate is referred to as the net erosion rate (E_{net}). The near-bed layer discussed above is incorporated into a model of the sediment bed, which is described below.

Erosion rate data obtained from Sedflume testing were analyzed to develop an understanding of the erosion properties of Patrick Bayou sediments (see Appendix B). The goal of that analysis was to develop a functional relationship between E_{gross} and other parameters that affect erosion rate. These relationships and parameters are incorporated into algorithms so that site-specific, spatially-variable erosion properties measured for the bayou can be represented in the model. Similar to previous studies (e.g., QEA 2008), it is assumed in this study that erosion rate is dependent on skin friction shear stress (Jones and Lick 2001):

$$\begin{aligned} E_{\text{gross}} &= A \tau_{\text{sf}}^n && \text{for } \tau_{\text{sf}} > \tau_{\text{cr}} \\ &= 0 && \text{for } \tau_{\text{sf}} \leq \tau_{\text{cr}} \end{aligned} \tag{A-16}$$

where E_{gross} is gross erosion rate (cm/s), τ_{sf} is skin friction shear stress (Pa), and τ_{cr} is critical shear stress (Pa), which is the shear stress at which a small, but measurable, rate of erosion occurs (generally less than $2 \text{ mm}/\text{hr}$). The erosion parameters, A and n , are site-specific and

may be spatially variable, both horizontally and vertically. Discussion of spatial variations in the erosion parameters in Equation A-16 is presented in Section 2.4.3 and Appendix B.

The erosion rate of each sediment size class is affected by the probability of suspension for that size class ($P_{\text{sus},k}$), which is given by (Jones and Lick 2001):

$$\begin{aligned} P_{\text{sus},k} &= 0 && \text{for } \tau_{\text{sf}} \leq \tau_{\text{c},k} \\ &= [\ln(\beta_1) - \ln(\beta_2)] / [1.39 - \ln(\beta_2)] && \text{for } \tau_{\text{sf}} \geq \tau \text{ and } \beta_1 \leq 4 \\ &= 1 && \text{for } \beta_1 > 4 \end{aligned} \tag{A-18}$$

and the non-dimensional parameters are:

$$\beta_1 = u^* / W_{s,k} \tag{A-18}$$

$$\beta_2 = u^*_{\text{crs},k} / W_{s,k} \tag{A-19}$$

The formulation presented in Equation A-17 was developed from the results of flume measurements of suspended and bedload transport of sand conducted by Guy et al. (1966). Jones and Lick (2001) analyzed the Guy et al. (1966) data, with Equation A-17 resulting from their analysis. Probability of suspension as a function of bed shear stress is shown in Figure A-4 for particle diameters of 130 and 540 μm . This figure shows that for a given shear stress value, the probability of suspension increases with decreasing particle size.

The particle-shielding factor is used to reduce the erosion flux of smaller particles within a graded bed (i.e., bed with wide range of particle sizes) that are sheltered by larger particles. The particle-shielding factor (S_k) for size class k is formulated as follows (Karim and Kennedy 1981, Rahuel et al. 1989):

$$\begin{aligned} S_k &= (d_k / d_m)^{0.85} && \text{for } d_k \leq d_m \\ &= 1 && \text{for } d_k > d_m \end{aligned} \tag{A-20}$$

where d_m is the mean particle diameter in the active layer. The relationship between the particle-shielding factor and particle diameter, for three values of mean particle diameter, is shown in Figure A-5. For a given particle diameter (d_k), the particle-shielding effect increases (i.e., S_k decreases) as the mean particle diameter increases. The particle-shielding factor was not included in the original version of the SEDZLJ algorithm (Jones and Lick 2001). The SEDZLJ algorithm was modified to include the particle-shielding factor (QEA 2008). The particle-shielding factor is consistent with erosion processes within a graded bed, where voids between larger particles provide areas where smaller particles may be shielded (i.e., “hide”) from the turbulence at the sediment-water interface that induces erosion. Thus, the particle-shielding factor is a mechanistic parameter that accounts for real processes that affect scour from a graded bed.

The sediment bed model used in the bed scour model is similar to the bed model described in Jones and Lick (2001). This bed model has been developed over the previous 20 years and used within the SEDZL and SEDZLJ algorithms (Ziegler and Lick 1988, Ziegler et al. 2000, Jones and Lick 2001, QEA 2008). The SEDZL/SEDZLJ bed model has been successfully used in over 30 sediment transport modeling studies, including: Lower Duwamish Waterway (Washington), Upper Hudson River, Lavaca Bay (Texas), Grasse River (New York), Upper Mississippi River (Minnesota), Watts Bar Reservoir/Tennessee River (Tennessee), and Patrick Bayou (Texas).

A multi-layer bed model is used in the SEDZLJ algorithm, with each bed layer having specific erosion rate parameters (i.e., τ_{cr} , A , and n). For this study, five bed layers are used, with the initial thickness of each layer being 5 or 6 cm, with the first (top) layer being 6-cm thick and the four deeper layers being 5-cm thick. Use of these layers in the bed model is based on the vertical variation in erosion rate data obtained from the Sedflume cores; the shear stress series were repeated in approximately 5-cm increments in a core during the Sedflume tests. Discretizing the bed into five layers allows specifying vertical variation in erosion properties, with the erodibility of cohesive sediment generally decreasing with depth in the bed, primarily due to consolidation processes. Additional discussion about the five-layer bed model is presented in Section 2.4.3 and Appendix B.

The effects of consolidation on erosion properties of deposited sediment are not explicitly incorporated into the bed model. Deposited sediment is added to layer 1 (i.e., surface layer) of the bed model and, thus, that sediment has the same erosion properties as the surface layer. This approach produces conservative results during a high-flow event because the erosion properties of sediment deposited prior to the event will not have been reduced due to consolidation.

Erosion from cohesive and non-cohesive beds is affected by bed armoring, which is a process that tends to limit the amount of bed scour during a high-flow event. Bed armoring occurs in a bed that contains a range of particle sizes (e.g., clay, silt, sand). During a high-flow event when erosion is occurring, finer particles (i.e., clay and silt) tend to be eroded at a faster rate than coarser particles (i.e., sand). The differences in erosion rates of various particle sizes creates a thin layer at the surface of the bed, referred to as the active layer, that is depleted of finer particles and enriched with coarser particles. This depletion-enrichment process can lead to bed armoring, where the active layer is primarily composed of coarse particles that have limited mobility.

After bed armoring occurs during a high-flow event, various physical mixing processes in the surface layer of the bed (e.g., bioturbation) can affect the armor layer. The effects of physical mixing processes on bed armoring are not well understood at the present time; these effects are not explicitly incorporated into the bed model and bed armoring algorithm. However, the effects of physical mixing processes are implicitly included into the bed model through use of the Sedflume data, which incorporates these effects into the erosion rate data. Physical mixing in the surface layer is one reason why near-surface sediment is generally more erodible than deeper sediment.

The bed armoring process is simulated using an active layer at the surface of the bed, with the gross erosion rate being affected by the composition of the active layer (Jones and Lick 2001). The active layer is a theoretical construct that approximates the near-bed layer mentioned during the description of gross deposition and erosion rates previously in this section. The active layer is part of a numerical algorithm and it was created as a “holding area” such that the bed model realistically represents the complex processes at the sediment-water interface. Even though the active-layer approach used in the model is a simplification

of various complex processes, it is conceptually realistic and has been shown to produce accurate results in previous modeling studies.

The surface-layer in the bed model (i.e., top 5-cm layer) is divided into two zones: 1) active layer; and 2) parent bed. The active layer is at the top of the surface layer and the parent bed is below it. The active layer interacts with the water column; erosion and deposition across the sediment-water interface occurs in the active layer. In this study, four size classes of sediment were used. Class 1 sediment represents cohesive sediment (i.e., clay and silt, less than 62 μm diameter). Class 2 sediment represents fine sand (i.e., 62 to 250 μm diameter). Class 3 sediment represents medium and coarse sand (i.e., 250 to 2,000 μm diameter). Class 4 represents gravel (i.e., greater than 2,000 μm diameter). The bed model tracks changes in the composition of the active layer associated with erosion and deposition; temporal changes in active layer composition affect the erosion process.

The active layer is composed of two sub-layers: 1) active-surface layer; and 2) active-buffer layer. The active-surface layer interacts with the water column, while the active-buffer layer controls interactions between the active-surface layer and the parent bed (Figure A-6). The original version of SEDZLJ did not separate the active layer into two sub-layers (Jones and Lick 2001). This modification of the SEDZLJ algorithm was made because initial model testing during a previous study, without the active layer being separated into two sub-layers, indicated that unrealistic deposition and erosion patterns were predicted (QEA 2008). It was determined that the original SEDZLJ algorithm tended to over-predict erosion due to repeated expansion and contraction of the active layer over the course of numerous tidal cycles; there was excessive interaction between the active and parent bed layers caused by “tidal pumping” of sediment from the parent bed to the active layer as the active layer expanded and contracted. The objective of separating the active layer into two sub-layers was to produce a more realistic representation of the interactions between the active and parent-bed layers in a tidal environment (QEA 2008).

The thickness of the active-surface layer is assumed to depend on bed shear stress and grain size distribution. The formulation used to calculate active-surface layer thickness (T_{AS}) is (Jones and Lick 2001):

$$T_{AS} = 2 d_m (\tau_{sf} / \tau_{cr}) \quad (A-21)$$

where d_m is the mean particle diameter in the active layer. The active-surface layer thickness is temporally and spatially variable, and it changes as the composition of the bed and bed shear stress change with time. The active-surface layer thickness is determined using Equation A-21, with the bed model tracking the mass per unit area using:

$$M_{AS} = \rho_{dry} T_{AS} \quad (A-22)$$

where M_{AS} is the total sediment mass per unit area in the active-surface layer and ρ_{dry} is the dry density of bed sediment. The thickness, or mass per unit area, of the active-surface layer changes with time as T_{AS} changes as a result of increases or decreases in mean particle diameter or bed shear stress. Let $\delta_{SB,k}$ represent changes in active-surface layer mass, for size class k , caused by temporal changes in M_{AS} . Expansion and contraction of the active-surface thickness (i.e., T_{AS}) causes interactions between the active-surface and active-buffer layers, which result in mass transfer between the two layers. For increasing M_{AS} (i.e., $M_{AS}^{N+1} > M_{AS}^N$, where the superscript N represents time-level N in the numerical model):

$$\delta_{SB,k} = f_{AB,k} (M_{AS}^{N+1} - M_{AS}^N) \quad (A-23)$$

where $f_{AB,k}$ is the fraction of size class k sediment in the active-buffer layer. For decreasing or constant M_{AS} (i.e., $M_{AS}^{N+1} \leq M_{AS}^N$):

$$\delta_{SB,k} = f_{AS,k} (M_{AS}^{N+1} - M_{AS}^N) \quad (A-24)$$

where $f_{AS,k}$ is the fraction of size class k sediment in the active-surface layer. The change in active-surface layer mass is calculated using:

$$M_{AS,k}^{N+1} = M_{AS,k}^N + \delta_{SB,k} + \Delta t (D_k - E_k - f_{AS,k} D_{tot} + f_{AB,k} E_{tot}) \quad (A-25)$$

where $M_{AS,k}$ is active-surface layer mass per unit area for size class k sediment, E_k is the erosion flux for size class k sediment, D_k is the deposition flux for size class k sediment, and Δt is the numerical time-step. The total deposition and erosion fluxes are given by:

$$D_{\text{tot}} = \sum D_k \quad (\text{A-26})$$

$$E_{\text{tot}} = \sum E_k \quad (\text{A-27})$$

where the summations are over the four size classes. In Equation A-27, the values of E_k are calculated using Equation A-15 for each size class k . Thus, E_{tot} is affected by the composition of the active-surface layer.

The terms on the right-hand-side of Equation A-25 correspond to the following changes in the mass of the active-surface layer: 1) $\delta_{\text{SB},k}$ is an increase in mass of class k sediment if the total active-surface layer mass is increasing (i.e., mass added from active-buffer layer) and it is a decrease in mass of class k sediment if the total active-surface layer mass is decreasing (i.e., mass lost to active-buffer layer); 2) $\Delta t D_k$ is an increase in mass of class k sediment due to deposition from the water column to the bed; 3) $\Delta t E_k$ is an decrease in mass of class k sediment due to erosion from the bed to the water column; 4) $\Delta t f_{\text{AS},k} D_{\text{tot}}$ is a decrease in mass of class k sediment caused by movement of sediment from the active-surface layer to the active-buffer layer due to deposition; and 5) $\Delta t f_{\text{AB},k} E_{\text{tot}}$ is an increase in mass of class k sediment caused by movement of sediment from the active-buffer layer to the active-surface layer due to erosion.

The change in active-buffer layer mass for size class k ($M_{\text{AB},k}$) is calculated using:

$$M_{\text{AB},k}^{N+1} = M_{\text{AB},k}^N - \delta_{\text{SB},k} + \Delta t [(f_{\text{AS},k} - f_{\text{AB},k})D_{\text{tot}} - (f_{\text{AB},k} - f_{\text{P},k})E_{\text{tot}}] \quad (\text{A-28})$$

The terms on the right-hand-side of Equation A-28 correspond to the following changes in the mass of the active-buffer layer: 1) $\delta_{\text{SB},k}$ is a decrease in mass of class k sediment if the total active-surface layer mass is increasing (i.e., mass lost to active-surface layer) and it is an increase in mass of class k sediment if the total active-surface layer mass is decreasing (i.e., mass added from active-surface layer); 2) $\Delta t f_{\text{AS},k} D_{\text{tot}}$ is an increase in mass of class k sediment caused by movement of sediment from the active-surface layer to the active-buffer layer due to deposition; 3) $\Delta t f_{\text{AB},k} D_{\text{tot}}$ is a decrease in mass of class k sediment caused by movement of sediment from the active-buffer layer to the parent-bed layer due to deposition; 4) $\Delta t f_{\text{AB},k} E_{\text{tot}}$ is a decrease in mass of class k sediment caused by movement of sediment from the active-buffer layer to the active-surface layer due to erosion; and 5) $\Delta t f_{\text{P},k} E_{\text{tot}}$ is an increase in mass

of class k sediment caused by movement of sediment from the parent-bed layer to the active-buffer layer due to erosion.

When the buffer layer is depleted of sediment, the active-surface layer interacts directly with the parent bed (Figure A-7). Let $\delta_{SP,k}$ represent changes in active-surface layer mass, for size class k, caused by temporal changes in M_{AS} and expansion/contraction interactions between the active-surface and parent-bed layers. For increasing M_{AS} :

$$\delta_{SP,k} = f_{P,k} (M_{AS}^{N+1} - M_{AS}^N) \quad (A-29)$$

where $f_{P,k}$ is the fraction of size class k sediment in the parent-bed layer. For decreasing or constant M_{AS} :

$$\delta_{SP,k} = f_{AS,k} (M_{AS}^{N+1} - M_{AS}^N) \quad (A-30)$$

The change in active-surface layer mass for size class k is calculated using:

$$M_{AS,k}^{N+1} = M_{AS,k}^N + \delta_{SP,k} + \Delta t (D_k - E_k - f_{AS,k} D_{tot} + f_{P,k} E_{tot}) \quad (A-31)$$

The terms on the right-hand-side of Equation A-31 correspond to the following changes in the mass of the active-surface layer: 1) $\delta_{SP,k}$ is an increase in mass of class k sediment if the total active-surface layer mass is increasing (i.e., mass added from parent-bed layer) and it is a decrease in mass of class k sediment if the total active-surface layer mass is decreasing (i.e., mass lost to parent-bed layer); 2) $\Delta t D_k$ is an increase in mass of class k sediment due to deposition from the water column to the bed; 3) $\Delta t E_k$ is a decrease in mass of class k sediment due to erosion from the bed to the water column; 4) $\Delta t f_{AS,k} D_{tot}$ is a decrease in mass of class k sediment caused by movement of sediment from the active-surface layer to the parent-bed layer due to deposition; and 5) $\Delta t f_{P,k} E_{tot}$ is an increase in mass of class k sediment caused by movement of sediment from the parent-bed layer to the active-surface layer due to erosion.

The change in parent-bed layer mass for size class k ($M_{P,k}$) is determined from:

$$M_{P,k}^{N+1} = M_{P,k}^N - \delta_{SP,k} + \Delta t (f_{AS,k} D_{tot} - f_{P,k} E_{tot}) \quad (A-32)$$

The terms on the right-hand-side of Equation A-32 correspond to the following changes in the mass of the parent-bed layer: 1) $\delta_{SP,k}$ is a decrease in mass of class k sediment if the total active-surface layer mass is increasing (i.e., mass lost to active-surface layer) and it is an increase in mass of class k sediment if the total active-surface layer mass is decreasing (i.e., mass added from active-surface layer); 2) $\Delta t f_{AS,k} D_{tot}$ is an increase in mass of class k sediment caused by movement of sediment from the active-surface layer to the parent-bed layer due to deposition; and 3) $\Delta t f_{P,k} E_{tot}$ is a decrease in mass of class k sediment caused by movement of sediment from the parent-bed layer to the active-surface (or active-buffer layer) due to erosion.

After the buffer layer is depleted, a new active-buffer layer is created when the active-surface layer decreases in thickness as a result of decreasing bed shear stress. For the condition when $M_{AB,k}^{N+1}$ equals zero and M_{AS} is decreasing (i.e., $M_{AS}^{N+1} \leq M_{AS}^N$), then the initial mass of the new active-buffer layer, for size class k, is:

$$M_{AB,k}^{N+1} = f_{P,k} (M_{AS}^N - M_{AS}^{N+1}) \quad (A-33)$$

This amount of mass is removed from the parent-bed layer, so that mass is conserved.

The fractions of each sediment size class are updated after the new sediment masses are calculated in each layer:

$$f_{AS,k} = M_{AS,k}^{N+1} / M_{AS}^{N+1} \quad (A-34)$$

$$f_{AB,k} = M_{AB,k}^{N+1} / M_{AB}^{N+1} \quad (A-35)$$

$$f_{P,k} = M_{P,k}^{N+1} / M_P^{N+1} \quad (A-36)$$

where M_{AS}^{N+1} , M_{AB}^{N+1} , and M_P^{N+1} are total sediment mass per unit area in the active-surface, active-buffer, and parent-bed layers, respectively.

The numerical algorithm presented above for the interactions between the active-surface, active-buffer, and parent-bed layers may be difficult to understand from a conceptual

viewpoint. The following sequence of figures is intended to clarify the mechanistic interactions between the three layers due to temporal variations in bed shear stress, which result in expansion and contraction of the active layer. It is assumed that initially (i.e., time = t_1) two layers exist: 1) active-surface layer (with thickness $T_{AS,1}$ corresponding to a shear stress value of $\tau_{sf,1}$); and 2) parent-bed layer (see Figure A-8). As the shear stress increases to $\tau_{sf,2}$ (which is greater than $\tau_{sf,1}$) at time = t_2 , the active-surface layer thickness increases to $T_{AS,2}$ and sediment is transferred from the parent-bed layer to the active-surface layer (Figure A-9). The shear stress reaches a maximum value at time = t_2 and decreases to a value of $\tau_{sf,3}$ at time = t_3 . As the shear stress decreases during this time interval (i.e., t_2 to t_3), an active-buffer layer is created as the active-surface layer contracts in size, which is the process that generates an active-buffer layer (Figure A-10). This new active-buffer layer was created from a portion of the active-surface layer that existed at time = t_2 ; sediment was transferred from the active-surface layer to the active-buffer layer. As the shear stress continues to decrease during the time interval between t_3 and t_4 , the active-surface and active-buffer layers decrease and increase in thickness, respectively (Figure A-11). The shear increases during the time interval between t_4 and t_5 , which causes sediment to be transferred from the active-buffer layer (which is contracting) to the active-surface layer (which is expanding) (see Figure A-12). Note that during the time interval between t_2 and t_5 , when the shear stress is less than the maximum value of $\tau_{sf,2}$, the sum of the thicknesses of the active-surface and active-buffer layers remains constant at a value of $T_{AS,2}$ (assuming that no deposition or erosion occurs). During the time interval between t_5 and t_6 , the active-buffer layer is destroyed, and sediment is transferred from the parent-bed layer to the active-surface layer, as the shear stress exceeds the original maximum value of $\tau_{sf,2}$ and the active-surface layer expands to a thickness greater than $T_{AS,2}$ (Figure A-13). As the shear stress decreases from the new maximum value of $\tau_{sf,6}$, a new active-buffer layer is created from the active-surface layer as that layer contracts in size (Figure A-14).

The structure of the bed model described above is based on heuristic concepts that were developed from a general understanding of cohesive bed processes. The overall concepts applied to, and general behavior of, the model are believed to be realistic and consistent with known processes. However, uncertainty exists in some details of the model structure (e.g., transfer of sediment between the active-surface, active-buffer, and parent-bed layers as the active layer expands and contracts). Due to the complexity of the model structure, a unique

methodology does not exist and a wide range of alternatives can be constructed from proposed general structure. However, the approach that is described above, and used in this modeling study, is consistent with a general understanding of cohesive bed processes and it does produce reasonable results.

A.4 EROSION PROCESSES: NON-COHESIVE BED

Non-cohesive sediment bed transport is dominated by gravitational, lift, and drag forces acting on individual particles. Cohesive forces are negligible compared to these other forces and are not evident in non-cohesive bed behavior. Non-cohesive beds generally contain only a small amount of clay and silt particles. Numerous laboratory and field studies have been conducted on the erosion properties of non-cohesive sediments; see van Rijn (1993) for an overview. These investigations have lead to the development of various formulations for quantification of non-cohesive suspended and bedload transport. Several investigators have evaluated the accuracy of different quantitative approaches using laboratory and field data (Garcia and Parker 1991, Voogt et al. 1991, van den Berg and van Gelder 1993). The results of these investigations have shown that the formulations developed by van Rijn (1984a, b, c) provide one of the best methods for calculating suspended load transport of non-cohesive sediments. The van Rijn equation have been successfully used in sediment transport modeling studies of riverine (Ziegler et al. 2000) and estuarine (van Rijn et al. 1990) systems over a wide range of flow and sediment conditions.

The numerical algorithm discussed below is used to calculate the erosion flux of sediment from a non-cohesive bed to the water column, where it is transported as suspended sediment. Following the van Rijn method, the equations presented below are used to calculate the erosion flux for sediment size class k , which is represented by an effective particle diameter (d_k). The critical bed-shear velocity for initiation of bedload transport ($u^*_{crb,k}$) is calculated using the Shields criteria (see Figure A-15):

$$u^*_{crb,k} = [(s-1) g d_k \theta_{cr,k}]^{0.5} \quad (A-37)$$

where θ_{cr} is the critical mobility parameter, which is approximated by (van Rijn 1993):

$$\begin{aligned}
\theta_{cr,k} &= 0.24 d_{*,k}^{-1} && \text{for } d_{*,k} \leq 4 \\
&= 0.14 d_{*,k}^{-0.64} && \text{for } 4 < d_{*,k} < 10 \\
&= 0.04 d_{*,k}^{-0.10} && \text{for } 10 < d_{*,k} < 20 \\
&= 0.013 d_{*,k}^{0.29} && \text{for } 20 < d_{*,k} < 150 \\
&= 0.055 && \text{for } d_{*,k} > 160
\end{aligned} \tag{A-38}$$

and $d_{*,k}$ is calculated using Equation A-13. Equation A-38 is a piece-wise fit to the Shields curve that was developed by van Rijn (1993). Critical shear stresses for initiation of bedload ($\tau_{crb,k}$) and suspended load ($\tau_{crs,k}$) transport are calculated as follows:

$$\tau_{crb,k} = \rho_w u_{*,crb,k}^2 \tag{A-39}$$

$$\tau_{crs,k} = \rho_w u_{*,crs,k}^2 \tag{A-40}$$

The relationships between particle diameter and the critical bed shear stresses for bedload and suspended load transport are shown in Figure A-16. For sediment class 1, which represents clay and silt, it is assumed that Equations A-12 and A-37 through A-40 can be extrapolated to particle sizes less than 62 μm (i.e., d^* less than 1.47).

If the bed shear stress exceeds the critical shear stress for suspended load transport, then the equilibrium sediment concentration ($C_{eq,k}$) at a reference height ($z = a$) above the bed is calculated using:

$$C_{eq,k} = 0.015 (d_k T_k^{1.5}) / (a d_{*,k}^{0.3}) \tag{A-41}$$

where T_k is the transport stage parameter, given by:

$$T_k = (u/u_{*,crs,k})^2 - 1 \quad \text{for } u > u_{*,crs,k} \tag{A-42}$$

The reference height (a) is calculated using:

$$a = \text{MAX} (0.01 h, k_{nik}) \tag{A-43}$$

where h is water depth and k_{nik} is the Nikuradse roughness height:

$$k_{nik} = 33 D_{90} \quad (A-44)$$

The erosion flux for size class k sediment for a non-armoring sediment bed ($E_{na,k}$) is calculated using:

$$E_{na,k} = -W_{s,k} (C_{a,k} - C_{eq,k}) \quad \text{for } C_{a,k} < C_{eq,k} \quad (A-45)$$

where $C_{a,k}$ is the suspended sediment concentration of size class k at $z = a$. For the three-dimensional model, $C_{a,k}$ is set equal to the suspended sediment concentration in the first grid cell above the bed. Similar to the cohesive bed discussed in Appendix A.3, bed armoring processes occur in the non-cohesive bed and those processes affect the erosion flux from that bed type. An active layer is assumed to exist at the surface of the non-cohesive bed, with the thickness of that layer calculated using Equation A-21. A bed model tracks changes in the composition of the non-cohesive active layer associated with erosion and deposition, as well as interactions between the active and parent bed layers. Thus, the erosion flux for size class k sediment from an armoring bed ($E_{non,k}$) is given by:

$$E_{non,k} = f_{non,a,k} S_k E_{na,k} \quad (A-46)$$

where $f_{non,a,k}$ is the fraction of class k sediment in the active layer of the non-cohesive bed and S_k is the particle-shielding factor (see Equation A-20). The particle-shielding factor (Karim and Kennedy 1981, Rahuel et al. 1989) was included in the erosion flux for an armoring bed because this factor accounts for the effects of differential erosion rates

List of Figures Cited In Appendix A

Figure A-1 Probability of Deposition for Cohesive Sediment Using the Krone Formulation.

Figure A-2 Probability of Deposition for Non-cohesive Sediment as a Function of Bed Shear Stress and Particle Diameter.

-
- Figure A-3 Settling Speed of Discrete Sediment Particles as a Function of Particle Diameter.
- Figure A-4 Probability of Suspension as a Function of Bed Shear Stress and Particle Diameter.
- Figure A-5 Particle Shielding Factor as a Function of Particle Size.
- Figure A-6 Schematic of Interactions Between the Water Column, Active Layer, and Parent-bed Layer When the Active-buffer Layer is Present.
- Figure A-7 Schematic of Interactions Between the Water Column, Active Layer, and Parent-bed Layer When the Active-buffer Layer is Not Present.
- Figure A-8 Initial Structure of Bed with No Active-buffer Layer at Time = t_1 .
- Figure A-9 Active-surface Layer Thickness Increases as Shear Stress Increases ($\tau_2 > \tau_1$) at Time = t_2 .
- Figure A-10 Active-surface Layer Thickness Decreases and Active-buffer Layer is Created as Shear Stress Decreases ($\tau_3 < \tau_2$) at Time = t_3 .
- Figure A-11 Active-surface Layer Thickness Decreases and Active-buffer Layer Thickness Increases as Shear Stress Continues to Decrease ($\tau_4 < \tau_3$) at Time = t_4 .
- Figure A-12 Active-surface Layer Thickness Increases and Active-buffer Layer Thickness Decreases as Shear Stress Increases ($\tau_5 > \tau_4$) at Time = t_5 .
- Figure A-13 Active-surface Layer Thickness Increases and Active-buffer Layer is Destroyed as Shear Stress Increases ($\tau_6 > \tau_5$, $\tau_6 > \tau_2$) at Time = t_6 .
- Figure A-14 Active-surface Layer Thickness Decreases and New Active-buffer Layer is Created as Shear Stress Decreases ($\tau_7 < \tau_6$) at Time = t_7 .
- Figure A-15 Initiation of Motion and Suspension for a Current Over a Plane Bed, $\theta = f(D^*)$, from van Rijn (1989).
- Figure A-16 Critical Shear Stress for Initiation of Suspended and Bedload Transport as a Function of Particle Diameter.

APPENDIX B
ANALYSIS OF EROSION RATE
(SEDFLUME) DATA

APPENDIX B

ANALYSIS OF EROSION RATE (SEDFLUME) DATA

A study was conducted to obtain data on the erosion properties of Patrick Bayou sediments. Twelve cores were collected in June 2007 from 12 locations in the bayou (see Figure 2-18). The sampling locations cover an area extending from the bayou mouth to 6000 ft upstream. Details of the field study, including core collection and processing, are described in SEI (2008). Erosion rates as a function of depth in the bed and shear stress were measured over the top 30 cm of each core using Sedflume, see Windward and QEA (2004) for a description of Sedflume and the erosion rate measurement process. Sediment samples were also obtained at 5-cm intervals from each core and analyzed for dry density and grain size distribution.

Erosion of a sediment bed depends on a number of factors, including, but not limited to: shear stress, grain size distribution, dry (bulk) density, TOC content, and gas content (Jepsen et al. 1997; Roberts et al. 1998). A simple illustration of the erosion process is presented in Figure 3-2. The rate at which sediment is removed from the consolidated sediment bed and transported to a thin near-bed layer that exists between the consolidated sediment bed and the water column is termed the gross erosion rate (E_{gross}). Some of the eroded sediment in the near-bed layer is re-deposited to the consolidated bed; the rate of re-deposition is referred to as the gross deposition rate (D_{gross}). The remainder of the eroded material in the near-bed layer is transported to the water column; this rate is referred to as the net erosion rate (E_{net}).

Erosion rate data obtained from Sedflume testing were analyzed to develop an understanding of the erosion properties of Patrick Bayou sediments. The goal of this analysis was to develop a functional relationship between E_{gross} and other parameters that affect erosion rate. Two parameters that affect E_{gross} are shear stress (τ) and bulk density (ρ) (Jepsen et al. 1997). An evaluation of Sedflume data from the Lower Duwamish Waterway (LDW), located near Seattle, WA, indicated minimal correlation exists system-wide between bulk density and erosion rate for LDW sediment (Windward and QEA 2008). Thus, in this study it was assumed that E_{gross} is only dependent on bed shear stress and that Equation A-16 defines that relationship.

The site-specific parameters in Equation A-16 (A , n , τ_{cr}) were determined using the erosion rate data collected during the Sedflume field study. The erosion rate properties of the 12 cores were analyzed using the following procedure. Each core was divided into five layers, with these layers representing the following depth intervals: 0-6, 6-11, 11-16, 16-21, 21-26 cm. These depth intervals were chosen because the shear stress series used in the Sedflume tests, where shear stress was increased from low to high values, were cycled over approximately 5-cm thick layers, with the top layer being 6-cm thick. The erosion rate data within each layer of a particular core were analyzed through application of a log-linear regression analysis between erosion rate and shear stress. The log-linear regression analysis produced values of A and n (see Equation B-1) for each layer in a particular core. The results of this analysis for the Sedflume cores with cohesive sediment are presented in Figures B-1 through B-12. The critical shear stresses, (τ_{cr}) were estimated from the shear stress values corresponding to $E_{gross} \leq 10^{-4}$ cm/s. The erosion rate parameters (A , n , τ_{cr}) for each core within the five depth intervals are listed in Tables B-1 through B-5. Note that the values of A and n in these tables correspond to units of cm/s for E_{gross} and Pa for bed shear stress in Equation A-16. The correlation coefficient (R^2) values presented in the tables are from the log-linear regression analysis, with perfect correlation corresponding to an R^2 value of one.

Table B-1
Erosion Rate Parameters for 0-6 cm Layer

Sediment Core ID	Proportionality Constant: A	Exponent: n	Correlation Coefficient (R^2)	Critical Shear Stress (Pa)
SF-1	0.0040	1.7	0.58	0.11
SF-2	0.0067	3.1	0.86	0.25
SF-3	0.0013	2.1	0.84	0.30
SF-4	0.0105	1.9	0.98	0.09
SF-5	0.0035	2.2	0.93	0.20
SF-6	0.00094	2.4	1.00	0.40
SF-7	0.0090	2.5	0.72	0.16
SF-8	0.0120	2.7	0.96	0.17
SF-9	0.0020	3.0	0.93	0.36
SF-10	0.0056	2.6	0.89	0.21
SF-11	0.0114	2.9	0.87	0.19
SF-12	0.0056	2.8	0.83	0.23

Table B-2
Erosion rate parameters for 6-11 cm layer

Sediment Core ID	Proportionality Constant: A	Exponent: n	Correlation Coefficient (R ²)	Critical Shear Stress (Pa)
SF-1	0.0045	2.4	0.98	0.20
SF-2 *	0.0016	2.9	0.90	0.38
SF-3	0.0040	3.2	0.96	0.32
SF-4	0.0031	2.3	0.94	0.23
SF-5	0.0019	3.2	0.99	0.39
SF-6	0.00081	2.1	0.74	0.36
SF-7 *	0.0016	2.9	N/A	0.38
SF-8 *	0.0016	2.9	1.00	0.38
SF-9	0.0011	4.5	0.99	0.58
SF-10	0.00086	1.9	0.99	0.31
SF-11	0.0240	1.6	0.89	0.03
SF-12	0.0015	2.8	1.00	0.38

* Average value for layer used because of unreliable correlation for that core and layer

Table B-3
Erosion Rate Parameters for 11-16 cm Layer

Sediment Core ID	Proportionality Constant: A	Exponent: n	Correlation Coefficient (R ²)	Critical Shear Stress (Pa)
SF-1	0.0034	2.7	1.00	0.27
SF-2	0.0013	3.8	1.00	0.51
SF-3	0.0150	1.9	0.77	0.07
SF-4	0.0035	2.6	1.00	0.26
SF-5	0.0026	2.2	0.97	0.23
SF-6	0.00042	2.4	0.86	0.55
SF-7 *	0.0017	2.7	0.02	0.35
SF-8	0.00012	3.9	0.85	0.96
SF-9	0.0019	3.0	0.84	0.37
SF-10 *	0.0017	2.7	1.00	0.35
SF-11	0.0093	1.9	0.88	0.09
SF-12 *	0.0017	2.7	1.00	0.35

* Average value for layer used because of unreliable correlation for that core and layer

Table B-4

Erosion Rate Parameters for 16-21 cm Layer

Sediment Core ID	Proportionality Constant: A	Exponent: n	Correlation Coefficient (R^2)	Critical Shear Stress (Pa)
SF-1	0.0032	2.8	0.97	0.29
SF-2	0.0012	2.8	1.00	0.40
SF-3	0.00027	2.1	0.94	0.62
SF-4	0.0046	2.7	0.82	0.24
SF-5	0.0027	2.2	0.88	0.23
SF-6	0.000019	4.2	0.98	1.49
SF-7	0.00033	2.3	0.73	0.59
SF-8	0.00005	4.2	0.88	1.18
SF-9	0.00045	3.4	0.84	0.64
SF-10	0.0083	2.8	0.86	0.21
SF-11	0.0252	2.4	0.88	0.10
SF-12	0.0066	2.4	0.99	0.18

Table B-5

Erosion Rate Parameters for 21-26 cm Layer

Sediment Core ID	Proportionality Constant: A	Exponent: n	Correlation Coefficient (R^2)	Critical Shear Stress (Pa)
SF-1*	0.0009	3.1	N/A	0.49
SF-2	0.0020	3.1	1.00	0.38
SF-3	0.00036	3.1	0.92	0.66
SF-4	0.0046	2.7	0.92	0.24
SF-5	0.0027	2.2	0.87	0.23
SF-6	0.000019	4.2	1.00	1.49
SF-7	0.00017	2.4	0.82	0.80
SF-8	0.000039	4.6	0.87	1.23
SF-9	0.00056	3.5	0.89	0.61
SF-10	0.0060	2.7	0.96	0.21
SF-11	0.0149	2.2	0.99	0.10
SF-12	0.000035	4.5	0.91	1.26

* Average value for layer used because of unreliable correlation for that core and layer

The effects of spatial variability, both horizontal and vertical, on the erodibility of Patrick Bayou sediment can be quantified through an evaluation of the average erosion rate ratio (R_{avg}). The first step in this analysis was to calculate average values of the A and n parameters in Equation A-16 for each of the five depth intervals. As discussed in Section 2.4.3, for a log-linear relationship (i.e., Equation A-16), the average exponent (n_{ave}) value for a depth interval is the arithmetic average of the n values for the cores within the interval. The average proportionality constant (A_{ave}) is determined by calculating the log-average value:

$$\log(A_{ave}) = (1/K) \sum \log(A_k) \quad (B-1)$$

where K is equal to the number of cores (i.e., 12). Using this approach, the average erosion parameters for the five layers in the bed model are listed in Table B-6, where E_{gross} and skin friction shear stress have units of cm/s and Pa, respectively.

Table B-6.
Vertical Variation in Average Erosion Rate Parameters

Depth Interval	Average Proportionality Constant: A_{ave}	Average Exponent: n_{ave}	Critical Shear Stress (Pa)
1: 0 – 6 cm	0.0046	2.5	0.21
2: 6 – 11 cm	0.0016	2.7	0.38
3: 11 – 16 cm	0.0017	2.7	0.35
4: 16 – 21 cm	0.0010	3.1	0.49
5: 21 – 26 cm	0.0009	3.1	0.49

Vertical variation in the average erosion rate ratio for the five depth intervals is evaluated as follows. First, calculate the average value of gross erosion rate for depth interval i ($^{ave}E_{gross,i}$, where i ranges from 1 to 5):

$$^{ave}E_{gross,i} = 1/N \sum A_{ave,i} \tau^{n_{ave,i}} \quad (B-2)$$

where the summation is over the bed shear stress range of 0.5 to 3 Pa in increments of 0.1 Pa, so N is equal to 26. Values of $A_{ave,i}$ and $n_{ave,i}$ for depth interval i are given in Table B-6. Using the values of $^{ave}E_{gross,i}$ for the five depth intervals, the average erosion rate ratios for depth intervals 1 through 5 were calculated using:

$$R_{ave,i} = ^{ave}E_{gross,i} / ^{ave}E_{gross,1} \quad (B-3)$$

where i ranges from 1 through 5. Thus, $R_{ave,i}$ represents the ratio of the erodibility of depth interval i to the average erodibility of depth interval 1 (i.e., 0-6 cm layer); $R_{ave,1}$ is equal to one. The vertical variation in $R_{ave,i}$ is shown on Figure B-13. These results show that the erodibility of Patrick Bayou sediment decreases with increasing depth in the bed, which is a typical characteristic of a cohesive sediment bed and is primarily due to increasing consolidation with increasing depth. Quantification of the changes in bed erodibility with depth in the bed (e.g., erodibility of 21-26 cm layer is about five times less than the erodibility of 0-6 cm layer) aids in interpreting predictions of the sediment transport model, especially during high-flow events.

A similar approach was used to quantify spatial differences in bed erodibility within the horizontal plane in the bayou. The average gross erosion rate for depth interval i in core k was calculated as follows:

$$^{ave}E_{gross,i,k} = 1/N \sum A_{i,k} \tau^{n,i,k} \quad (B-4)$$

where the summation is over the bed shear stress range of 0.5 to 3 Pa in increments of 0.1 Pa, so N is equal to 26. Values of $A_{i,k}$ and $n_{i,k}$ for depth interval i in core k are given in Tables B-1 through B-5. Using the values of $^{ave}E_{gross,i}$ for the five depth intervals, the average erosion rate ratio for depth interval i in core k was calculated using:

$$R_{i,k} = ^{ave}E_{gross,i,k} / ^{ave}E_{gross,i} \quad (B-5)$$

Thus, $R_{i,k}$ represents the ratio of the erodibility of depth interval i in core k to the average erodibility of depth interval i . The results of this analysis are discussed in Section 2.4.3.

List of Figures Cited In Appendix B

- Figure B-1 Comparison of Data (symbols) to Results of Log-linear Regression (dashed line) for Core SF-1.
- Figure B-2 Comparison of Data (symbols) to Results of Log-linear Regression (dashed line) for Core SF-2.
- Figure B-3 Comparison of Data (symbols) to Results of Log-linear Regression (dashed line) for Core SF-3.
- Figure B-4 Comparison of Data (symbols) to Results of Log-linear Regression (dashed line) for Core SF-4.
- Figure B-5 Comparison of Data (symbols) to Results of Log-linear Regression (dashed line) for Core SF-5.
- Figure B-6 Comparison of Data (symbols) to Results of Log-linear Regression (dashed line) for Core SF-6.
- Figure B-7 Comparison of Data (symbols) to Results of Log-linear Regression (dashed line) for Core SF-7.
- Figure B-8 Comparison of Data (symbols) to Results of Log-linear Regression (dashed line) for Core SF-8.
- Figure B-9 Comparison of Data (symbols) to Results of Log-linear Regression (dashed line) for Core SF-9.
- Figure B-10 Comparison of Data (symbols) to Results of Log-linear Regression (dashed line) for Core SF-10.
- Figure B-11 Comparison of Data (symbols) to Results of Log-linear Regression (dashed line) for Core SF-11.
- Figure B-12 Comparison of data (symbols) to Results of Log-linear Regression (dashed line) for core SF-12.
- Figure B-13 Vertical Variation in Sediment Erodibility in Patrick Bayou Sediment.

APPENDIX C

BOUNDARY CONDITIONS FOR 14-YEAR SIMULATION

APPENDIX C

BOUNDARY CONDITIONS FOR 14-YEAR SIMULATION

The 14-year simulation discussed in Sections 2 and 3 required specification of boundary conditions and forcing functions for input to the watershed, hydrodynamic and sediment transport models. Information and data were compiled for the 14-year period from 1993 through 2006. Subsequent processing of these information and data produced the necessary model inputs. Graphical presentations of the model inputs for the 14-year period are presented in this appendix.

The primary boundary conditions and forcing functions for the watershed and hydrodynamic models are: precipitation in the surrounding watershed, freshwater inflow to the bayou, and tidal elevation in the HSC. Time histories of these model inputs for each year during the 14-year period are presented on Figures C-1 through C-14. Note that the freshwater inflow to the bayou, which is used as an input to the hydrodynamic model, is predicted by the watershed model.

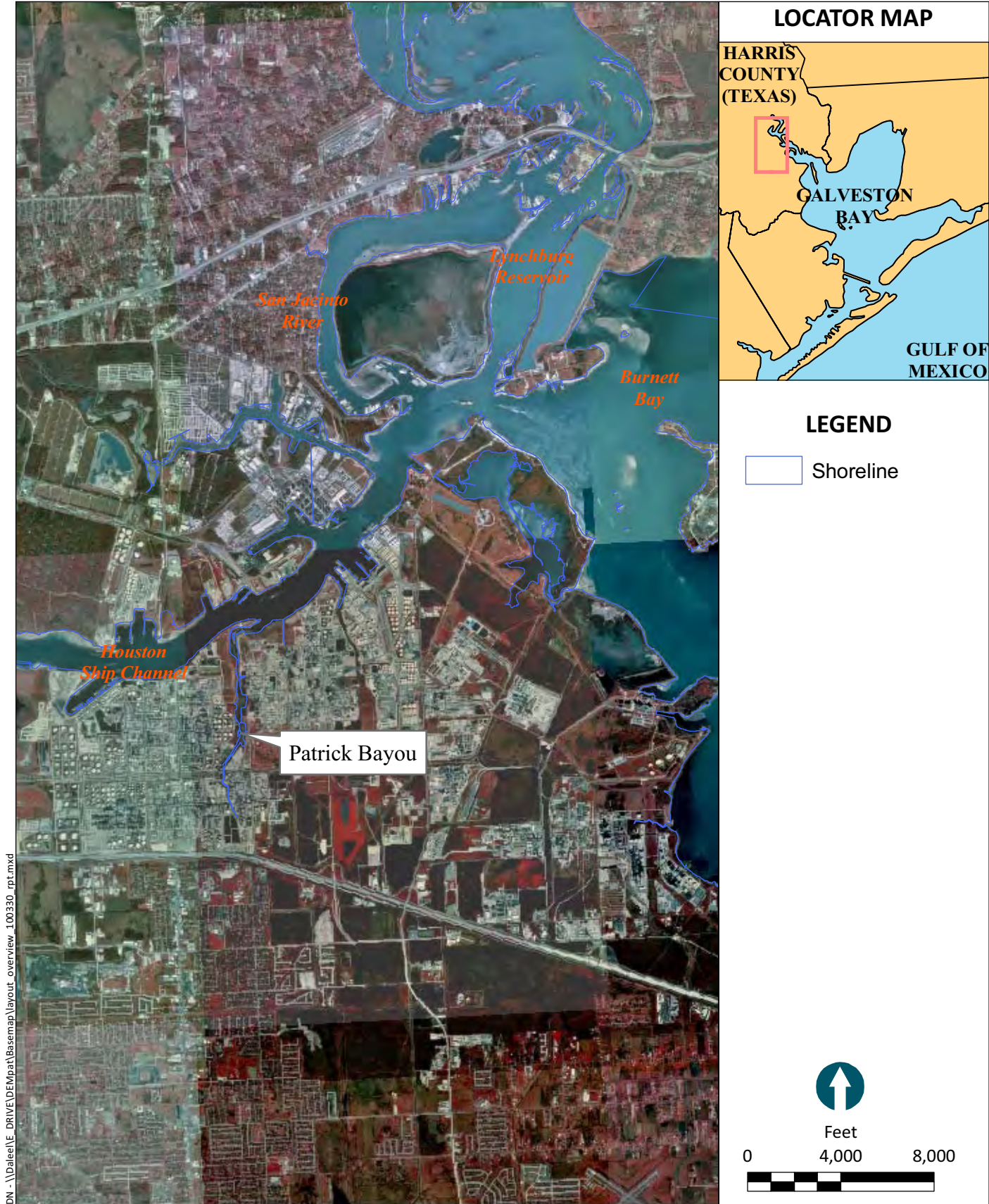
The sediment transport model requires specification of incoming sediment load from the two primary tributaries to the bayou: Main inflow (station PB075) and East Fork. The procedure for determining the incoming sediment loads from these tributaries was discussed in Section 2.4.4. Time histories of TSS concentration at the Main inflow and East Fork for the 14-year period are shown on Figure C-15 through C-21. Variations in the annual average freshwater inflow and total sediment load to the bayou for the 14-year period are shown on Figure C-22.

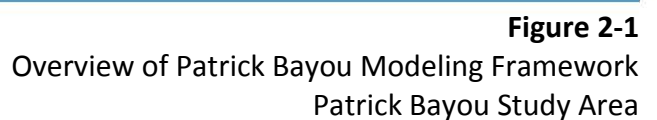
List of Figures Cited In Appendix C

- Figure C-1 Time history of precipitation, freshwater inflow and tidal elevation boundary conditions for 1993.
- Figure C-2 Time history of precipitation, freshwater inflow and tidal elevation boundary conditions for 1994.

-
- Figure C-3 Time History of Precipitation, Freshwater Inflow and Tidal Elevation Boundary Conditions for 1995.
- Figure C-4 Time History of Precipitation, Freshwater Inflow and Tidal Elevation Boundary Conditions for 1996.
- Figure C-5 Time History of Precipitation, Freshwater Inflow and Tidal Elevation Boundary Conditions for 1997.
- Figure C-6 Time History of Precipitation, Freshwater Inflow and Tidal Elevation Boundary Conditions for 1998.
- Figure C-7 Time History of Precipitation, Freshwater Inflow and Tidal Elevation Boundary Conditions for 1999.
- Figure C-8 Time History of Precipitation, Freshwater Inflow and Tidal Elevation Boundary Conditions for 2000.
- Figure C-9 Time History of Precipitation, Freshwater Inflow and Tidal Elevation Boundary Conditions for 2001.
- Figure C-10 Time History of Precipitation, Freshwater Inflow and Tidal Elevation Boundary Conditions for 2002.
- Figure C-11 Time History of Precipitation, Freshwater Inflow and Tidal Elevation Boundary Conditions for 2003.
- Figure C-12 Time History of Precipitation, Freshwater Inflow and Tidal Elevation Boundary Conditions for 2004.
- Figure C-13 Time History of Precipitation, Freshwater Inflow and Tidal Elevation Boundary Conditions for 2005.
- Figure C-14 Time History of Precipitation, Freshwater Inflow and Tidal Elevation Boundary Conditions for 2006
- Figure C-15 Time History of TSS Concentration Boundary Conditions for 1993 and 1994.
- Figure C-16 Time History of TSS Concentration Boundary Conditions for 1995 and 1996.

-
- Figure C-17 Time History of TSS Concentration Boundary Conditions for 1997 and 1998.
- Figure C-18 Time History of TSS Concentration Boundary Conditions for 1999 and 2000.
- Figure C-19 Time History of TSS Concentration Boundary Conditions for 2001 and 2002.
- Figure C-20 Time History of TSS Concentration Boundary Conditions for 2003 and 2004.
- Figure C-21 Time History of TSS Concentration Boundary Conditions for 2005 and 2006.
- Figure C-22 Annual Variation in Average Total Inflow Rate and Total Sediment Load
During 14-year Period.





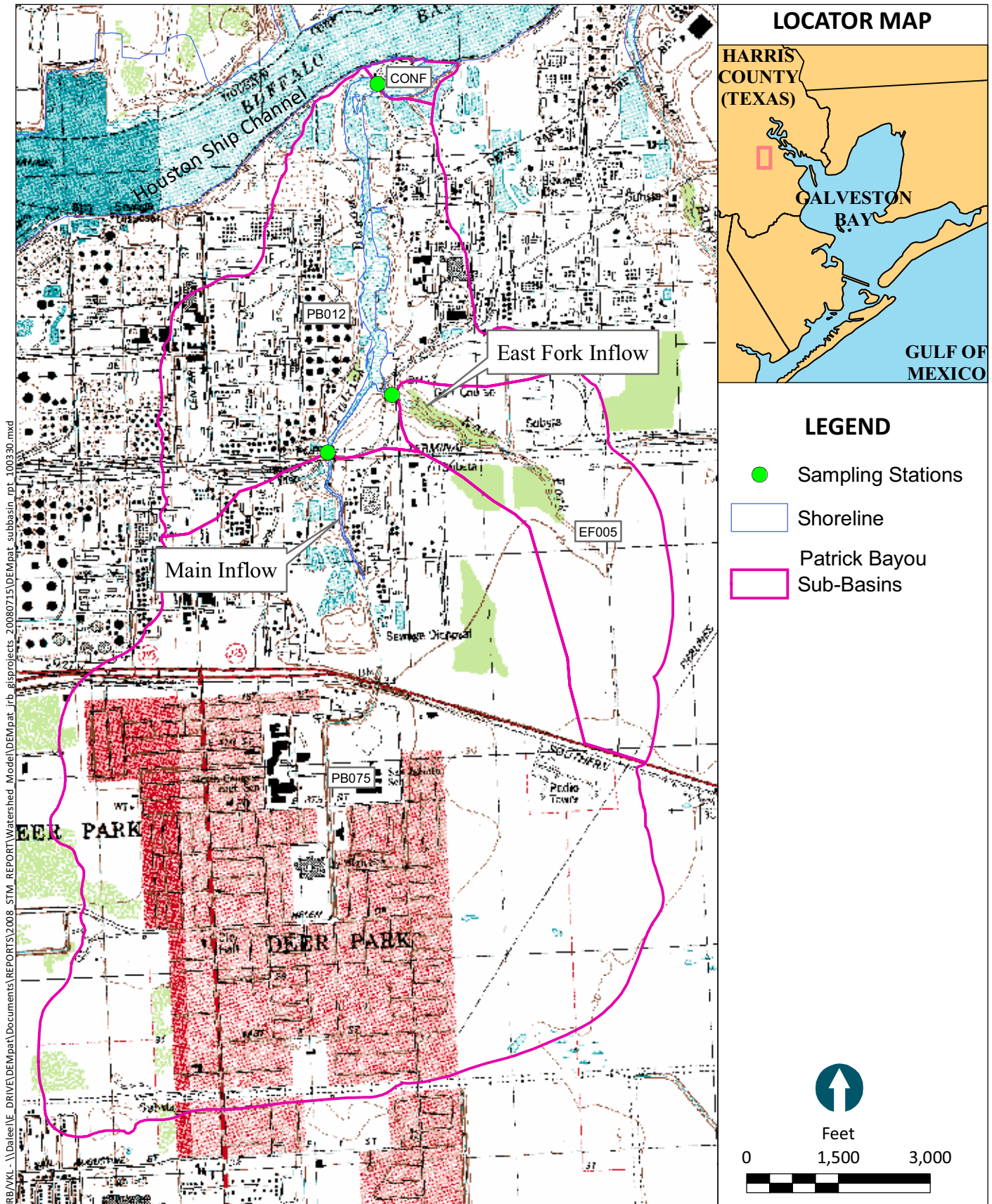


Figure 2-2

Watershed Sub-basin Delineation
Patrick Bayou Study Area

J:\B\NKL - \Dale\I-E_DRIVE\DEM\pat\Documents\REPORTS\2008_STM_REPORT\Watershed_Model\DEM\pat_jrb_gis\projects_20080715\DEM\pat_precip_rpt_100330.mxd

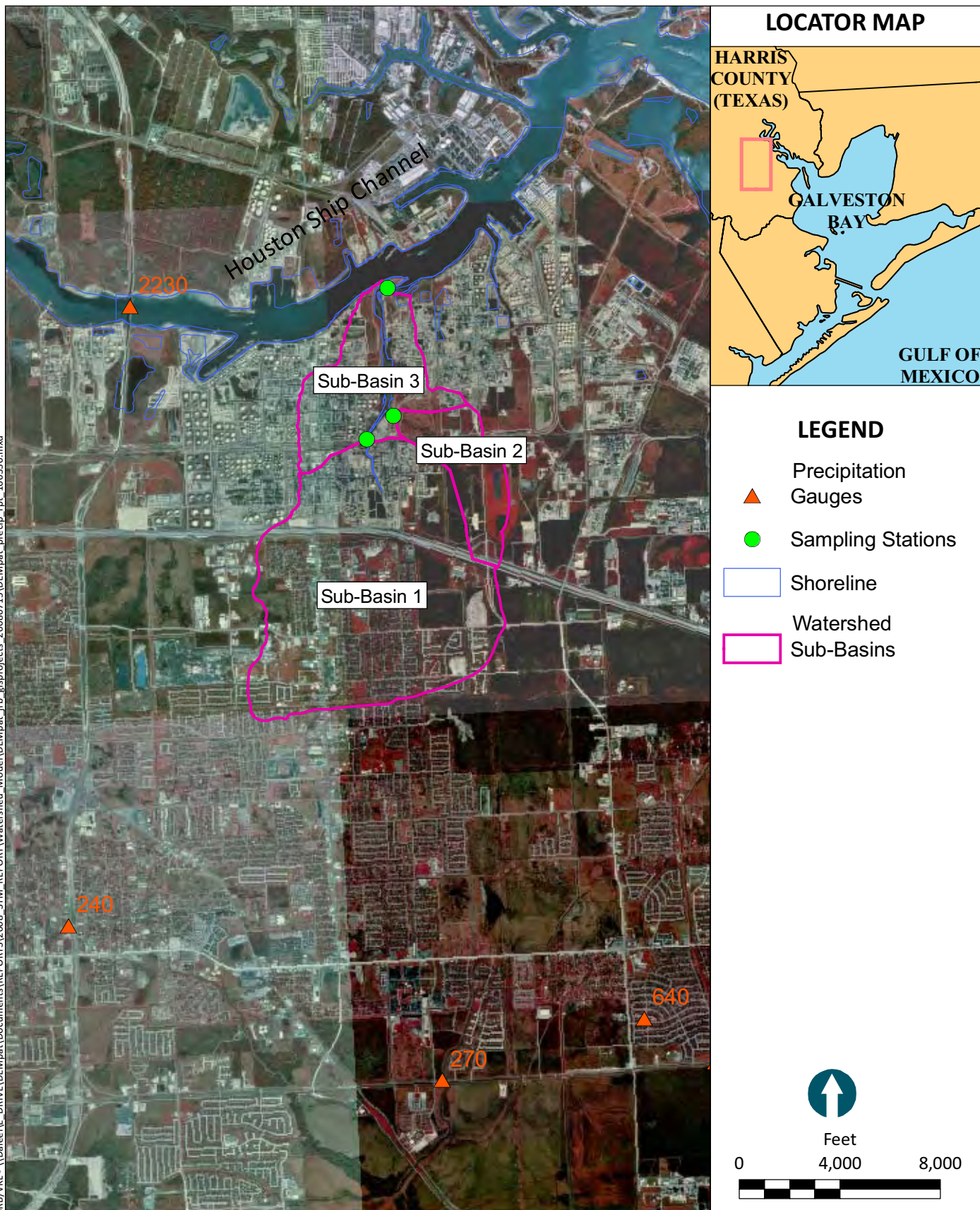


Figure 2-3

Location of Precipitation Gauges in Harris County Used in Watershed Model Patrick Bayou Study Area

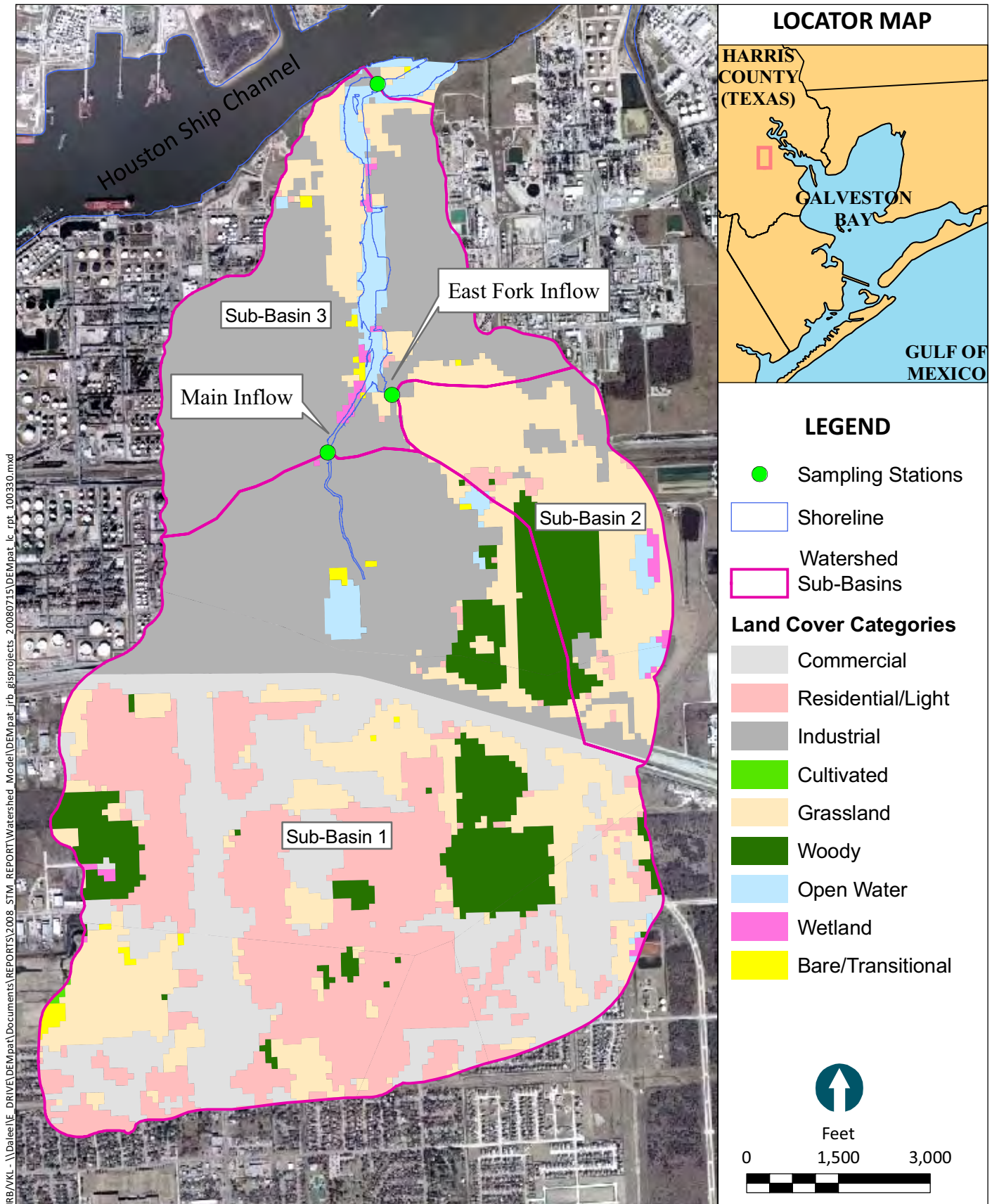


Figure 2-4

Land Use Categories for Watershed Sub-basins
Patrick Bayou Study Area

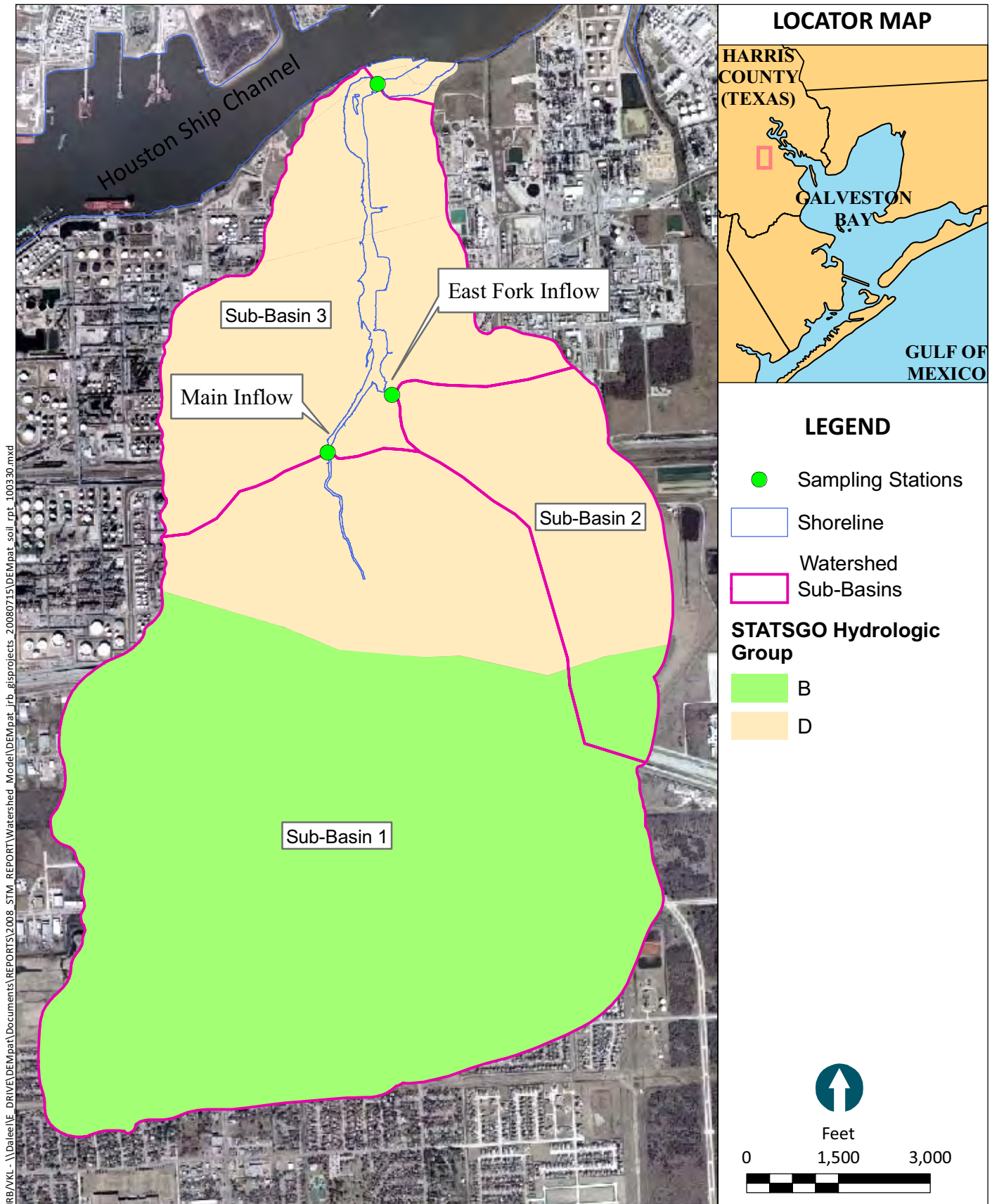


Figure 2-5

Hydrologic Soil Groups for Watershed Sub-basins
Patrick Bayou Study Area

JB/VKL - \\Dale\\E_DRIVE\\DEM\\pat\\Documents\\REPORTS\\2008_STM_REPORT\\Watershed_Model\\DEM\\pat_jrb_gis\\projects_20080715\\DEM\\pat_sampling_rpt_100330.mxd

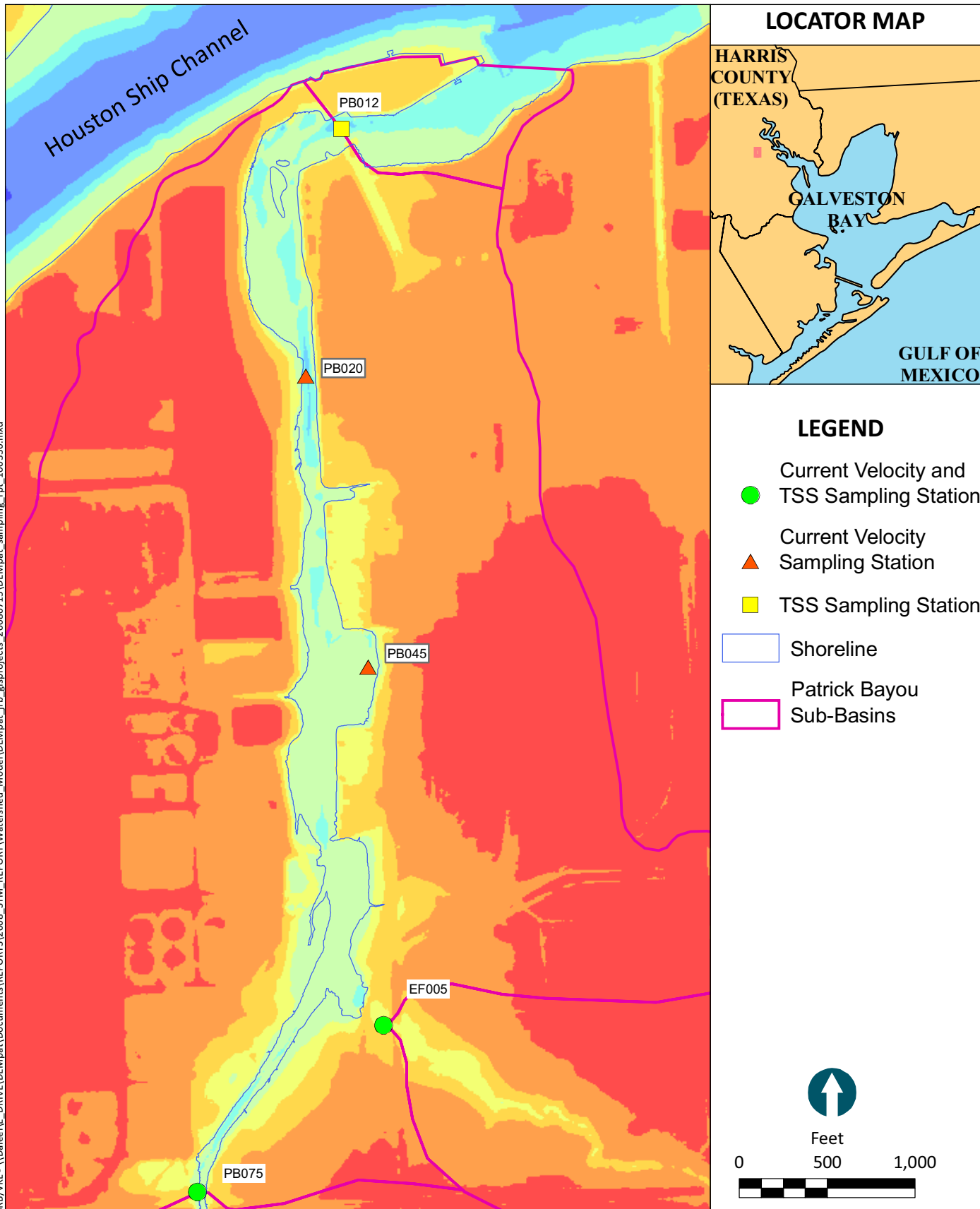


Figure 2-6

October 2006 Storm Event Sampling Locations
Patrick Bayou Study Area

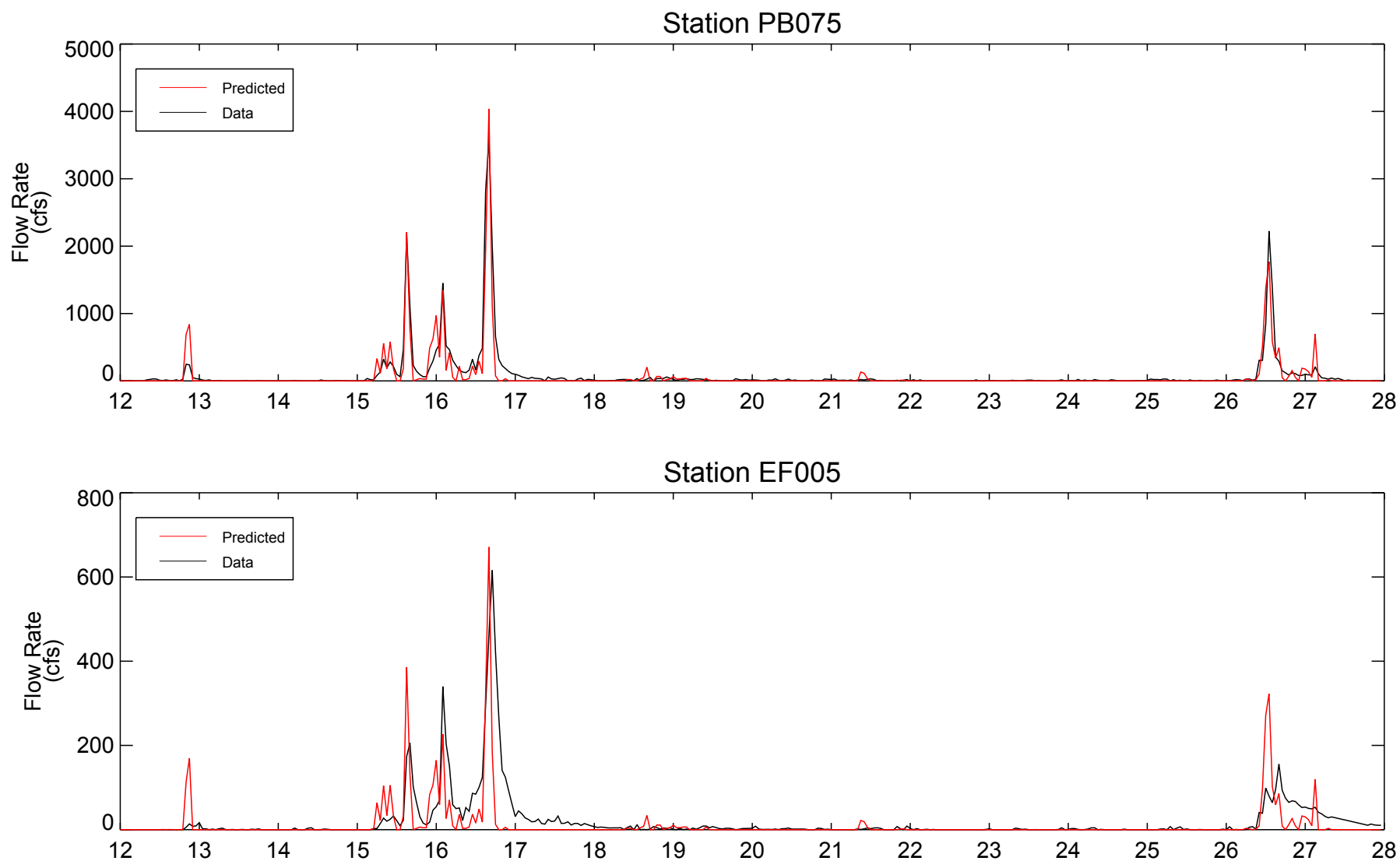


Figure 2-7
Comparisons of Measured and Predicted Flow Rates at Stations PB075 and EF005 Between October 12 and 28, 2006
Patrick Bayou Study Area



DN\\VKL-\\Dalee\\E_DRIVE\\DEM\\pat\\Analysis\\Model\\Inputs\\GRID\\grid_rpt_100331.mxd

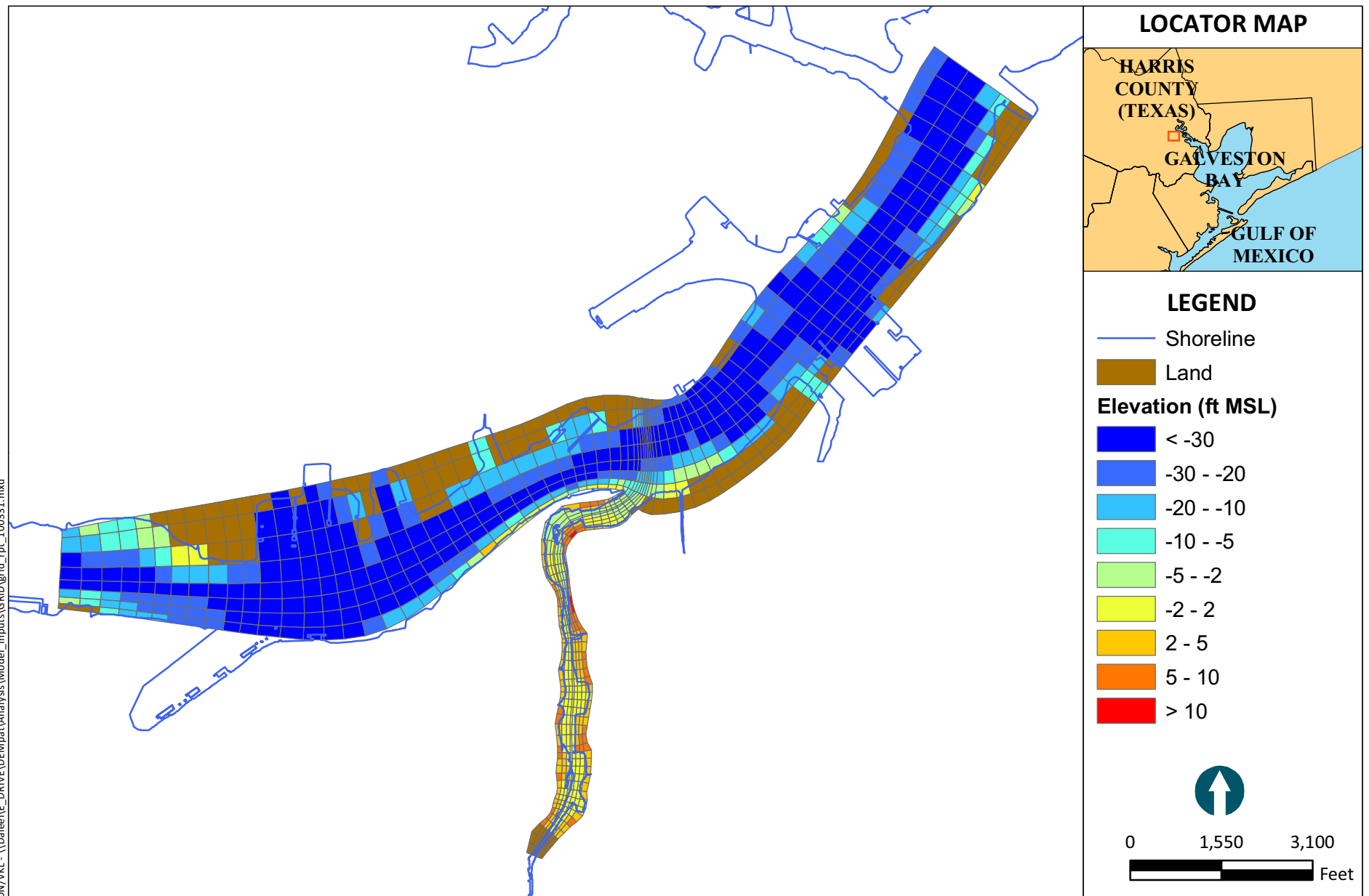


Figure 2-8

Numerical Grid and Projected Bathymetry
Patrick Bayou Study Area

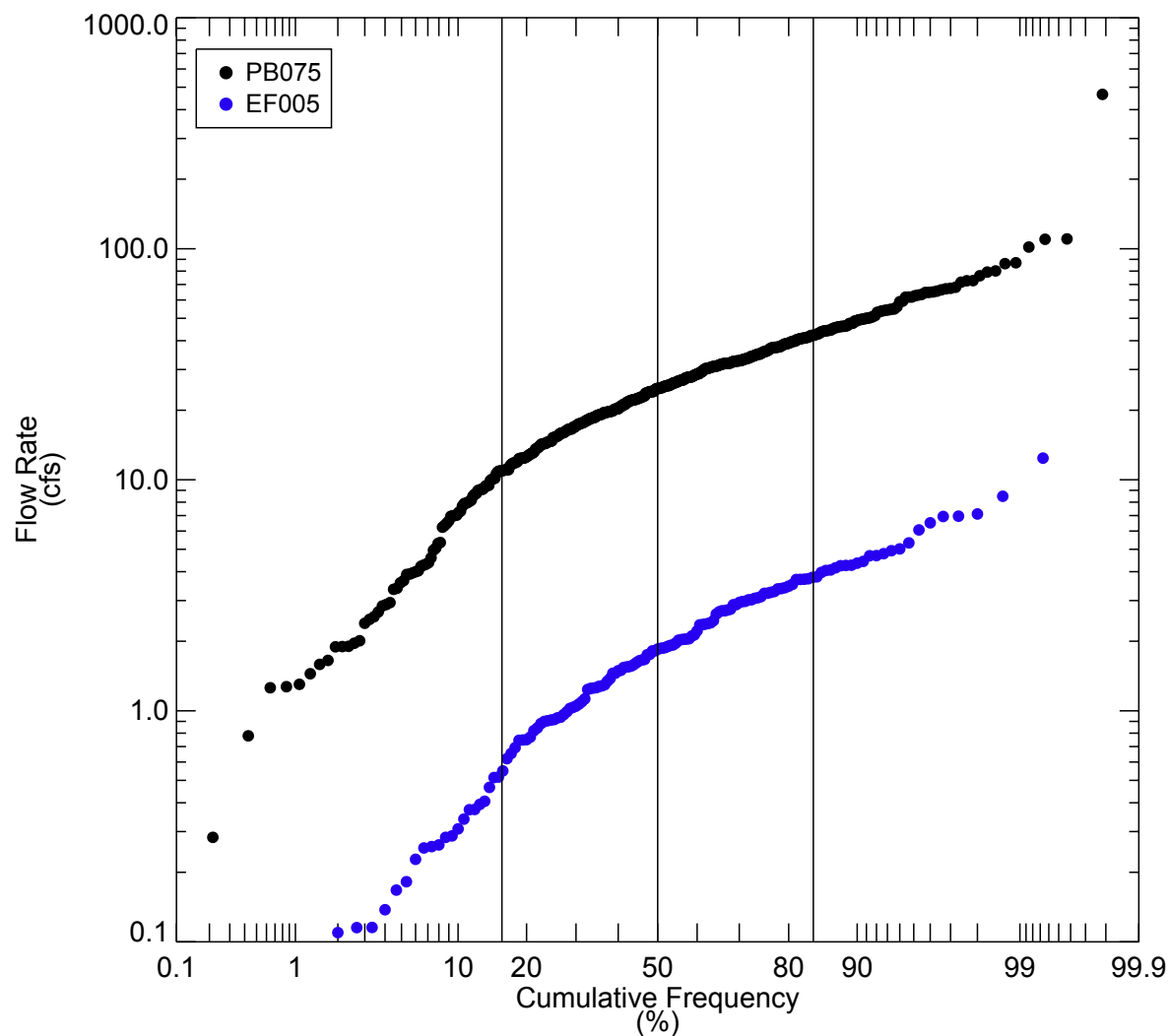


Figure 2-9
 Cumulative Frequency Distribution of Measured Flow Rate During Days with No
 Precipitation at Stations PB075 and EF005 Used to Estimate Base Flow
 Note: Flow rate was estimated based on ADCP data collected between 10/11/2006 and 12/12/2007
 Patrick Bayou Study Area

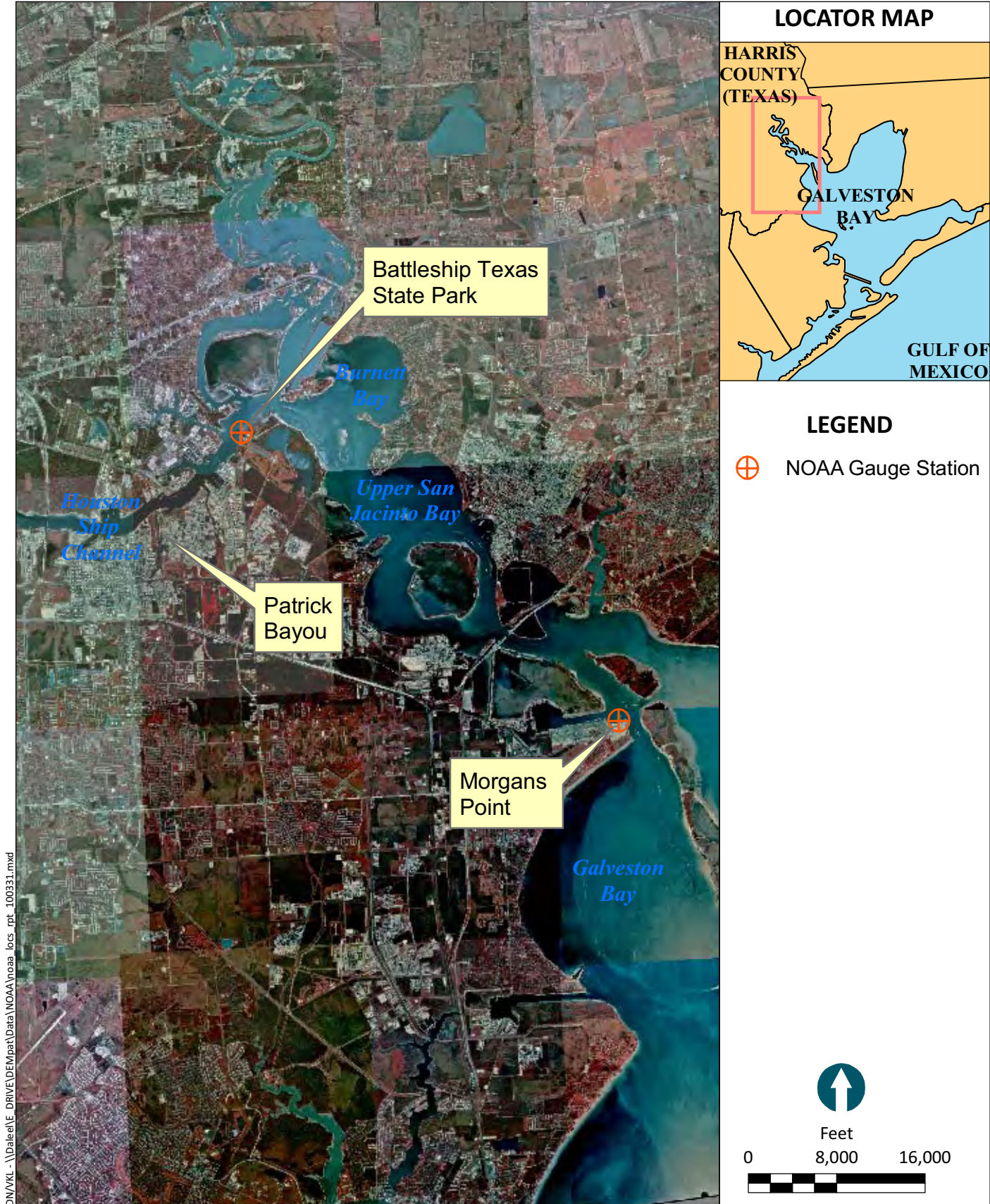


Figure 2-10

Location of NOAA Tidal Gauge Stations at Battleship Texas State Park and Morgans Point Patrick Bayou Study Area

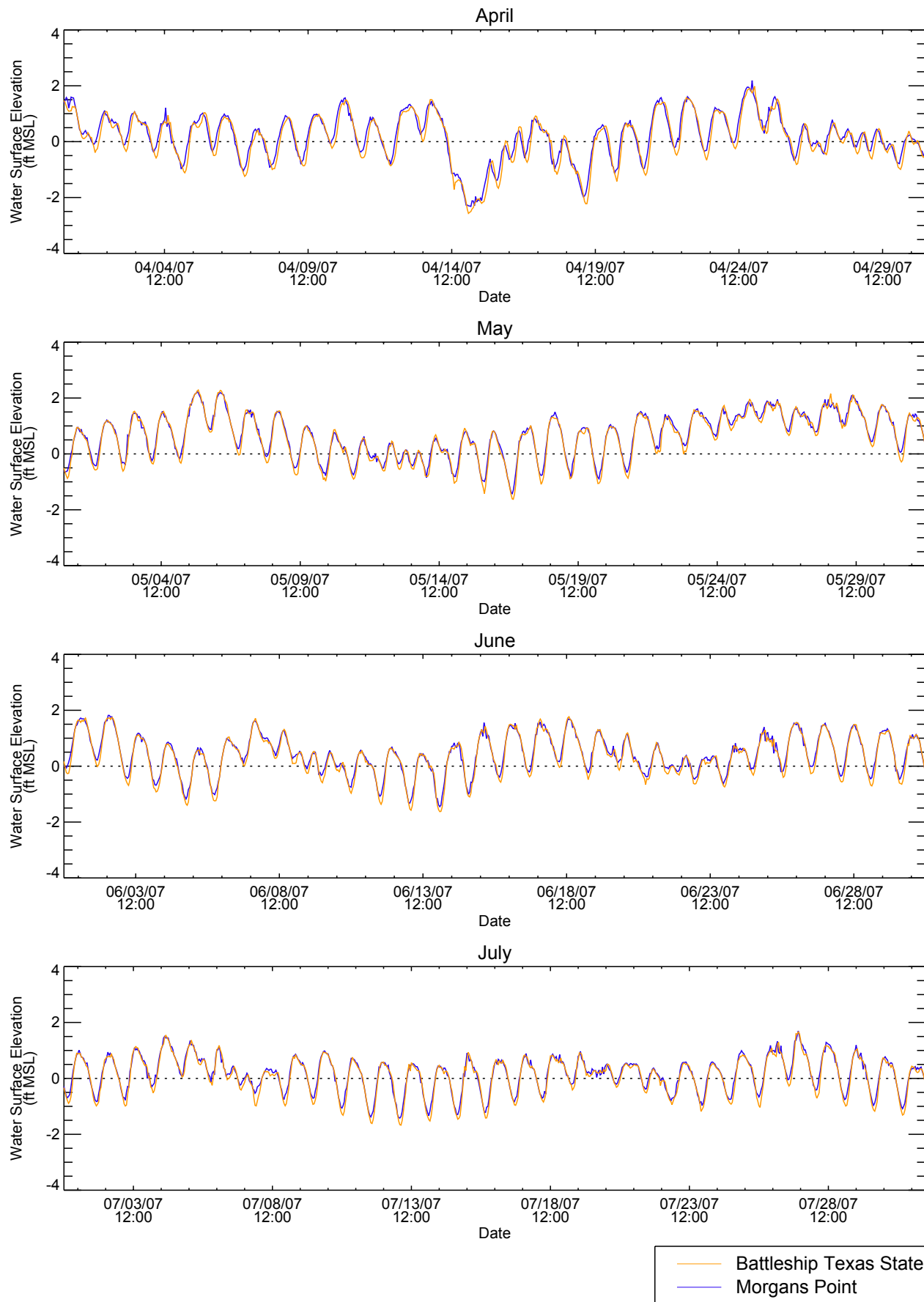


Figure 2-11
 Comparison of Water Surface Elevations Measured at Morgans Point and
 Battleship Texas State Park Gauging Stations Between April and July 2007
 Patrick Bayou Study Area

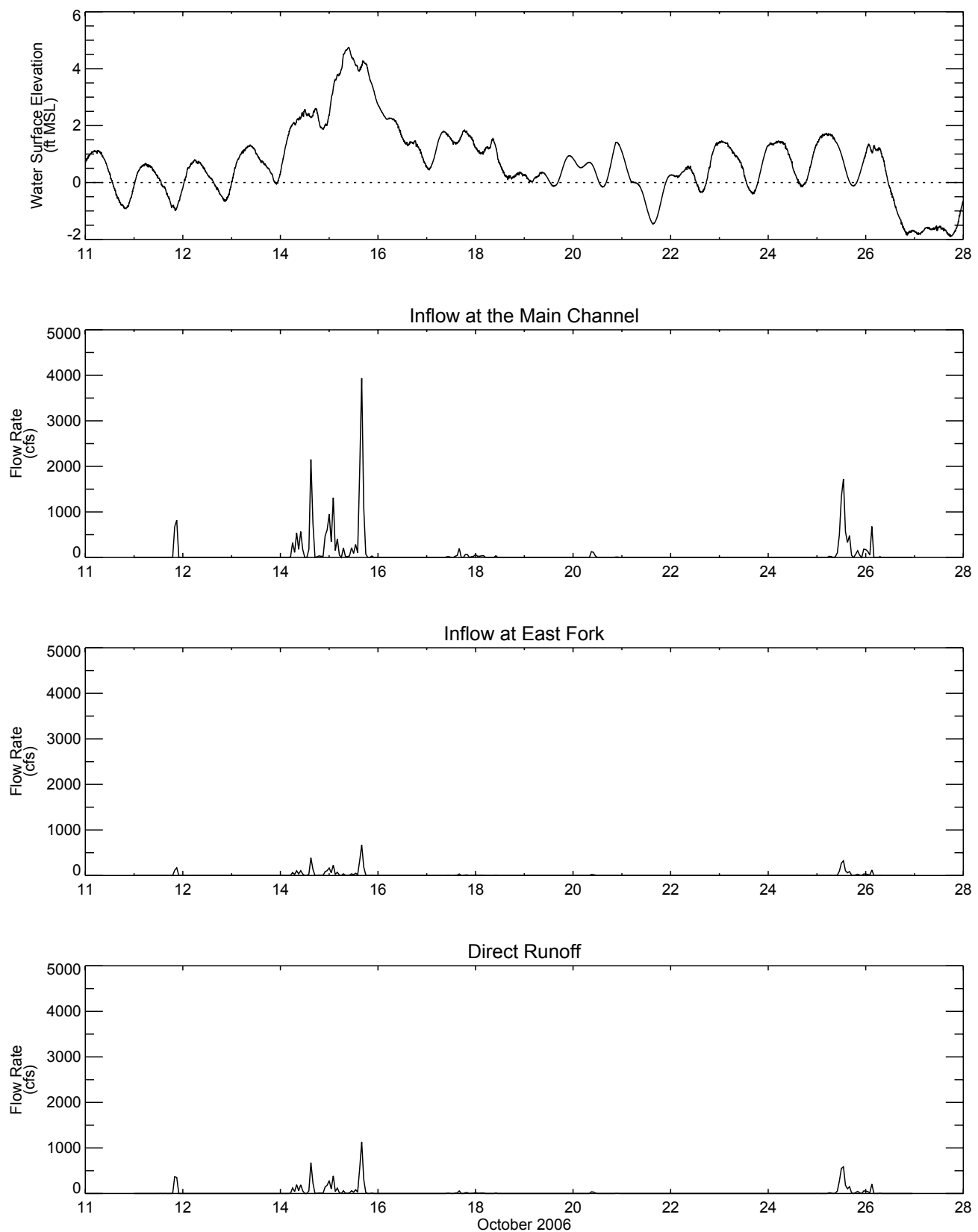


Figure 2-12
Time History of Flow Rate and Water Surface Elevation
During October 2006 Calibration Period

Note: Stage height from NOAA gauge station 8770743
(Battleship Texas State Park). Flow predicted by watershed model.

Patrick Bayou Study Area



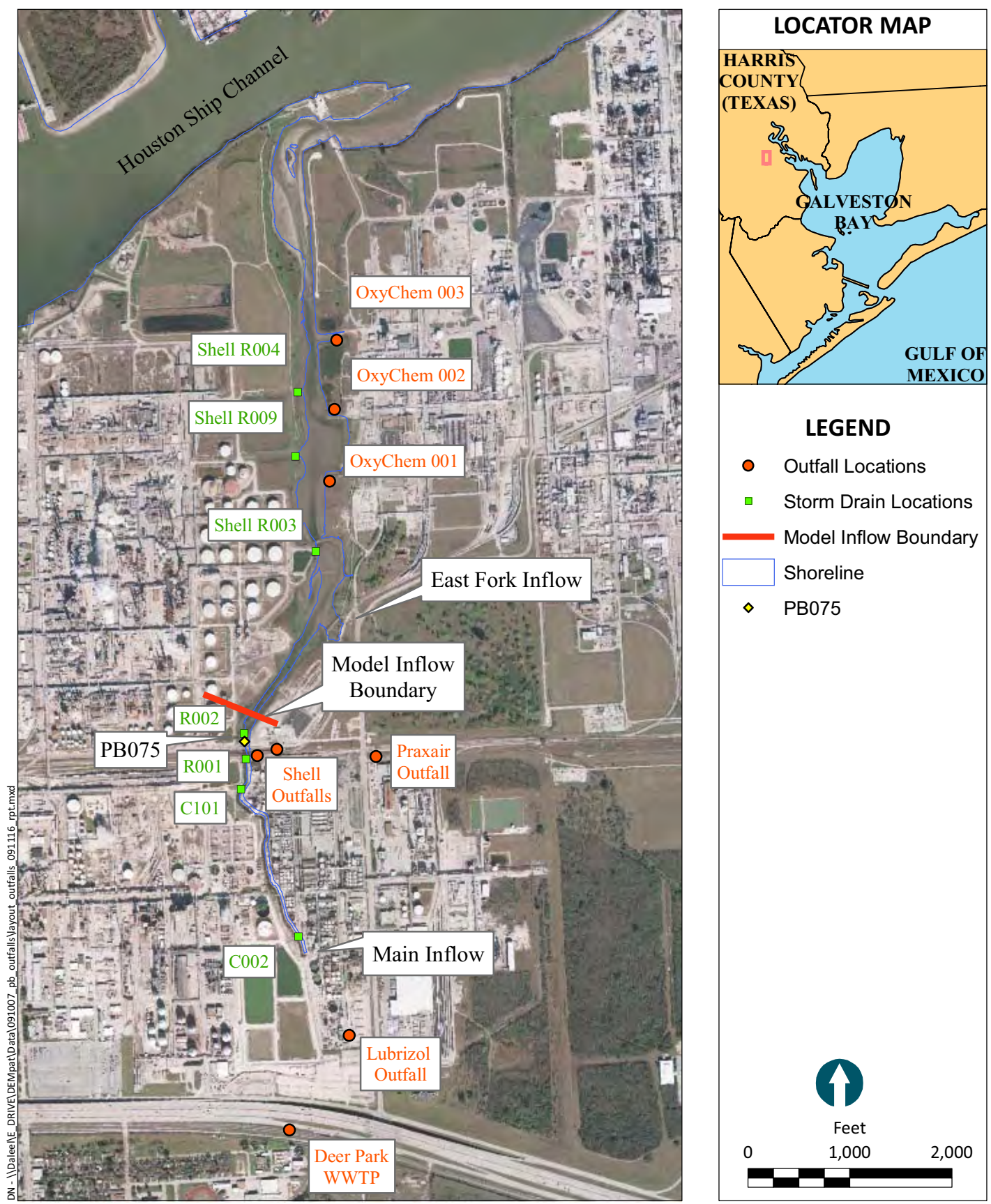


Figure 2-13
Locations of outfalls and storm drains
Patrick Bayou Study Area

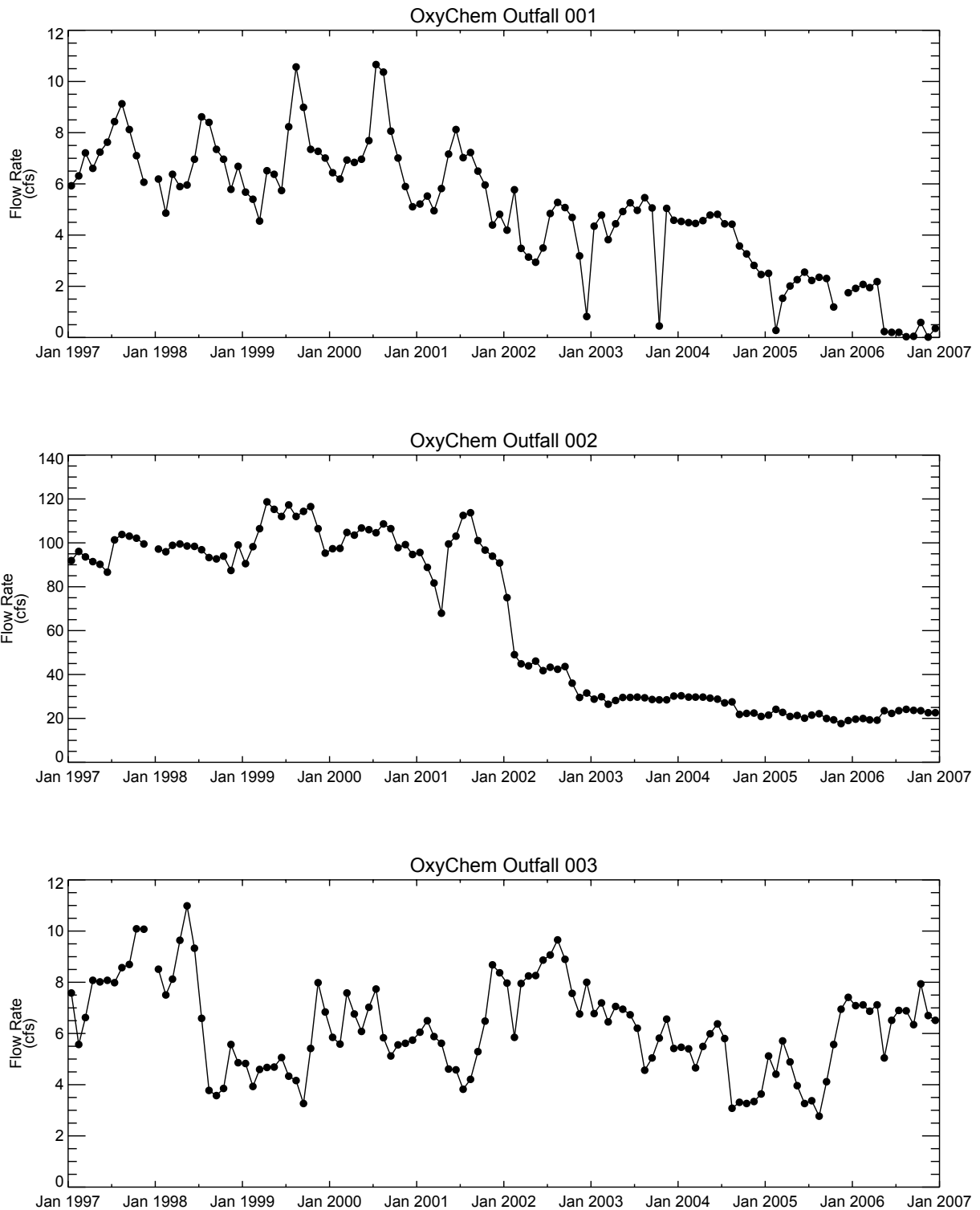


Figure 2-14
Monthly Average Flow Rates in OxyChem Outfalls001, 002, and 003
Between 1997 and 2006
Patrick Bayou Study Area



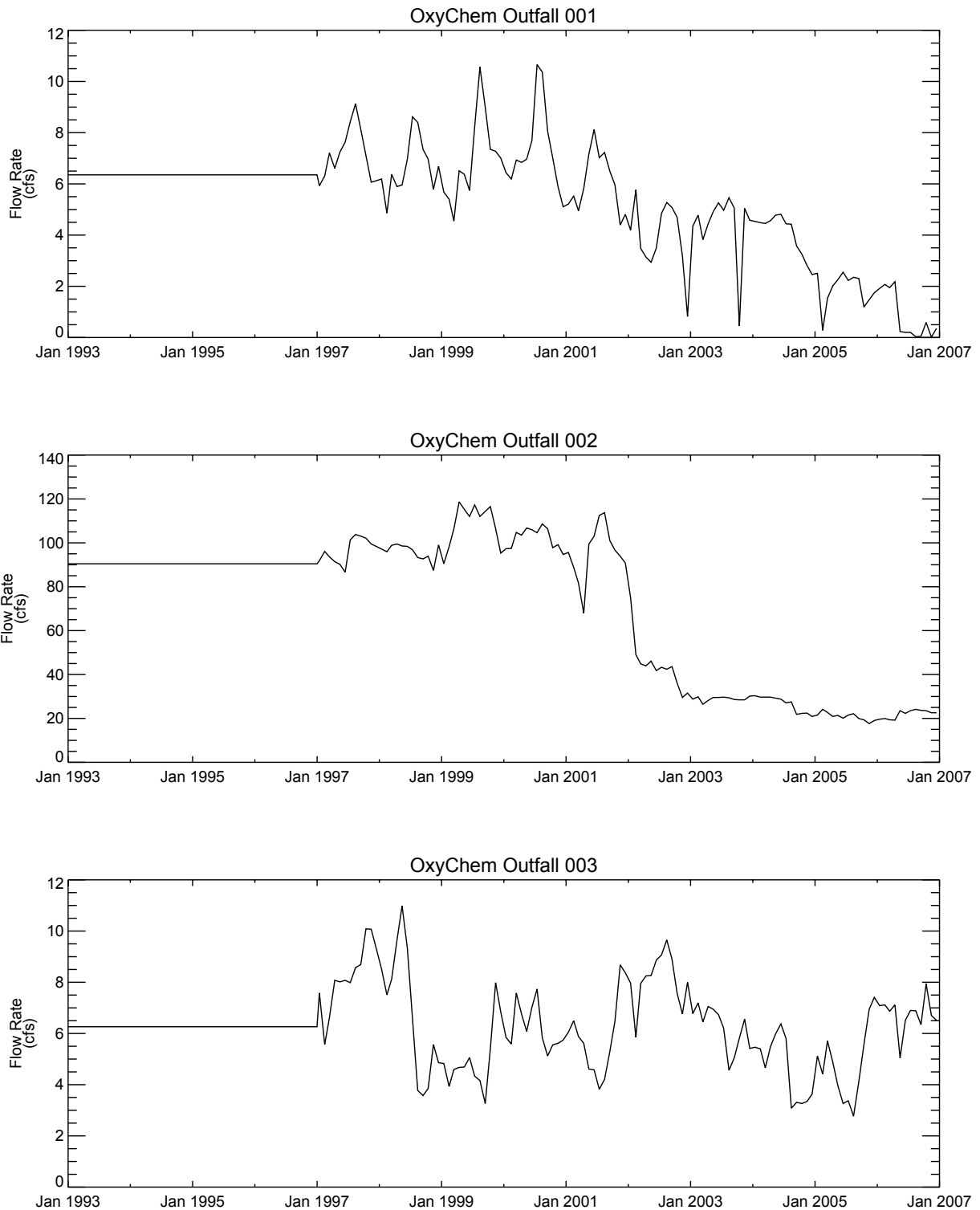


Figure 2-15
Monthly Average Flow Rates in OxyChem Outfalls 001, 002, and 003
Between 1993 and 2006 for Model Input
Patrick Bayou Study Area



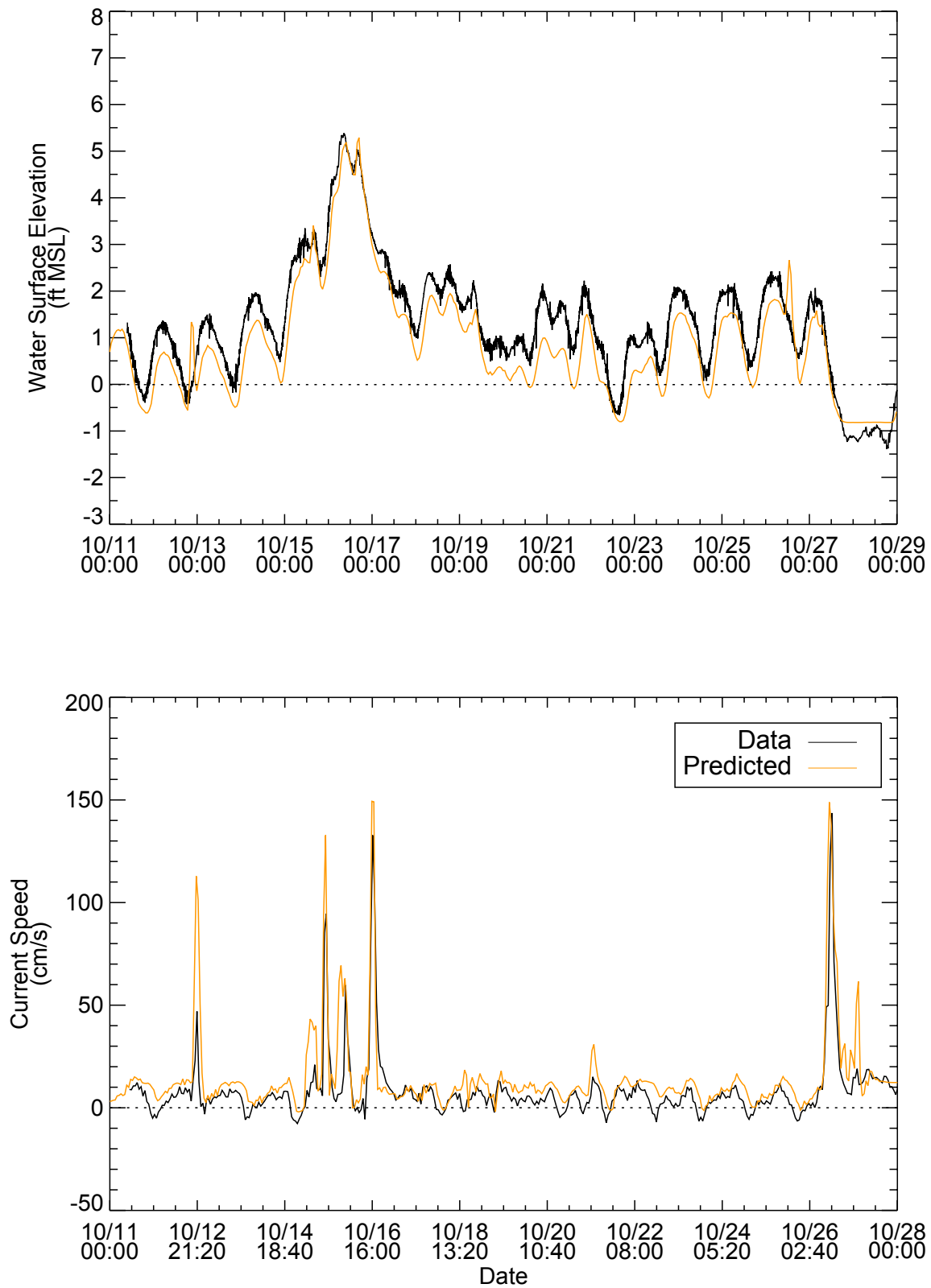


Figure 2-16
 Comparisons of Measured and Predicted Water Surface Elevation and Current
 Speed at Station PB020 During October 2006 Calibration Period
 Patrick Bayou Study Area

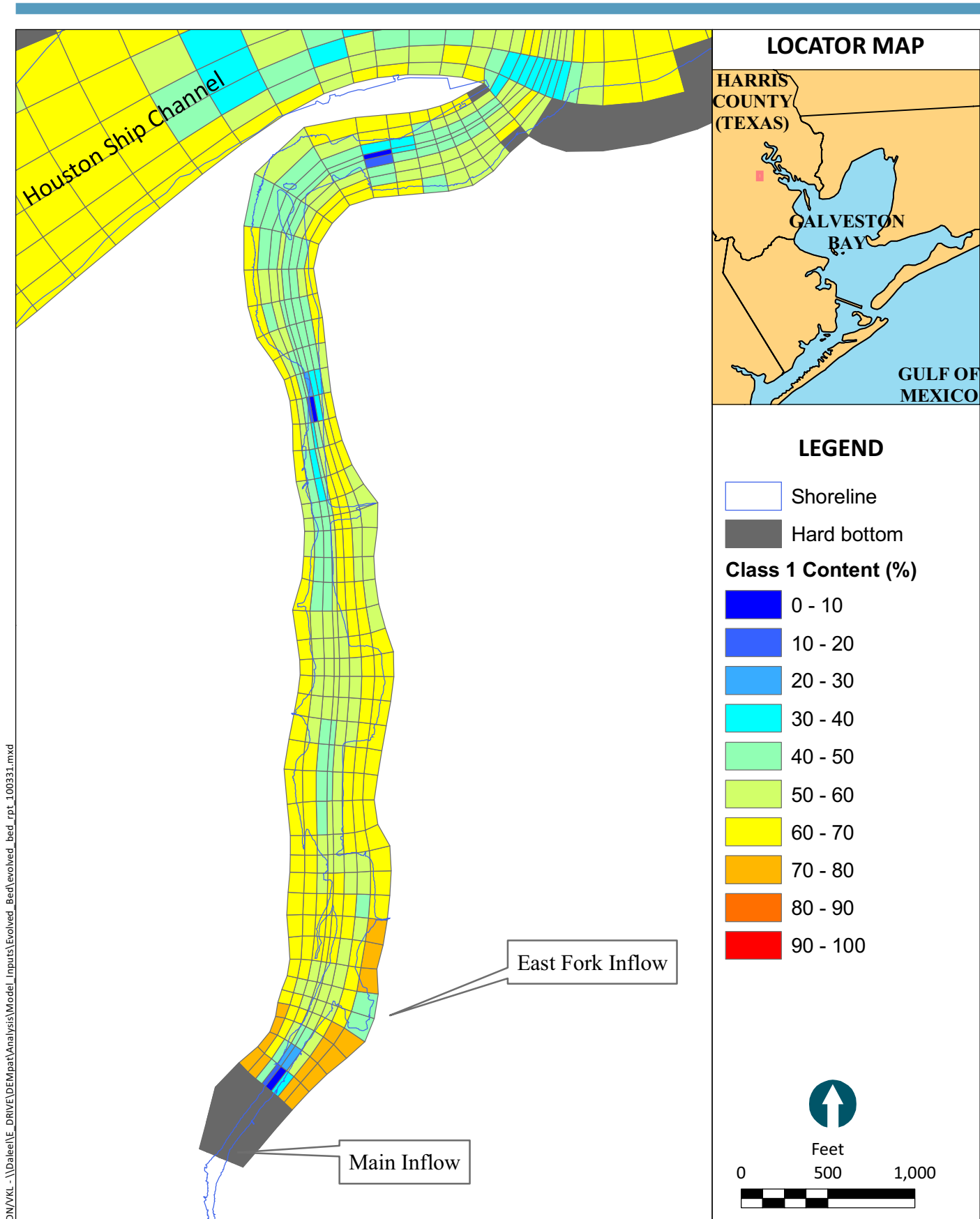


Figure 2-17

Spatial Distribution of Evolved Bed Composition Used as Initial Conditions for Model Simulations: Class 1 Sediment
Patrick Bayou Study Area

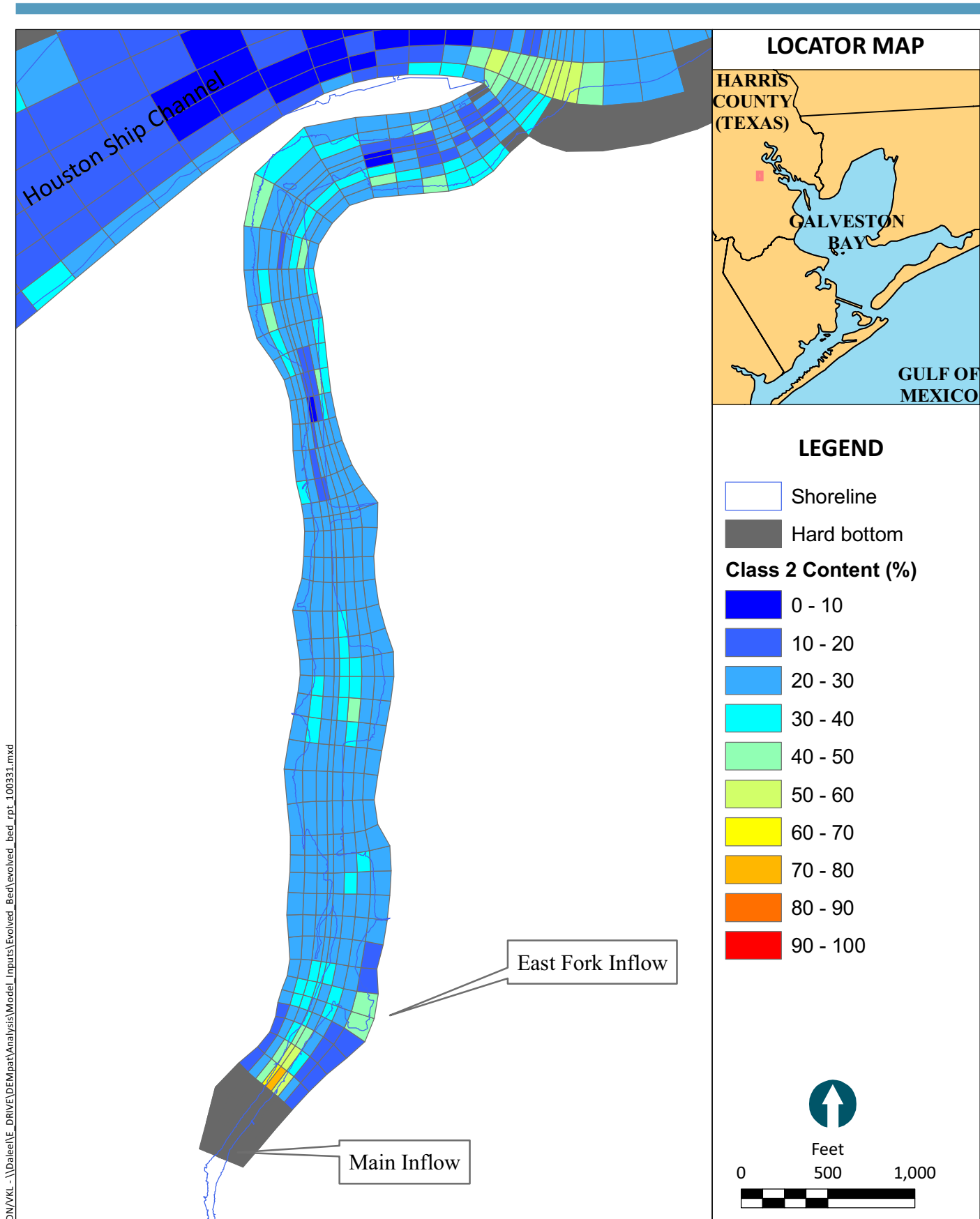
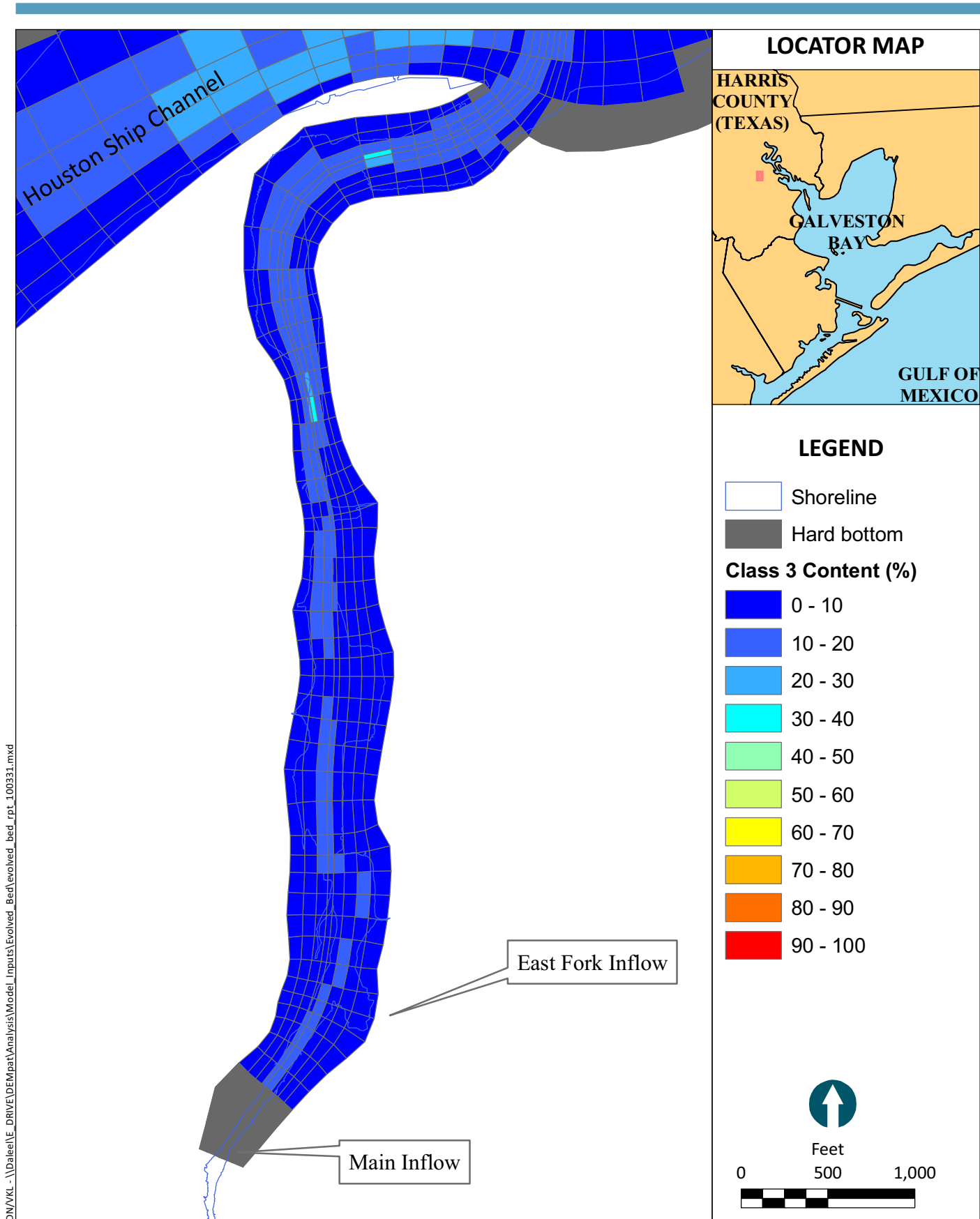


Figure 2-18

Spatial Distribution of Evolved Bed Composition Used as Initial Conditions for Model Simulations: Class 2 Sediment
Patrick Bayou Study Area



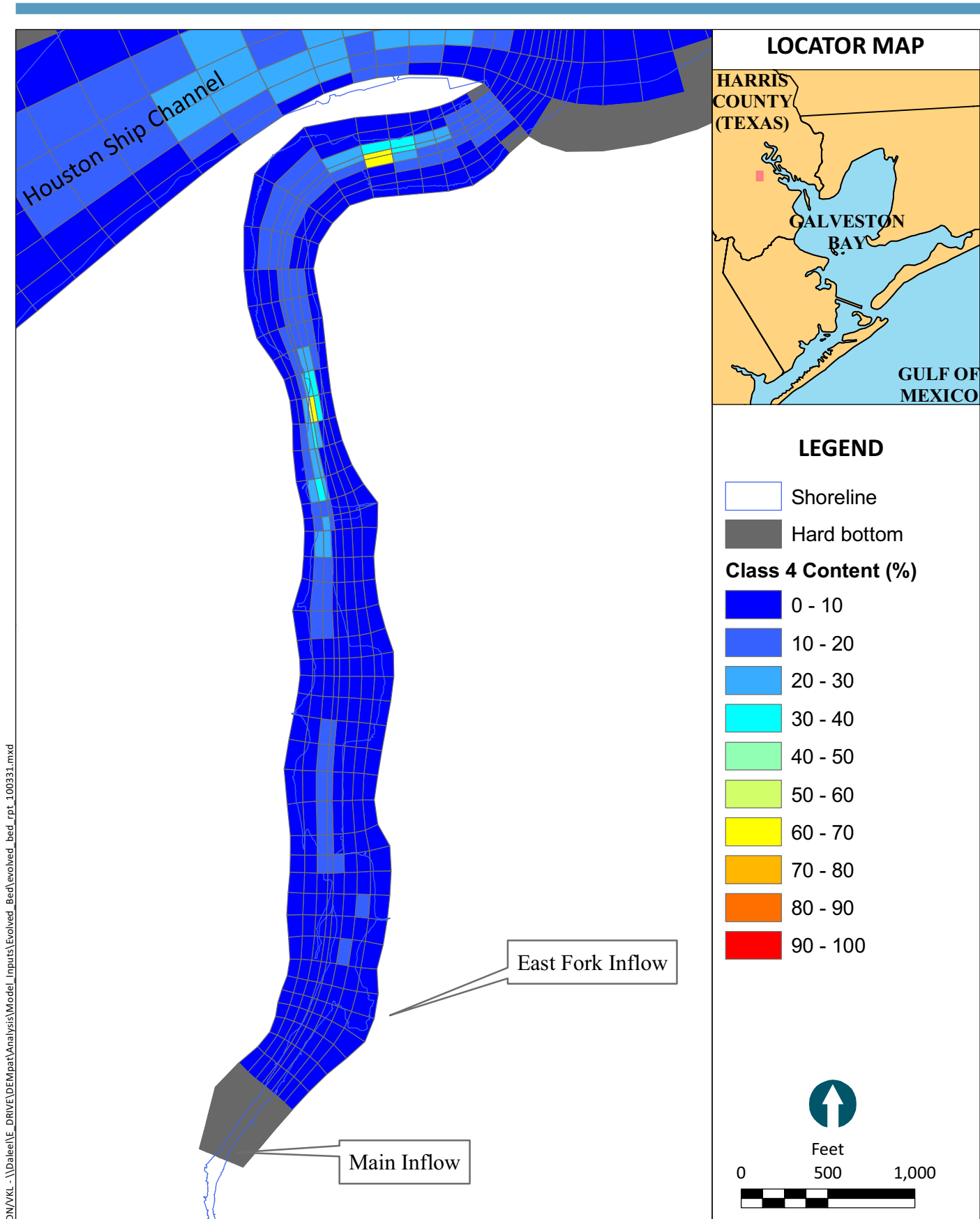


Figure 2-20

Spatial Distribution of Evolved Bed Composition Used as Initial Conditions for Model Simulations: Class 4 Sediment
Patrick Bayou Study Area

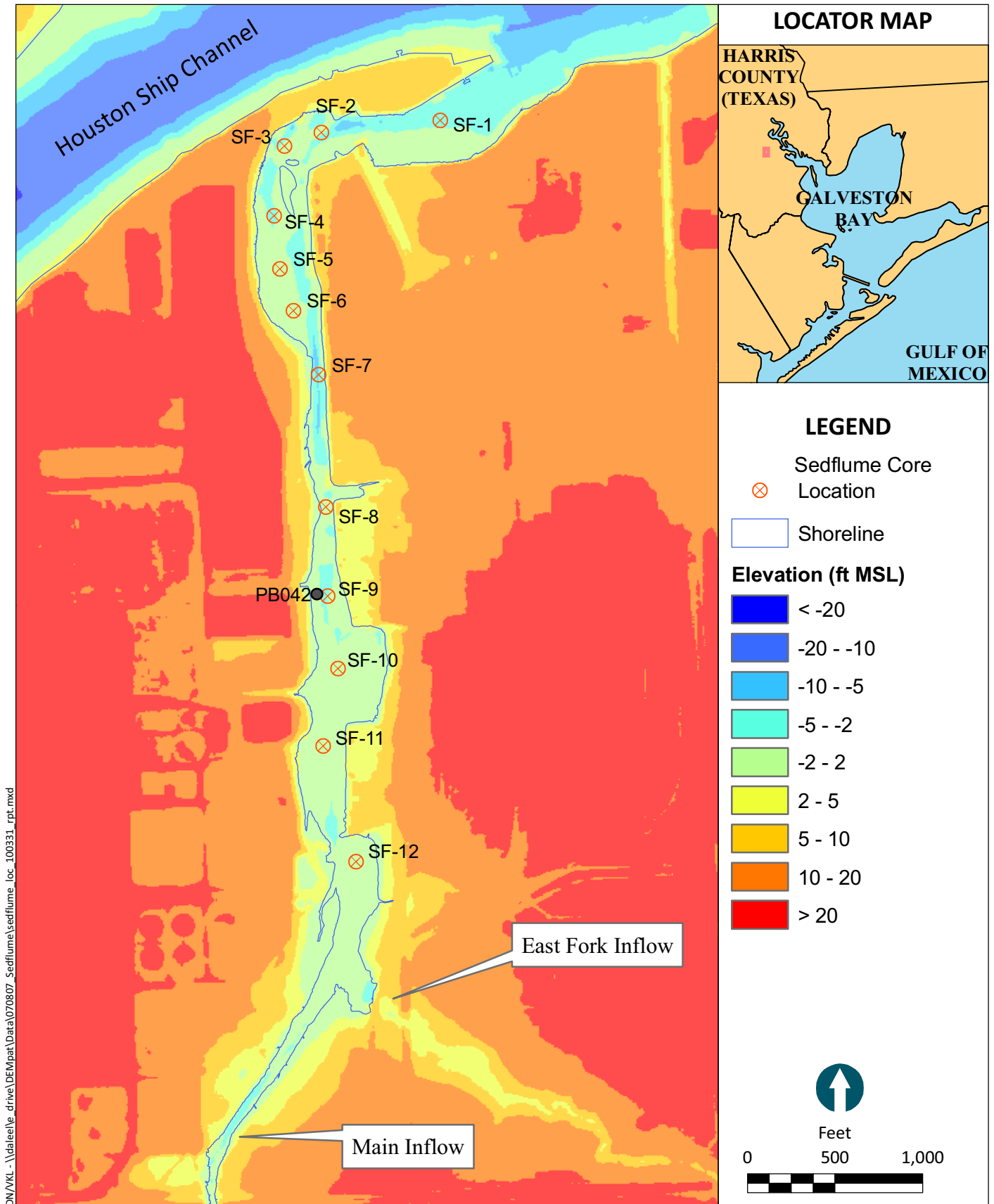


Figure 2-21

Erosion rate (Sedflume) Core Locations
Patrick Bayou Study Area

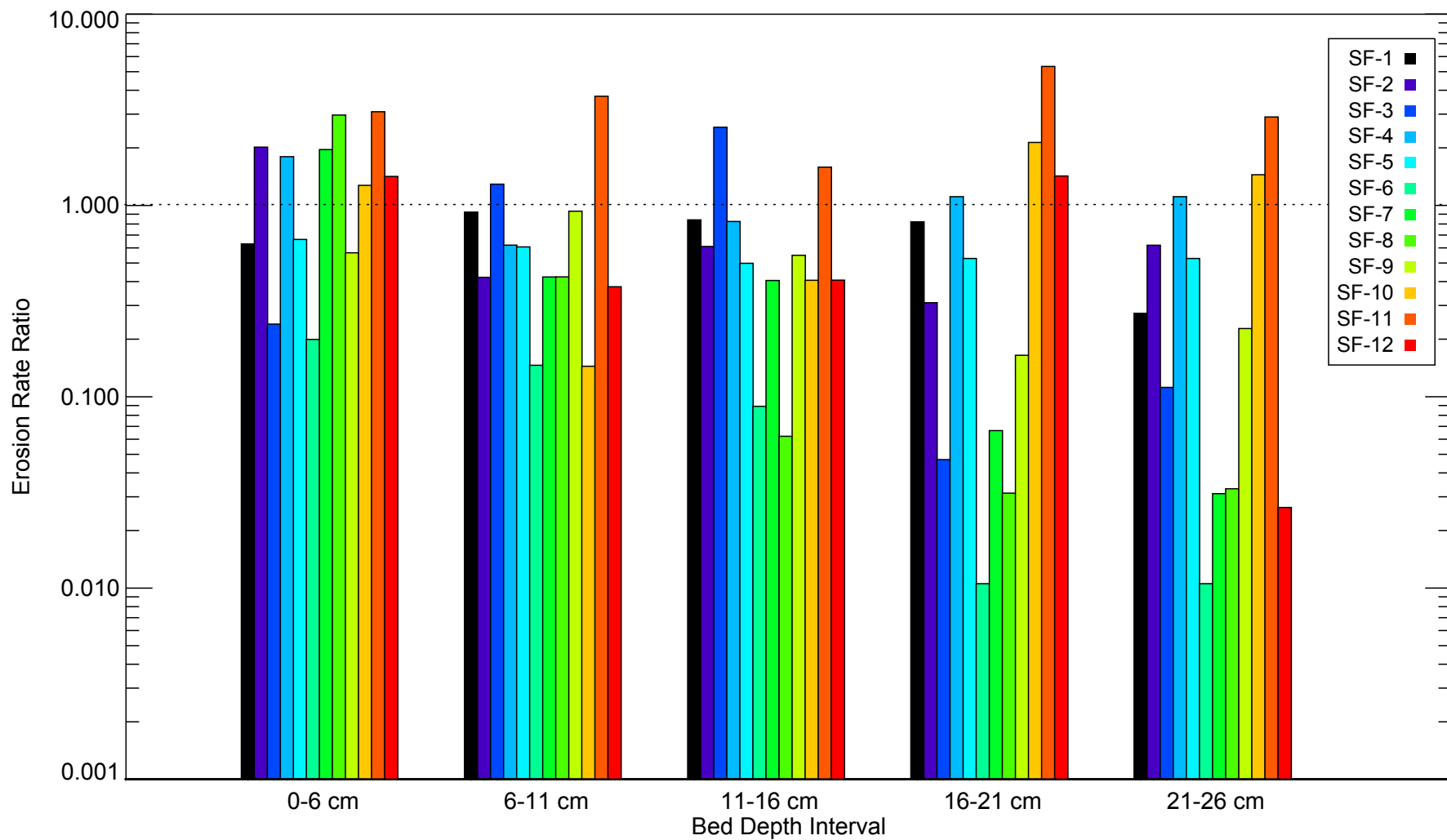


Figure 2-22
Comparison of Erosion Rate Ratio for Sedflume Cores Collected in Patrick Bayou
Patrick Bayou Study Area

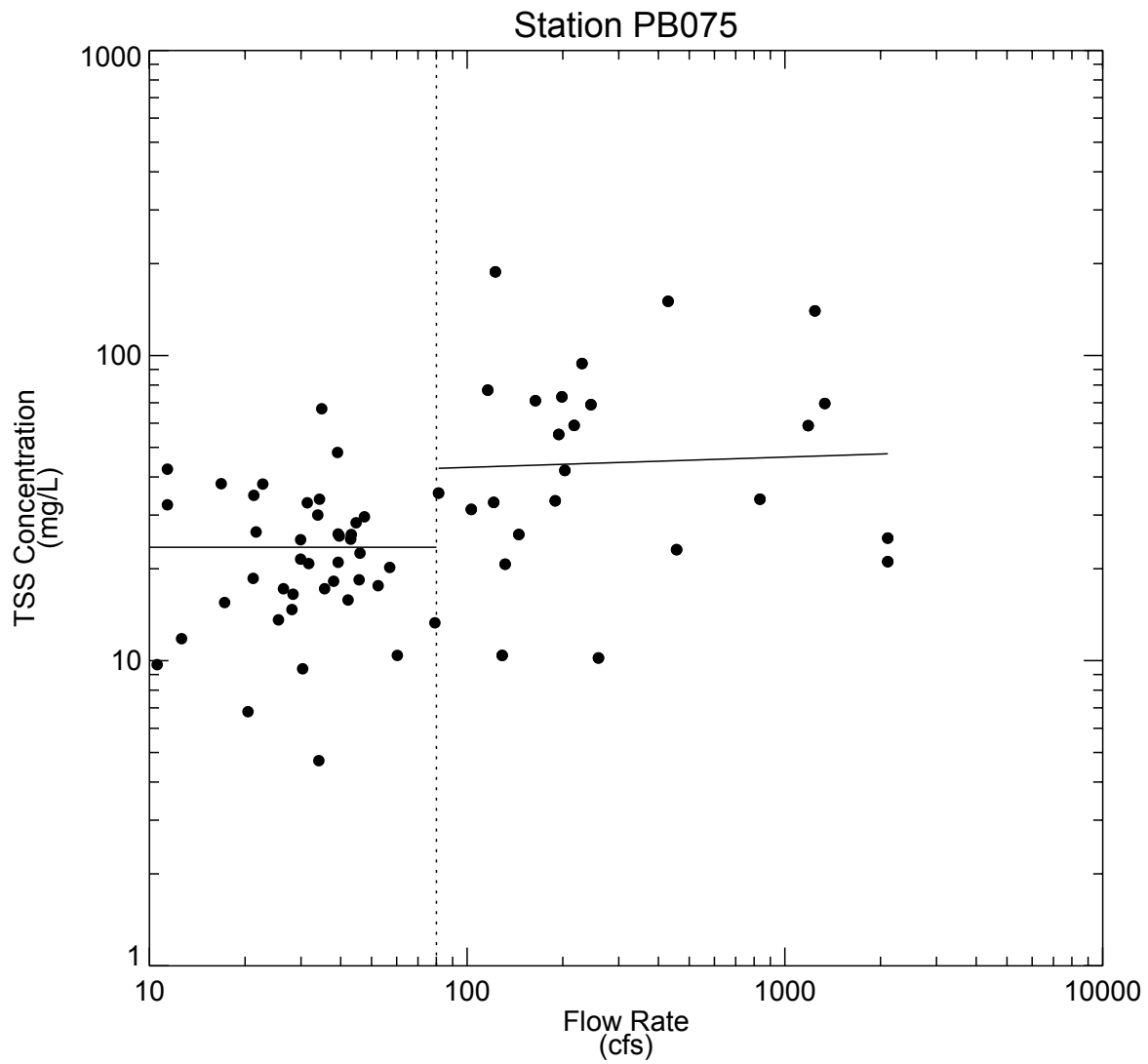


Figure 2-23

Sediment Rating Curve for Station PB075

Note: Data collected during calibration period: October 11 to November 6 (2006)

Patrick Bayou Study Area



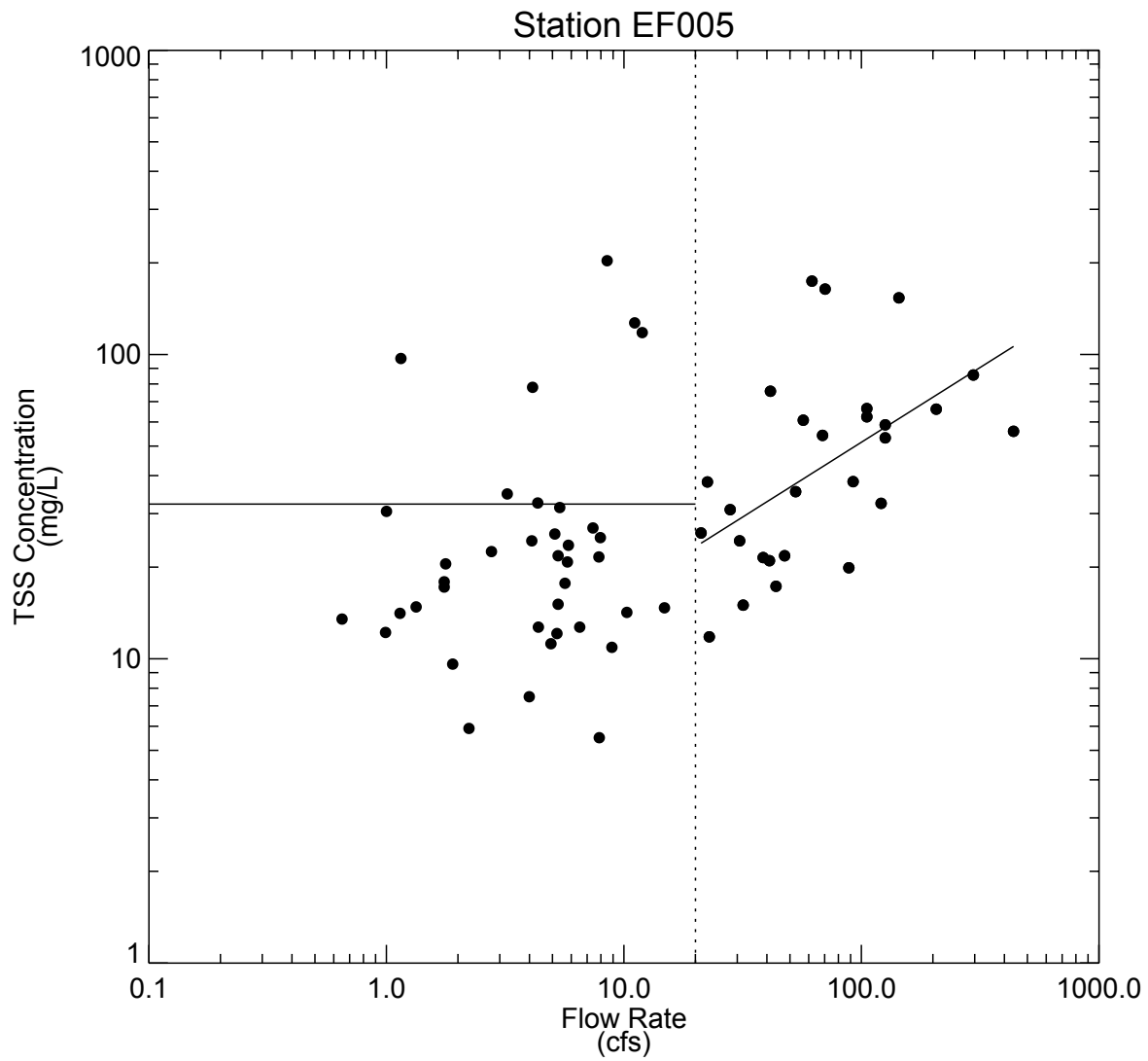


Figure 2-24

Sediment Rating Curve for Station EF005

Note: Data collected during calibration period: October 11 to November 6 (2006).

Patrick Bayou Study Area



DN\\VKL-\\Daleel\\E_DRIVE\\DEM\\pat\\Data\\080401_tss\\tss_layout_100331_rpt.mxd

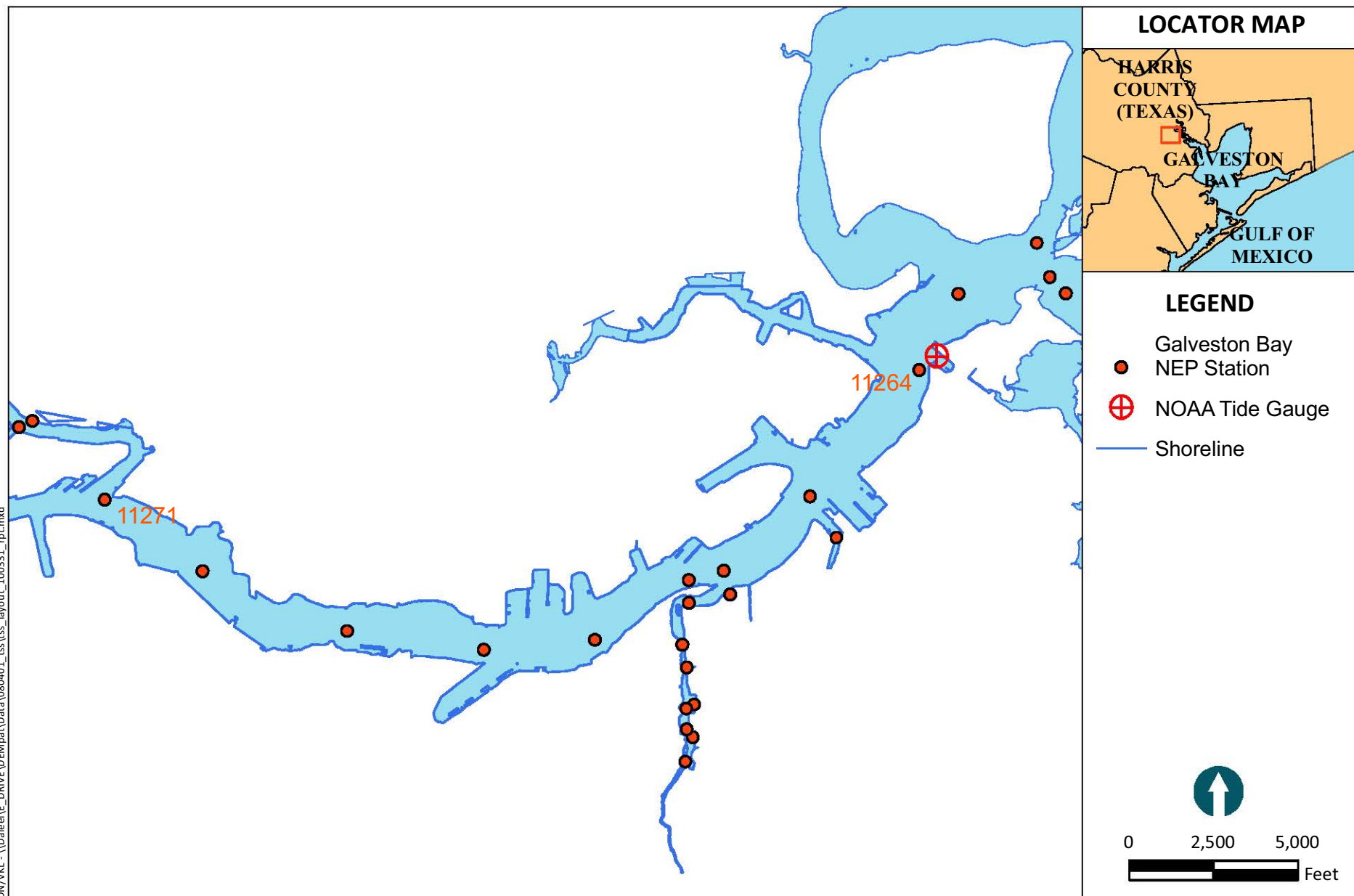


Figure 2-25

Location of Galveston Bay National Estuary Program Sampling Stations Near Patrick Bayou
Patrick Bayou Study Area

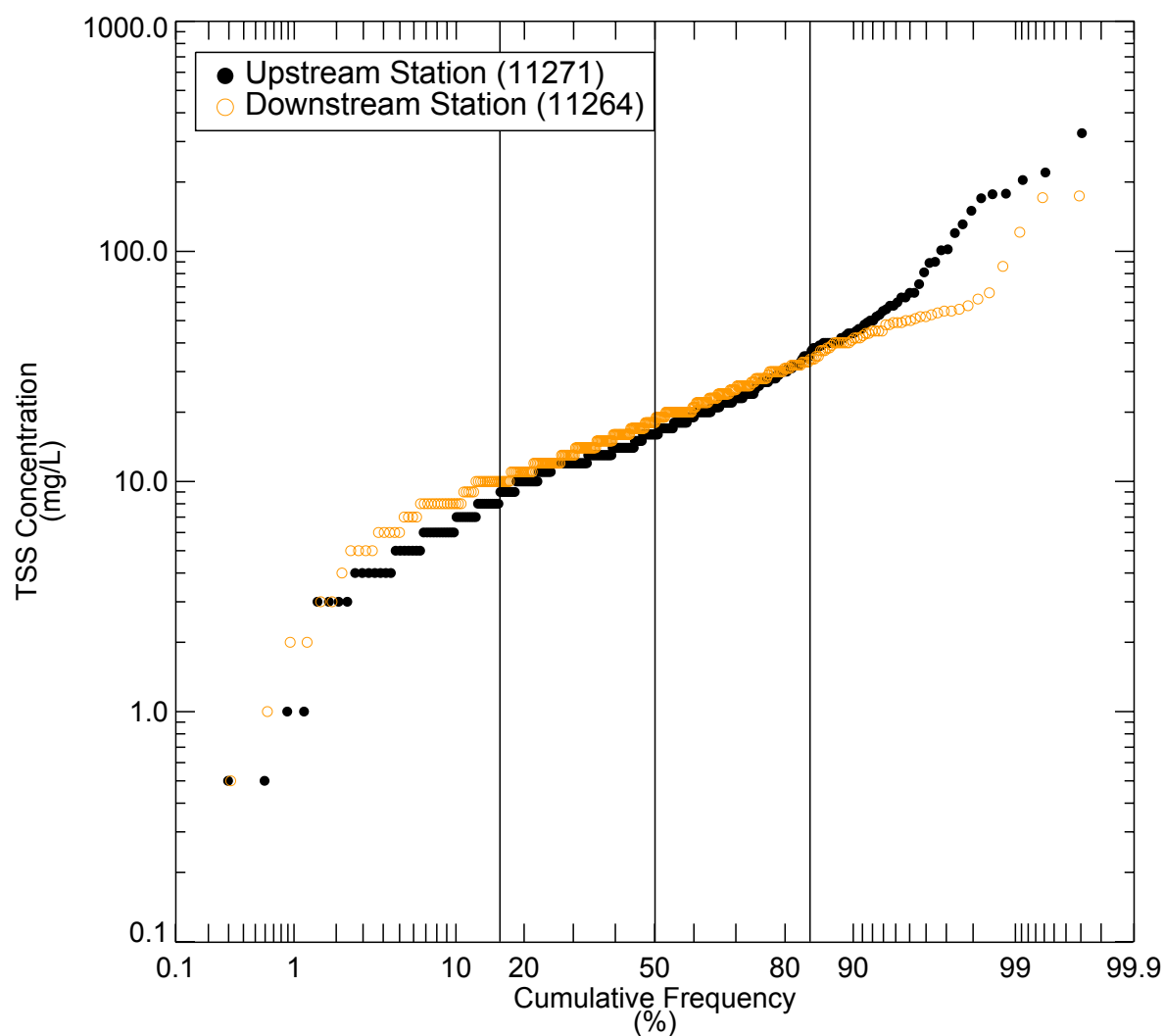


Figure 2-26
 Comparison of Cumulative Frequency Distributions for Historical TSS
 Concentration Data Collected at Two HSC Stations
 Patrick Bayou Study Area

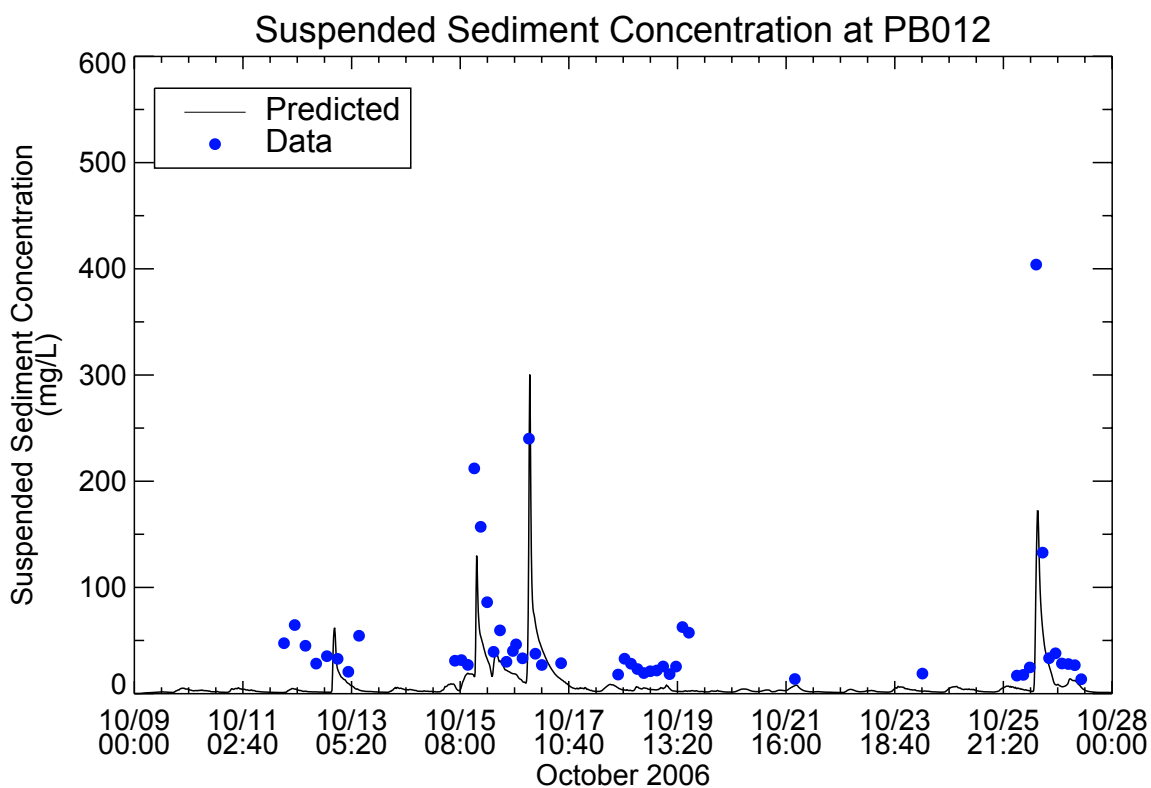
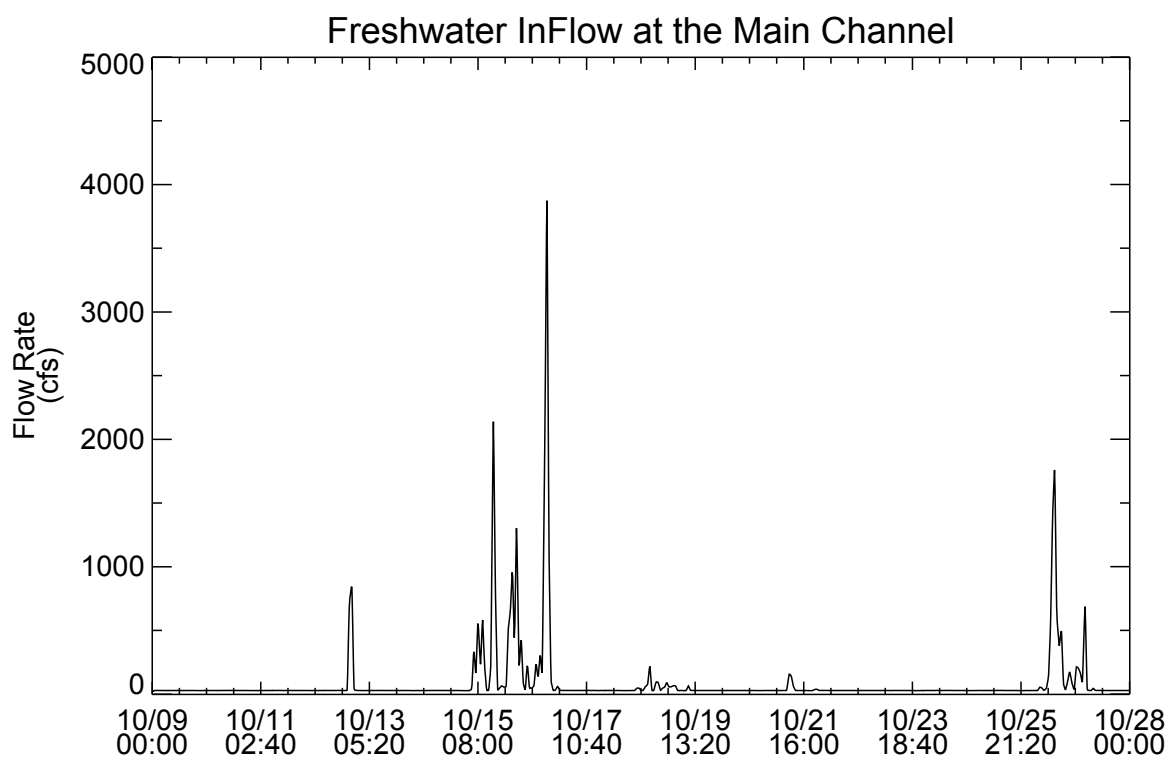


Figure 2-27
Comparisons of Measured and Predicted TSS Concentrations at Station PB012 During
October 2006 Calibration Period
Patrick Bayou Study Area

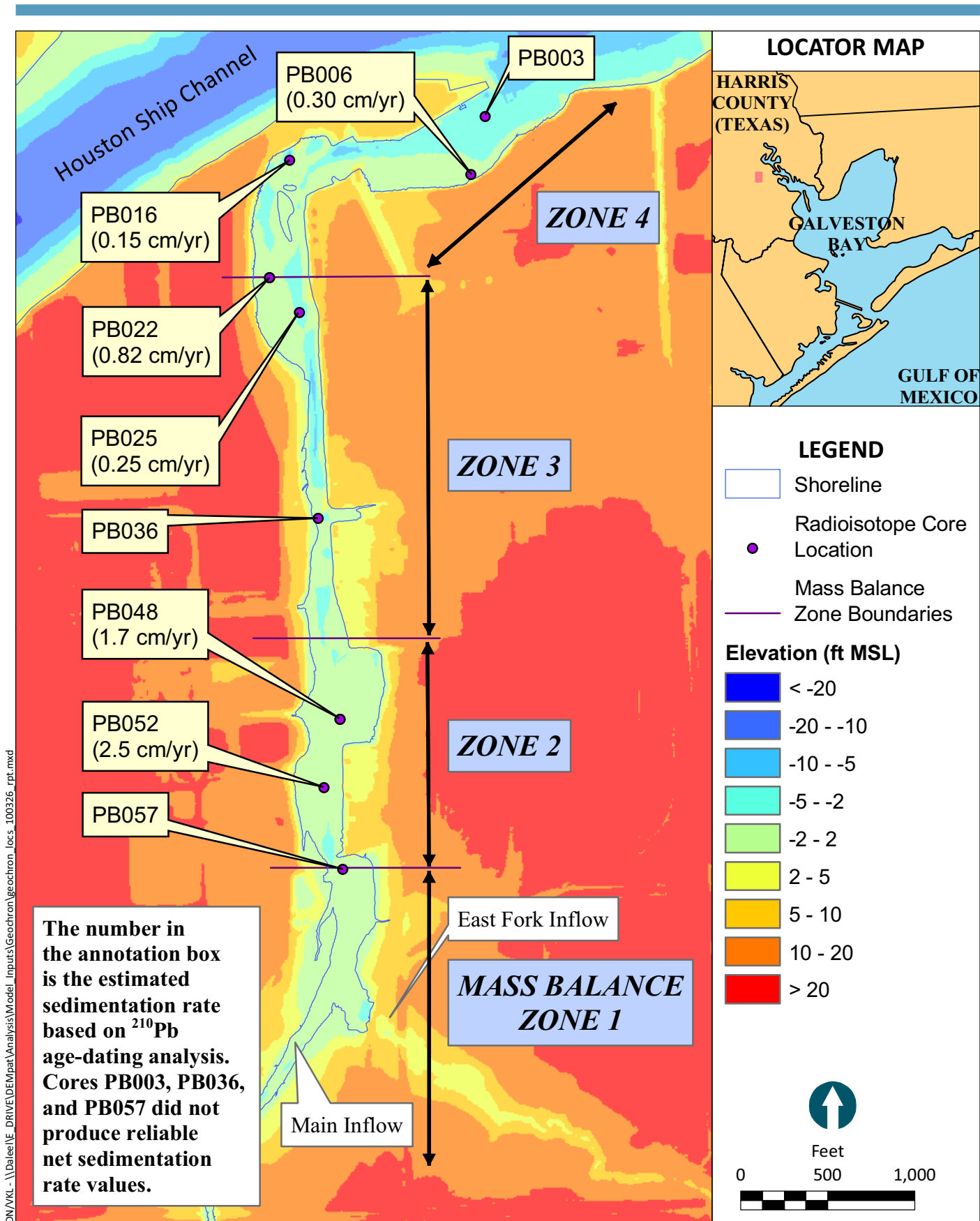


Figure 2-28

Radioisotope Core Sampling Locations
and Mass Balance Zone delineation
Patrick Bayou Study Area

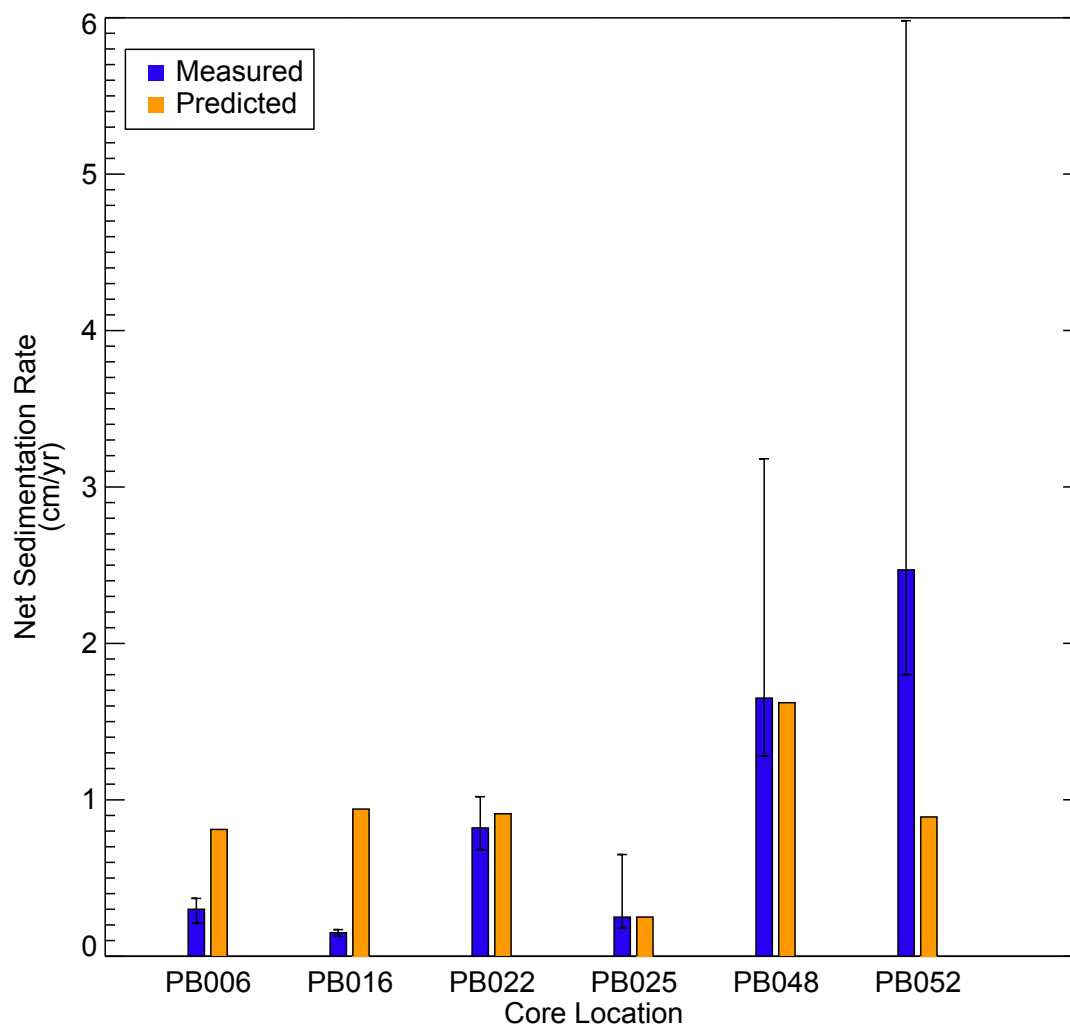


Figure 2-29
Comparison of Measured and Predicted NSR for 14-year Simulation
Patrick Bayou Study Area

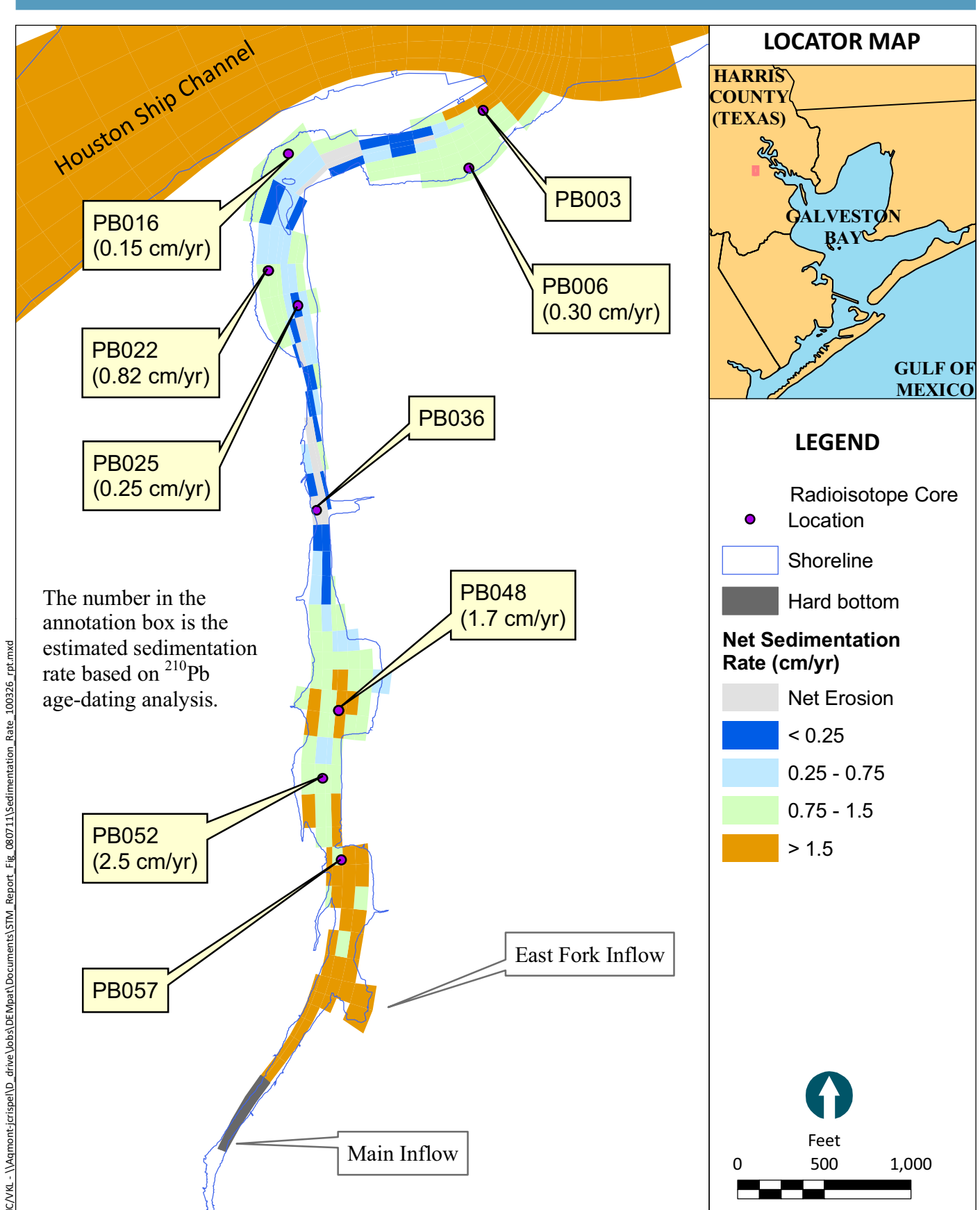


Figure 2-30

Spatial Distribution of Predicted Net Sedimentation Rate in Patrick Bayou for 14-year Period (1993-2006)
Patrick Bayou Study Area

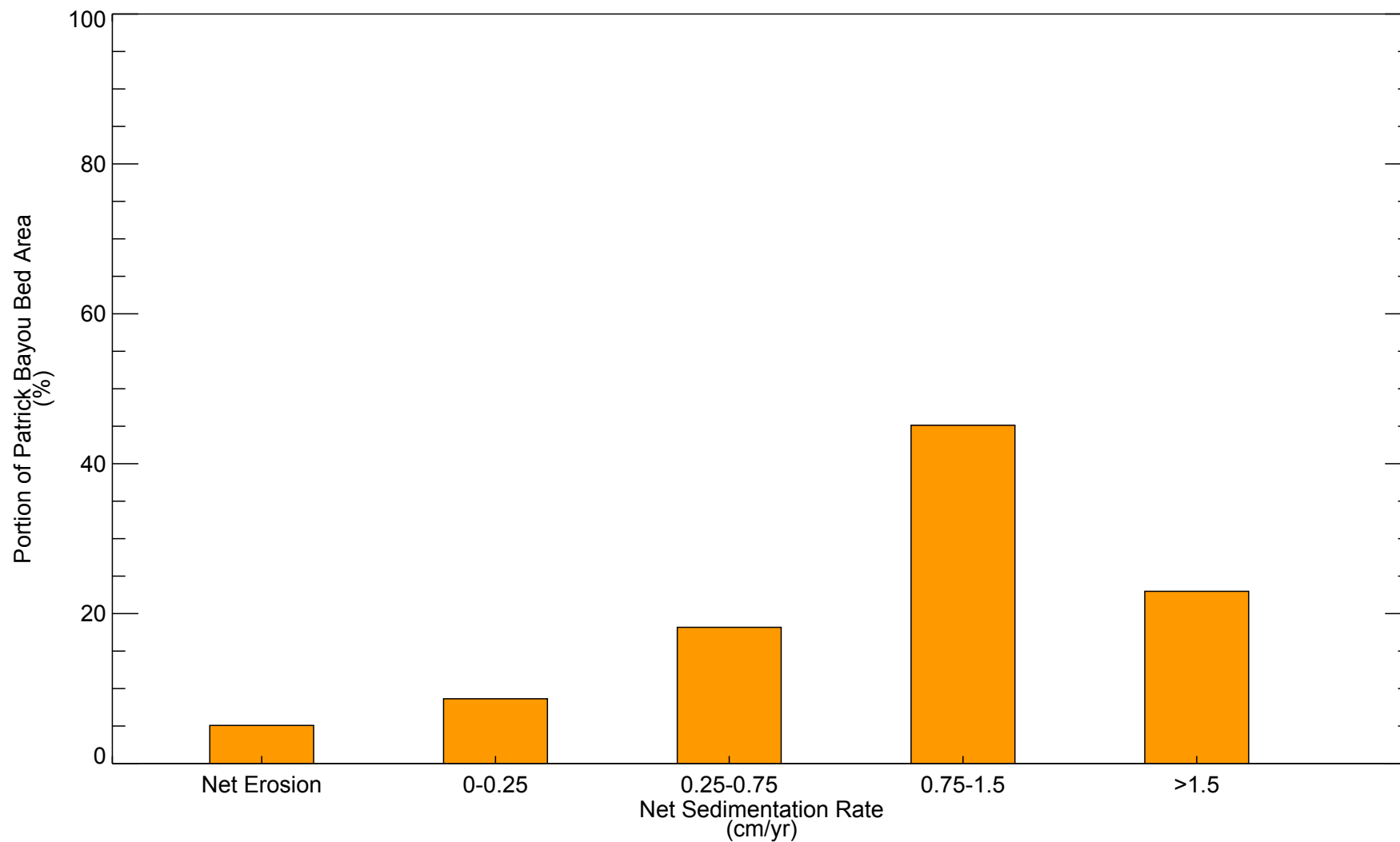


Figure 2-31
Areal Distribution of Predicted Net Sedimentation Rates for 14-year
Simulation (1993-2006)
Patrick Bayou Study Area

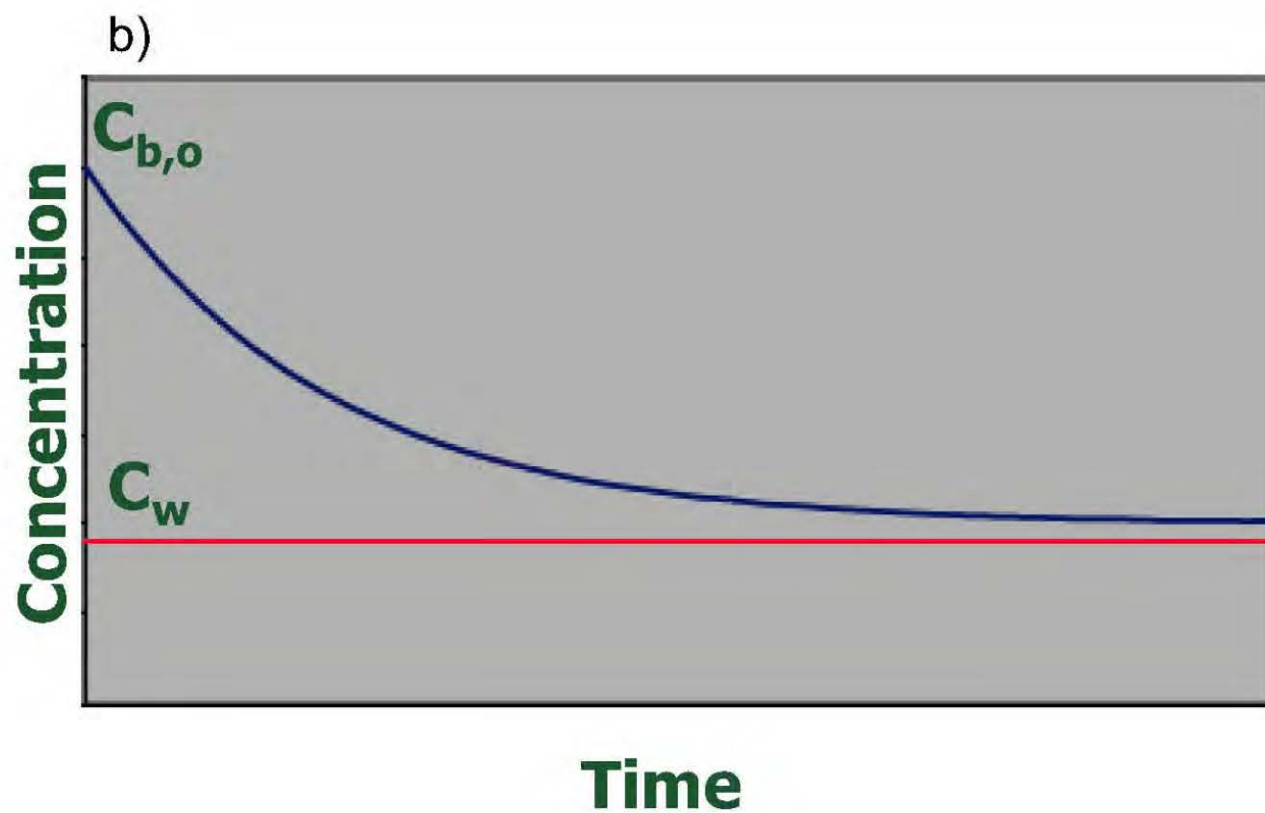
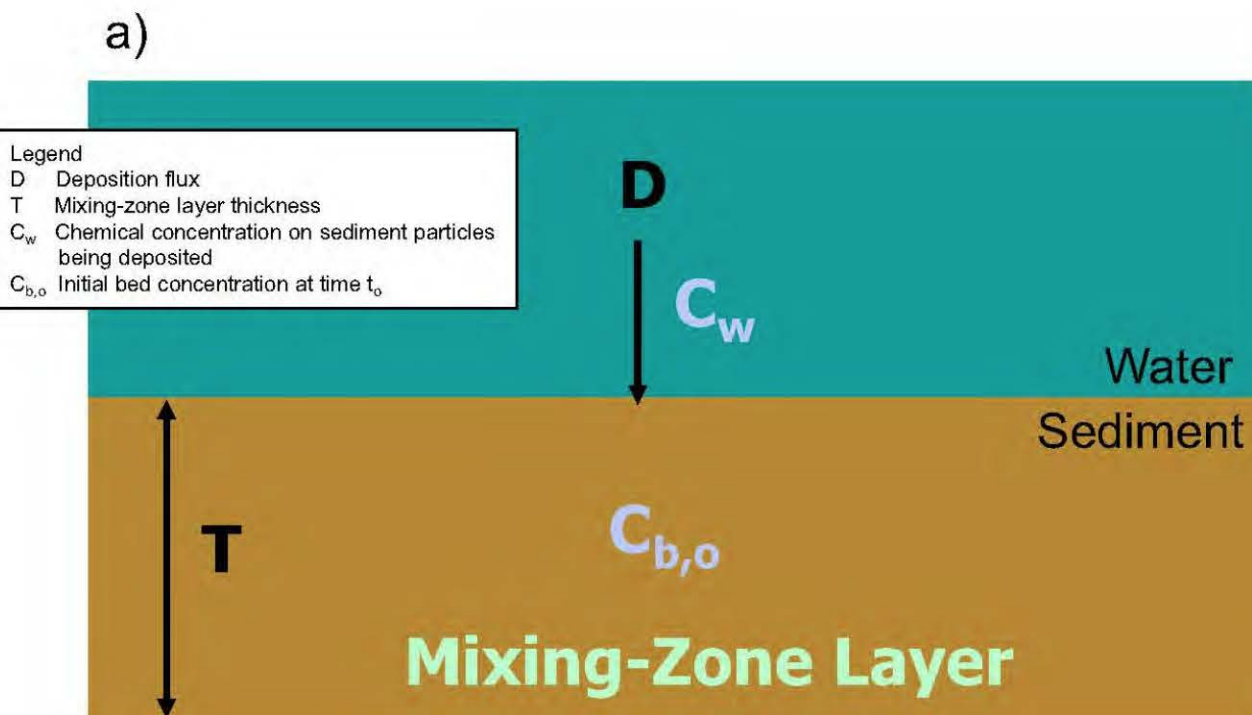


Figure 2-32

a) Schematic of Idealized Deposition and Mixing-zone Layer Model
b) Time History of Exponential Decreasing Chemical Concentration for
Idealized Mixing-zone Layer model
Patrick Bayou Study Area

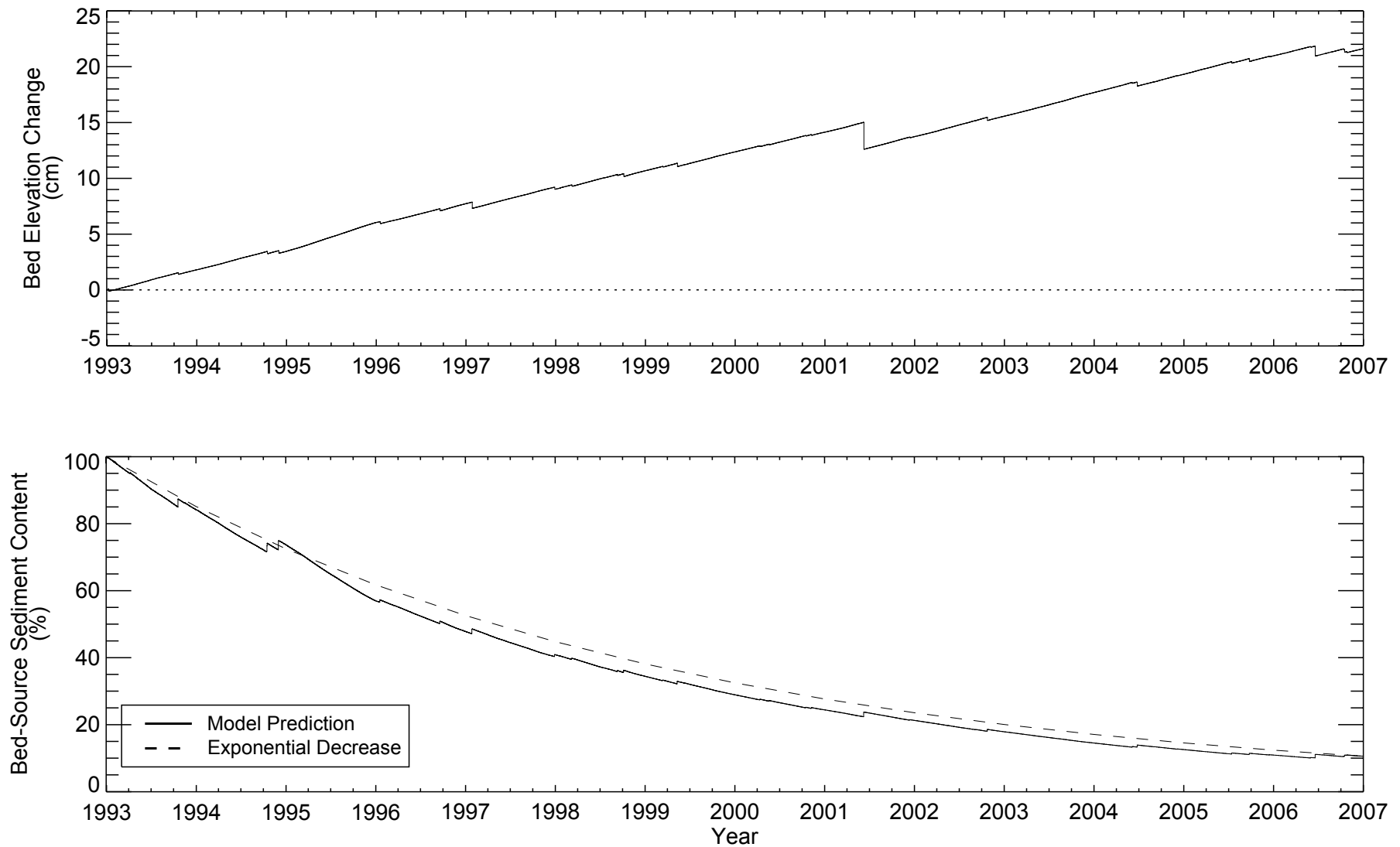


Figure 2-33
Predicted Bed Elevation Change and Mixing-zone Layer Bed Content at Station PB003
Patrick Bayou Study Area

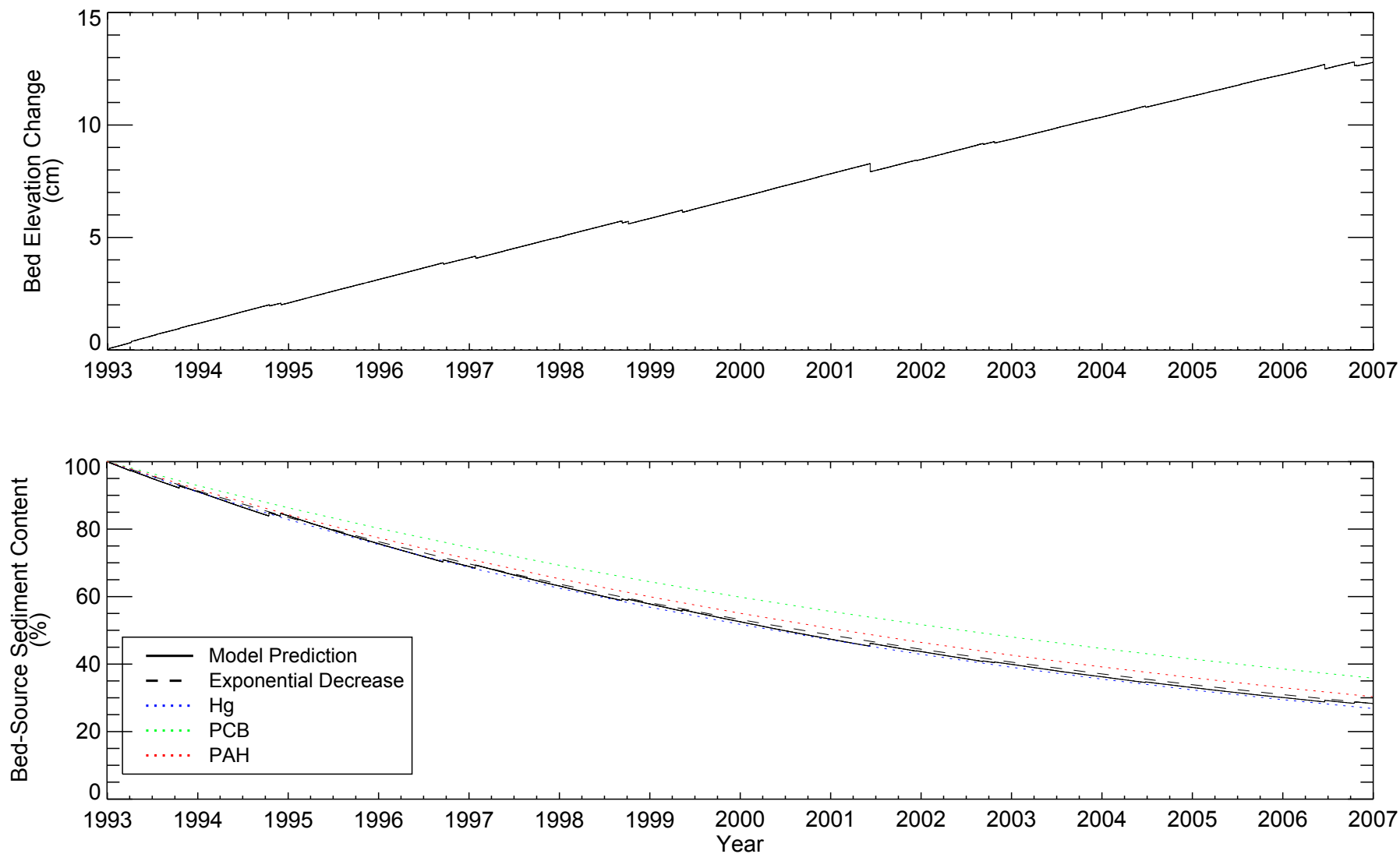


Figure 2-34
 Predicted Bed Elevation Change and Mixing-zone Layer Bed Content at Station PB022
 Patrick Bayou Study Area

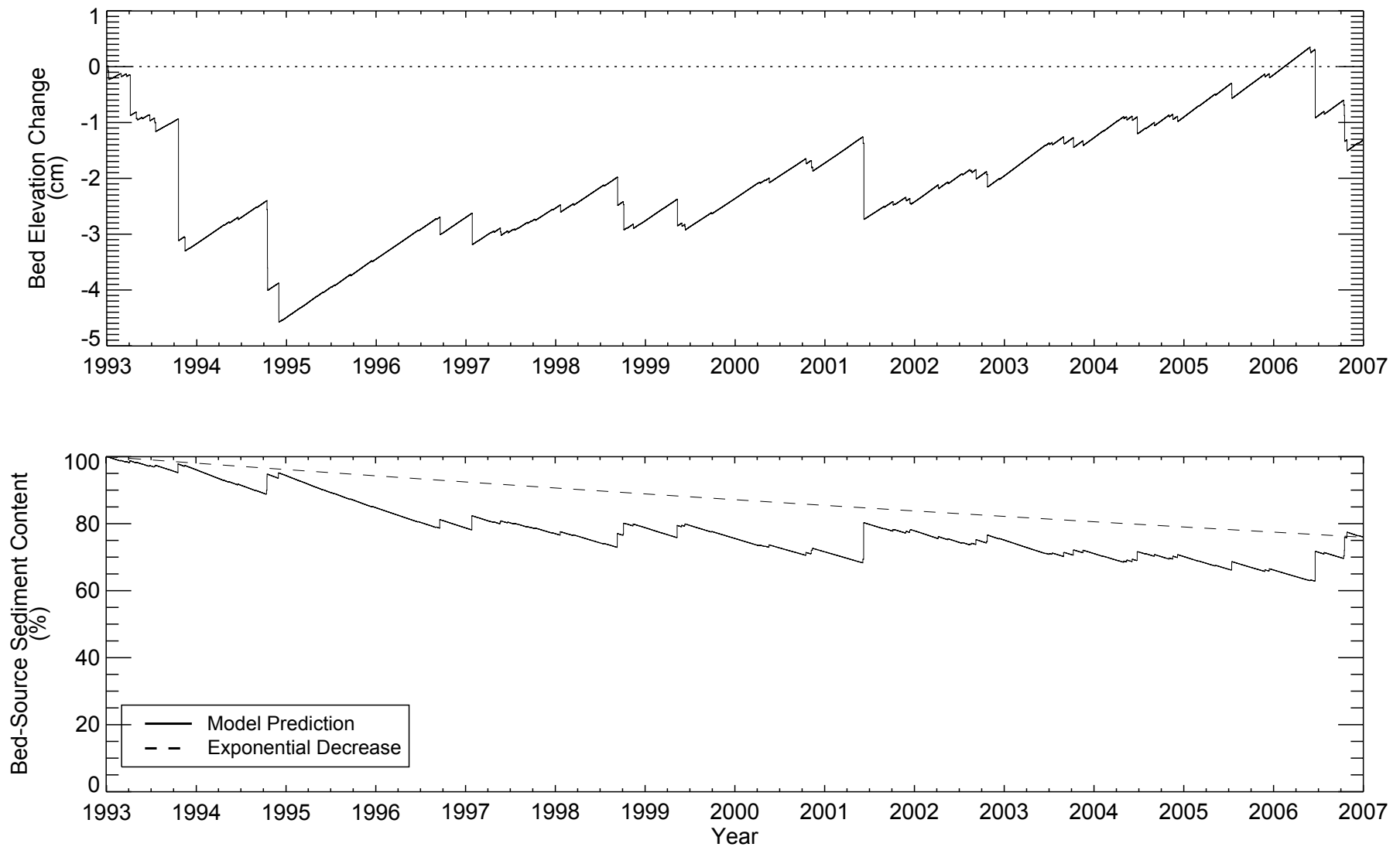


Figure 2-35
Predicted Bed Elevation Change and Mixing-zone Layer Bed Content at Station PB036
Patrick Bayou Study Area

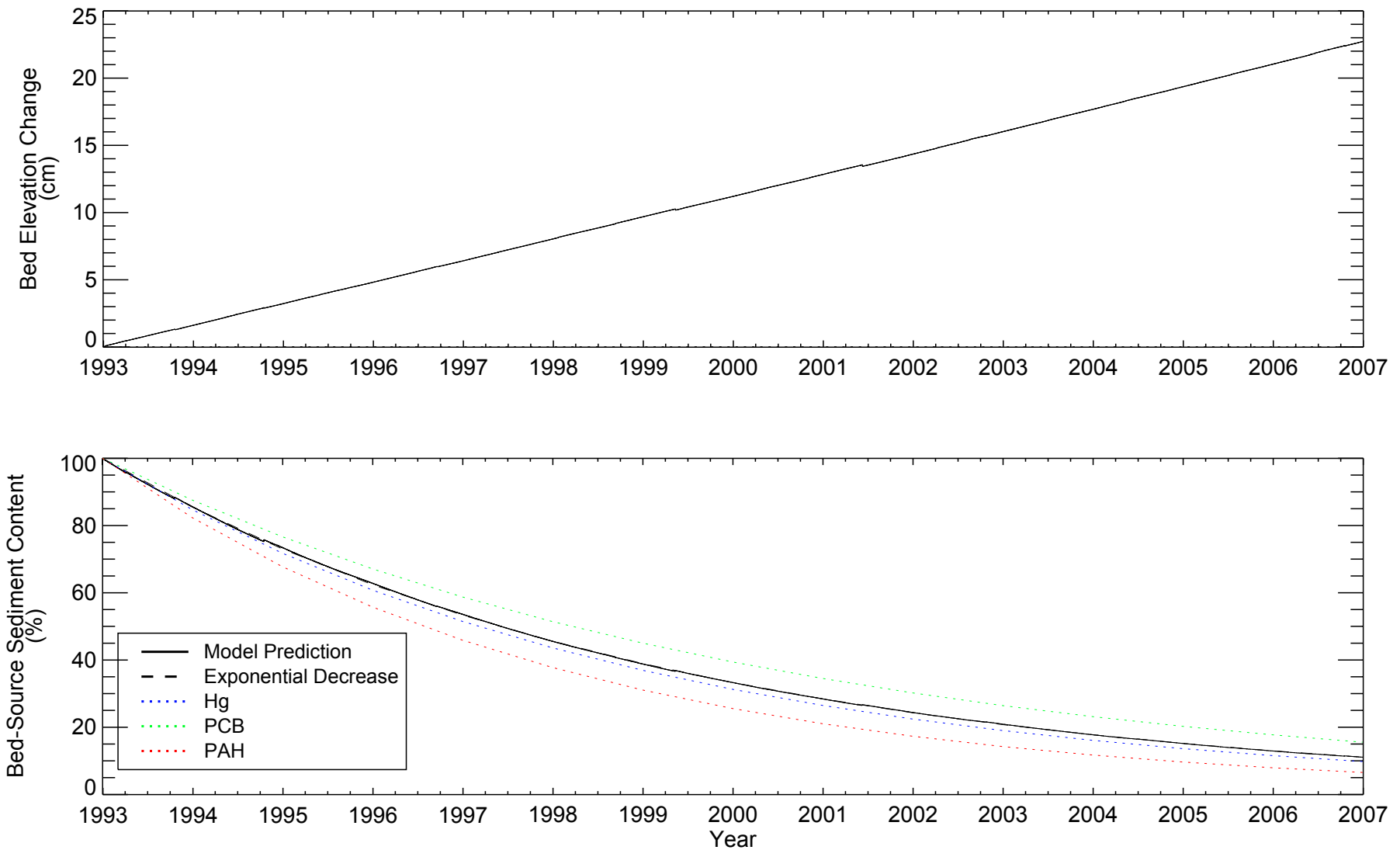


Figure 2-36
Predicted Bed Elevation Change and Mixing-zone Layer Bed Content at Station PB048
Patrick Bayou Study Area

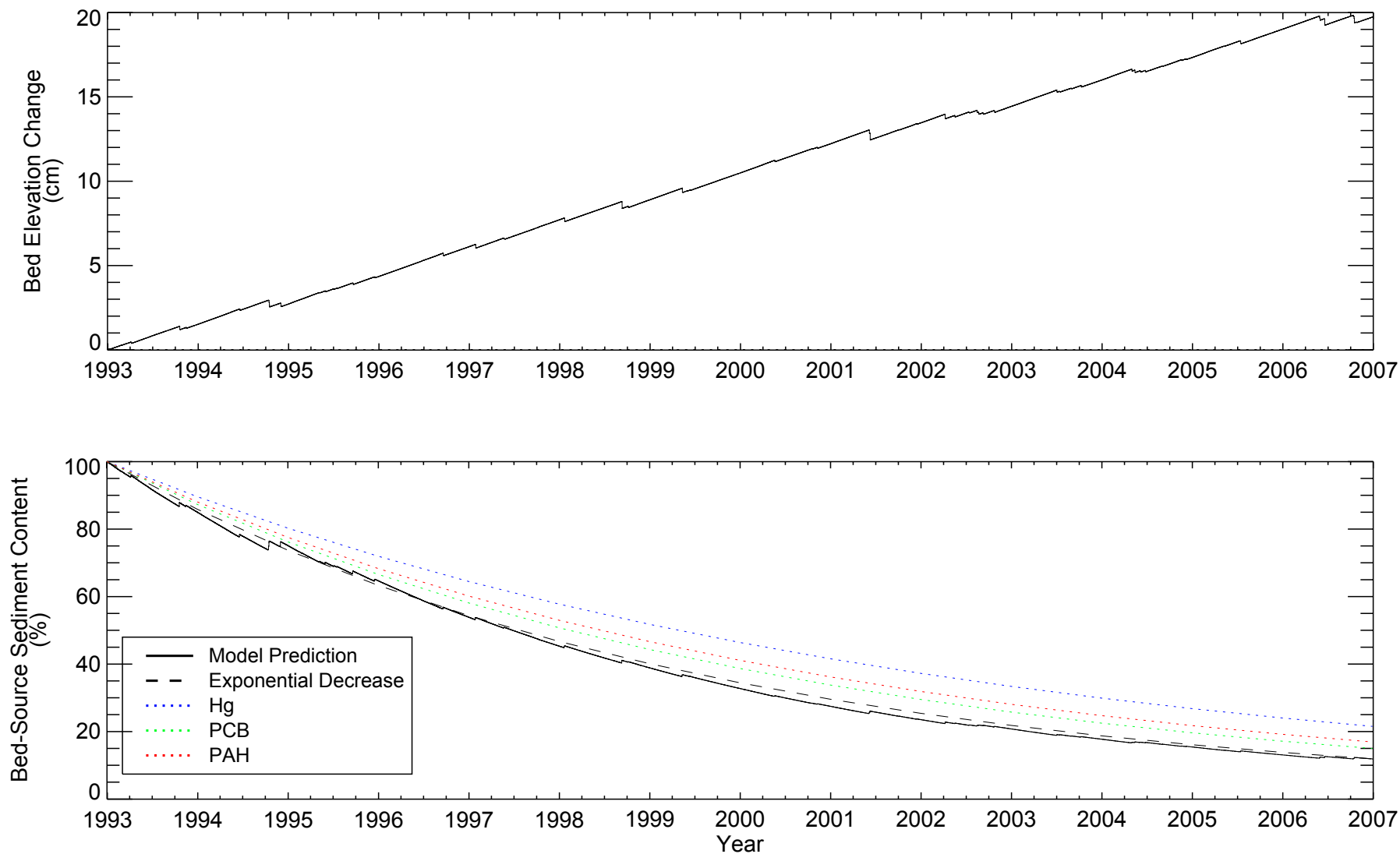


Figure 2-37
 Predicted Bed Elevation Change and Mixing-zone Layer Bed Content at Station PB057
 Patrick Bayou Study Area

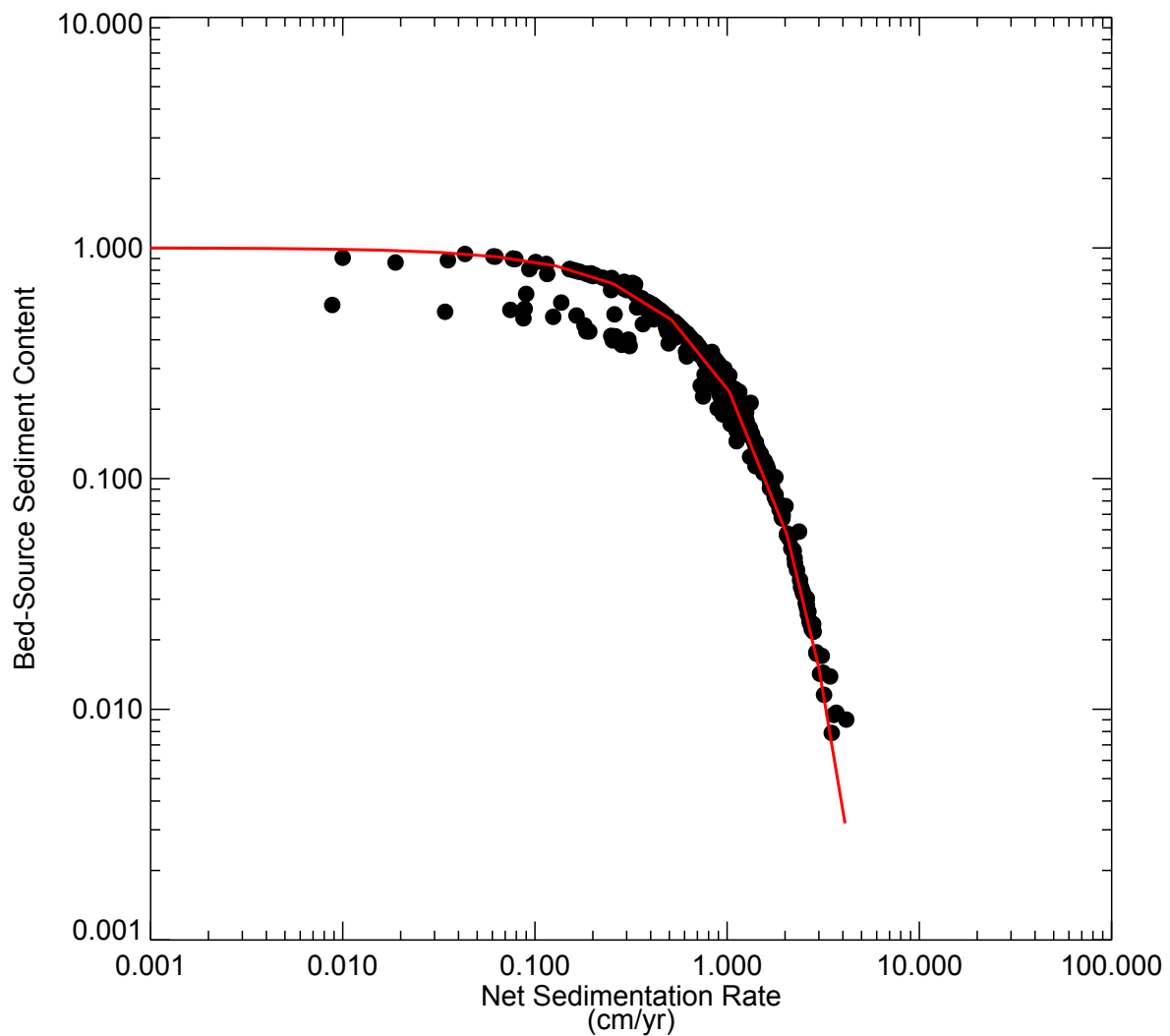


Figure 2-38

Relationship between Predicted Net Sedimentation Rate and Bed-source Sediment
Content in Mixing-zone Layer at End of 14-year Period

Note: Red line is theoretical relationship based on exponential decrease due to deposition
Patrick Bayou Study Area

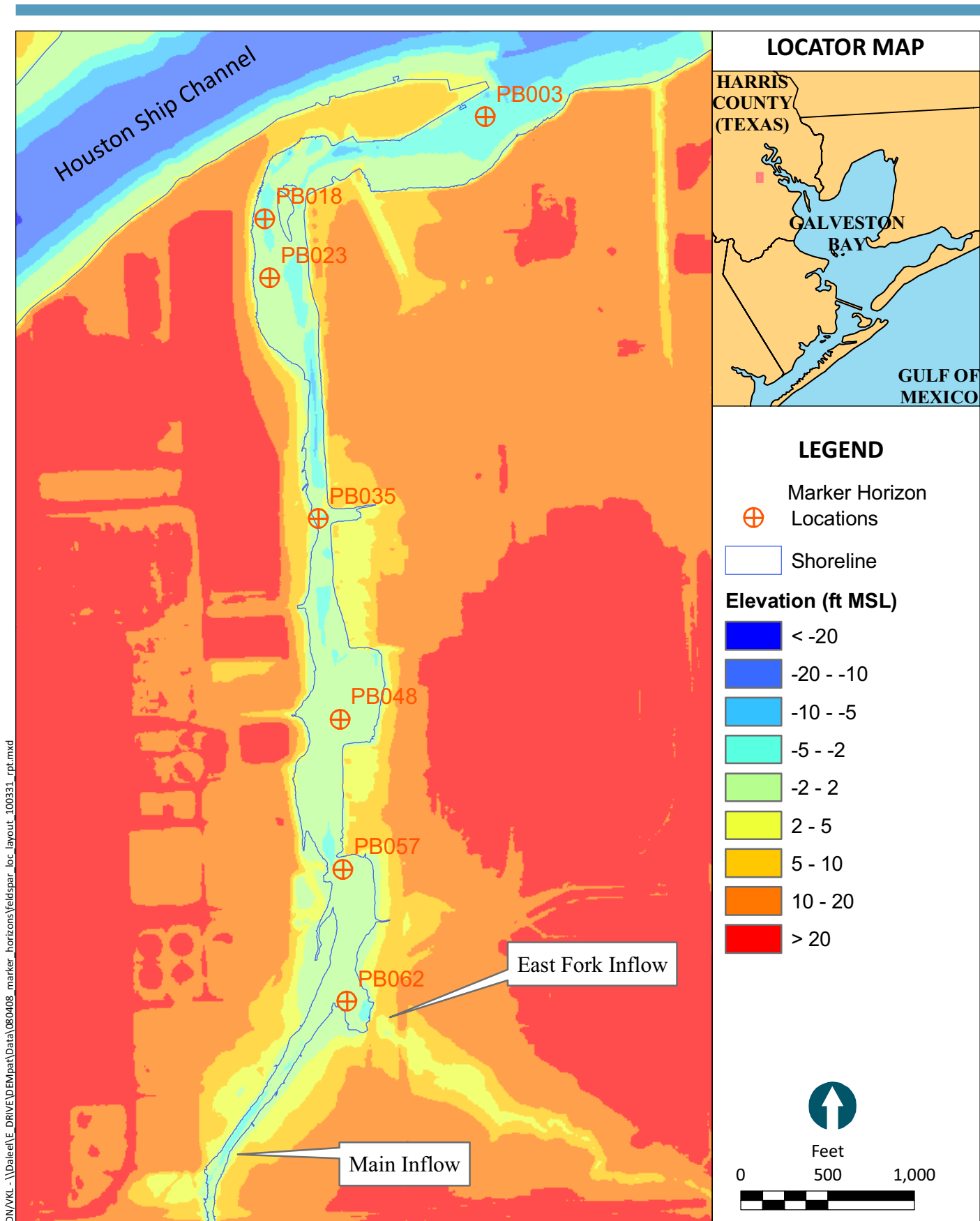


Figure 3-1

Locations of Sediment Marker Horizon Stations
Patrick Bayou Study Area

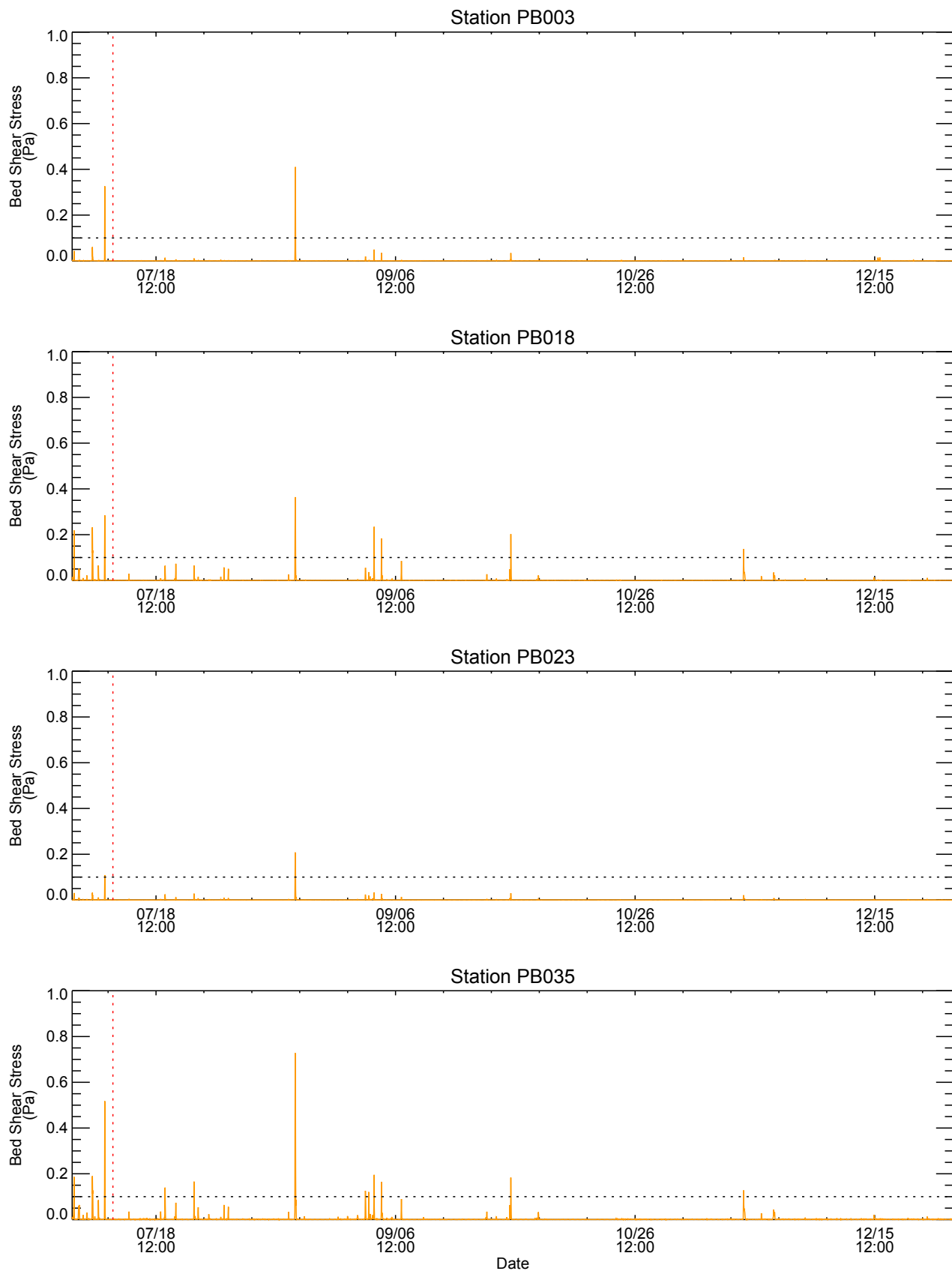


Figure 3-2

Predicted Bed Shear Stress at Marker Horizon Stations PB003, PB018, PB023, and PB035:
July-December 2007

Note: Dotted horizontal line represents typical critical shear stress (0.1 Pa). Red dotted vertical line represents approximate time of marker horizon placement (week of July 9).
Patrick Bayou Study Area



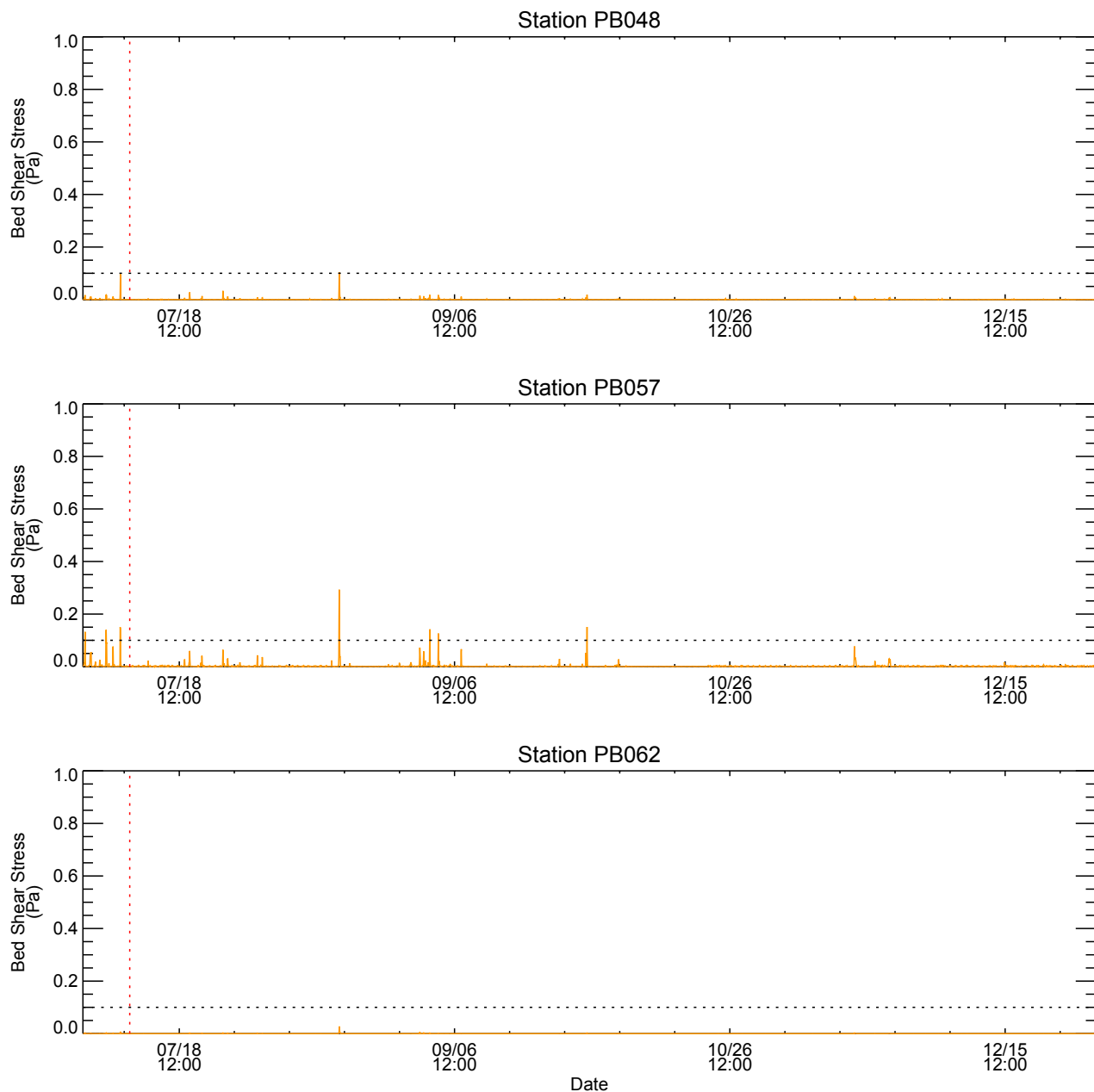


Figure 3-3
 Predicted Bed Shear Stress at Marker Horizon Stations PB048, PB057, PB062, and PB035: July-December 2007

Note: Dotted horizontal line represents typical critical shear stress (0.1 Pa). Red dotted vertical line represents approximate time of marker horizon placement (week of July 9).

Patrick Bayou Study Area



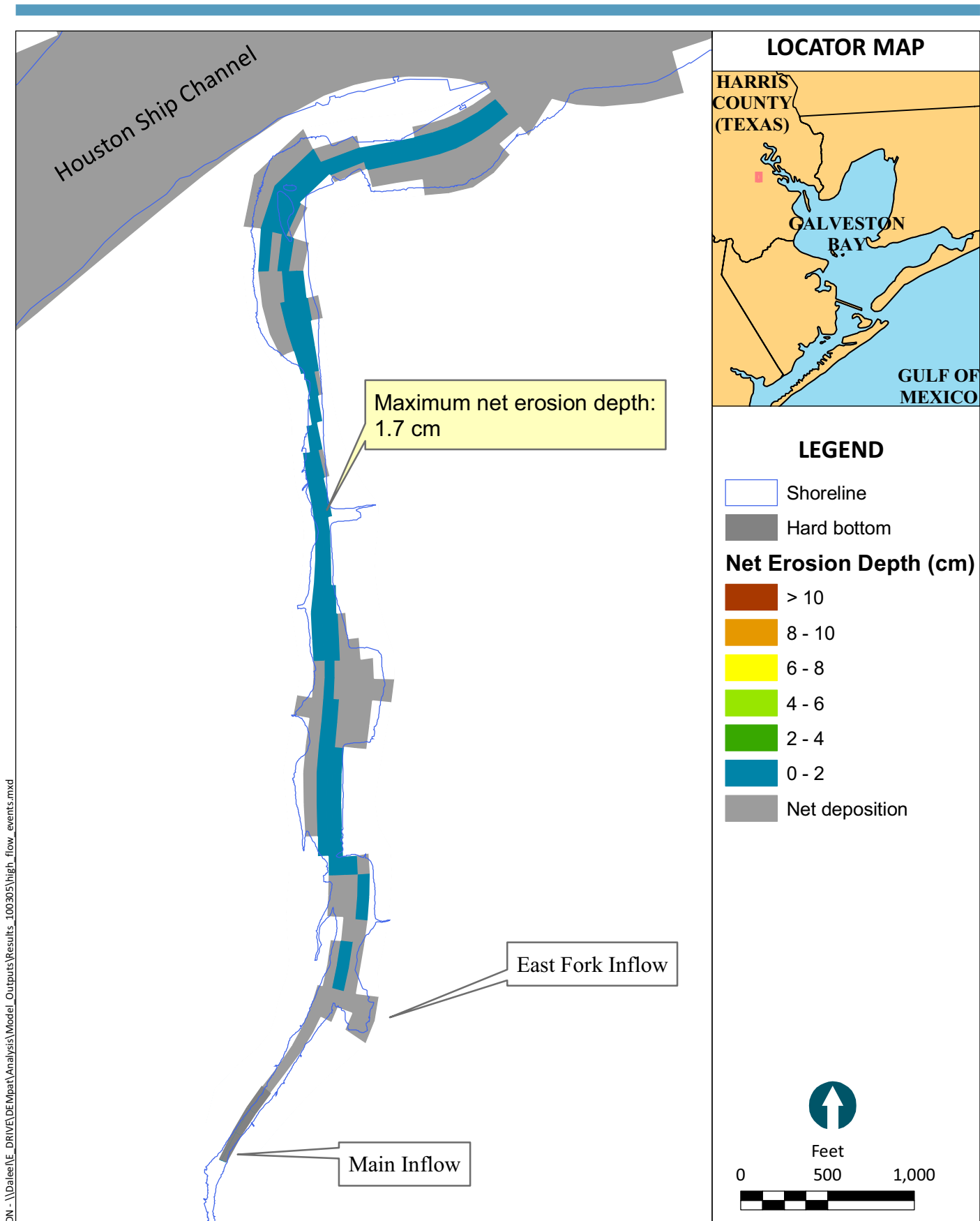


Figure 3-4

Spatial Distribution of Predicted Net Erosion Depth During
2-year High-flow Event
Patrick Bayou Study Area

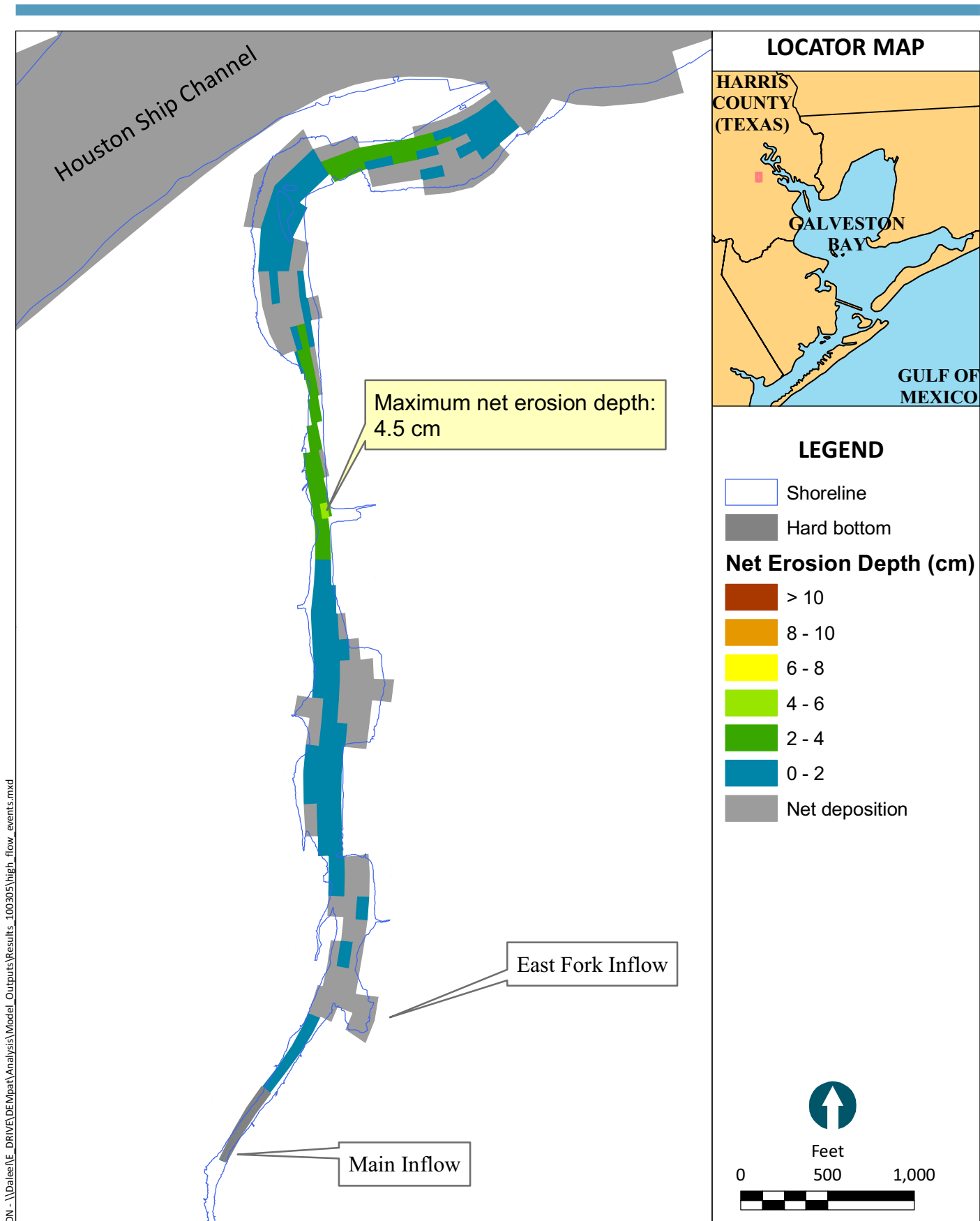


Figure 3-5

Spatial Distribution of Predicted Net Erosion Depth
During 10-year High-flow Event
Patrick Bayou Study Area

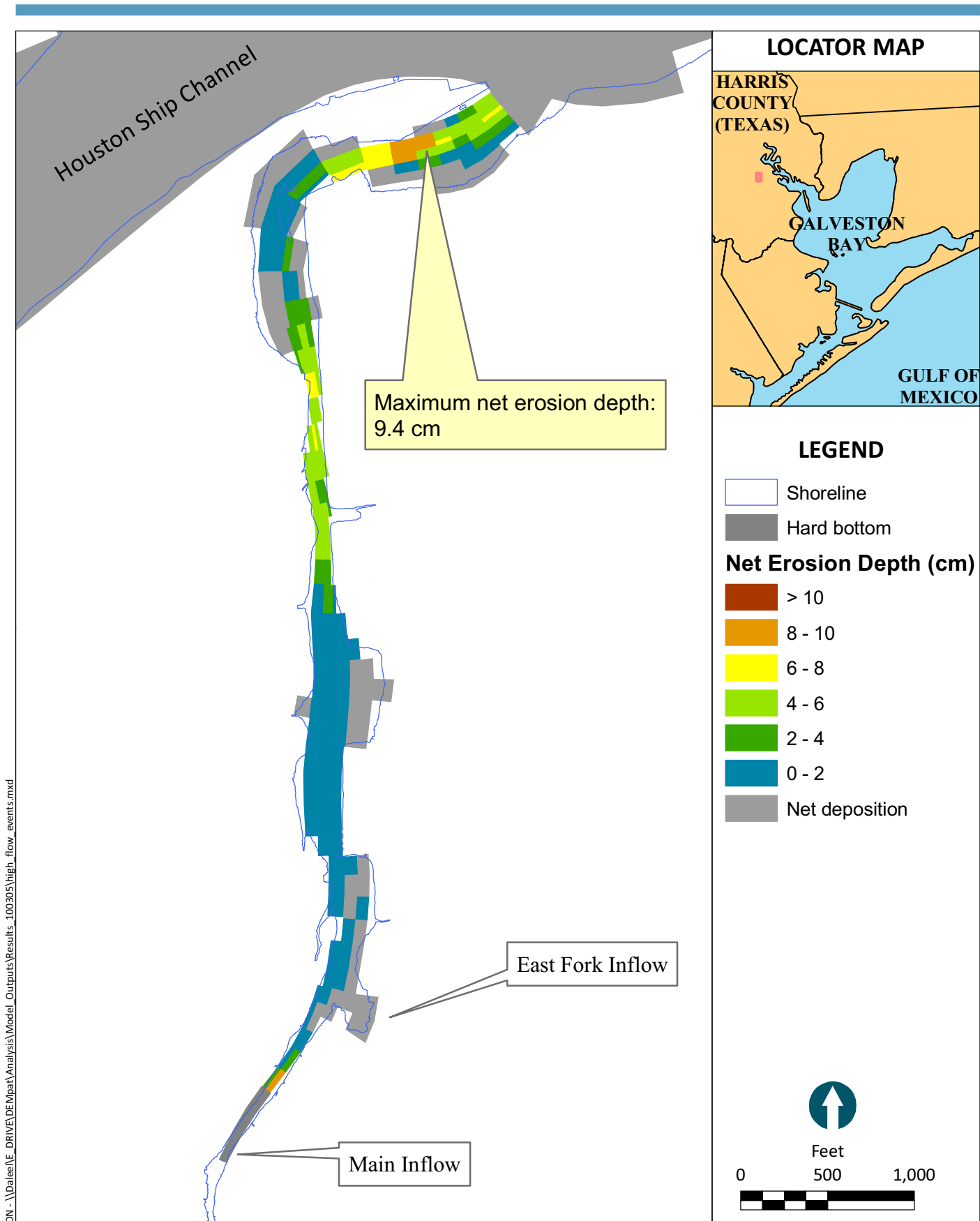


Figure 3-6

Spatial Distribution of Predicted Net Erosion Depth
During 100-year High-flow Event
Patrick Bayou Study Area

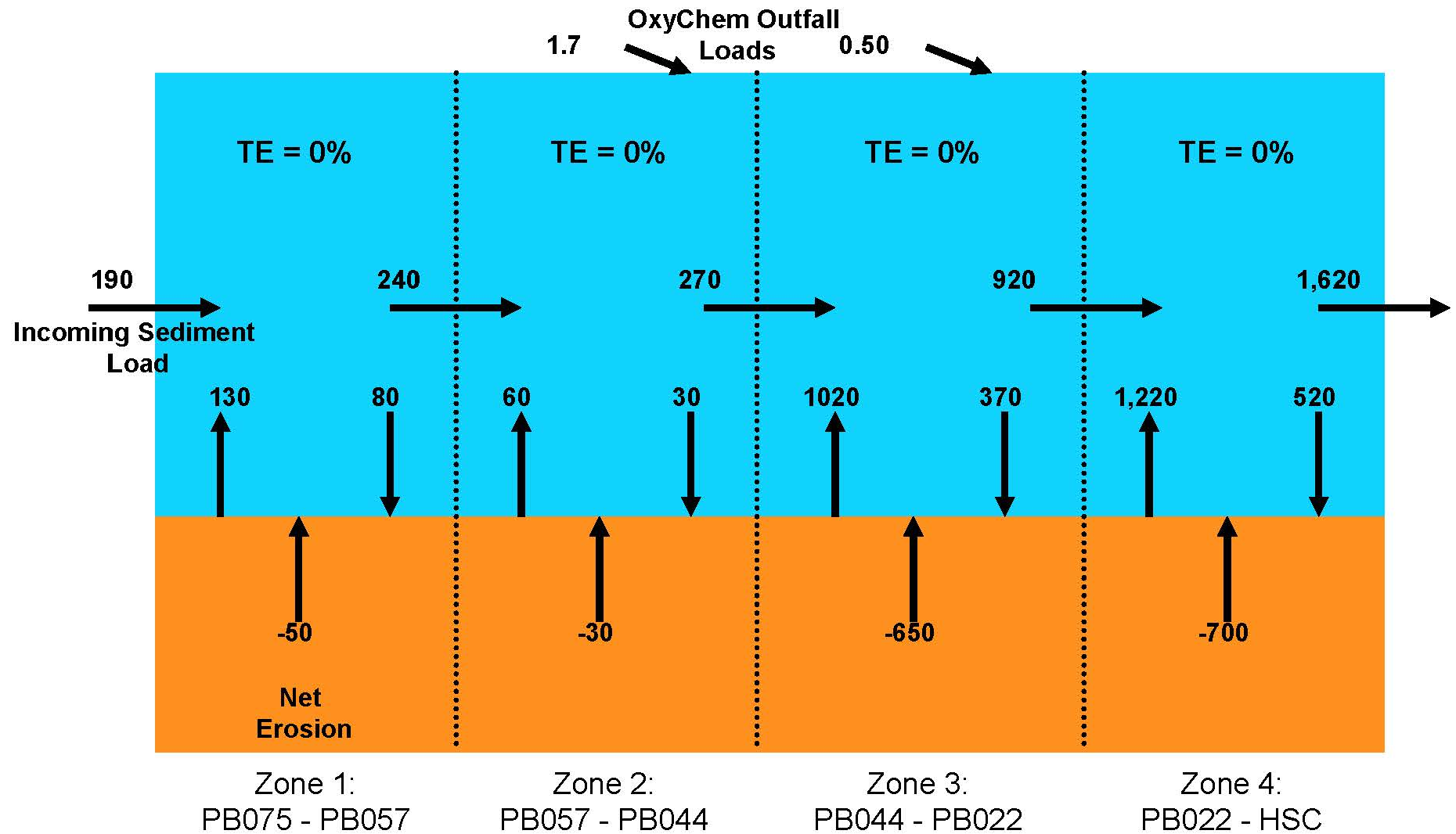


Figure 3-7

Predicted Sediment Mass Balance During 100-yr High-flow Event

Note: Mass units are metric tons. Trapping efficiency is percentage of incoming sediment load that is deposited within a reach.

Patrick Bayou Study Area

DN\\VKL-\\Dalee\\E_DRIVE\\DEM\\pat\\Analysis\\Model\\Inputs\\GRID\\grid_fine_rpt_100331.mxd

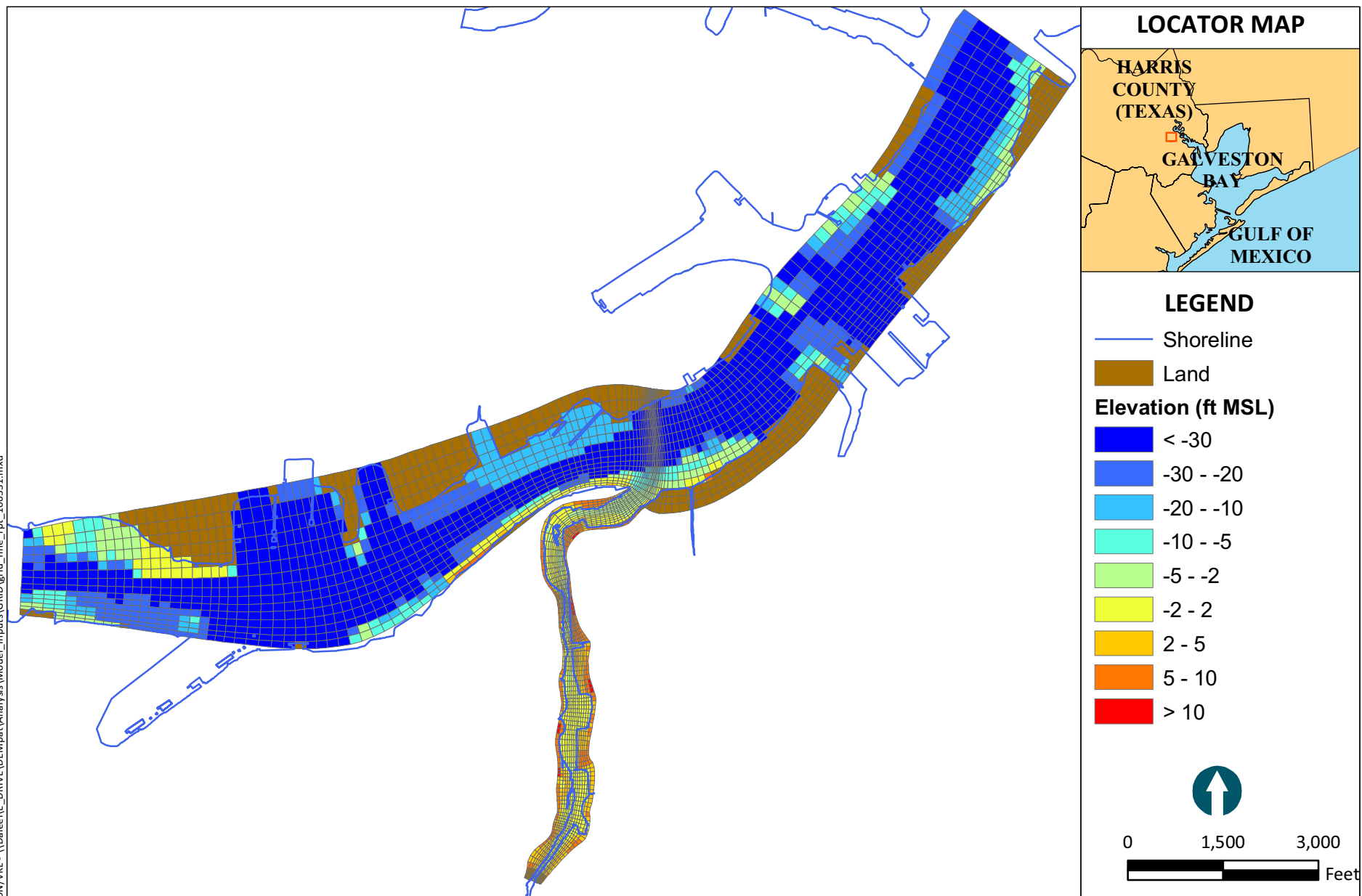
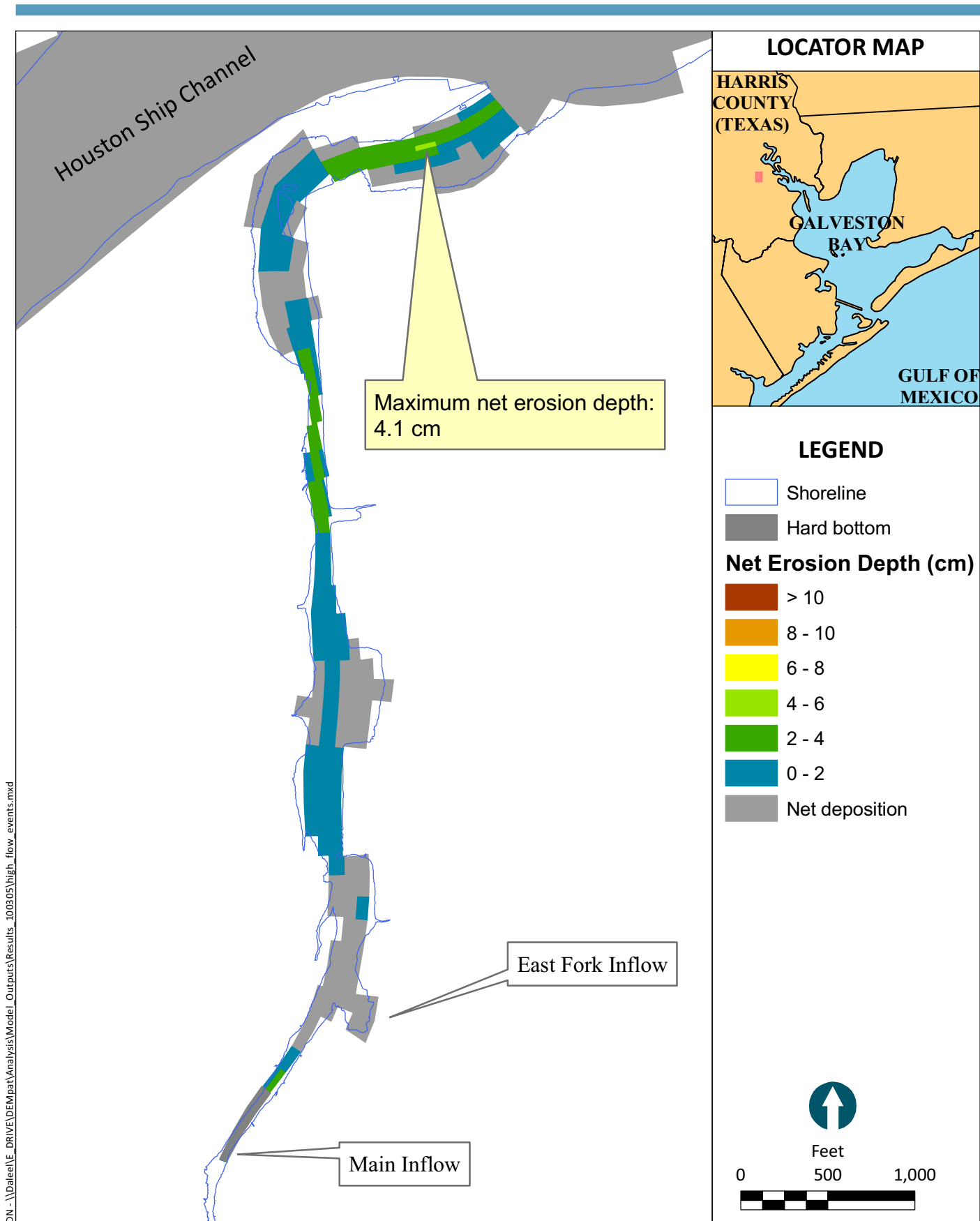


Figure 3-8

High-resolution Numerical Grid and Projected Bathymetry for Sensitivity Simulations
Patrick Bayou Study Area



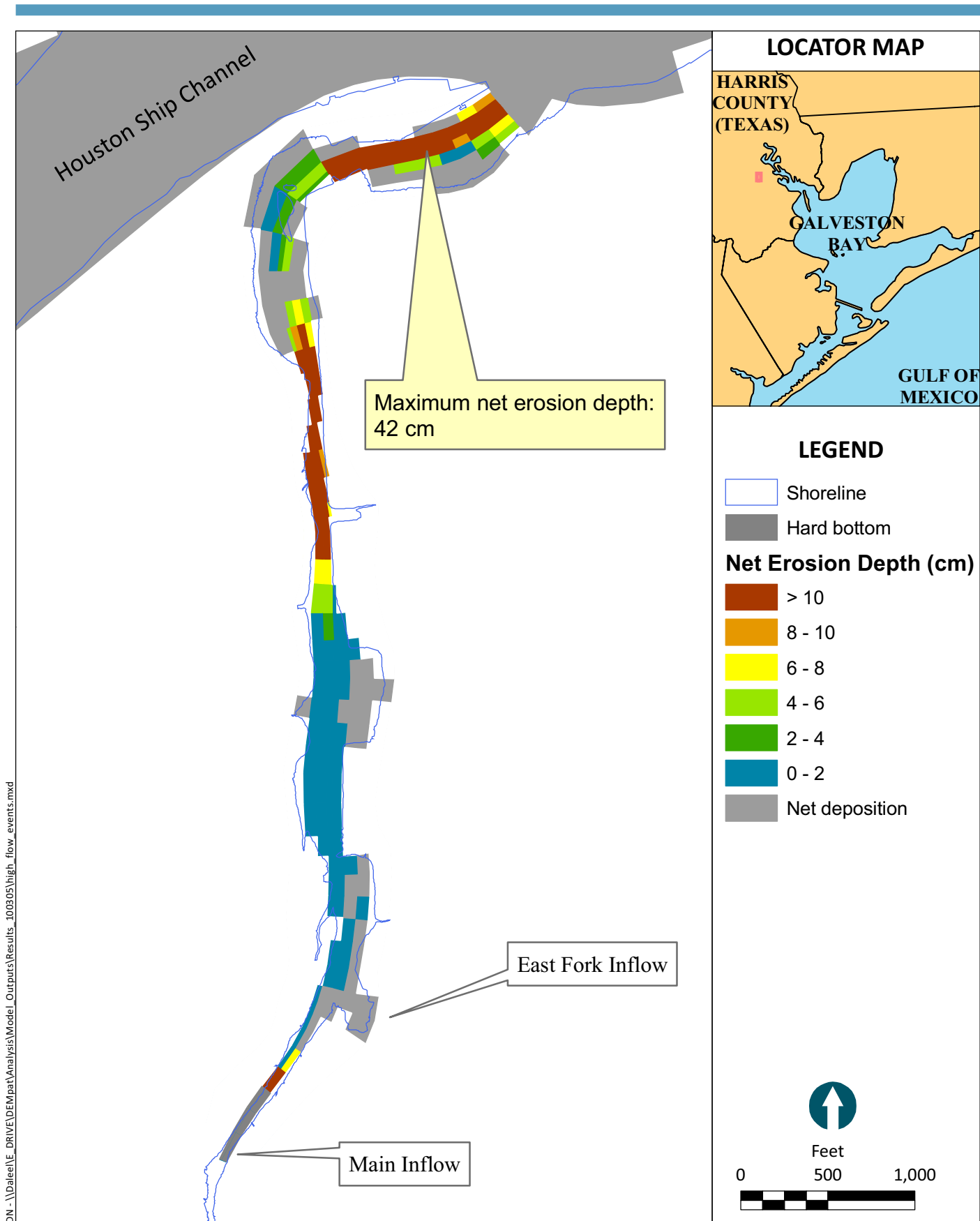


Figure 3-10

Spatial Distribution of Predicted Net Erosion Depth During 100-year High-flow Sensitivity Simulation: Upper-bound Erosion

Parameters

Patrick Bayou Study Area



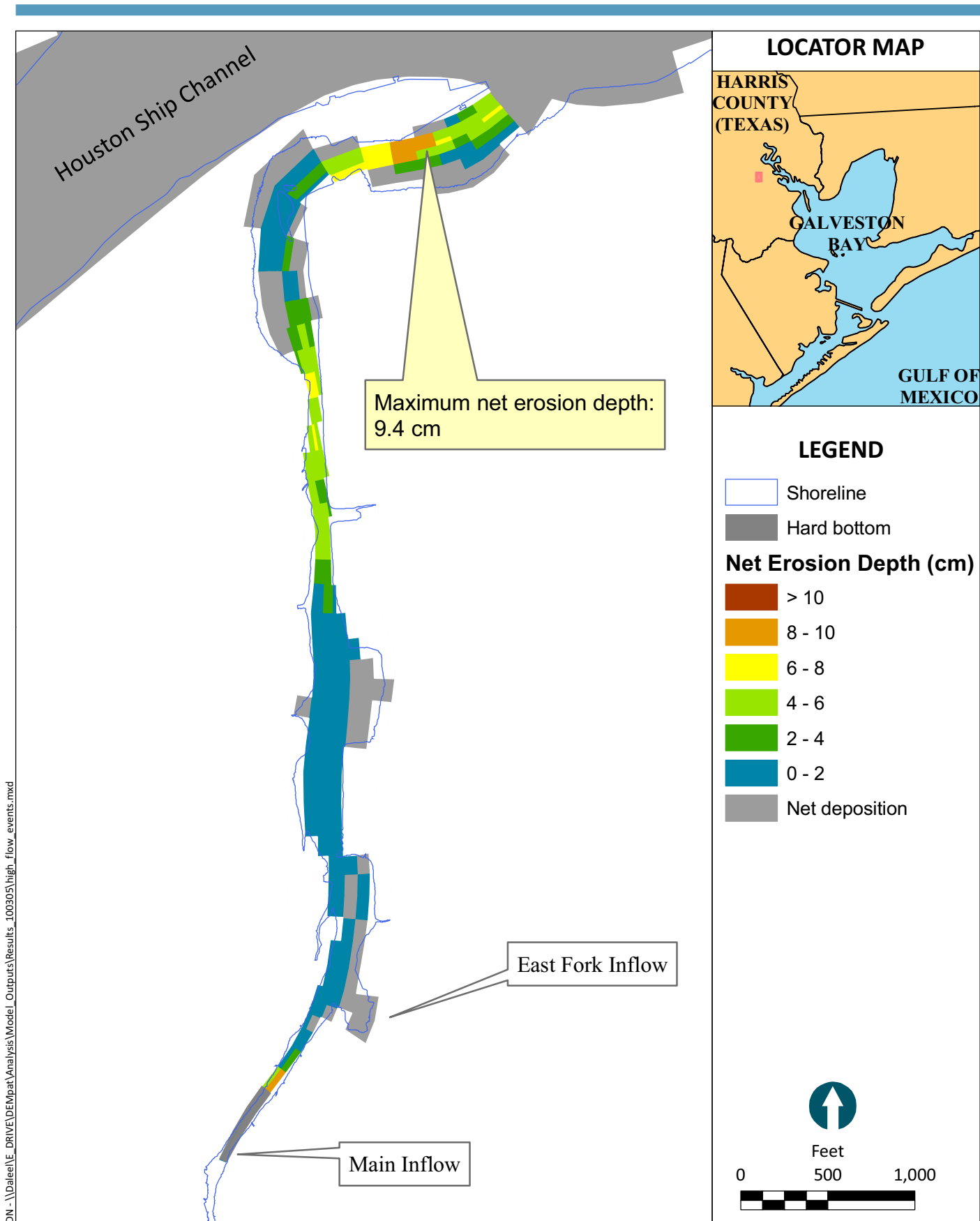


Figure 3-11

Spatial Distribution of Predicted Net Erosion Depth During 100-year High-flow Sensitivity Simulation: Lower-bound Upstream Sediment Load

Patrick Bayou Study Area



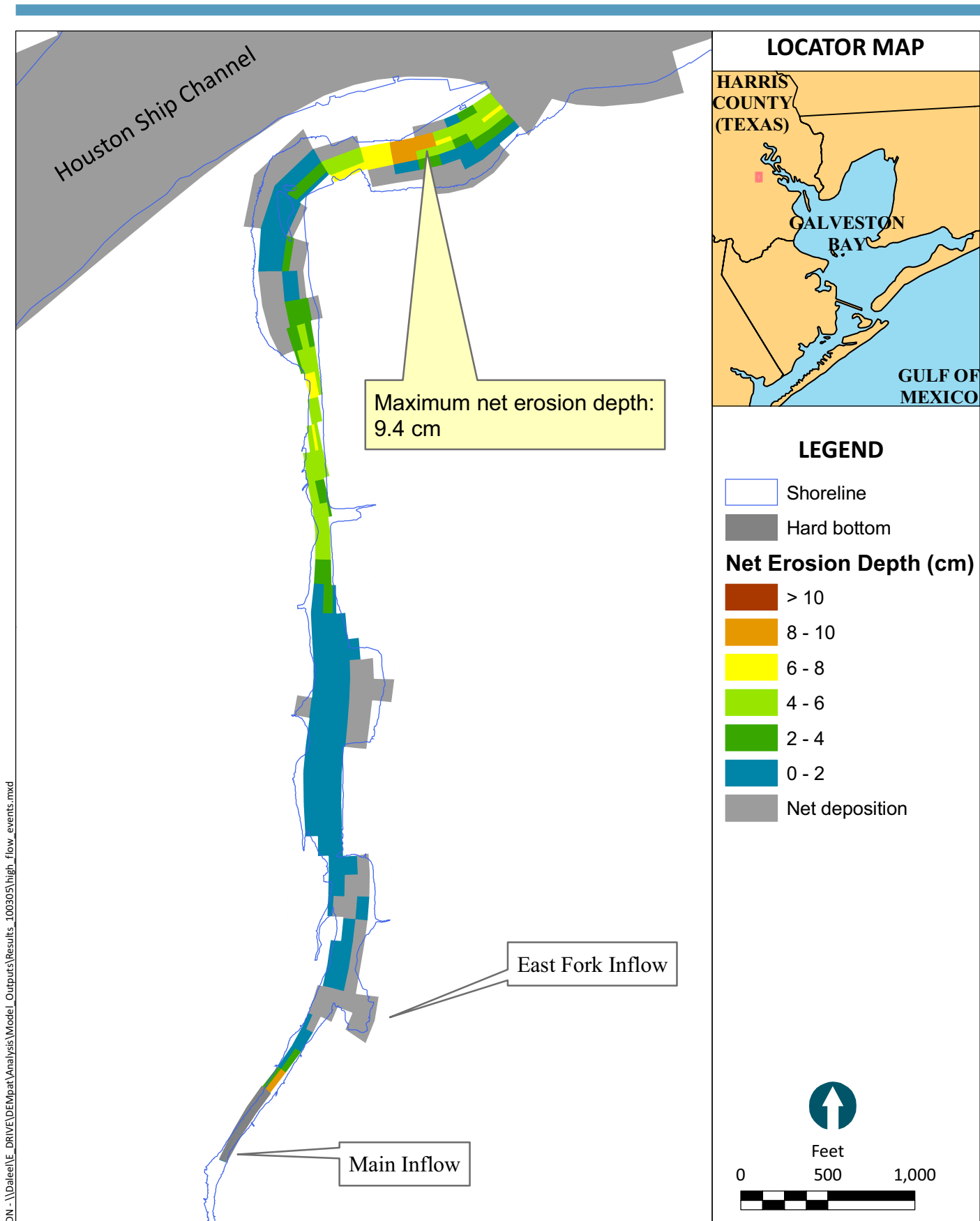


Figure 3-12

Spatial Distribution of Predicted Net Erosion Depth During 100-year High-flow Sensitivity Simulation: Upper-bound Upstream Sediment Load
Patrick Bayou Study Area

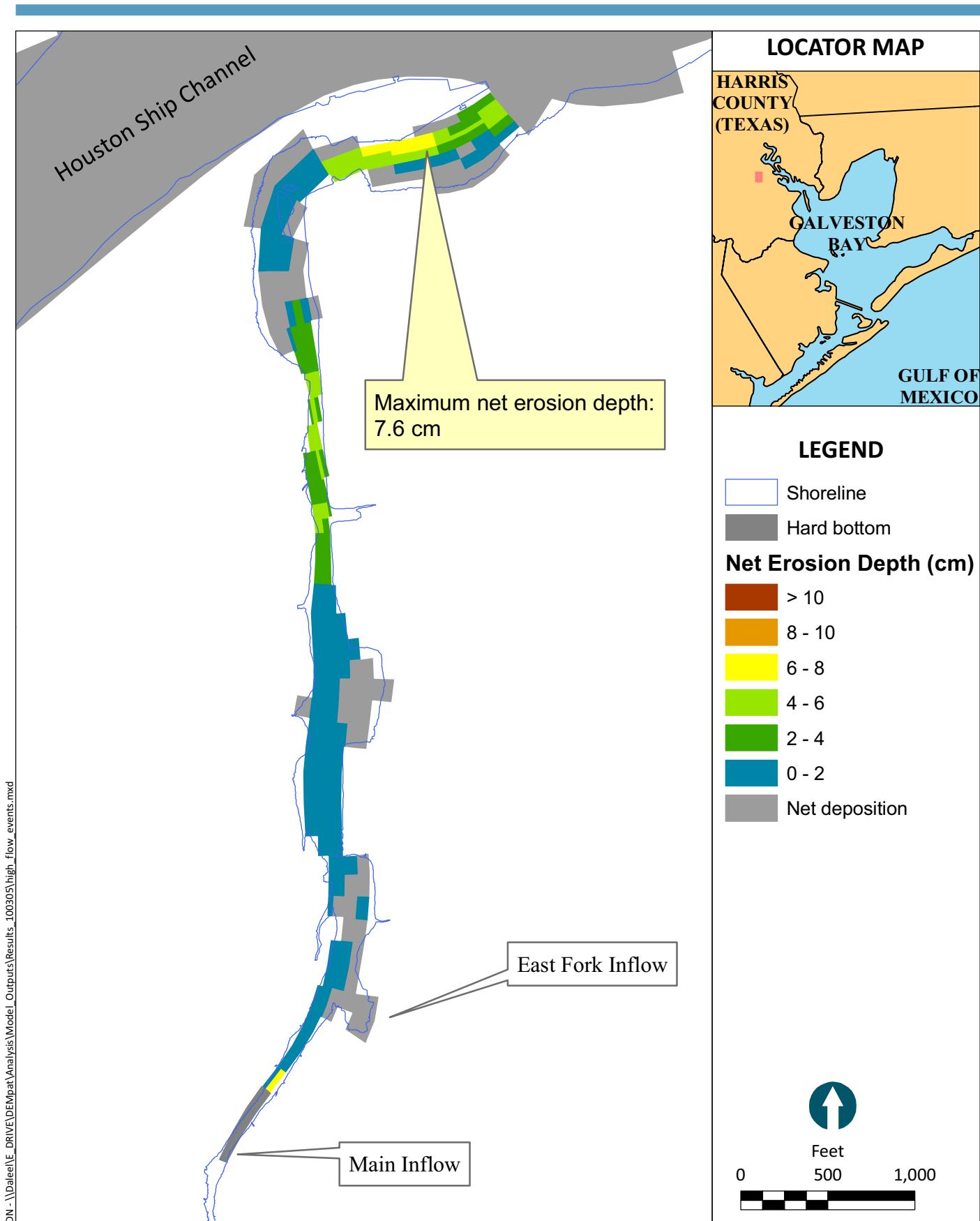


Figure 3-13

Spatial Distribution of Predicted Net Erosion Depth During
100-year High-flow Sensitivity Simulation: Lower-bound
Effective Bed Roughness Height
Patrick Bayou Study Area

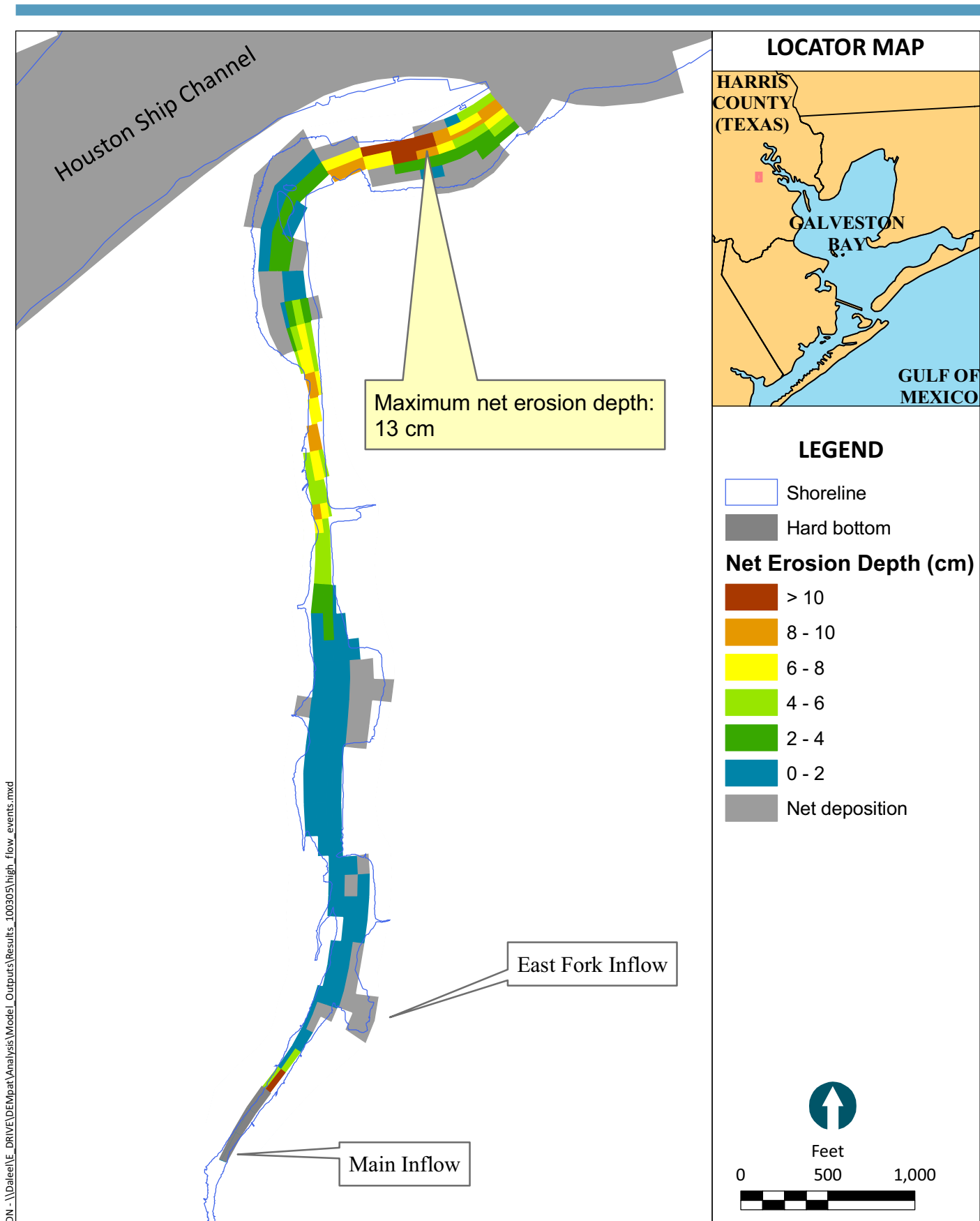


Figure 3-14

Spatial Distribution of Predicted Net Erosion Depth During 100-year High-flow Sensitivity Simulation: Upper-bound Effective Bed Roughness Height
Patrick Bayou Study Area



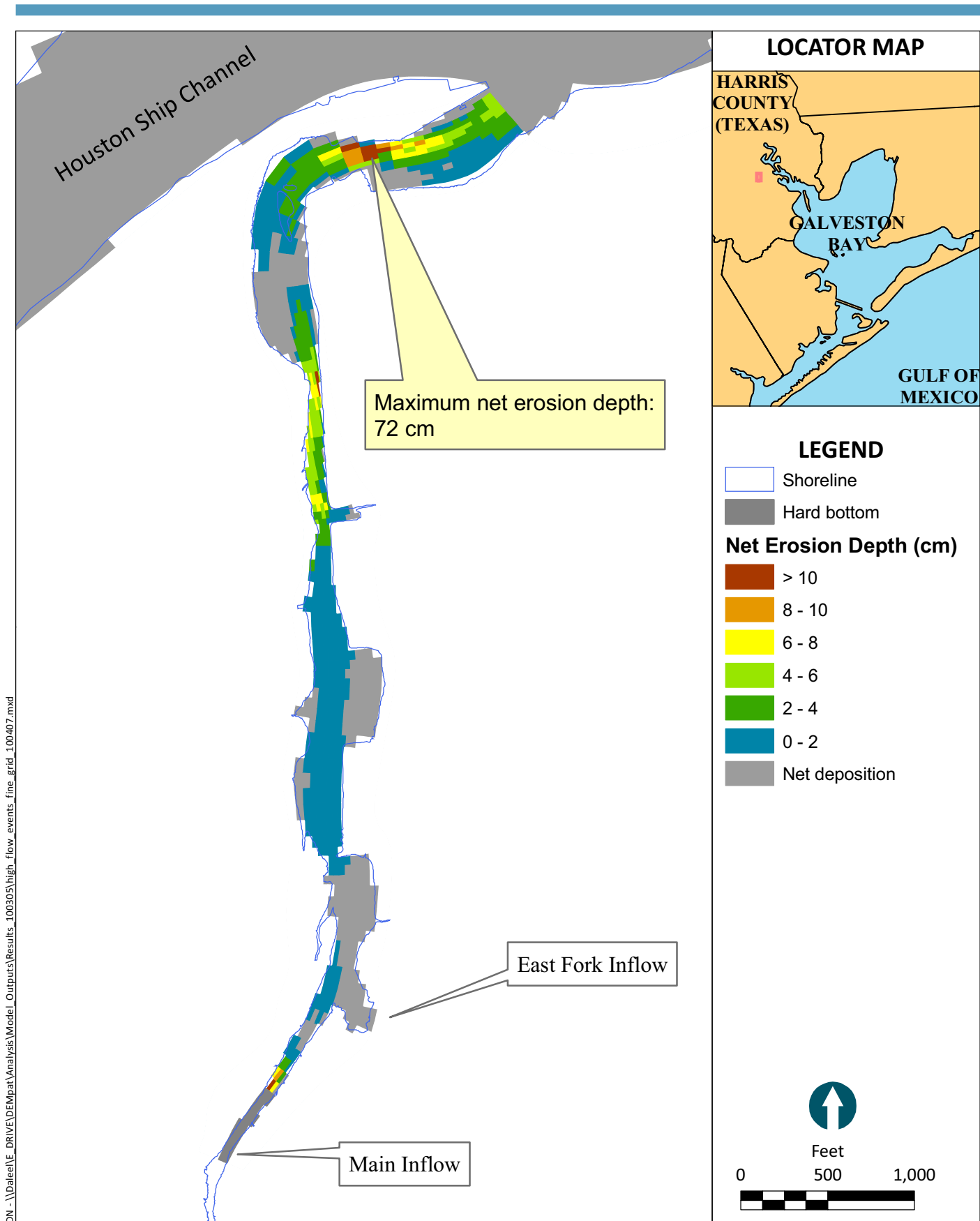


Figure 3-15

Spatial Distribution of Predicted Net Erosion Depth During 100-year High-flow Sensitivity Simulation: High-resolution Grid
Patrick Bayou Study Area

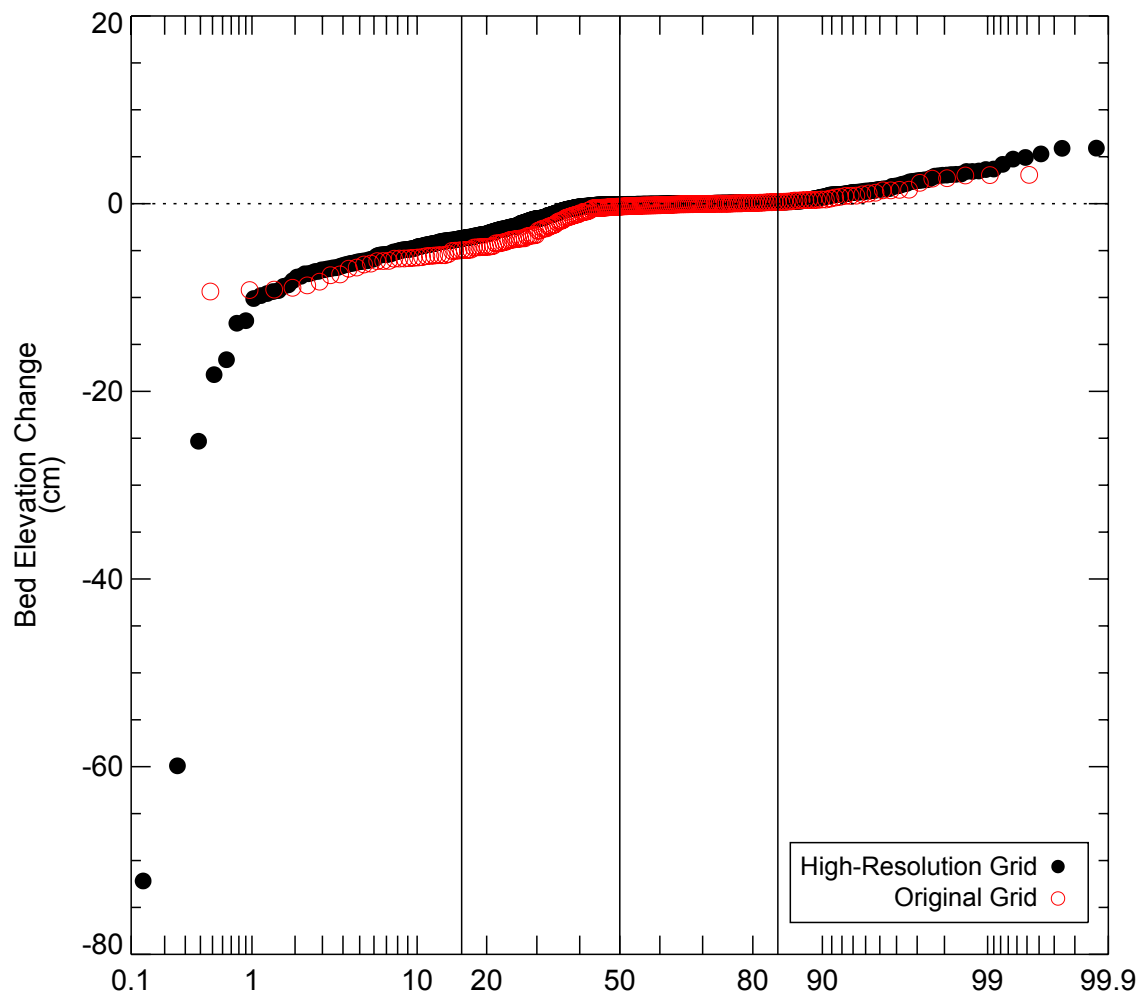


Figure 3-16
 Cumulative Frequency Distribution of Bed Elevation Change During 100-year Flood
 Simulation for Original and High-resolution Grids
 Note: Results shown only in the study area and channel
 Patrick Bayou Study Area

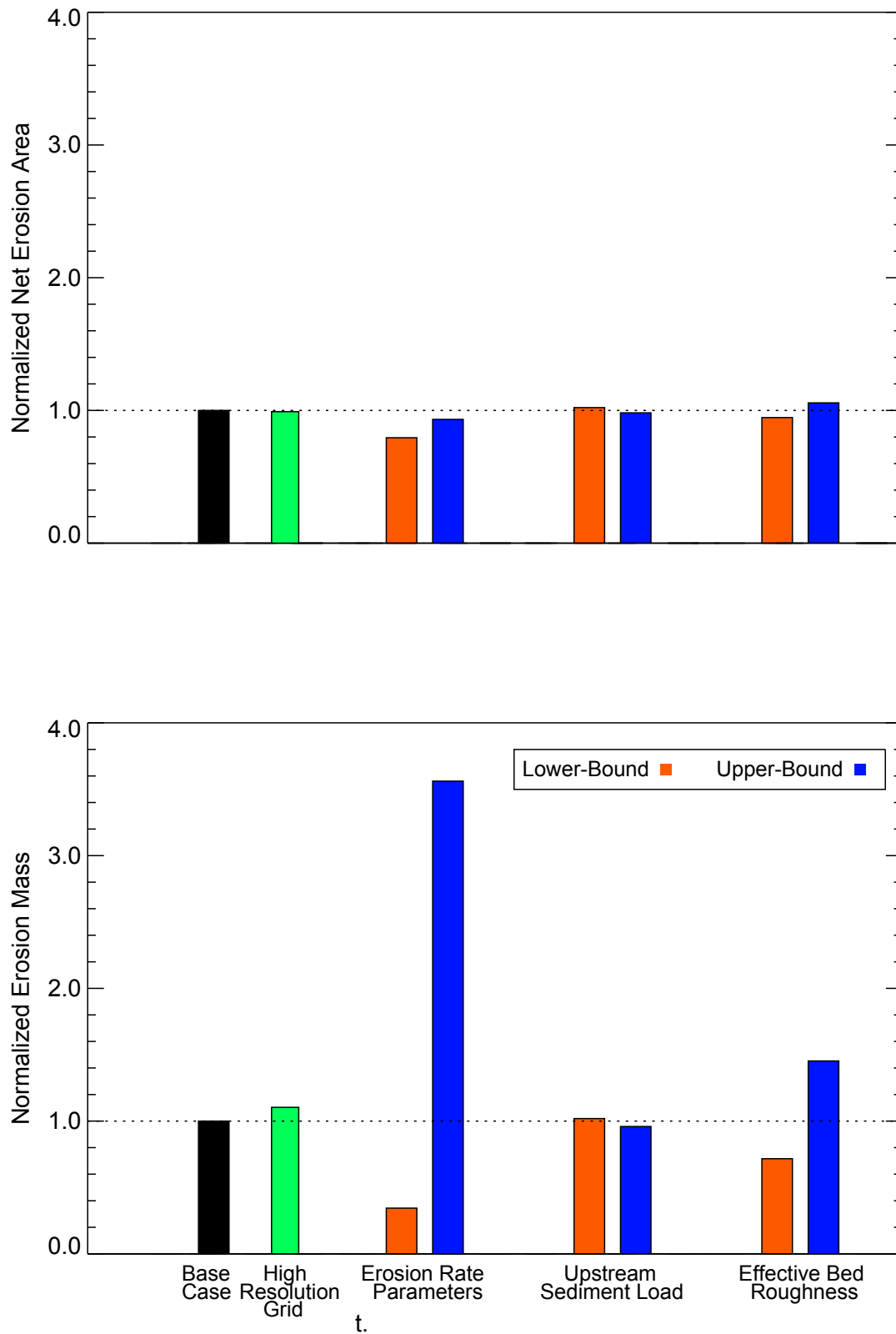
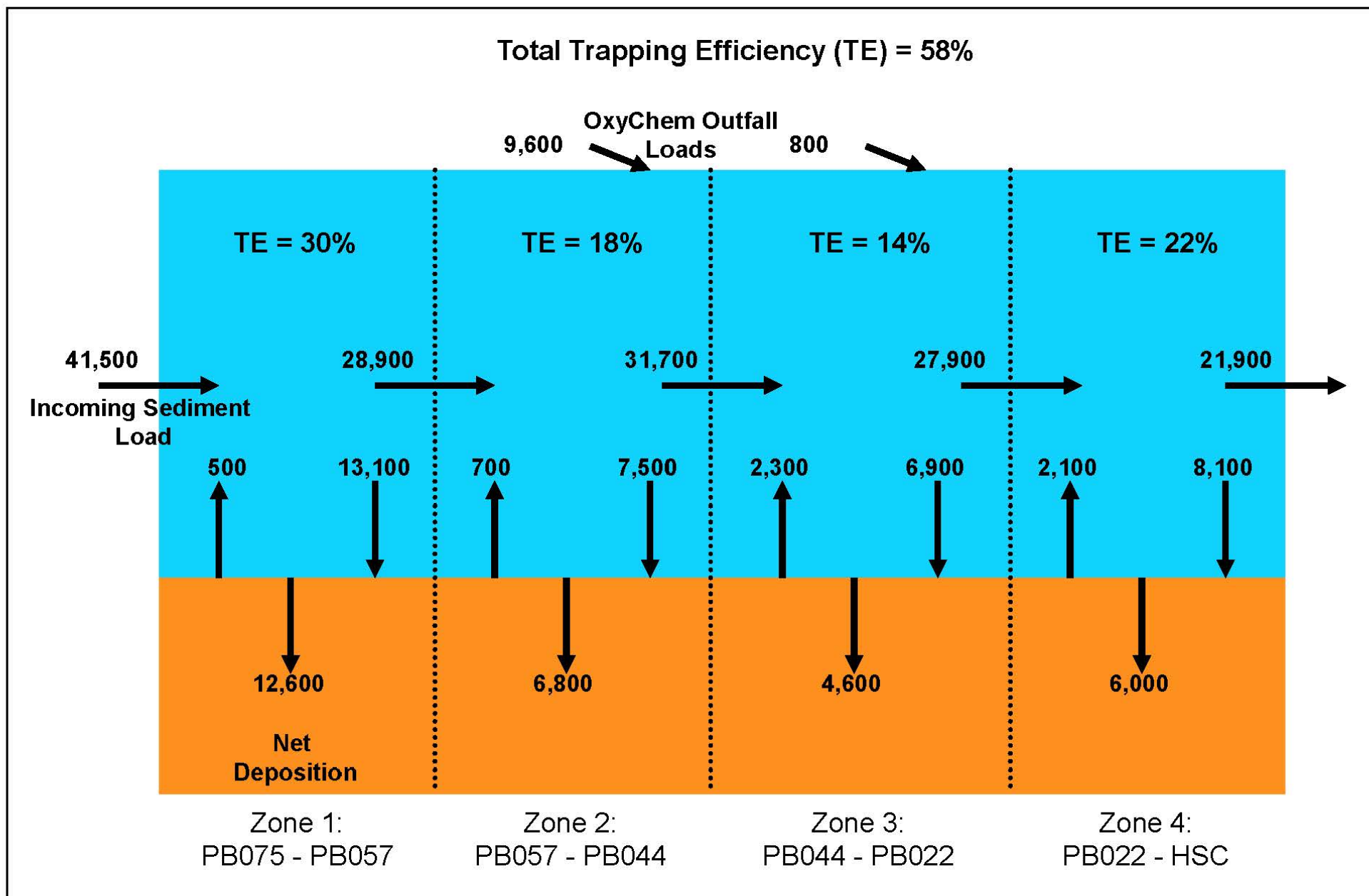
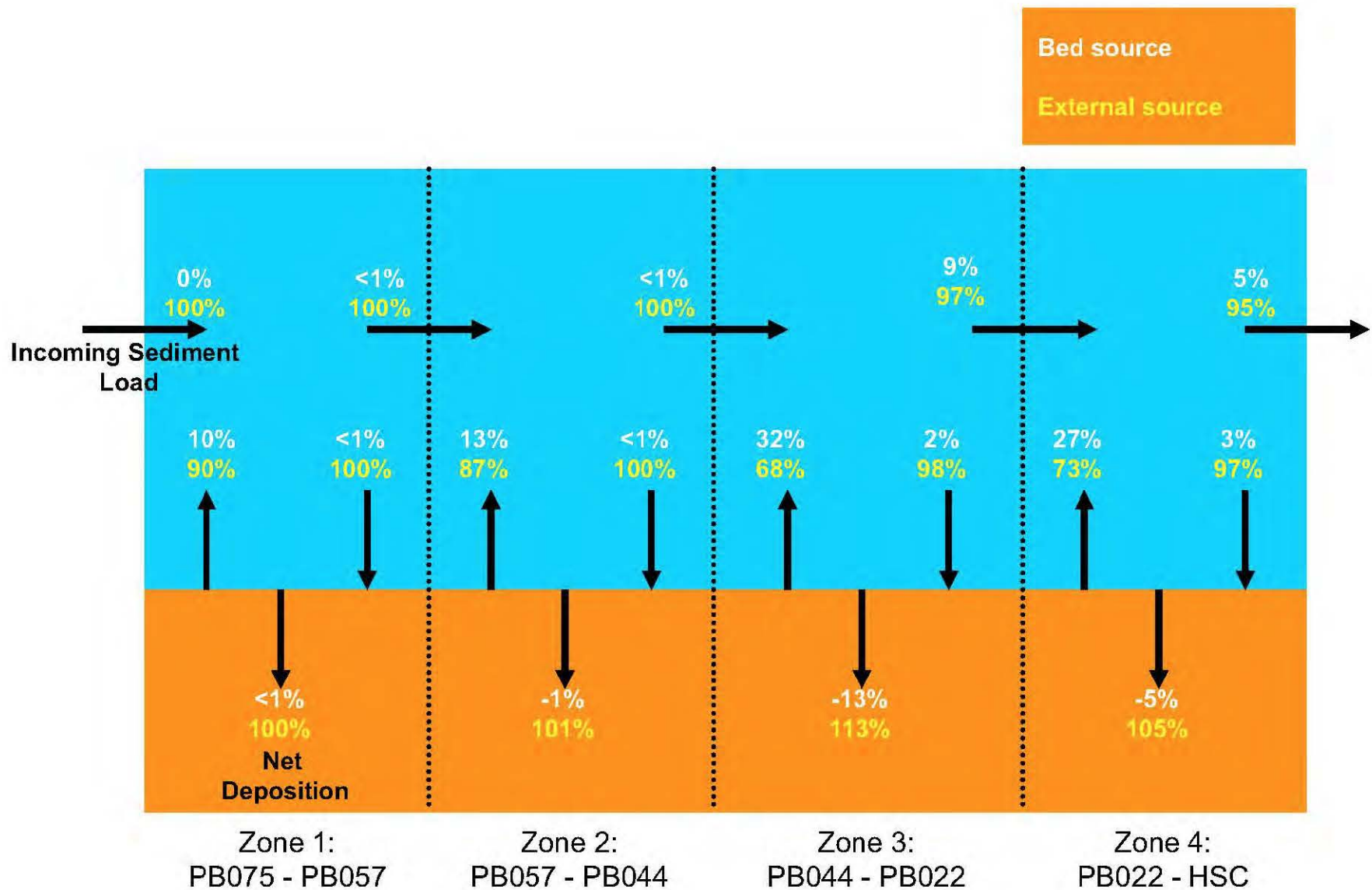
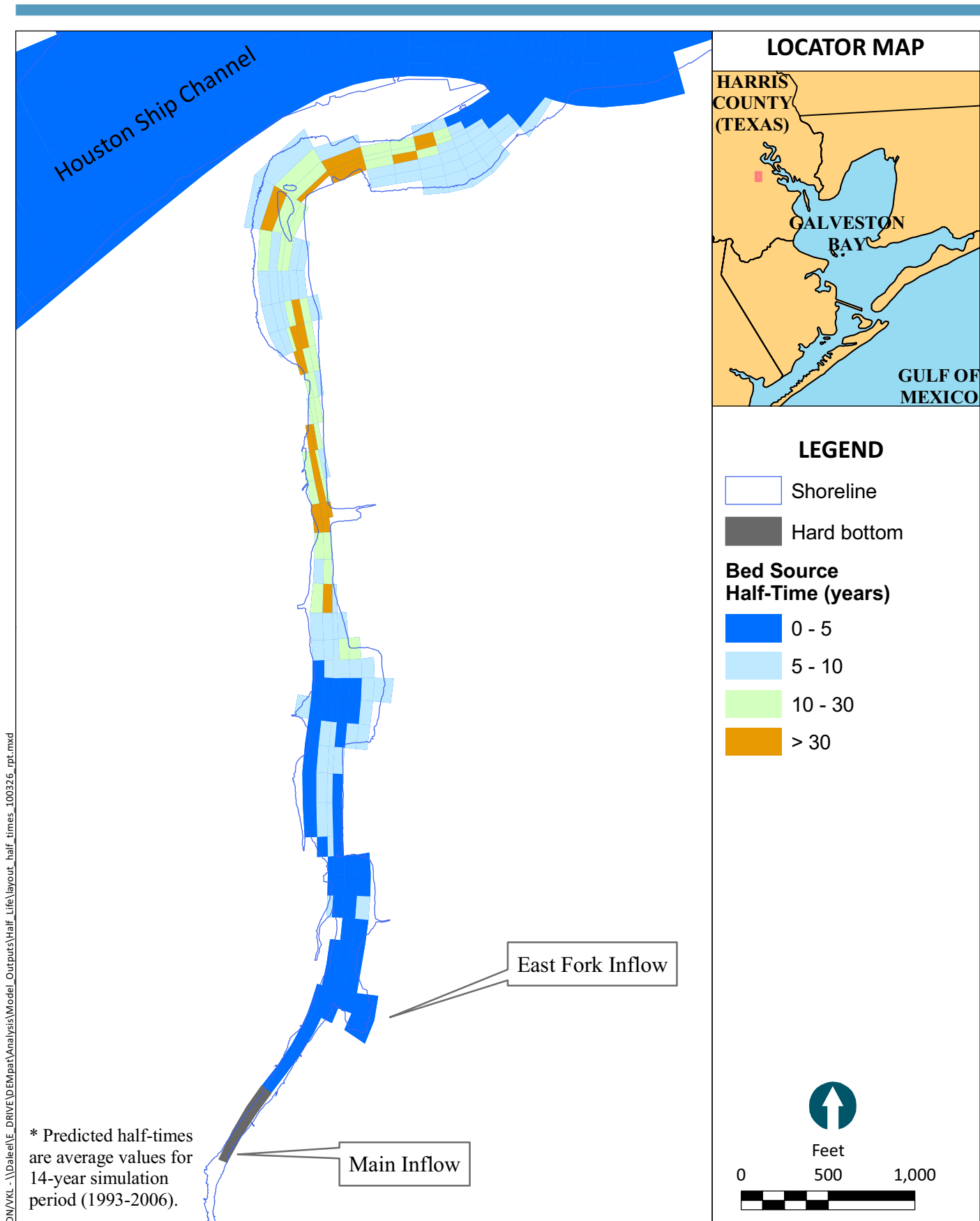


Figure 3-17
 Comparison of Normalized Net Erosion Area and Net Erosion Mass for Base Case and Sensitivity Simulations During 100-year high-Flow Event
 Patrick Bayou Study Area







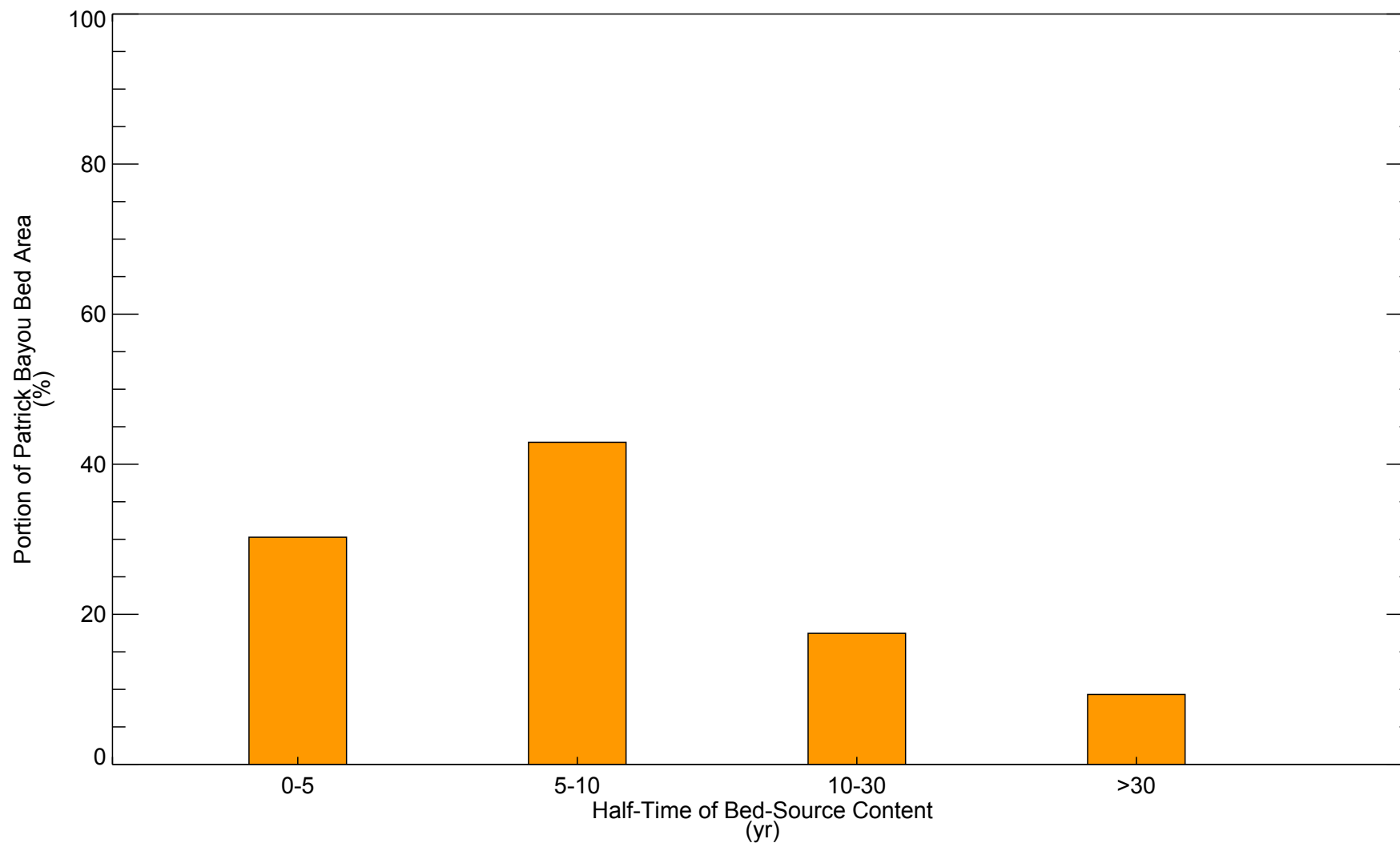


Figure 3-21
Areal Distribution of Predicted Half-time of Bed-source Sediment in Mixing-zone Layer (0-10 cm)
Patrick Bayou Study Area

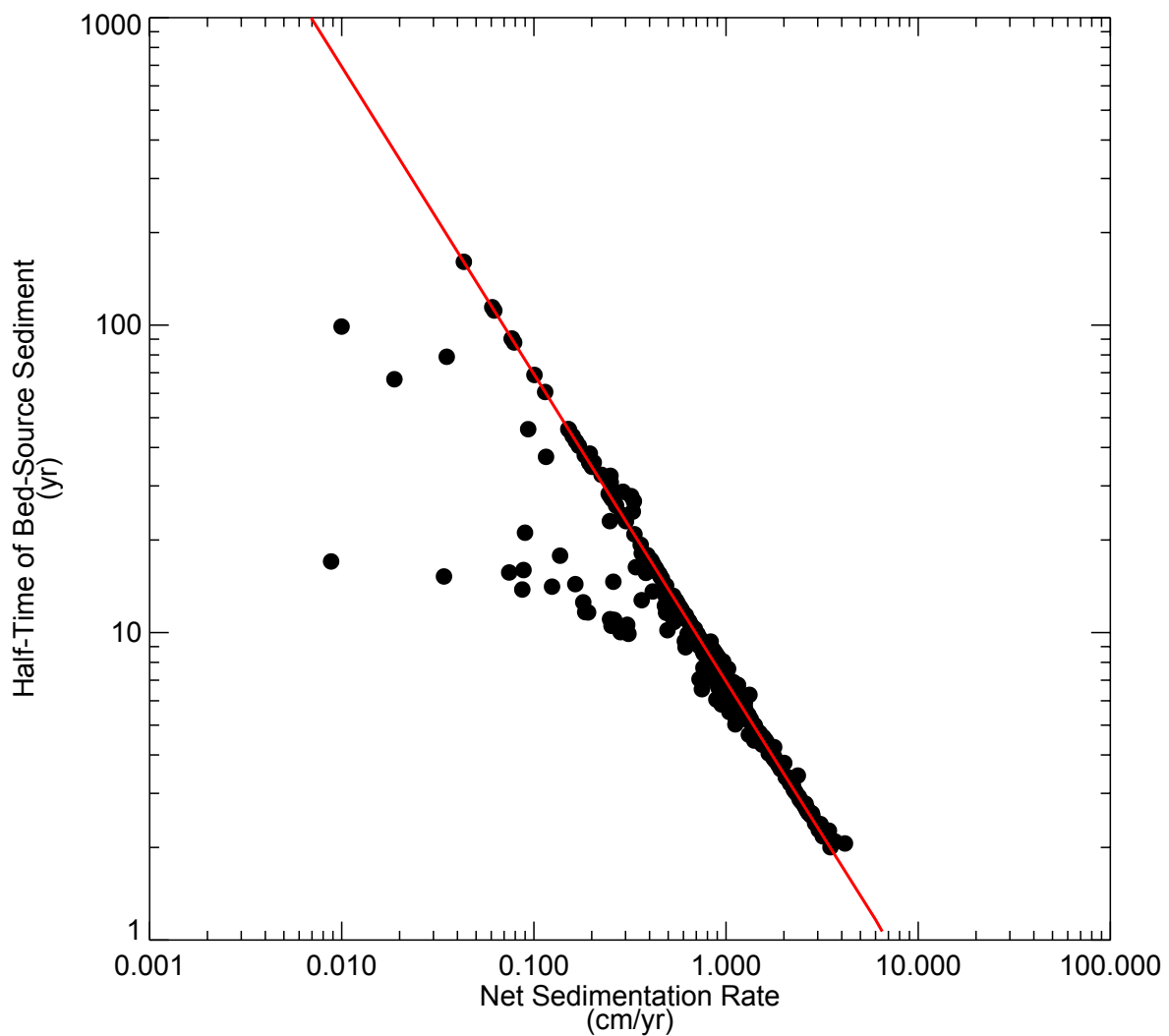


Figure 3-22
 Relationship Between Predicted Net Sedimentation Rate and Half-time of Bed-source
 Sediment in Mixing Zone Layer
 Note: Red line is theoretical relationship based on exponential decrease due to deposition
 Patrick Bayou Study Area

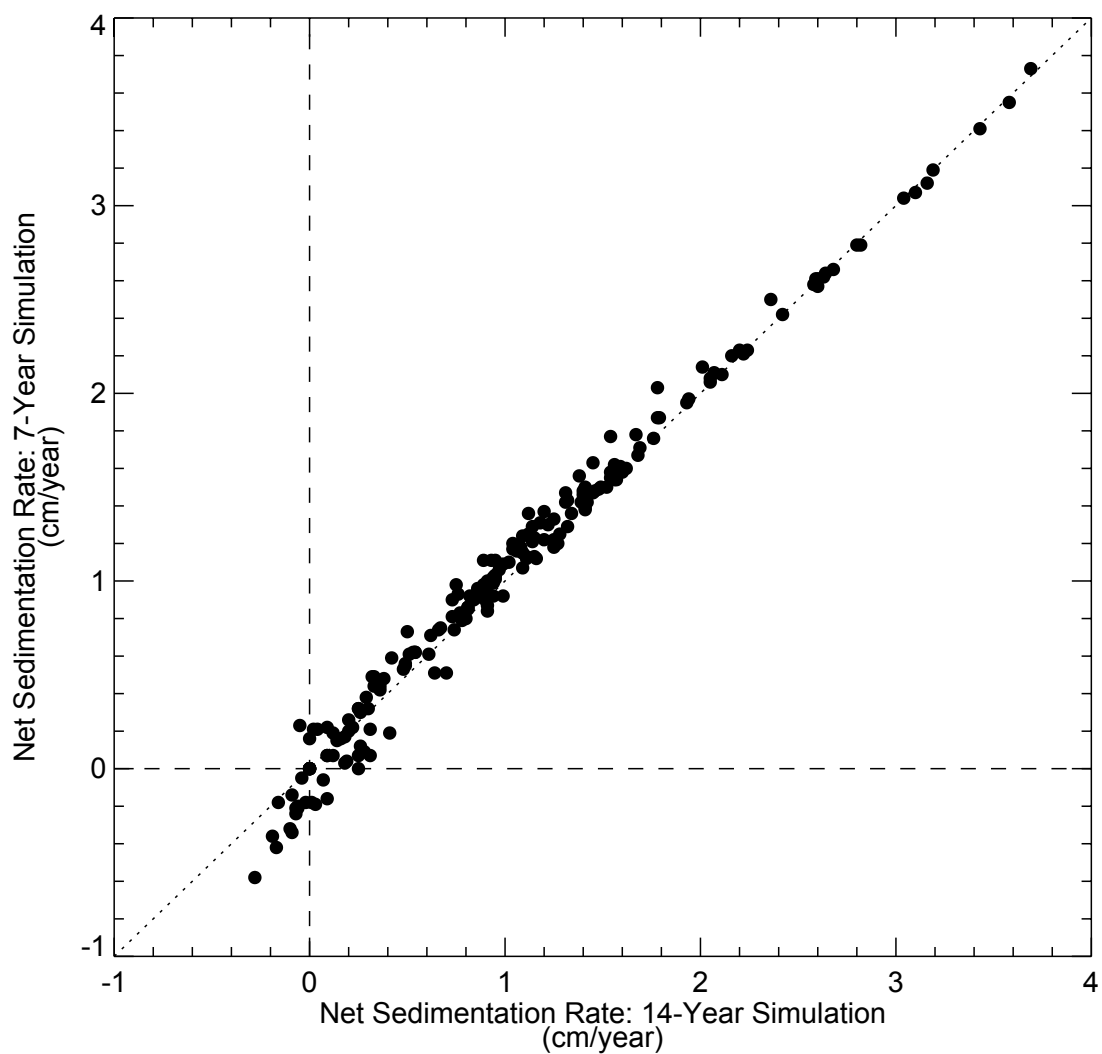


Figure 3-23
Comparison of Predicted Net Sedimentation Rates at End of 7- and 14-year
Simulations Periods
Patrick Bayou Study Area

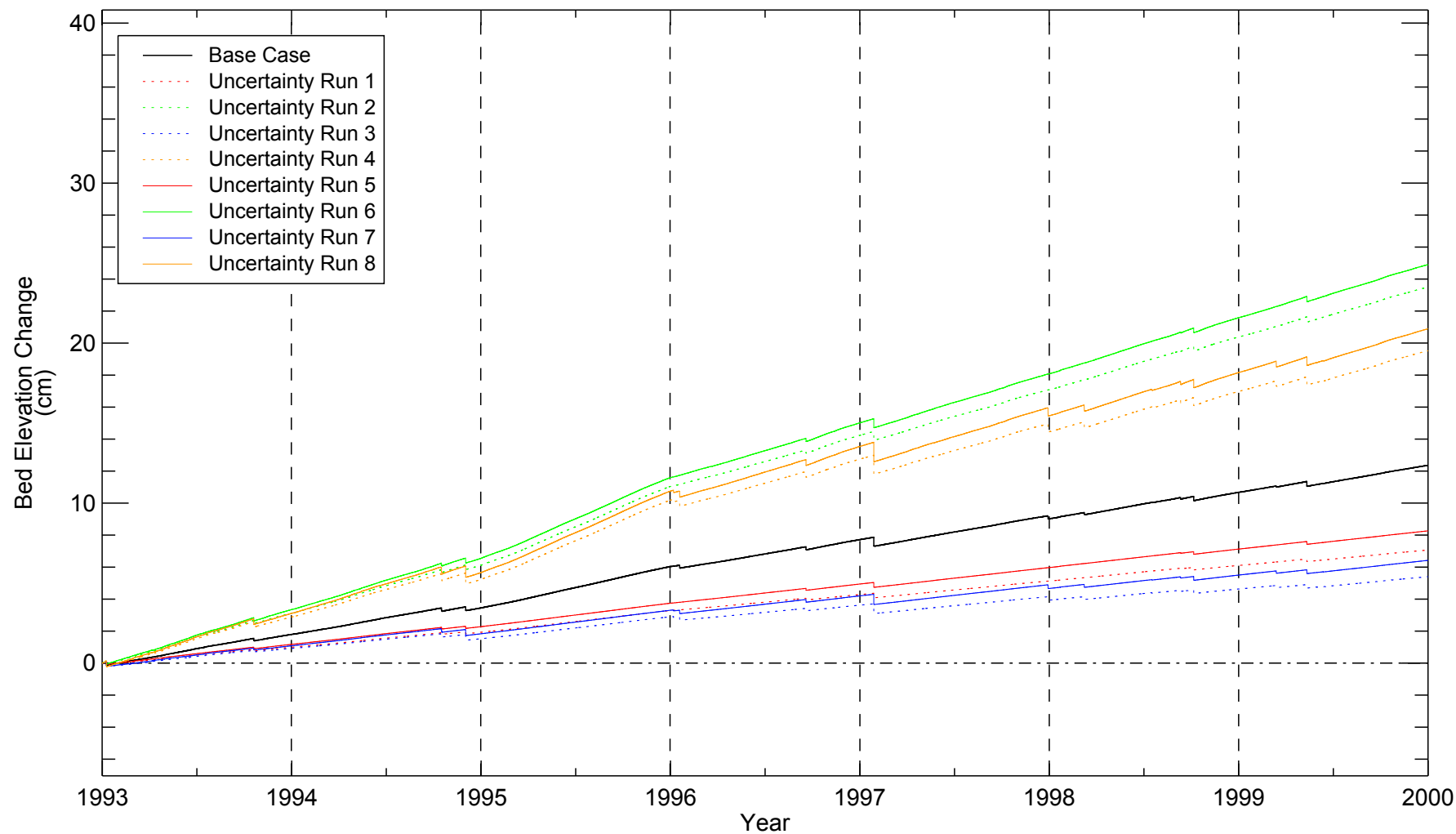


Figure 3-24

Time Histories of Predicted Bed Elevation Change at Station PB003 for Base-case and Uncertainty Simulations
Patrick Bayou Study Area

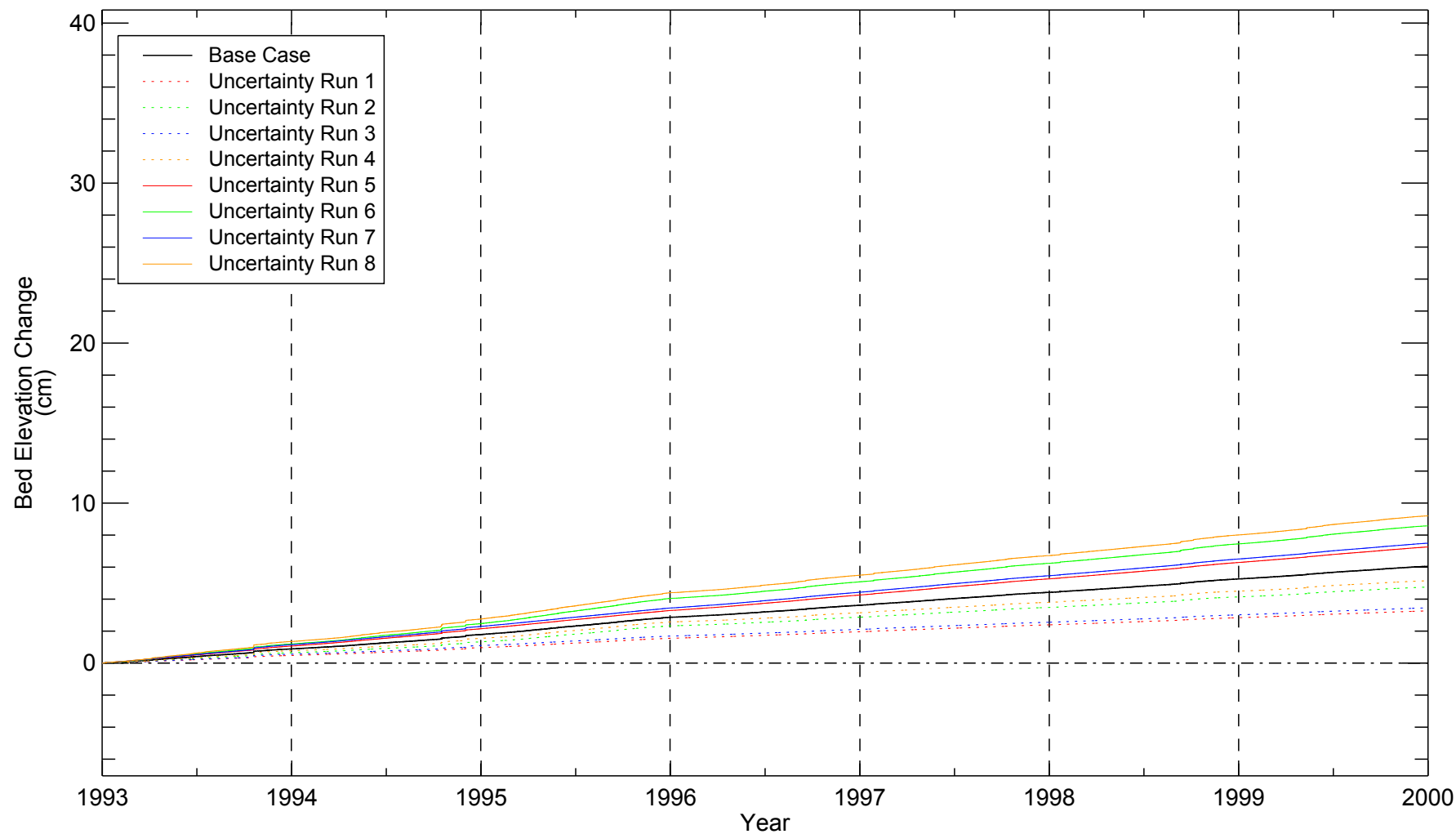


Figure 3-25
Time Histories of Predicted Bed Elevation Change at Station PB006 for Base-case and
Uncertainty Simulations
Patrick Bayou Study Area

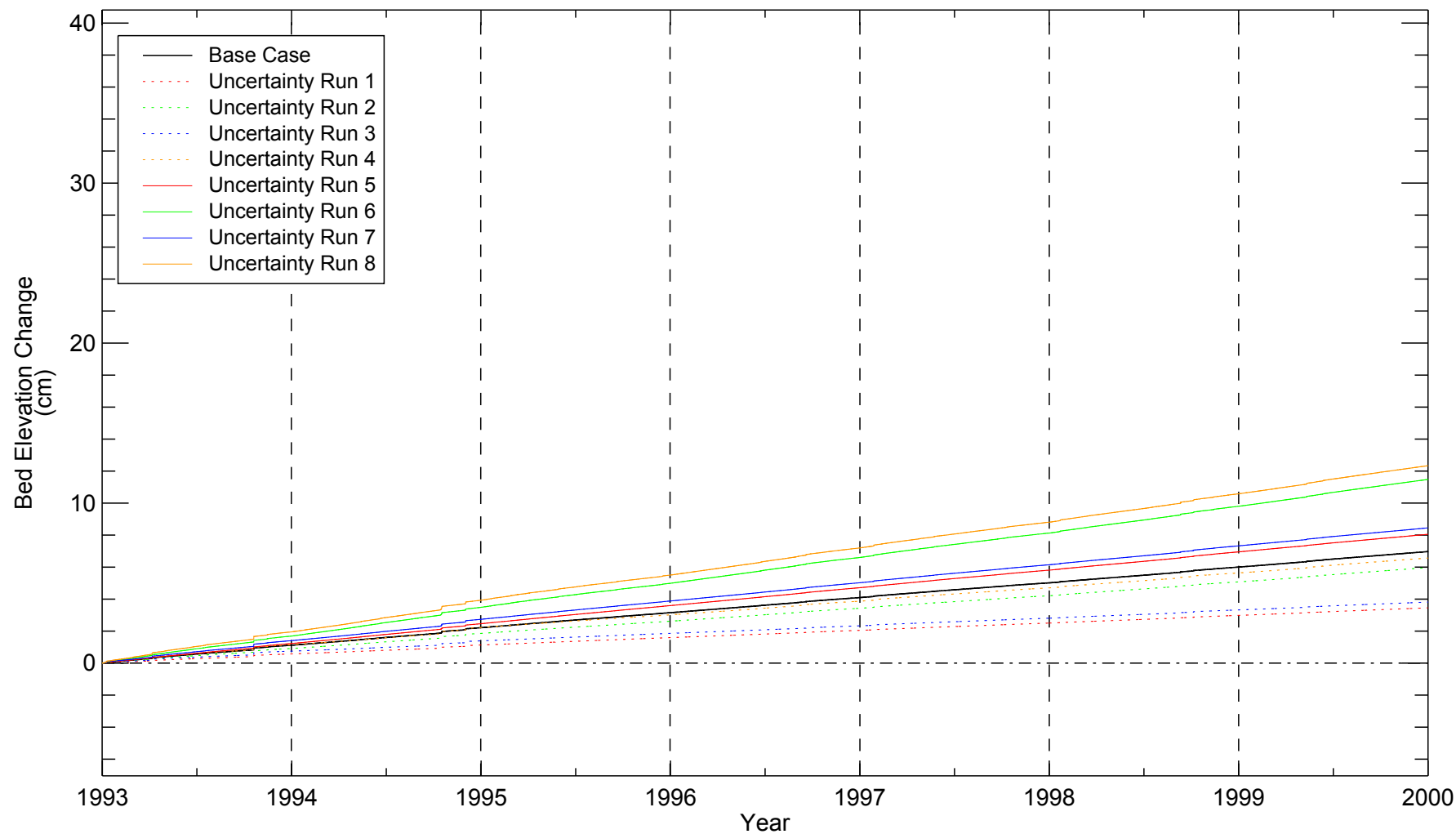


Figure 3-26
Time Histories of Predicted Bed Elevation Change at Station PB016 for Base-case and
Uncertainty Simulations
Patrick Bayou Study Area

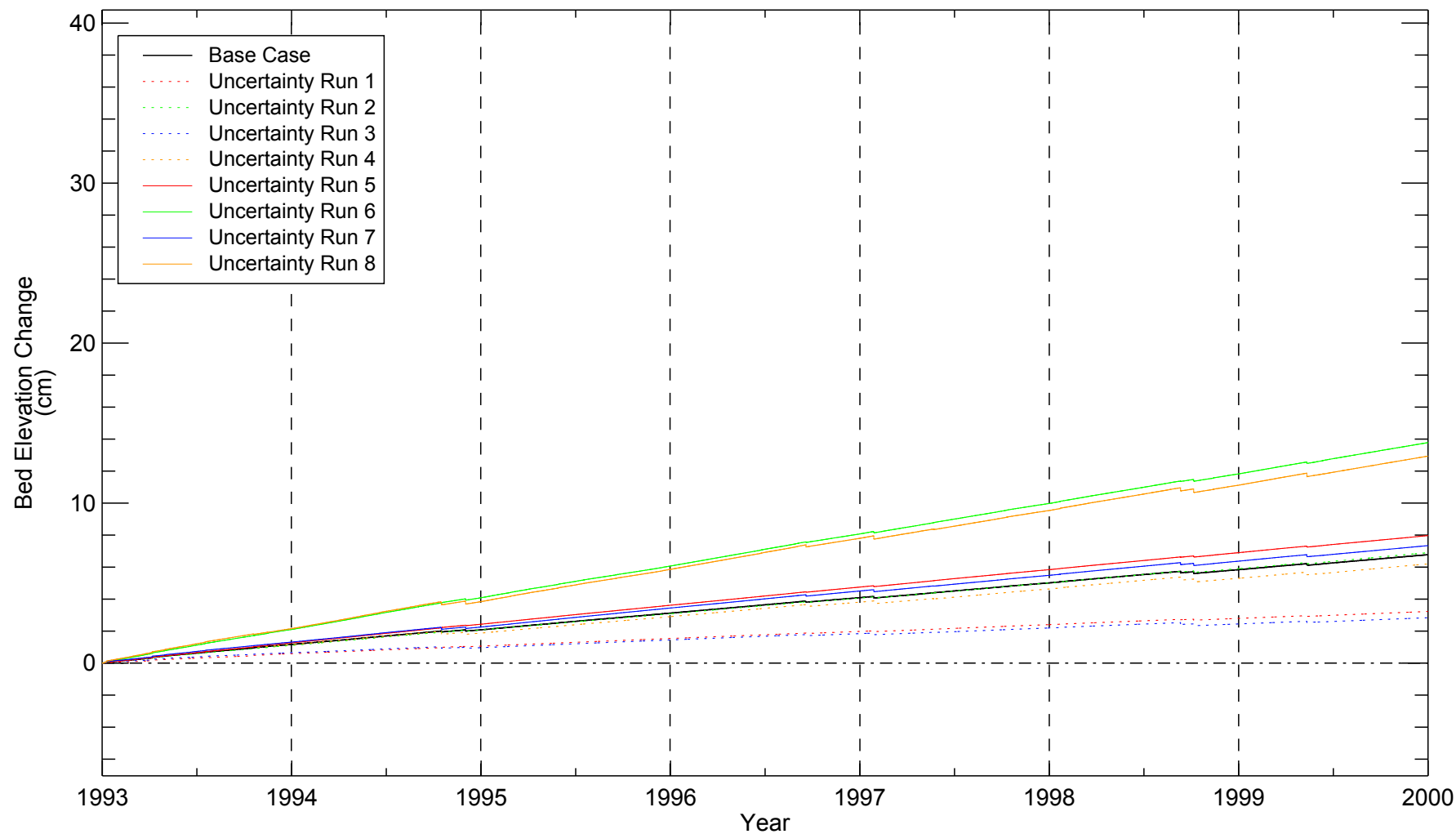


Figure 3-27
Time Histories of Predicted Bed Elevation Change at Station PB022 for Base-case
and Uncertainty Simulations
Patrick Bayou Study Area

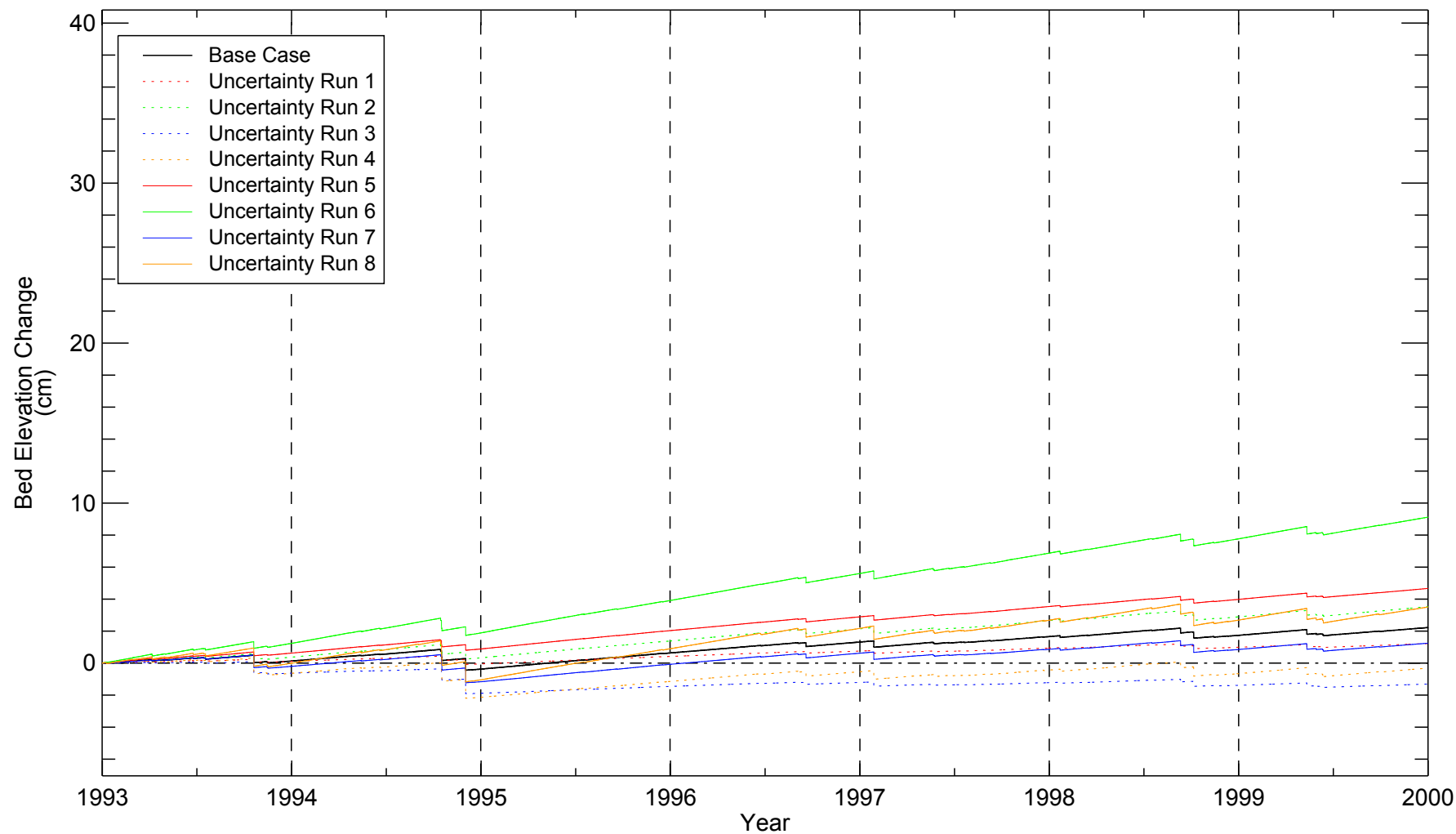


Figure 3-28
Time Histories of Predicted Bed Elevation Change at Station PB025 for Base-
case and Uncertainty Simulations
Patrick Bayou Study Area

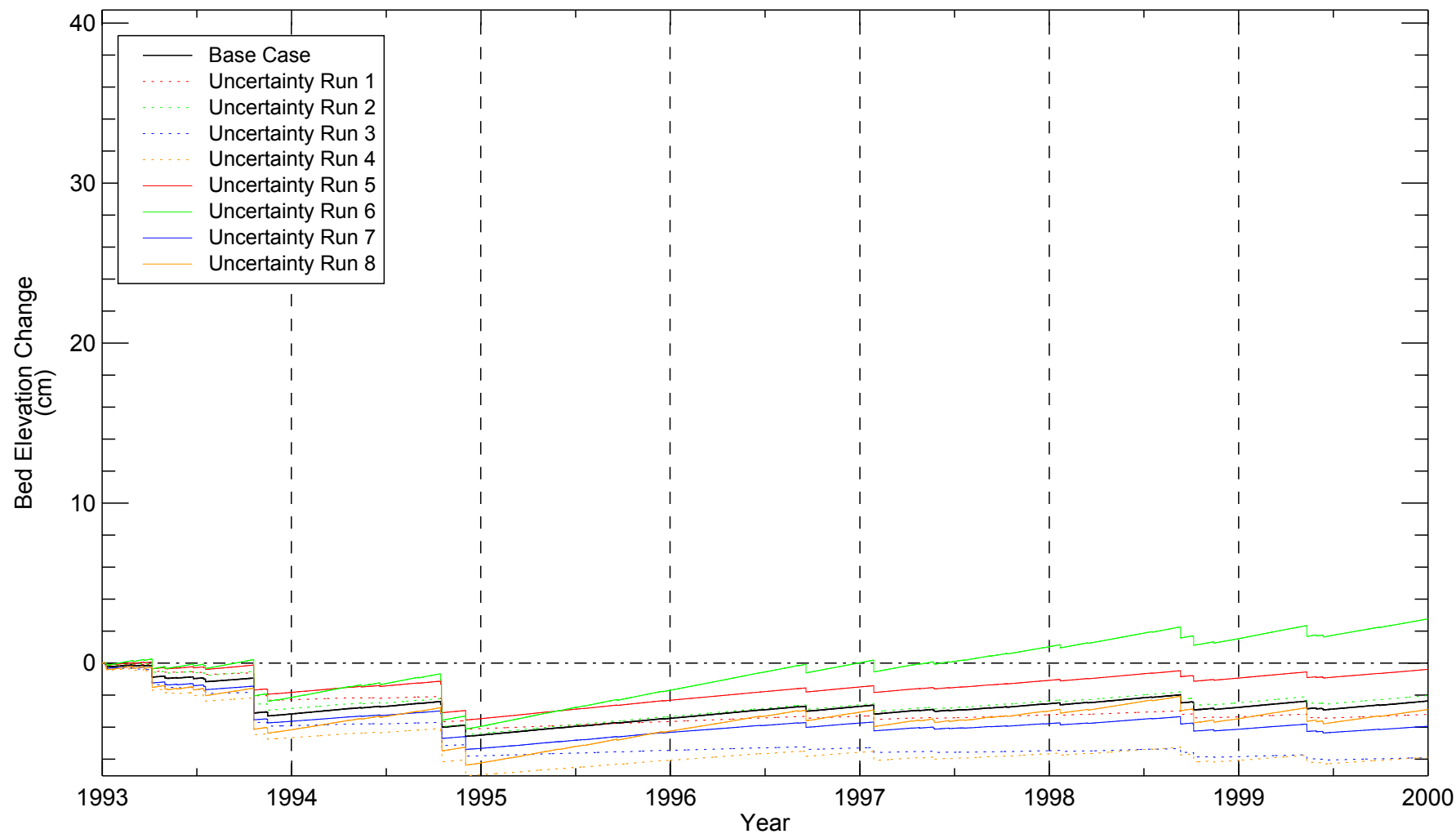


Figure 3-29
Time Histories of Predicted Bed Elevation Change at Station PB036 for Base-case and
Uncertainty Simulations
Patrick Bayou Study Area

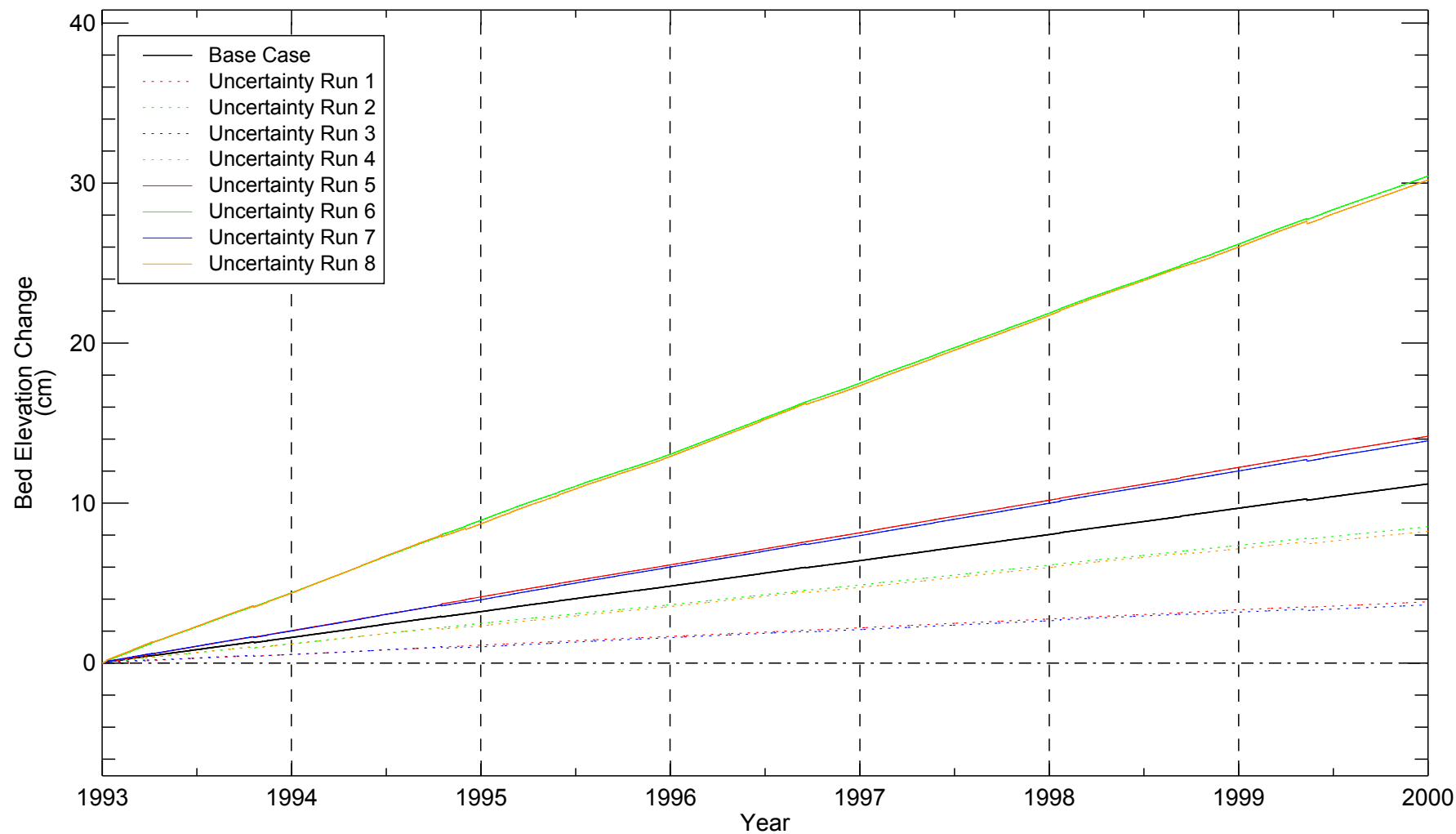


Figure 3-30
Time Histories of Predicted Bed Elevation Change at Station PB048 for Base-case
and Uncertainty Simulations
Patrick Bayou Study Area

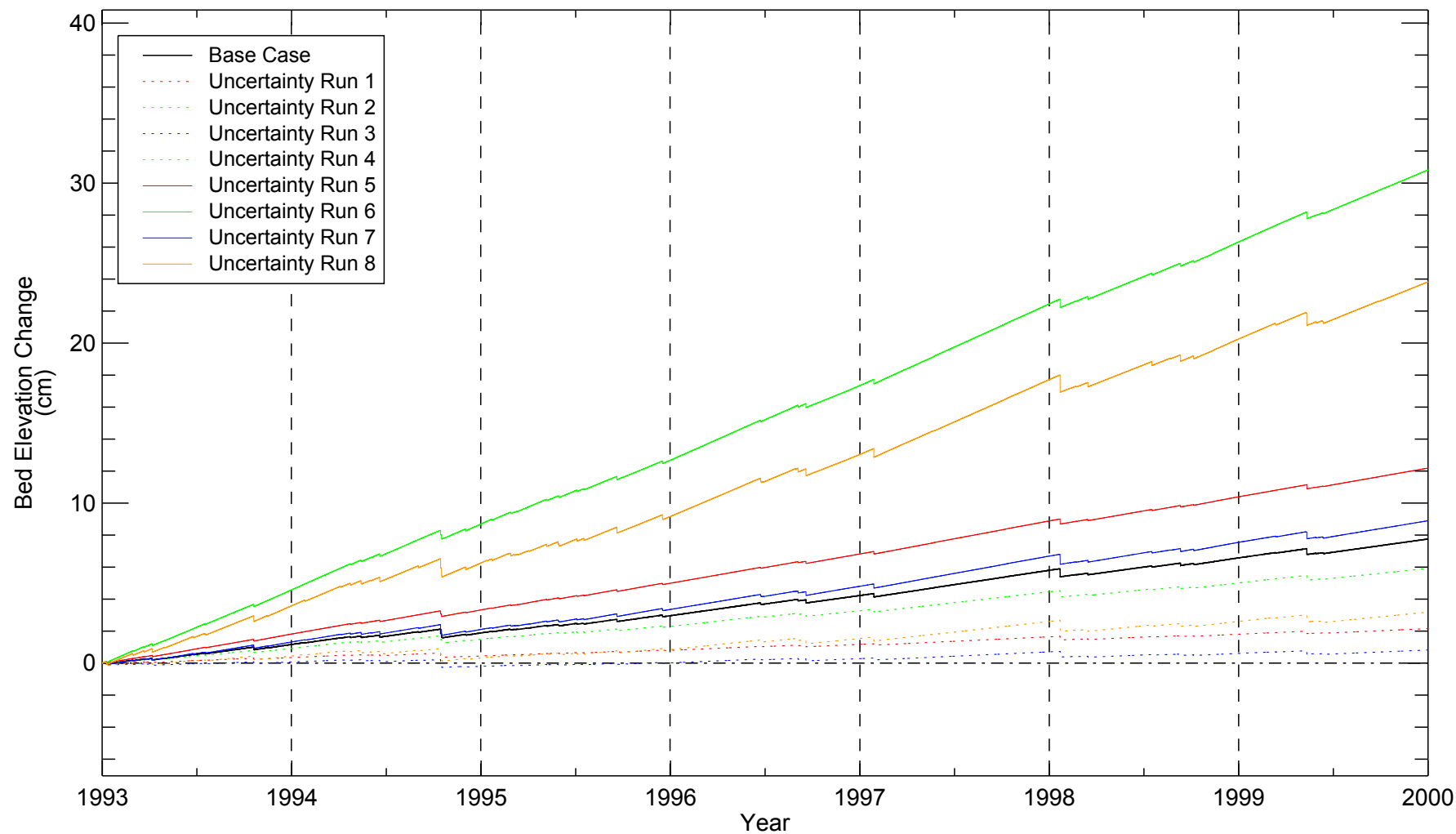


Figure 3-31
Time Histories of Predicted Bed Elevation Change at Station PB052 for Base-case and Uncertainty Simulations
Patrick Bayou Study Area

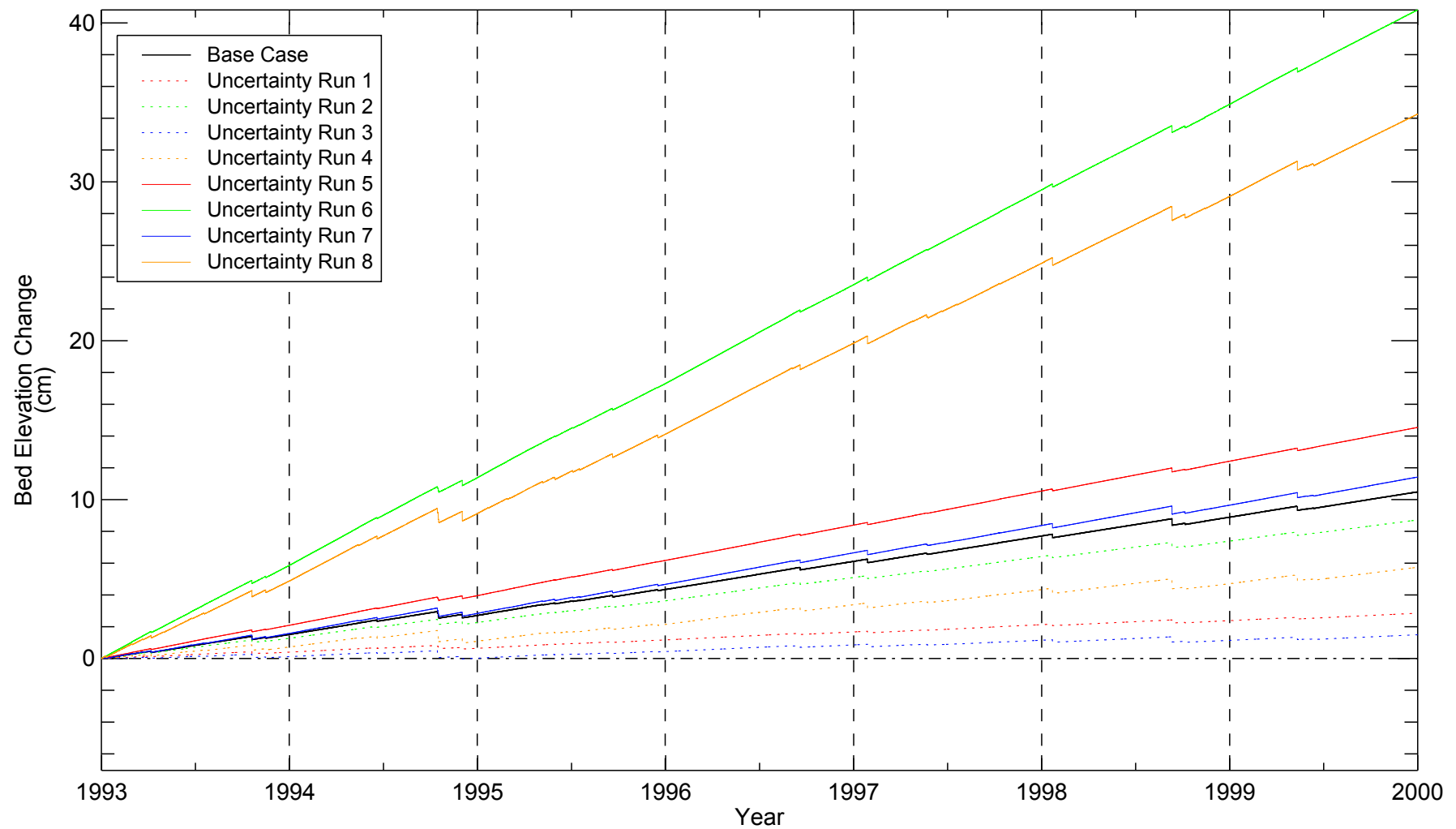


Figure 3-32
Time Histories of Predicted Bed Elevation Change at Station PB057 for Base-case and
Uncertainty Simulations
Patrick Bayou Study Area

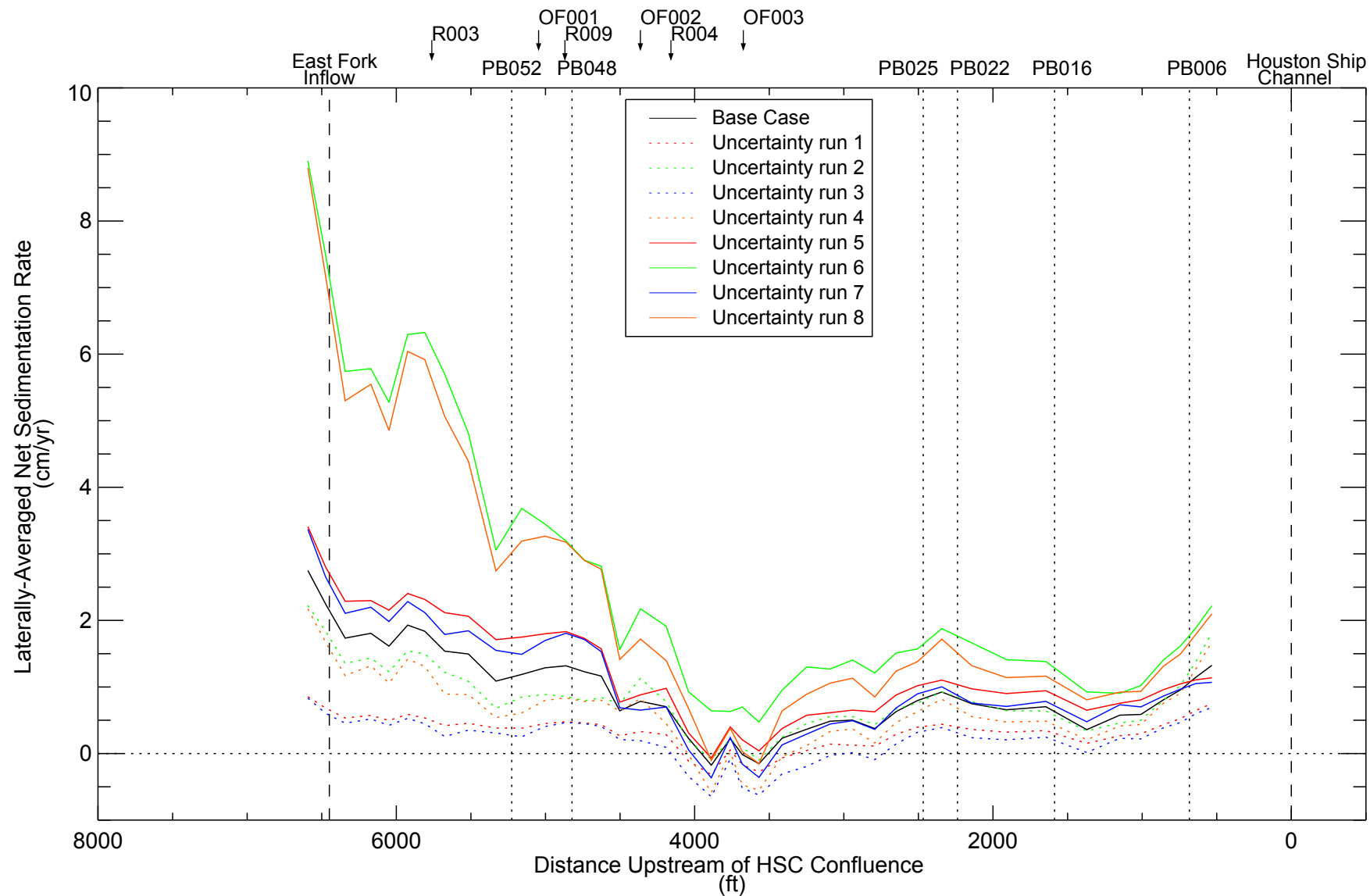


Figure 3-33
Comparison of Laterally-averaged Net Sedimentation Rates at End of 7-year Period for
Uncertainty Simulations
Patrick Bayou Study Area

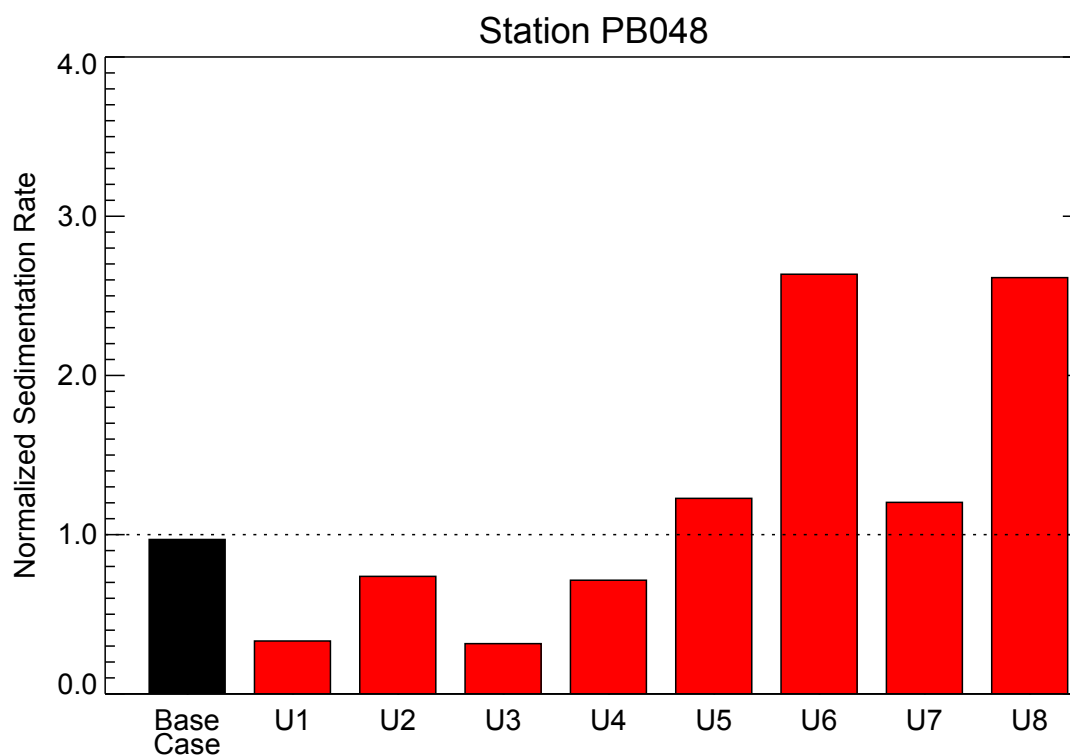
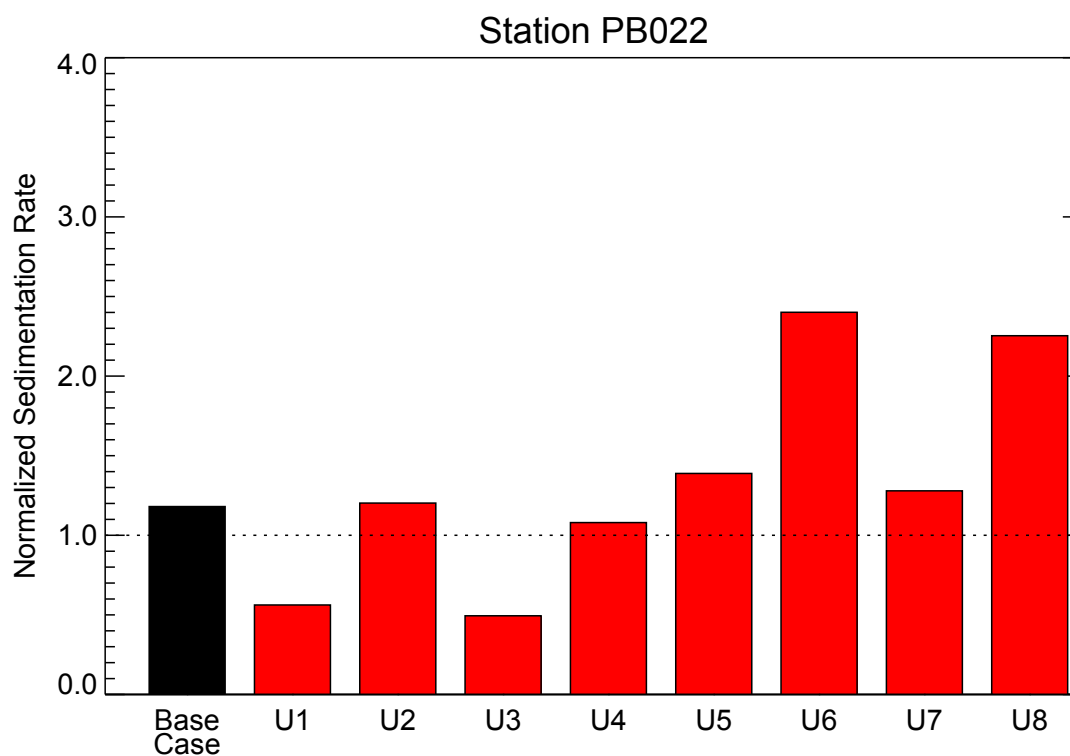


Figure 3-34
Comparison of Normalized Net Sedimentation Rates at Stations PB022 and PB048
for Uncertainty Simulations

Note: Predicted net sedimentation rates (NSR) are normalized to measured NSR at PB022 (0.82 cm/yr) and PB048 (1.65 cm/yr).
 Patrick Bavou Study Area

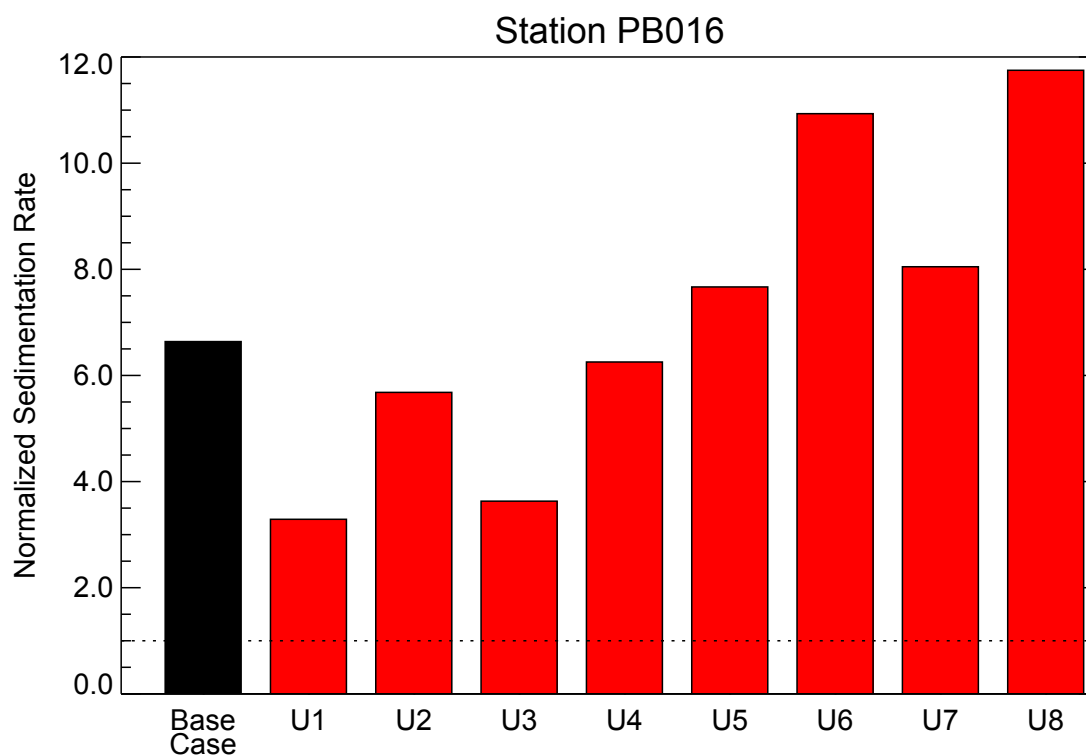
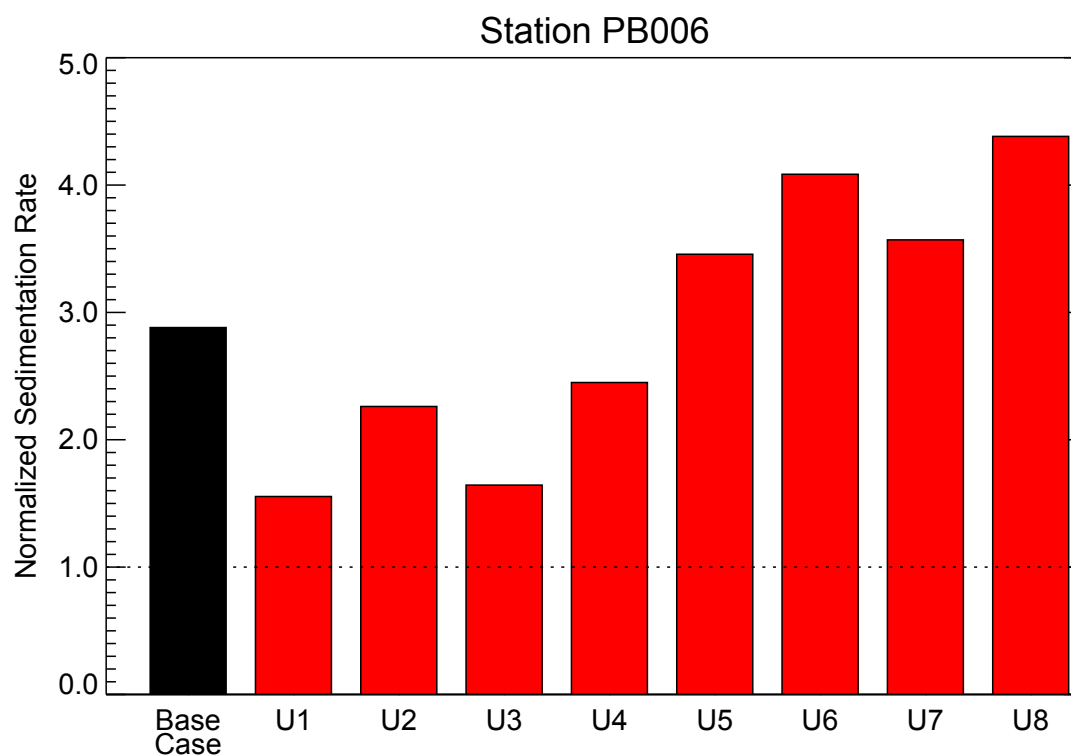


Figure 3-35
Comparison of Normalized Net Sedimentation Rates at Stations PB006 and PB016 for Uncertainty Simulations

Note: Predicted net sedimentation rates (NSR) are normalized to measured NSR at PB022 (0.82 cm/yr) and PB048 (1.65 cm/yr).

Patrick Bayou Study Area

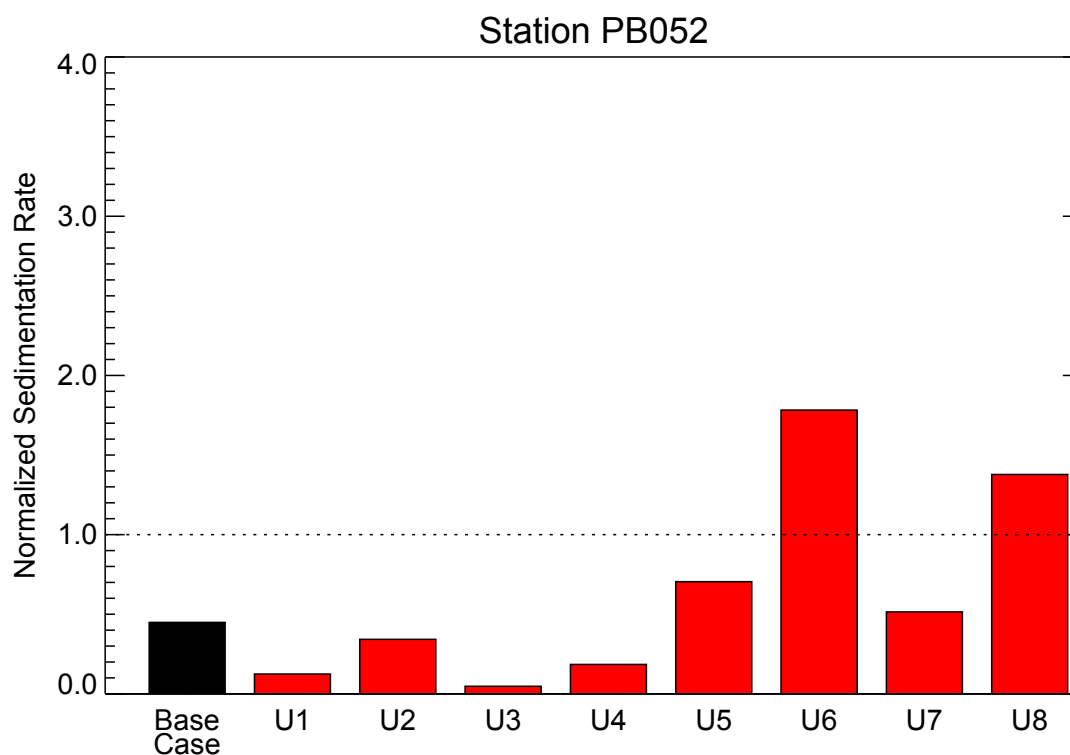
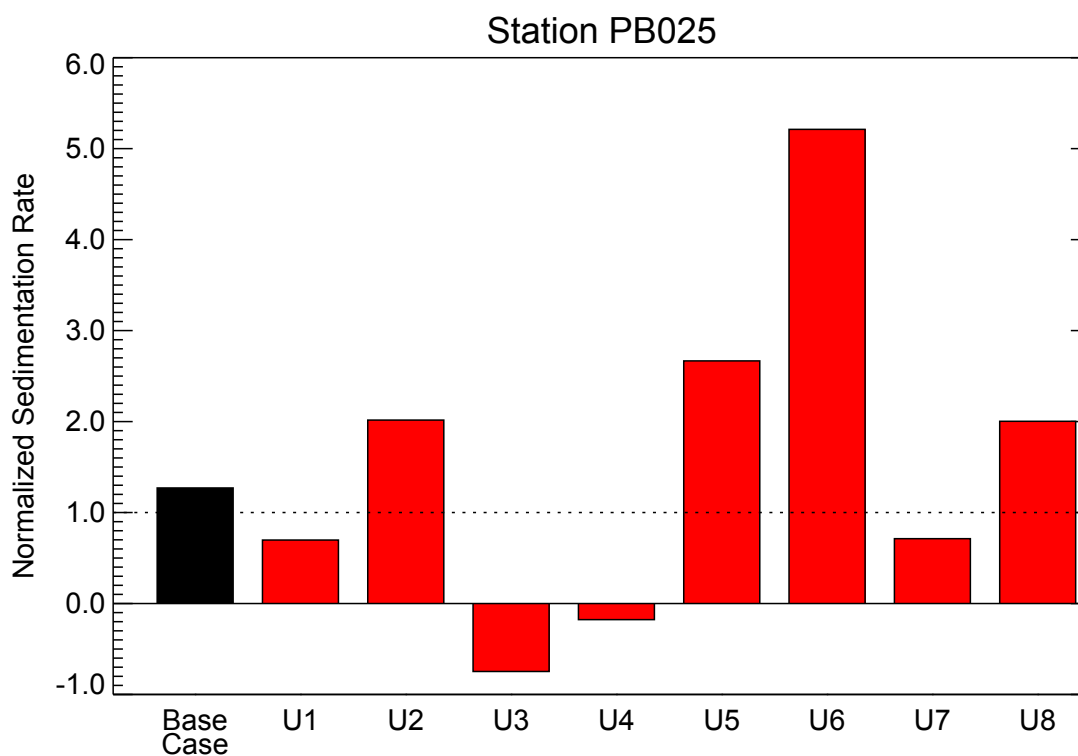


Figure 3-36
Comparison of Normalized Net Sedimentation Rates at Stations PB025 and PB052 for
Uncertainty Simulations
 Note: Predicted net sedimentation rates (NSR) are normalized to measured NSR at PB022 (0.82 cm/yr) and PB048 (1.65 cm/yr).
 Patrick Bayou Study Area

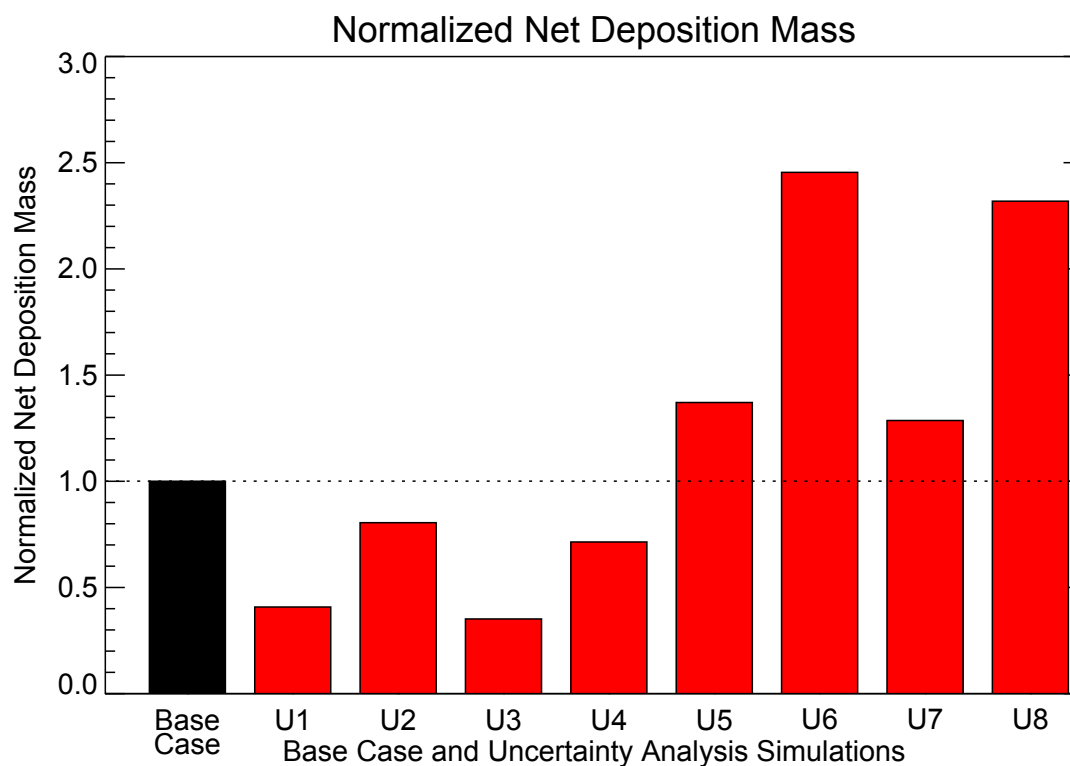
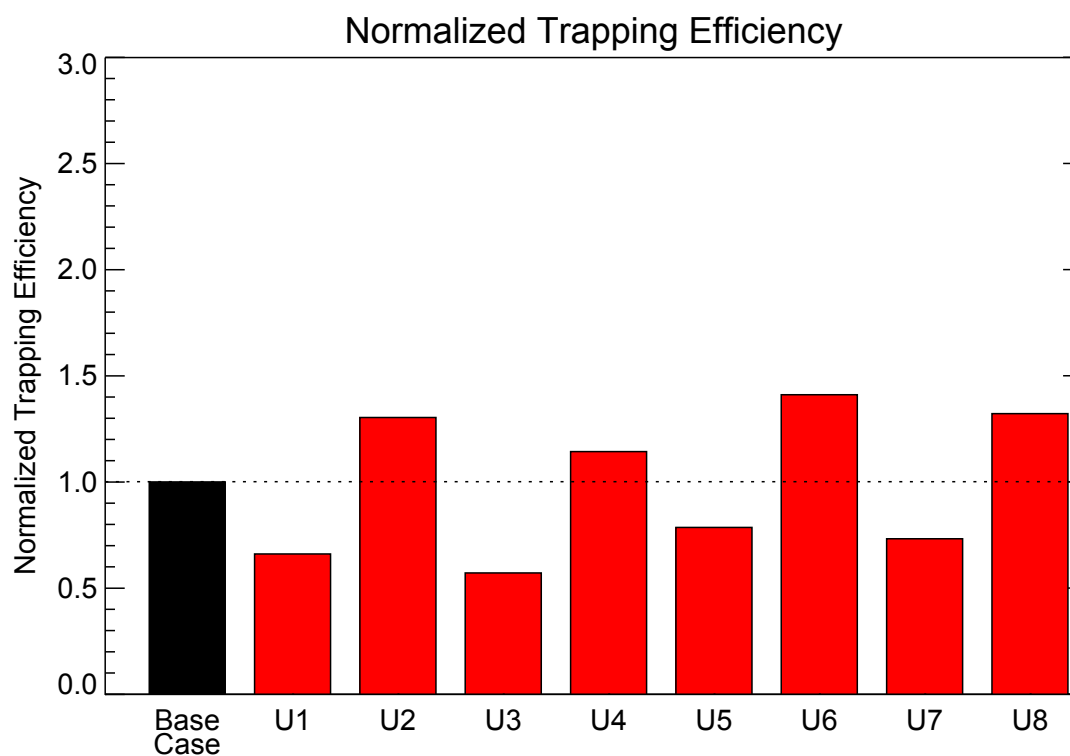
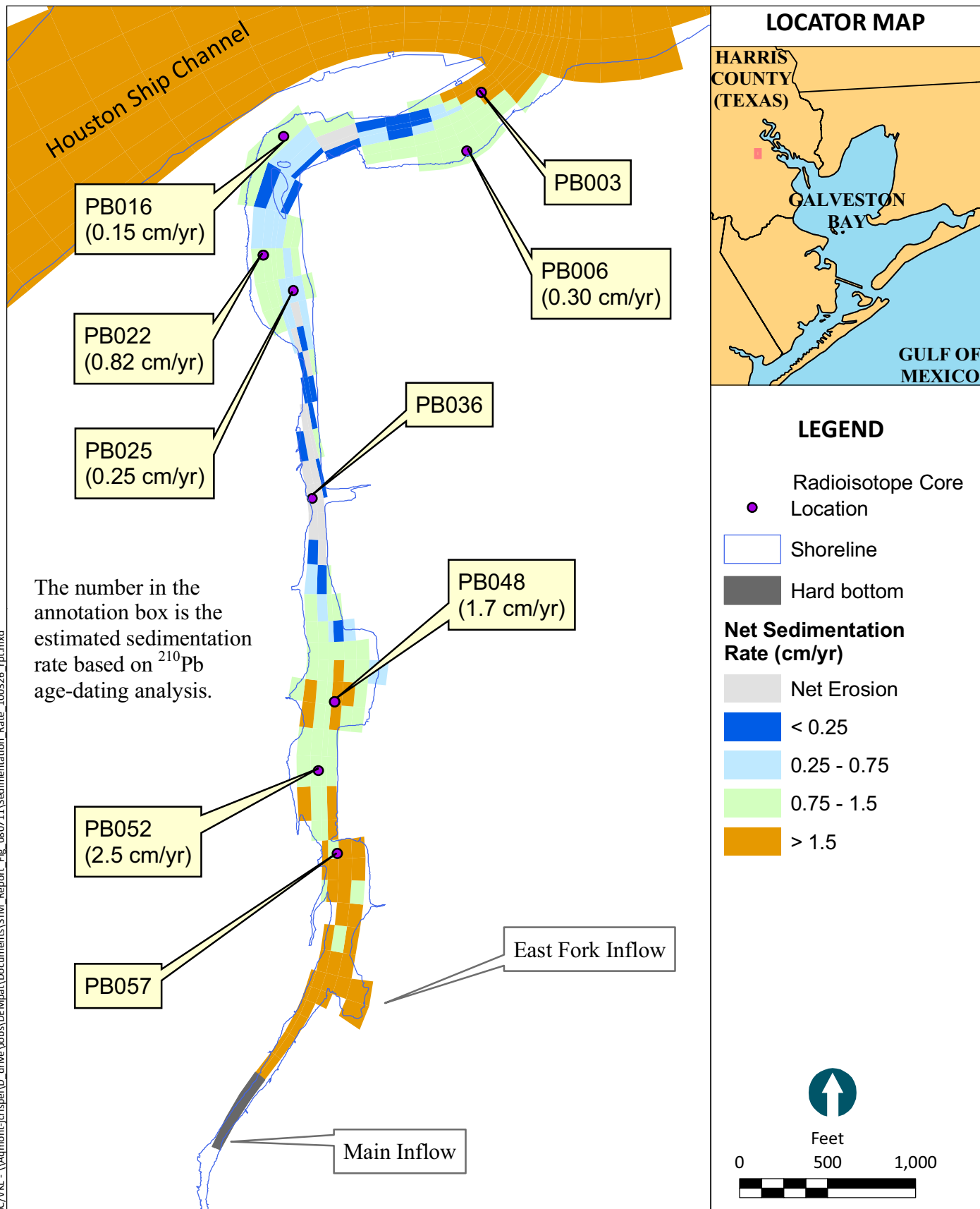


Figure 3-37
Comparison of Normalized Trapping Efficiency and Net Deposition Mass for
Uncertainty Simulations
 Note: Uncertainty simulation results are normalized with respect to base case results.
 Patrick Bayou Study Area

IC:\VLA...\\Aqmont-jcrispel\drive\Jobs\DEMPat\Documents\STM_Report_Fig_080711\Sedimentation_Rate_100326_rpt.mxd



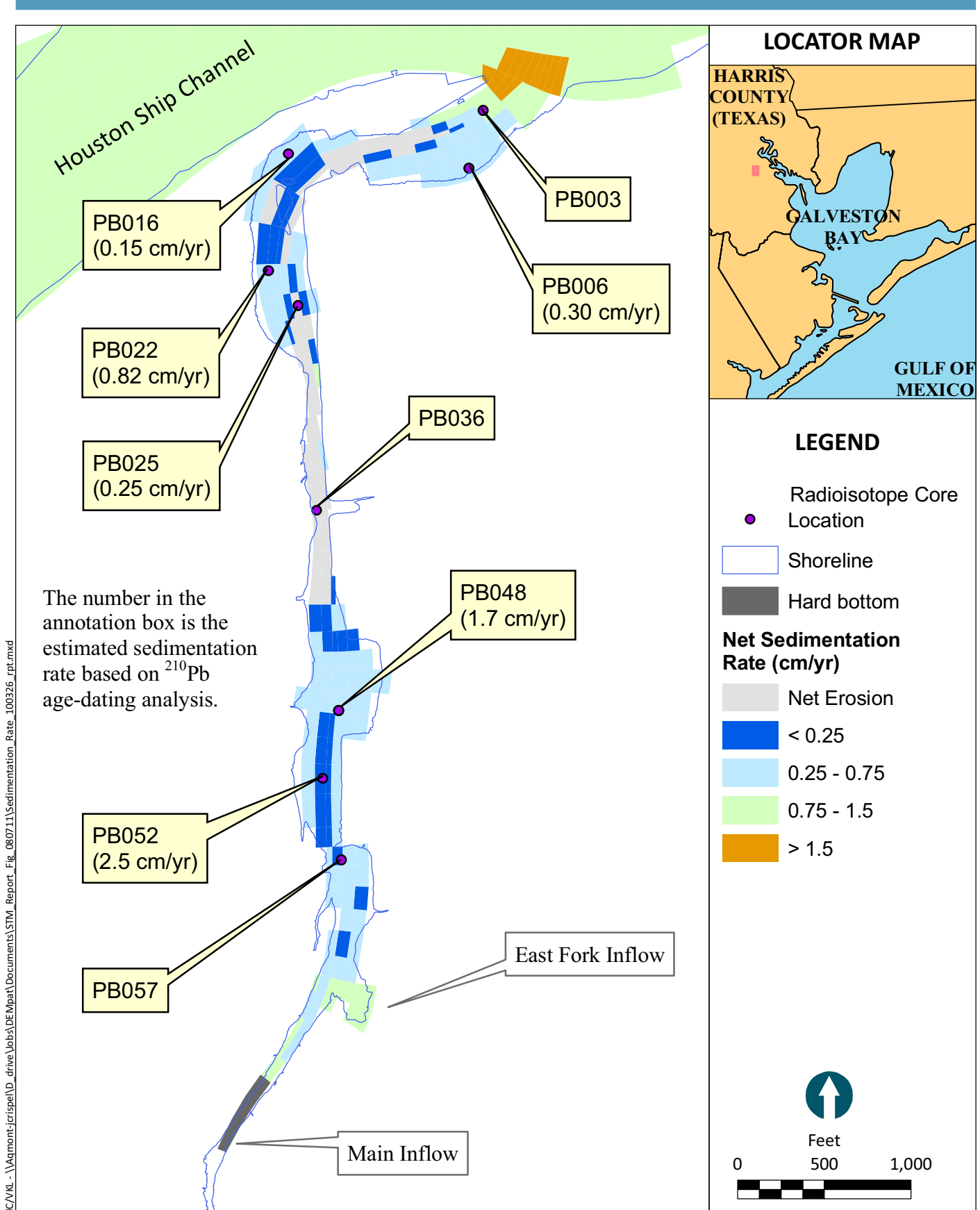


Figure 3-39

Spatial Distribution of Predicted Net Sedimentation Rate at End of
7-year Period Lower-bound Simulation
Patrick Bayou Study Area



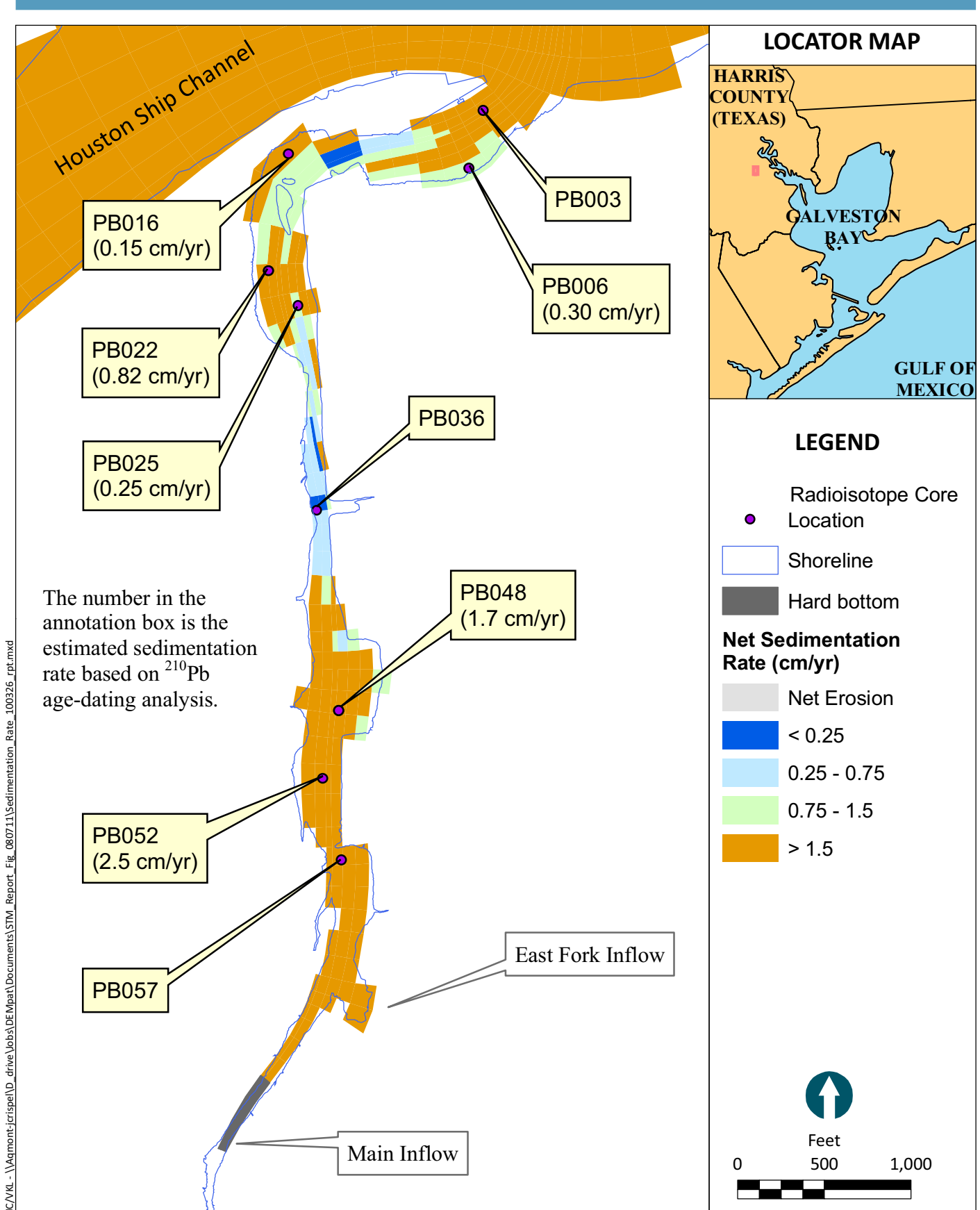


Figure 3-40

Spatial Distribution of Predicted Net Sedimentation Rate at End of 7-year Period: Upper-bound Simulation
Patrick Bayou Study Area

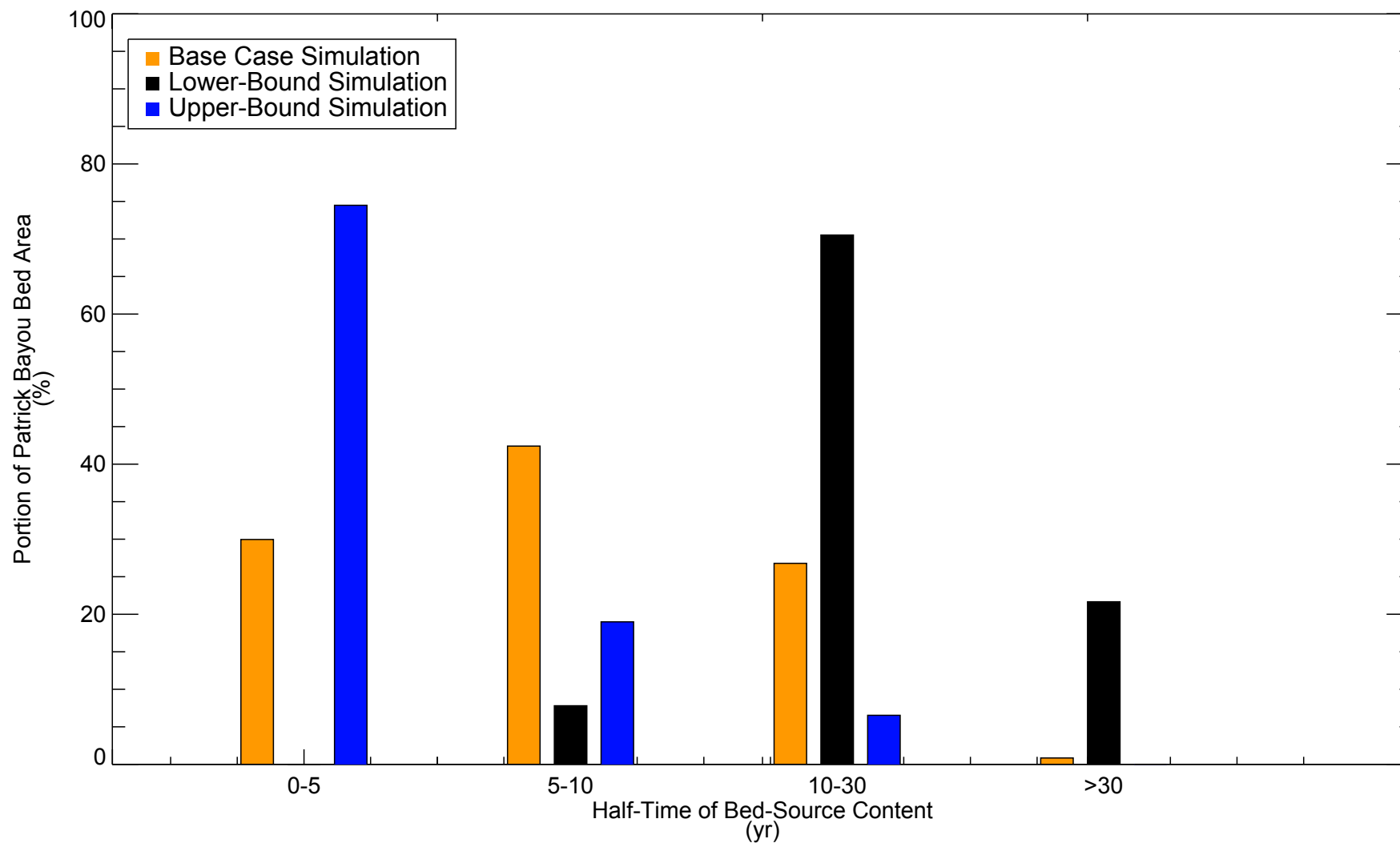


Figure 3-41

Comparison of Areal Distributions of Predicted Half-time of Bed-source Sediment in Mixing-Zone Layer (0-10 cm) for Base-case and Bounding Simulations
Patrick Bayou Study Area

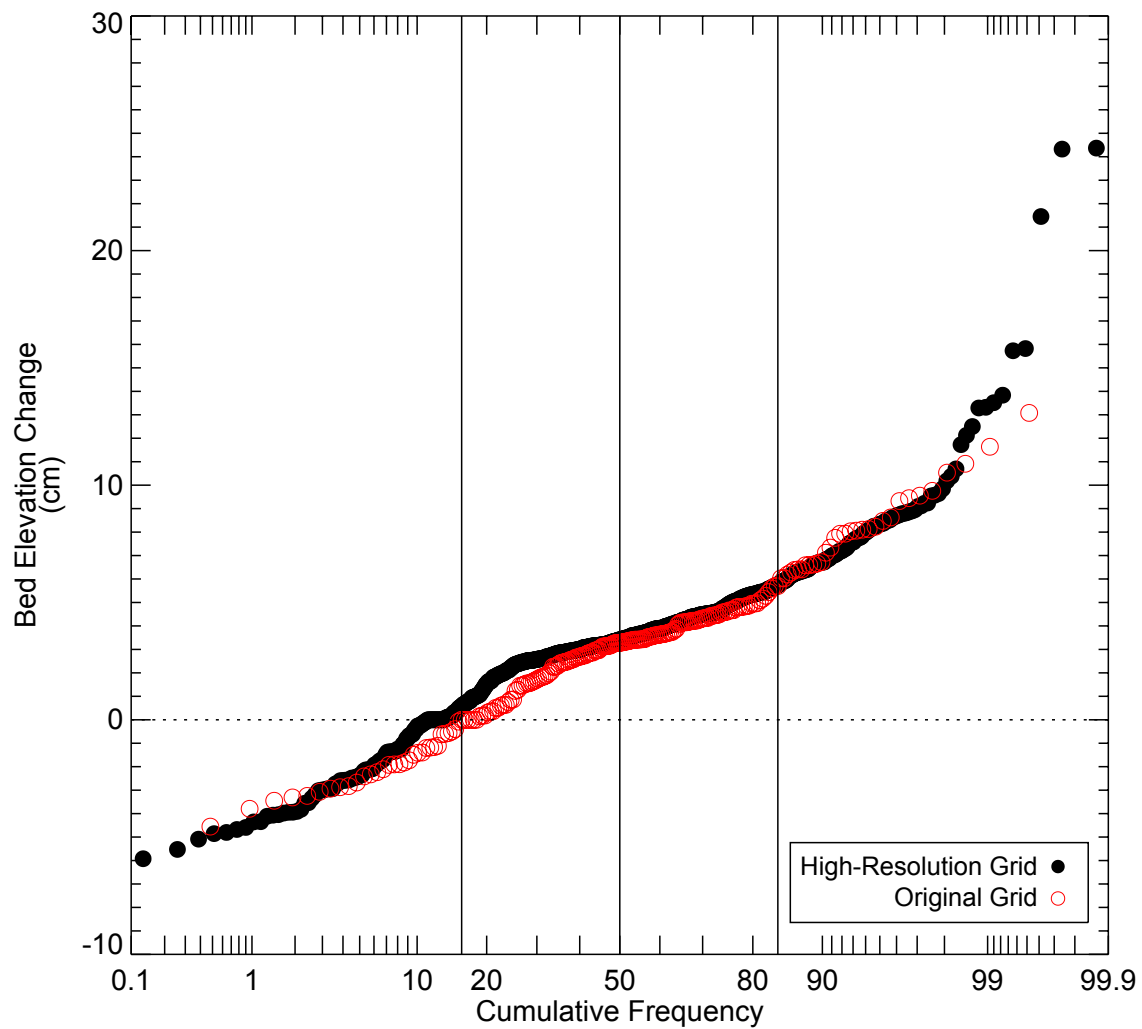
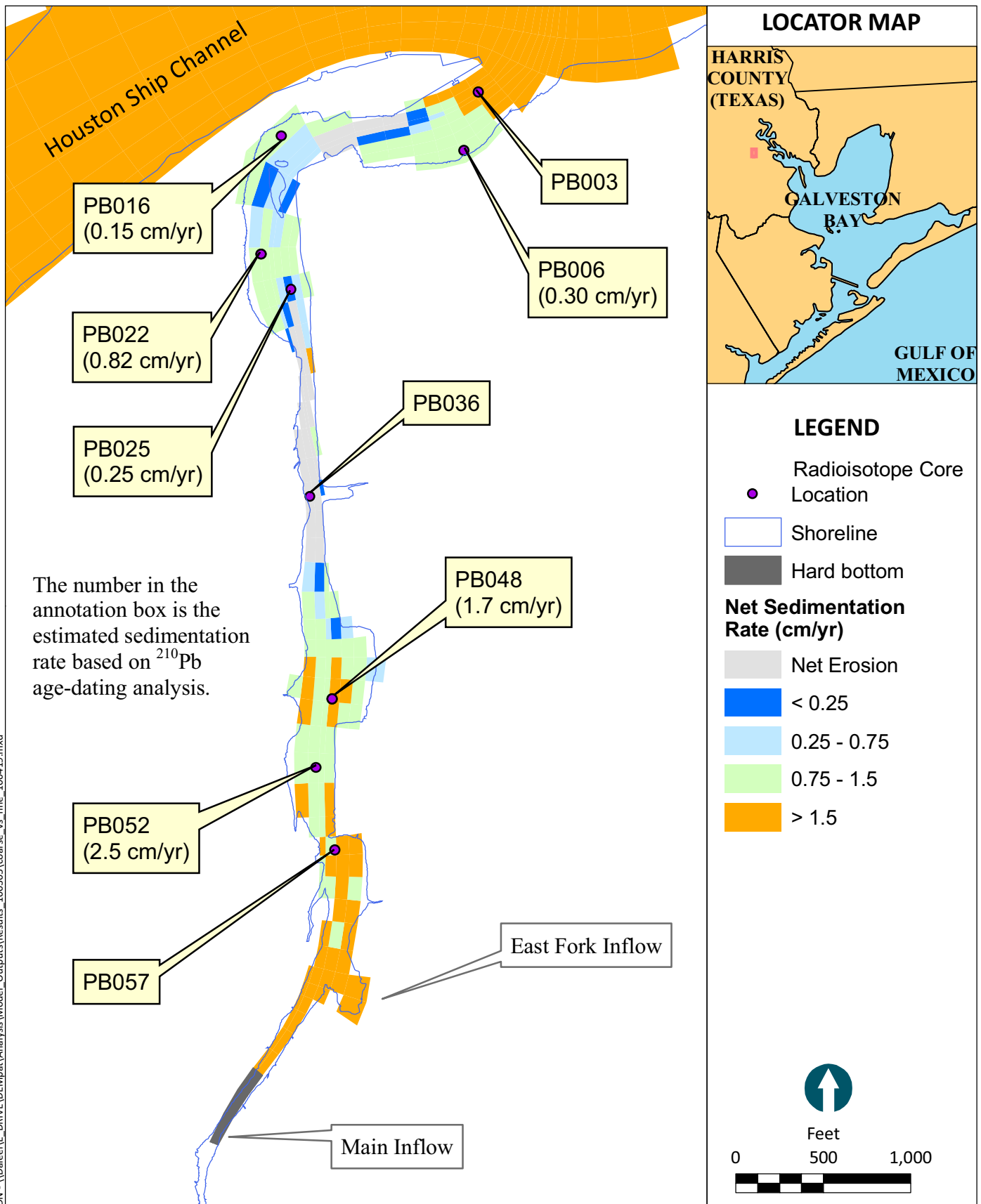


Figure 3-42
 Cumulative Frequency Distributions of Bed Elevation Change During 3-year Period
 (1993-1995) for Original and High-resolution Grids
 Note: Results shown only in the study area and channel.
 Patrick Bayou Study Area

DN - \\Daleel\DRIVE\DEMPat\Analysis\Model_Outputs\Results_100305\coarse_vs_fine_100419.mxd



DN - \\Daleel\DRIVE\DEMPat\Analysis\Model_Outputs\Results_100305\coarse_vs_fine_100419.mxd

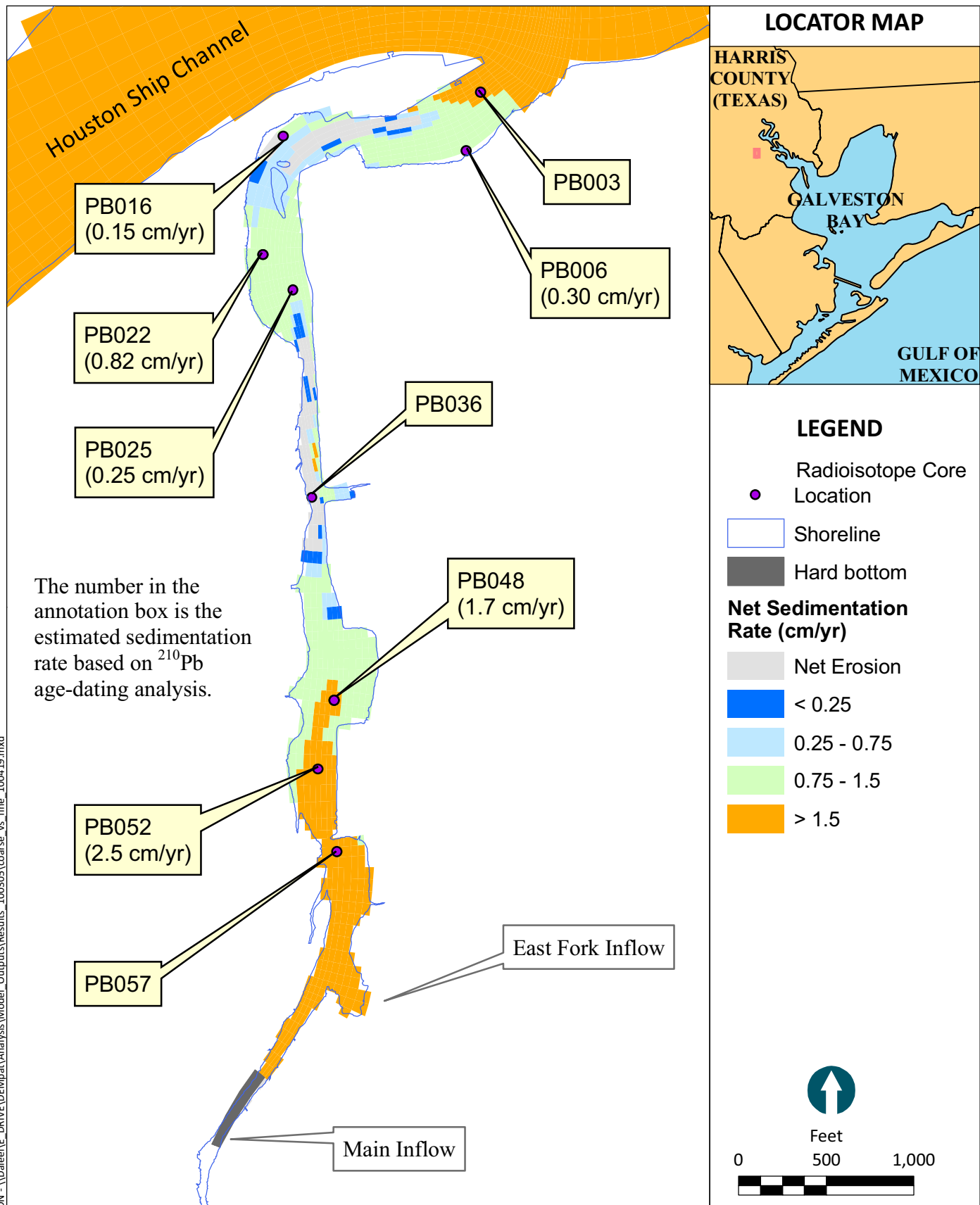


Figure 3-44

Spatial Distribution of Predicted Net Sedimentation Rate in Patrick Bayou for 3-year Period(1993-1995): High-resolution Grid Patrick Bayou Study Area



DN - \\Daleel\DRIVE\DEMPat\Analysis\Model_Outputs\Results_100305\coarse_vs_fine_100419.mxd

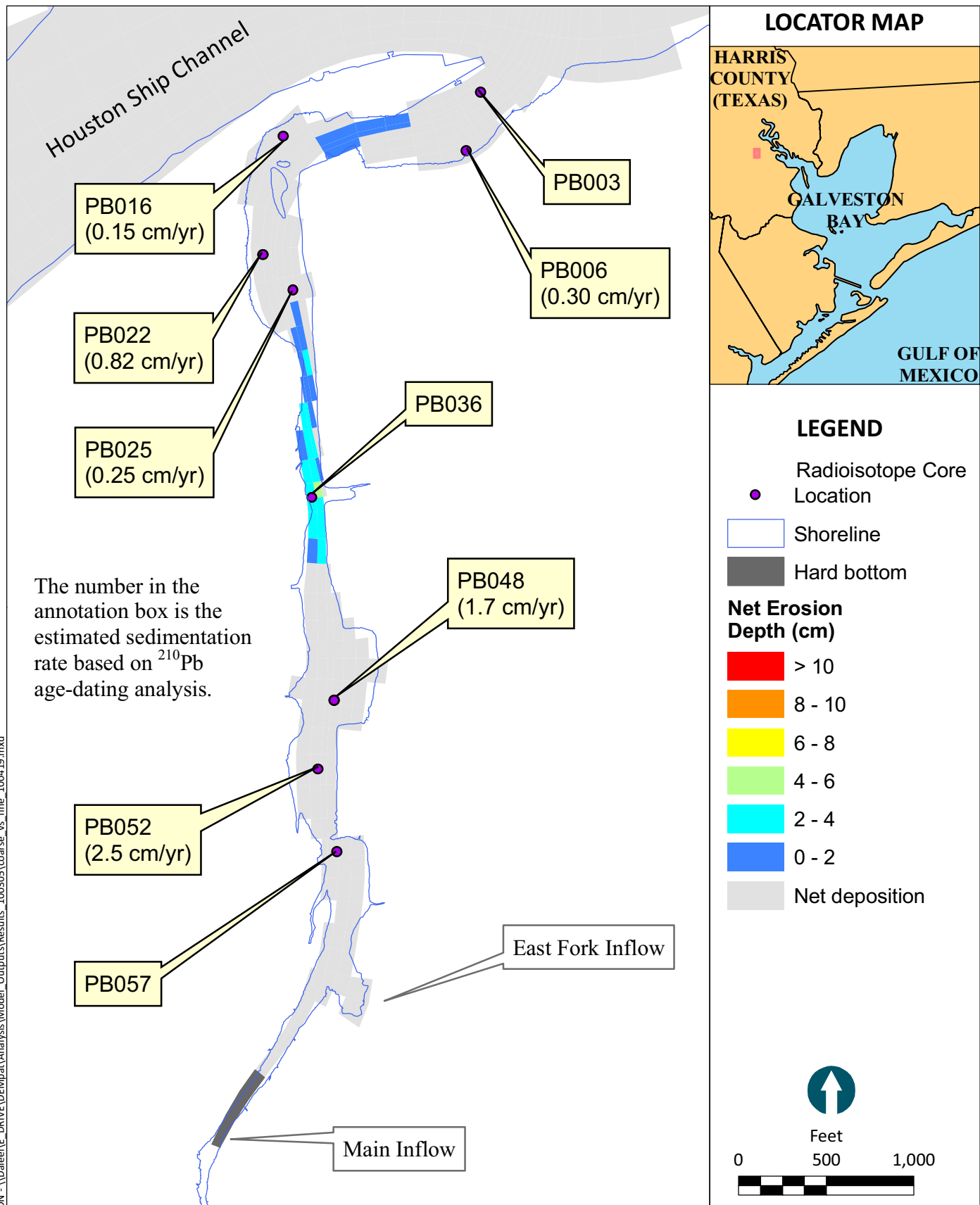


Figure 3-45

Spatial Distribution of Predicted Net Erosion Depth in Patrick Bayou for 3-year period (1993-1995): Original Grid
Patrick Bayou Study Area



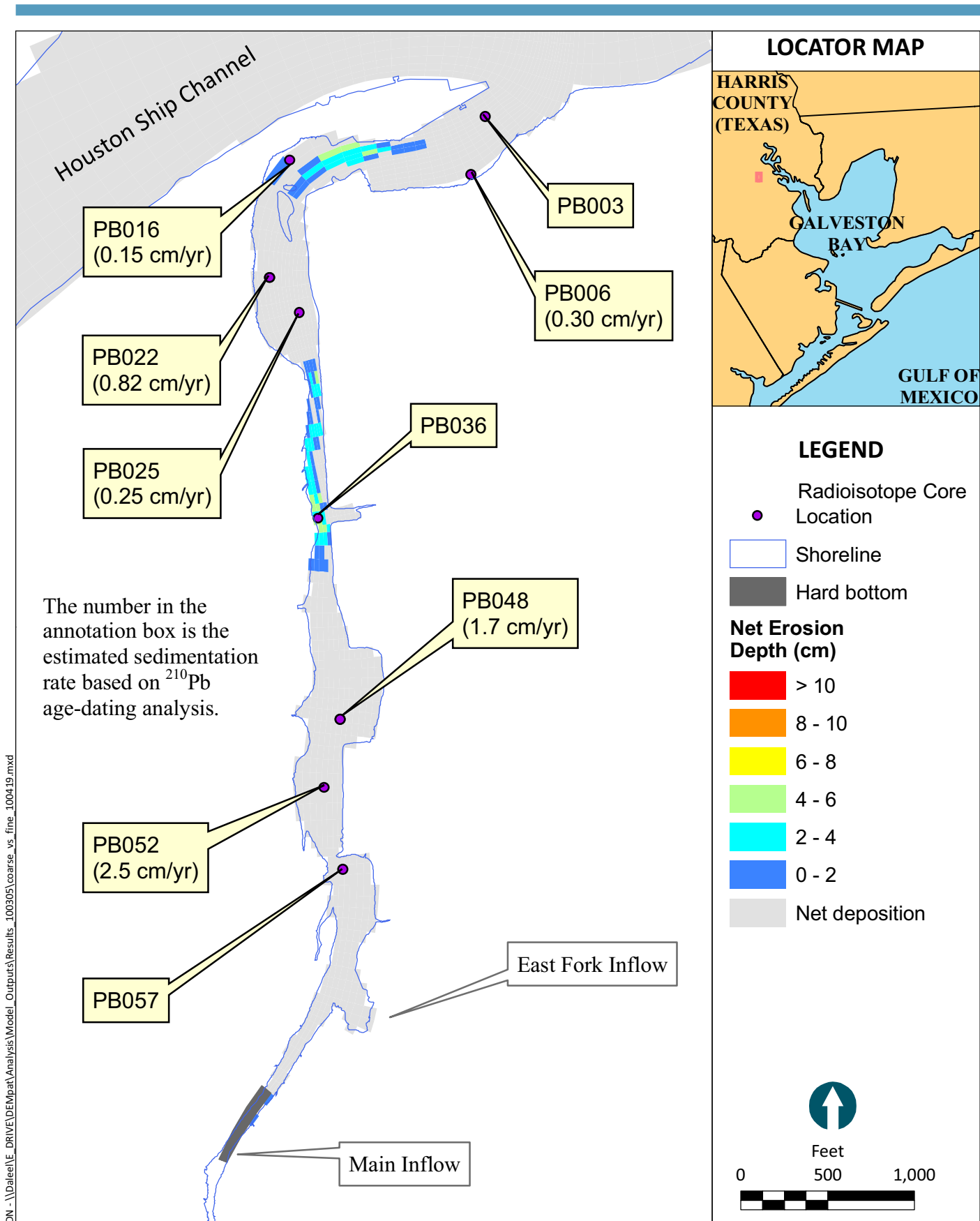


Figure 3-46

Spatial Distribution of Predicted Net Erosion Depth in Patrick Bayou for 3-year period (1993-1995): High-resolution Grid
Patrick Bayou Study Area



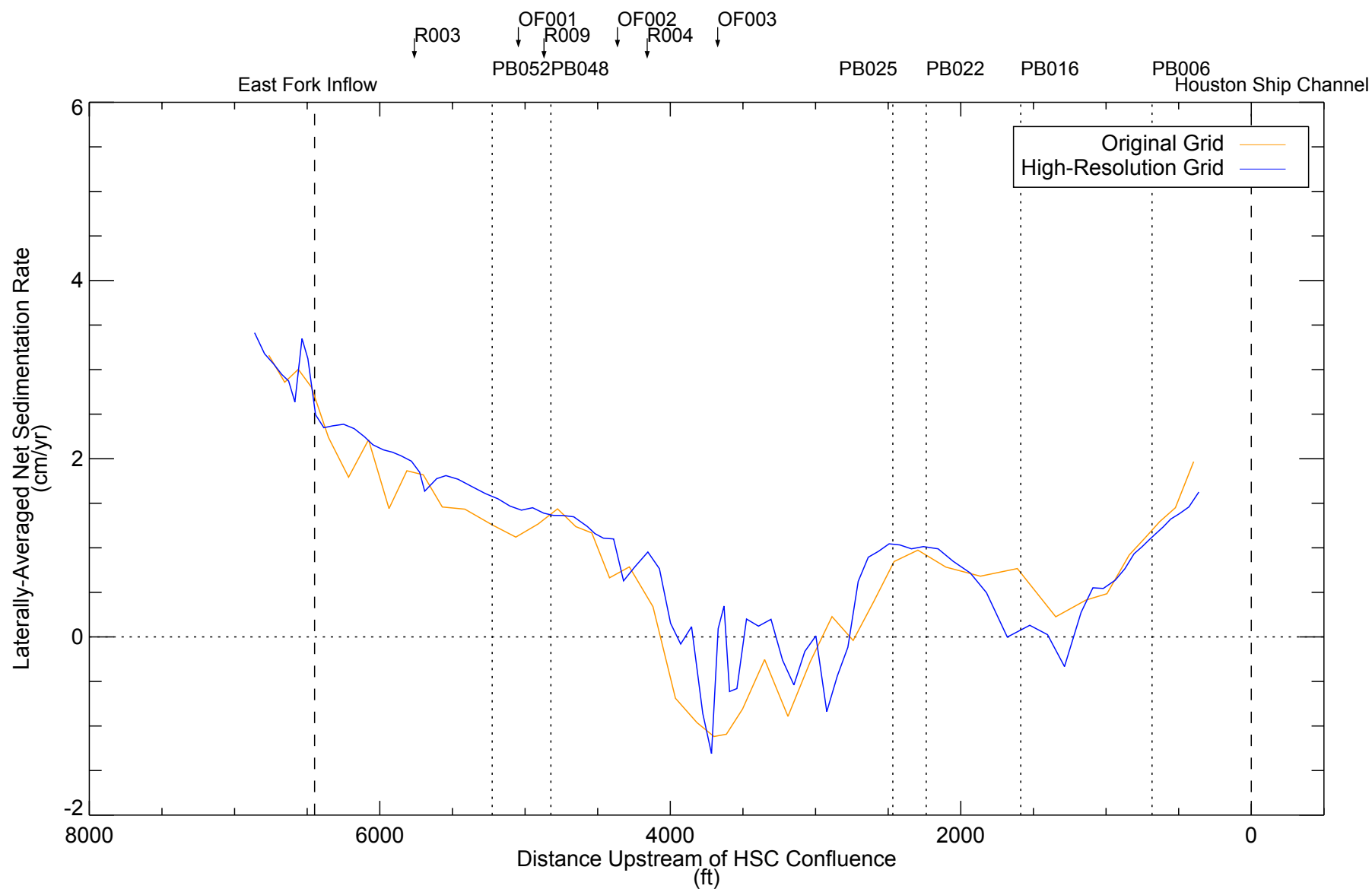


Figure 3-47

Spatial Distributions of Laterally-averaged Net Sedimentation Rates at End of 3-year Period (1993-1995) for Original and High-resolution Grids

Note: Model predicted sediment depths based on end of 3-yr period (1993-1995). Area-weighted averages calculated at each lateral transect. Model results only for the main channel, floodplain results excluded.

Patrick Bayou Study Area



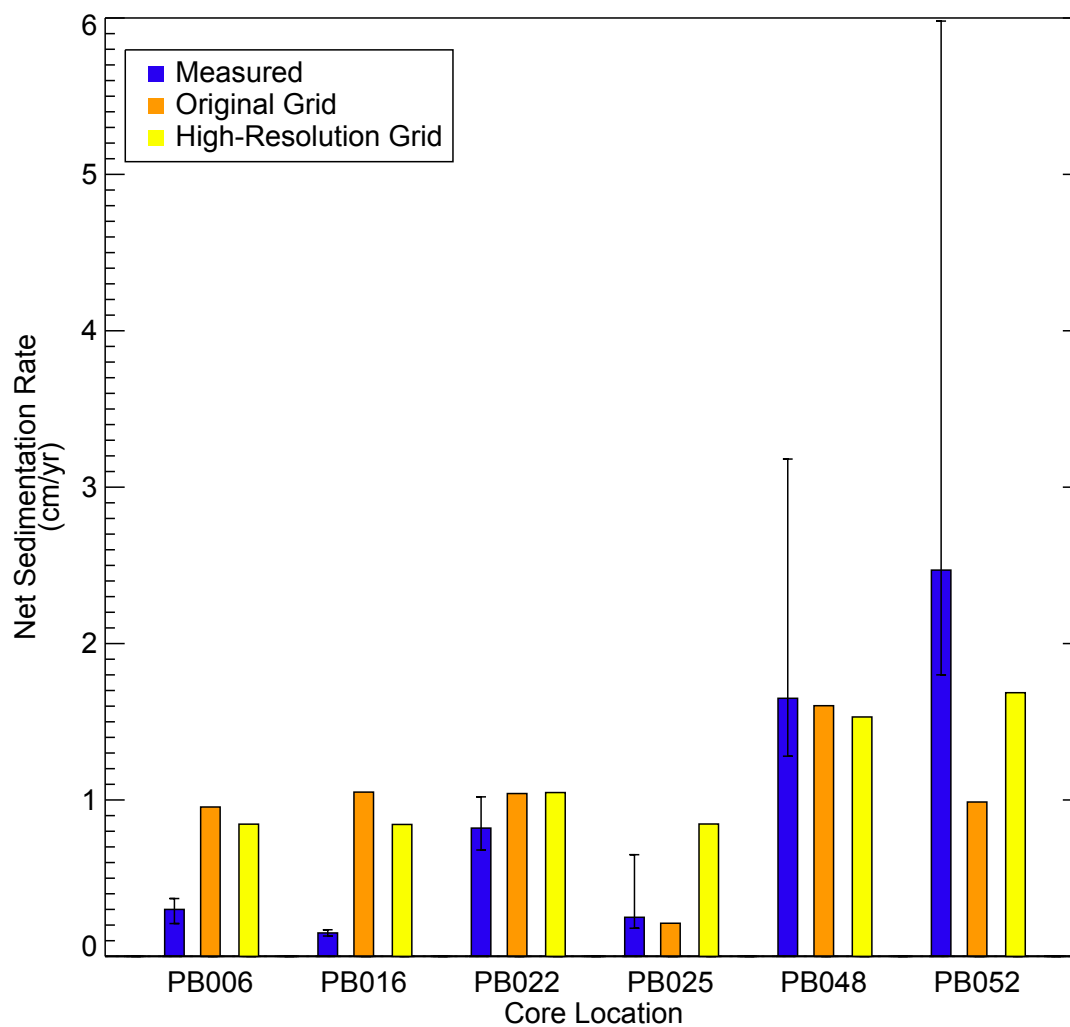


Figure 3-48

Comparison of Measured and Predicted NSR Values for 3-year Period (1993-1995) for Original and High-resolution Grids

Note: Model predicted sediment depths based on end of 3-yr period (1993-1995). Datacores collected in 2007 and 2009. Error bars represent range in measured NSRs.

Patrick Bayou Study Area



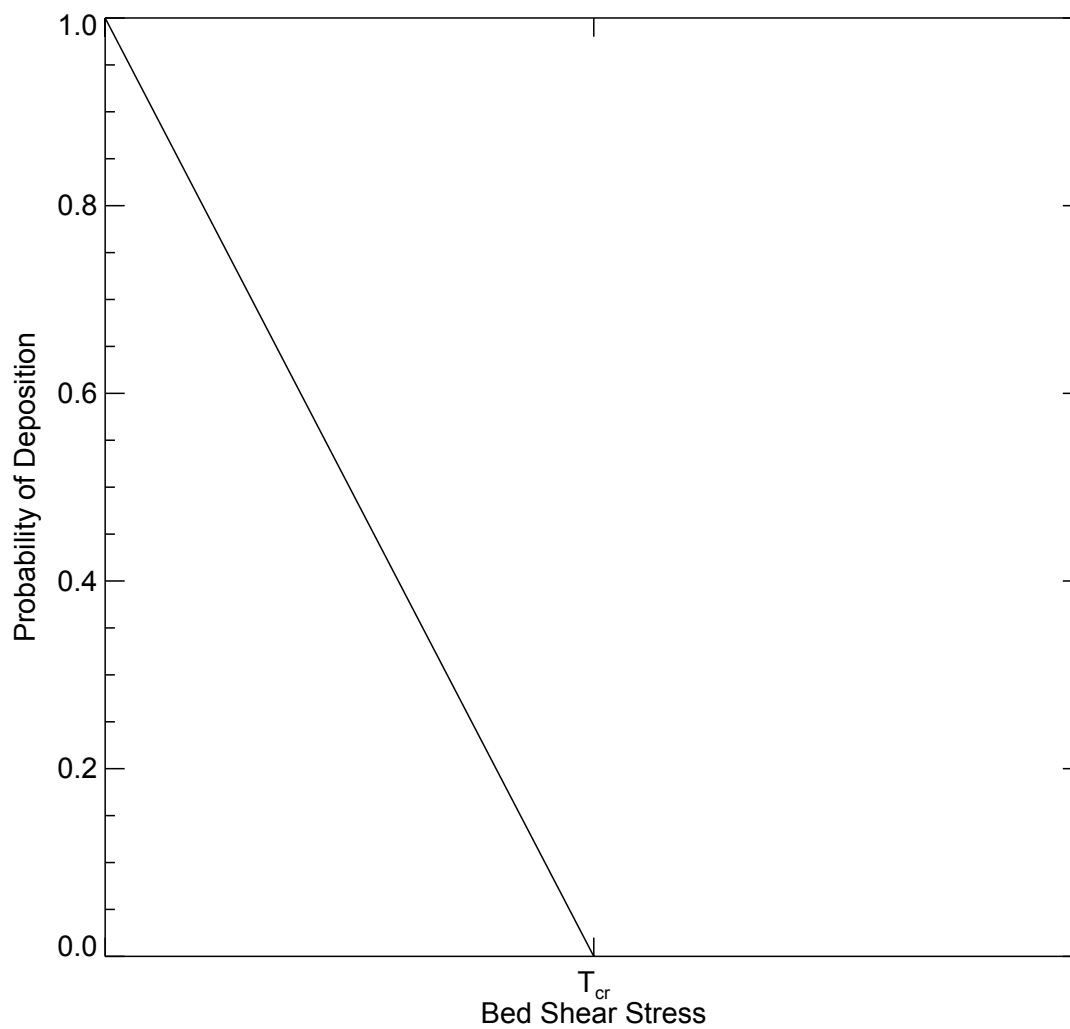


Figure A-1
Probability of Deposition for Cohesive Sediment Using the Krone Formulation
Patrick Bayou Study Area

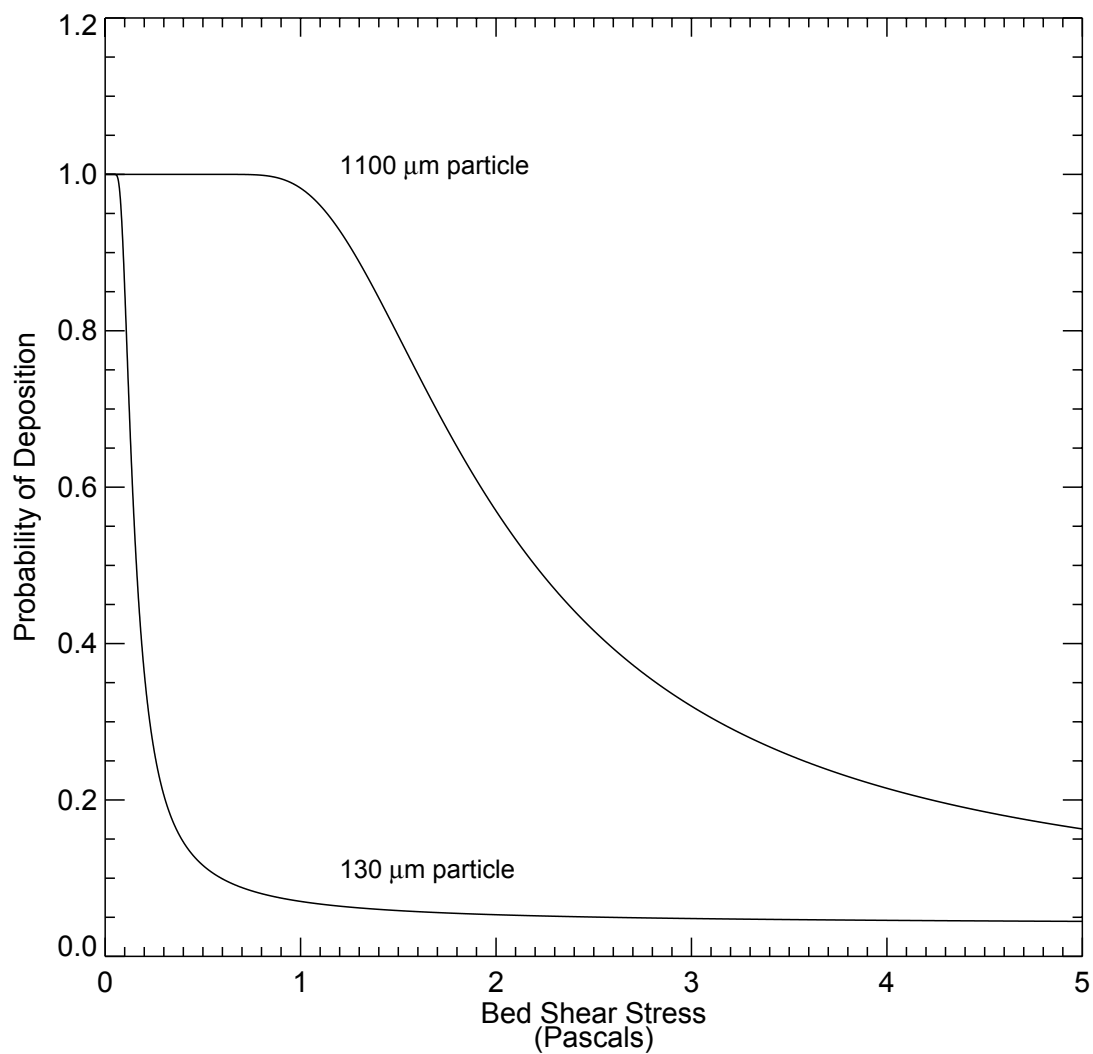


Figure A-2
Probability of Deposition for Non-cohesive Sediment as a Function of Bed Shear Stress and Particle Diameter
Patrick Bayou Study Area

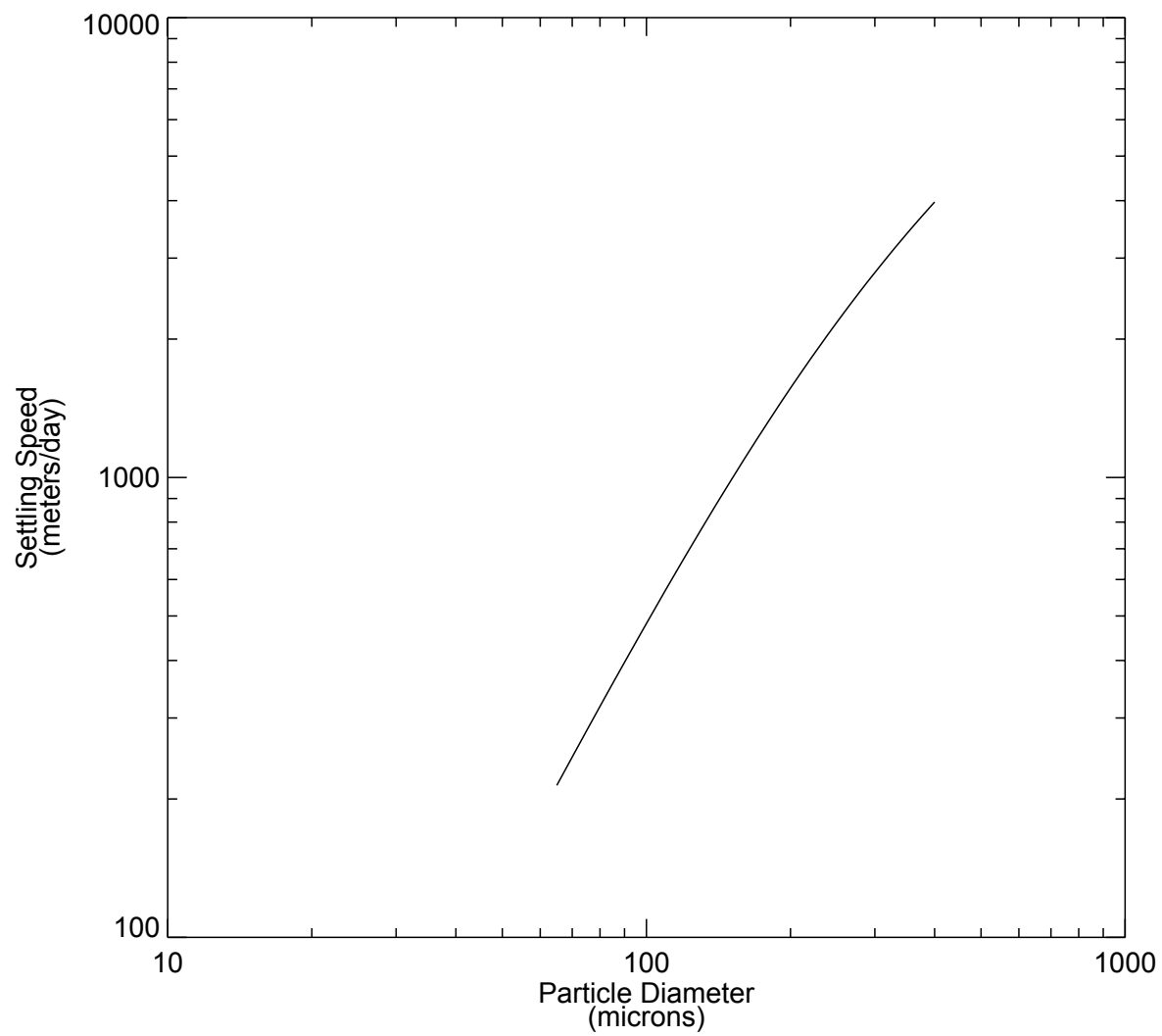


Figure A-3
Settling Speed of Discrete Sediment Particles as a Function of Particle Diameter
Patrick Bayou Study Area

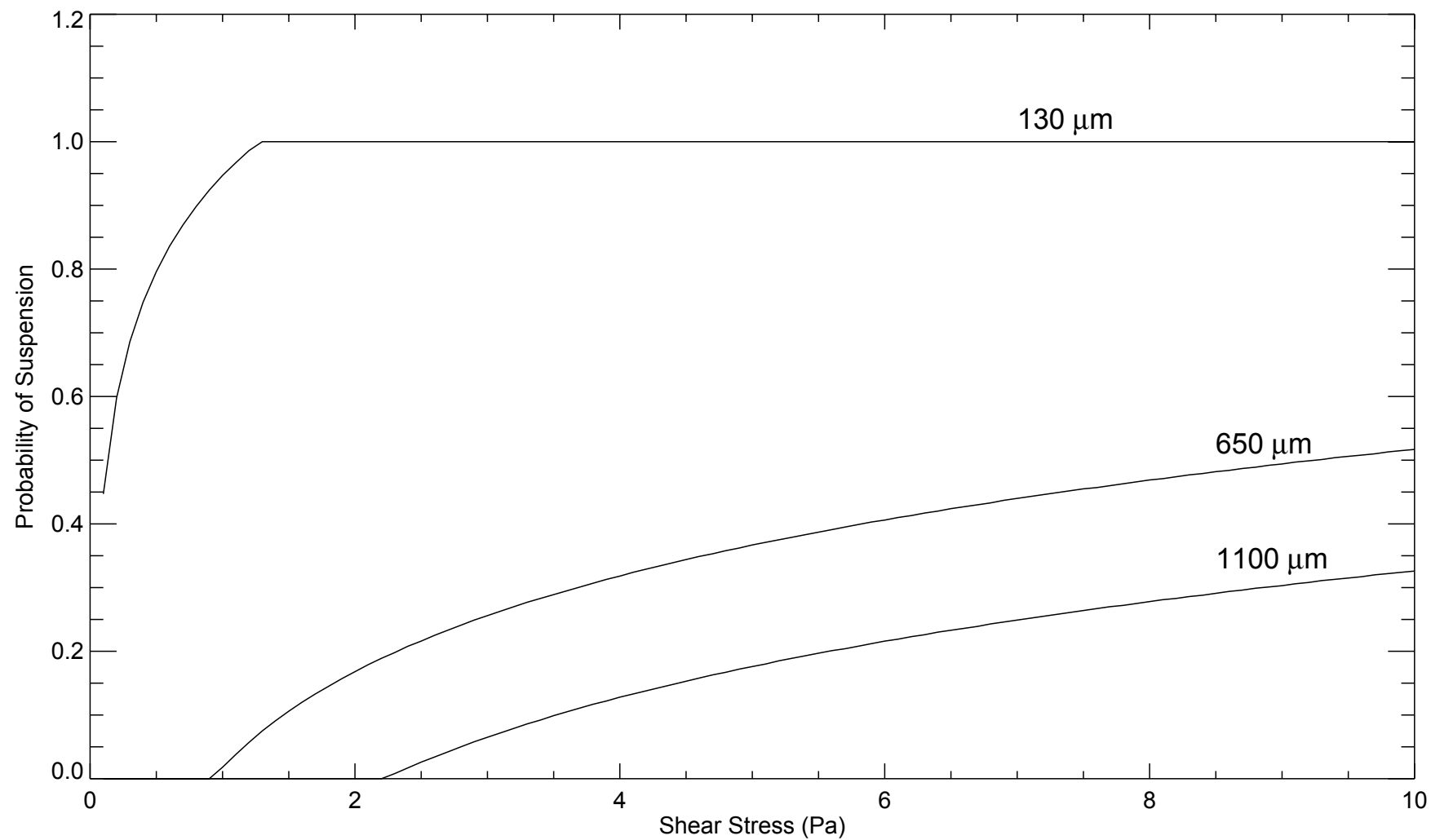


Figure A-4
Probability of Suspension for Particle Diameters 130 μm , 650 μm and 1100 μm
Patrick Bayou Study Area

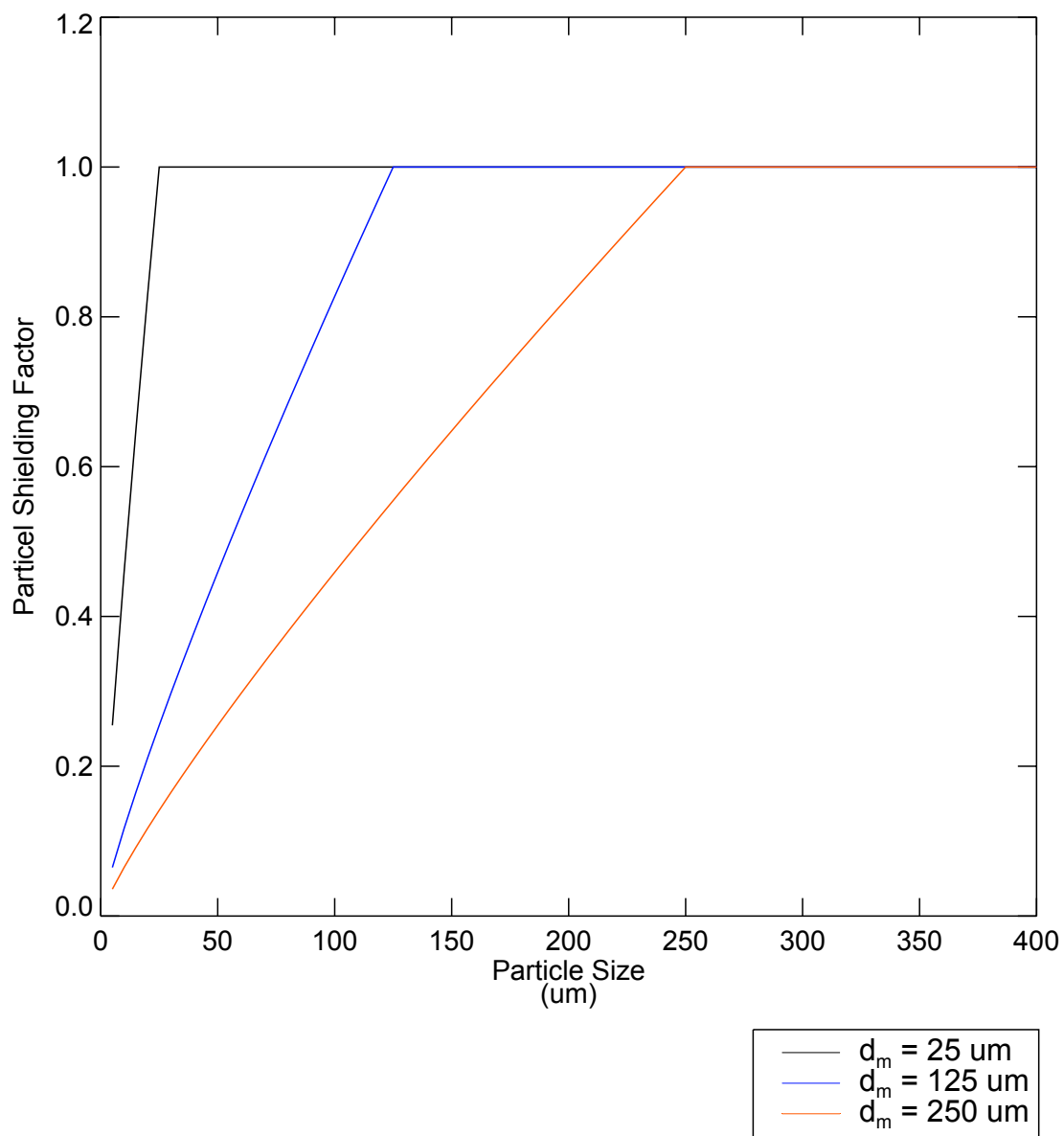


Figure A-5

Particle Shielding Factor as a Function of Particle Size

Note: Particle shielding factor is calculated as: $S_k = (d_k/d_m)^{0.85}$, when $d_k < d_m$, otherwise set $S_k = 1$.
where d_k = particle size, d_m = mean particle diameter.

Patrick Bayou Study Area



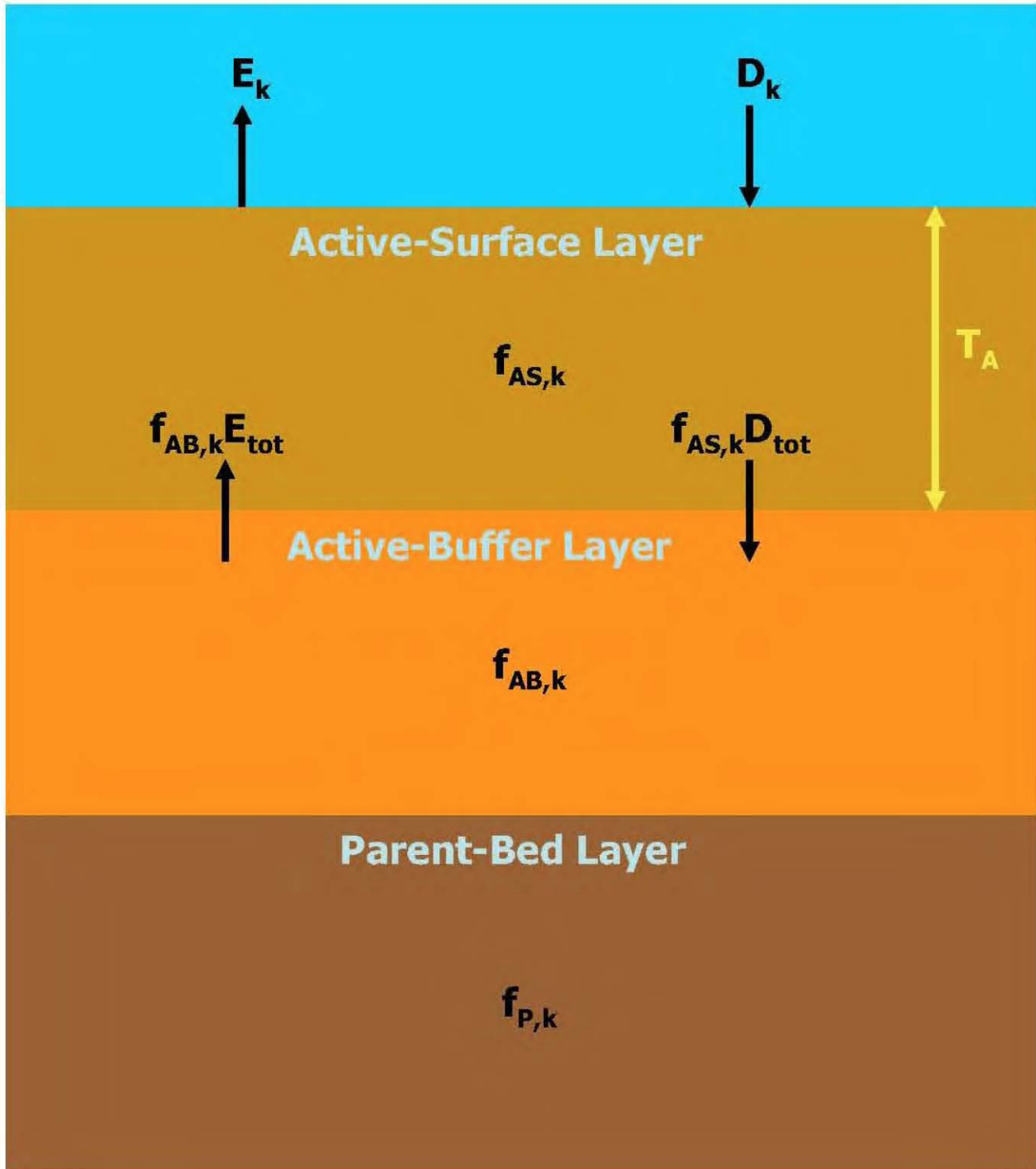


Figure A-6

Schematic of Interactions between the Water Column, Active Layer, and Parent-bed Layer when the Active-buffer Layer is Present
Patrick Bayou Study Area

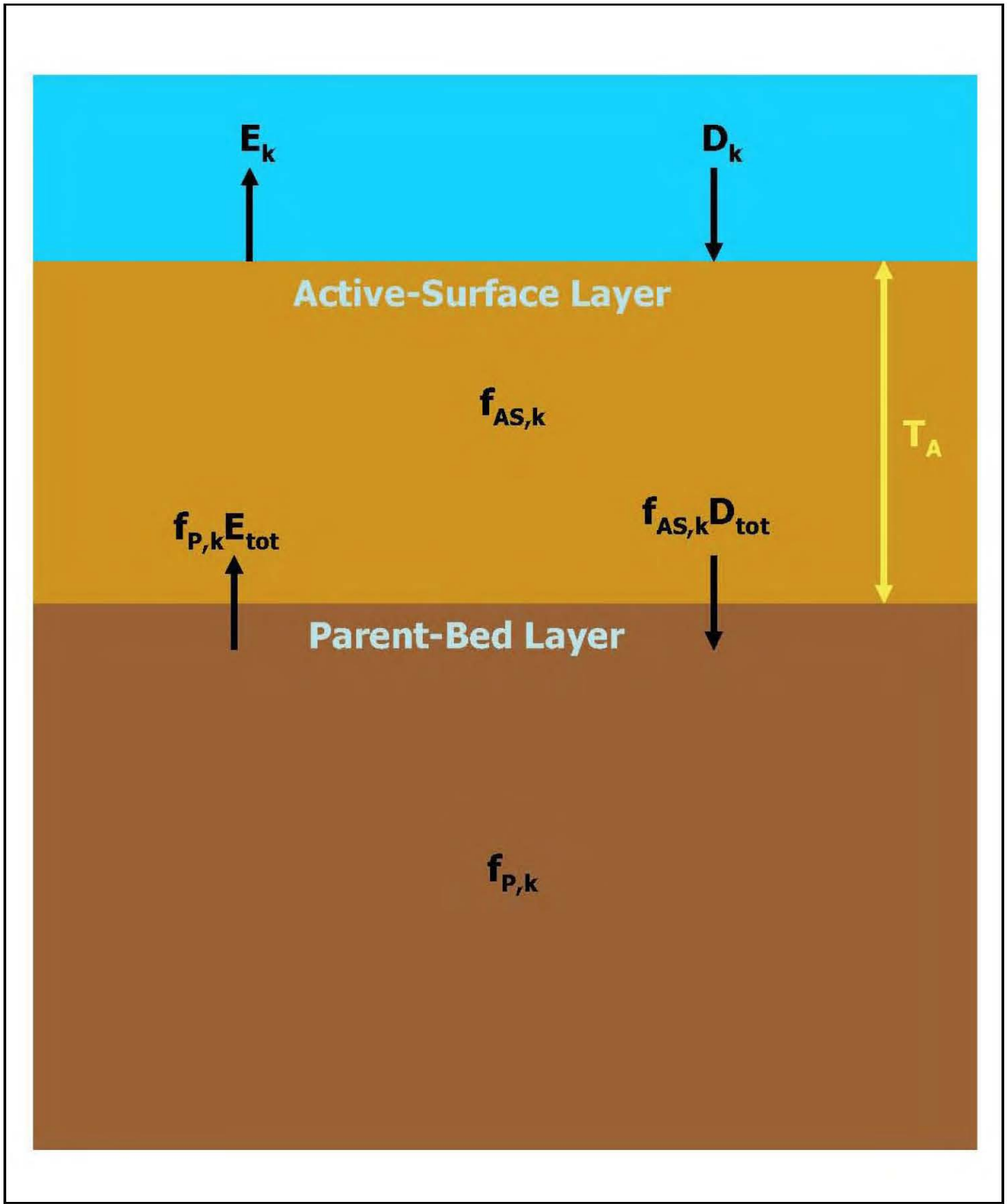


Figure A-7

Schematic of Interactions between the Water Column, Active Layer, and Parent-bed Layer when the Active-buffer Layer is Not Present
Patrick Bayou Study Area

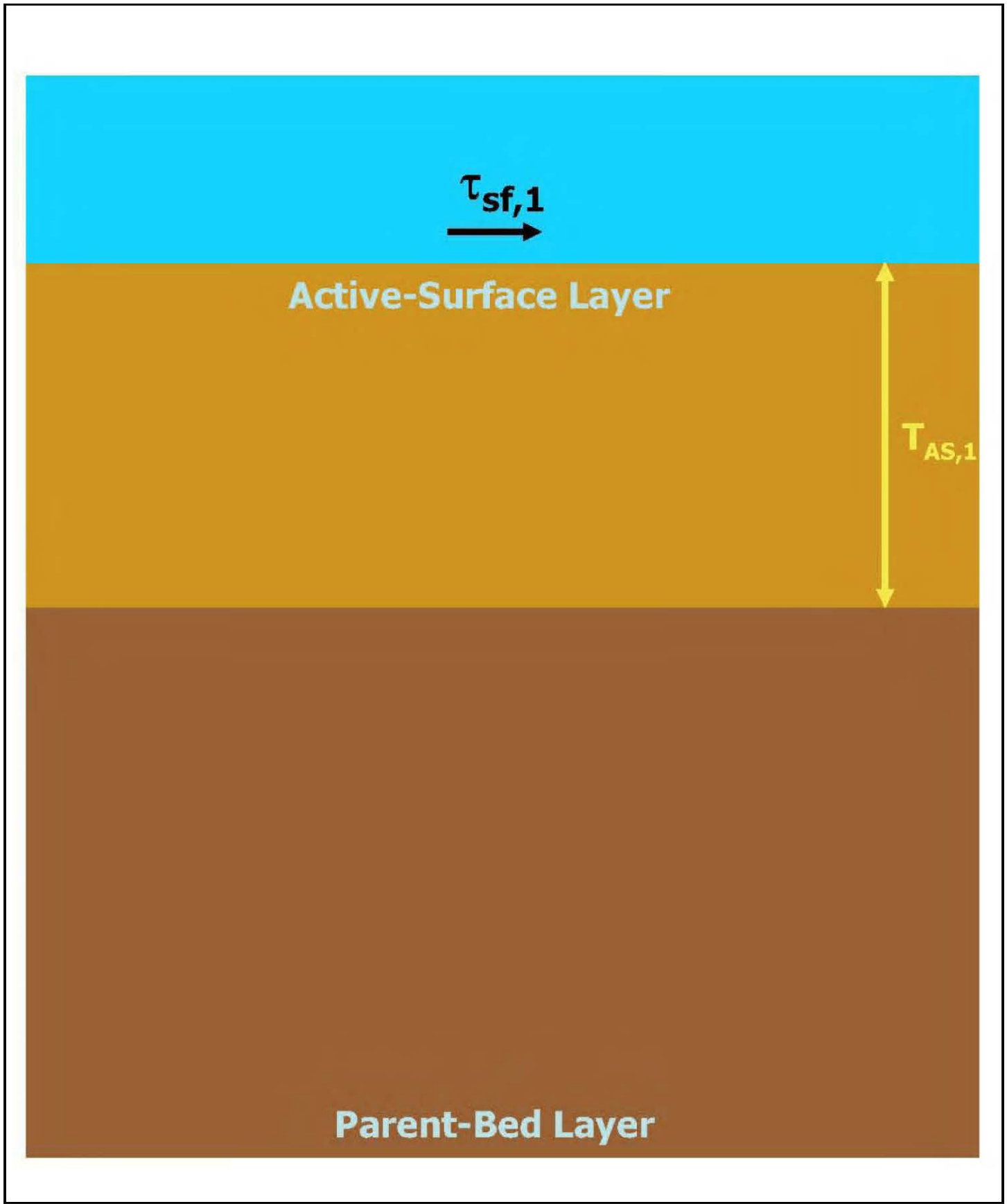


Figure A-8

Initial Structure of Bed with No Active-buffer Layer at Time = t_1
Patrick Bayou Study Area

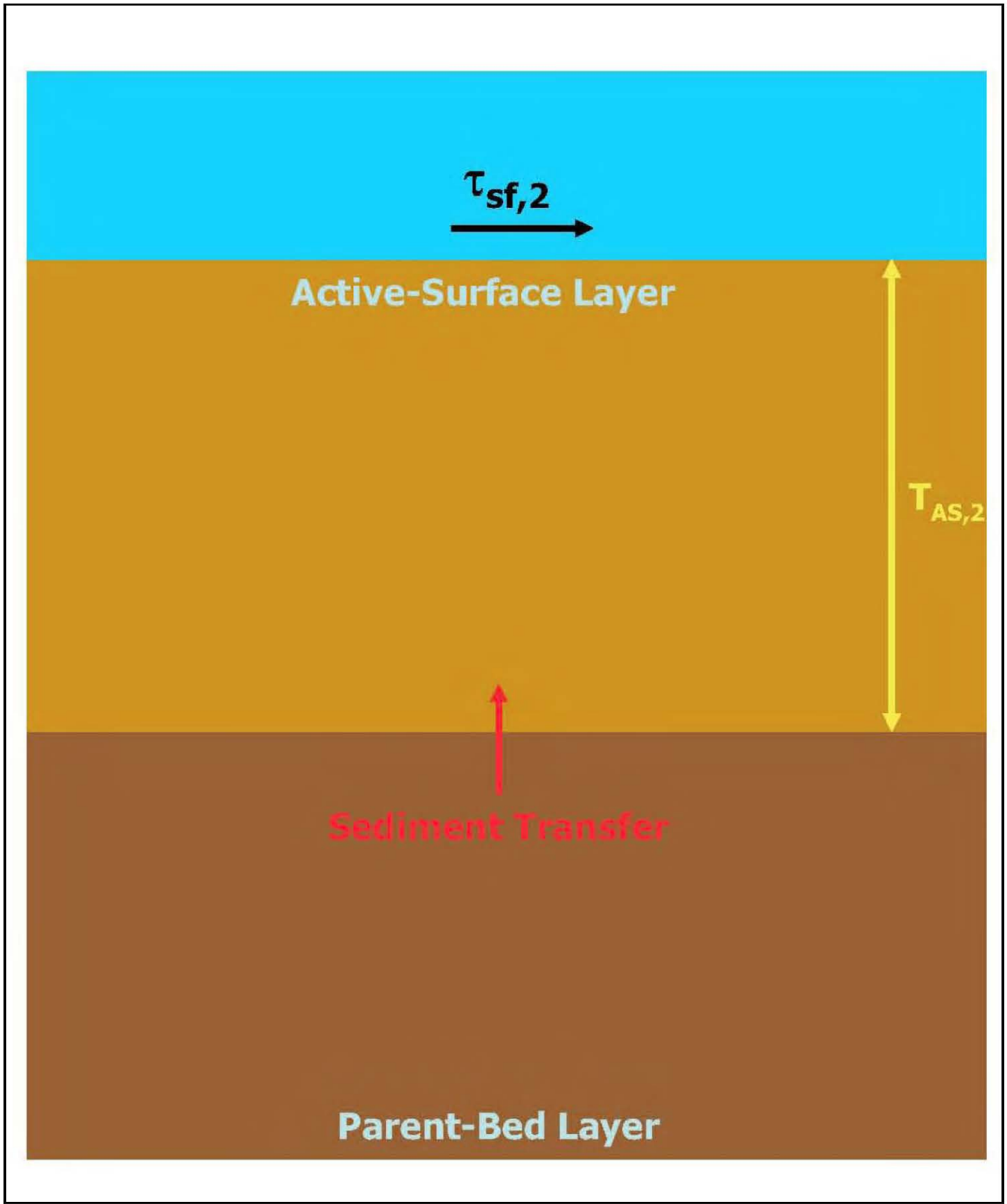


Figure A-9

Active-surface Layer Thickness Increases as Shear Stress Increases ($\tau_2 > \tau_1$) at Time = t_2
Patrick Bayou Study Area

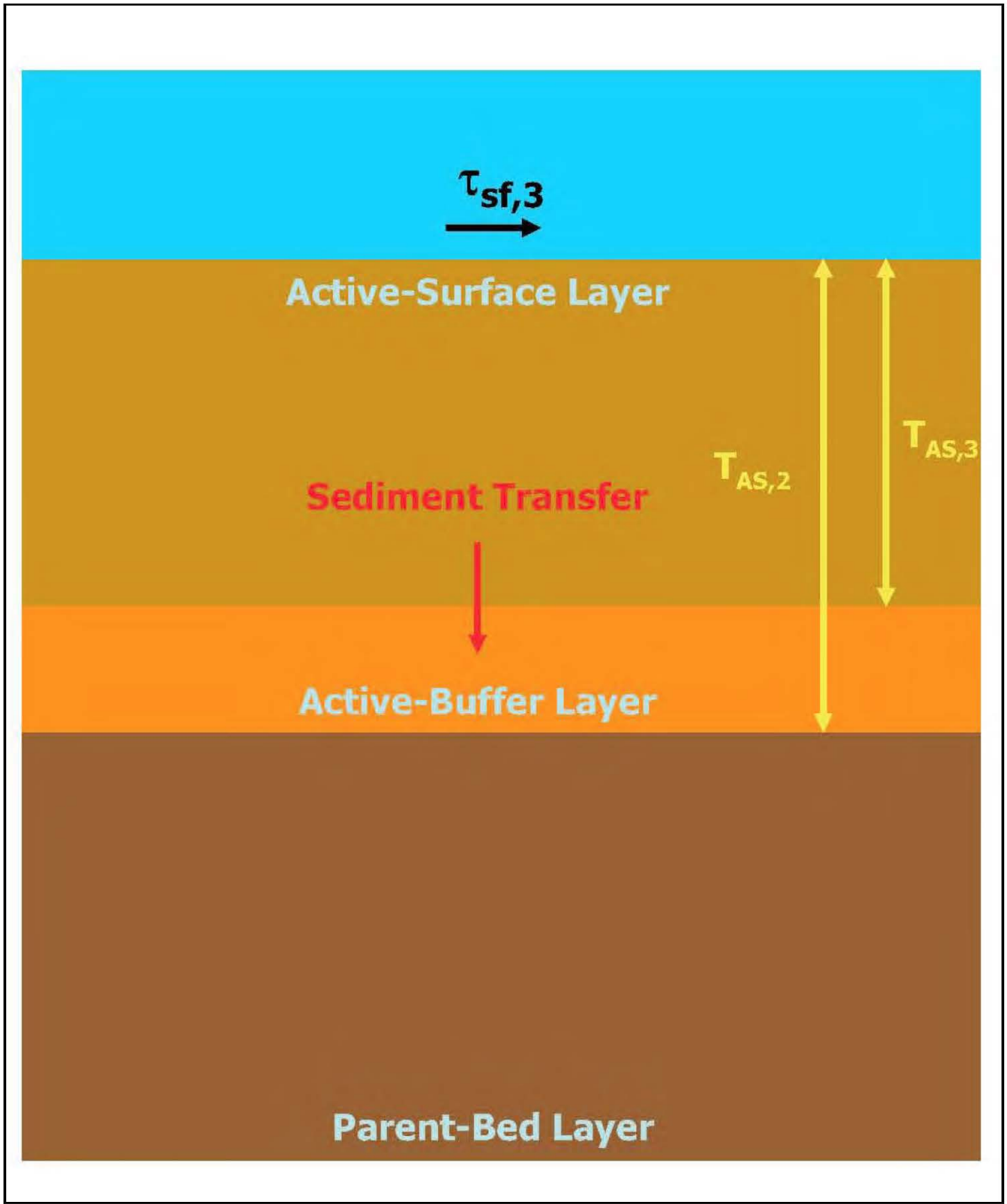


Figure A-10

Active-surface Layer Thickness Decreases and Active-buffer Layer is Created
as Shear Stress Decreases ($\tau_3 < \tau_2$) at Time = t_3
Patrick Bayou Study Area

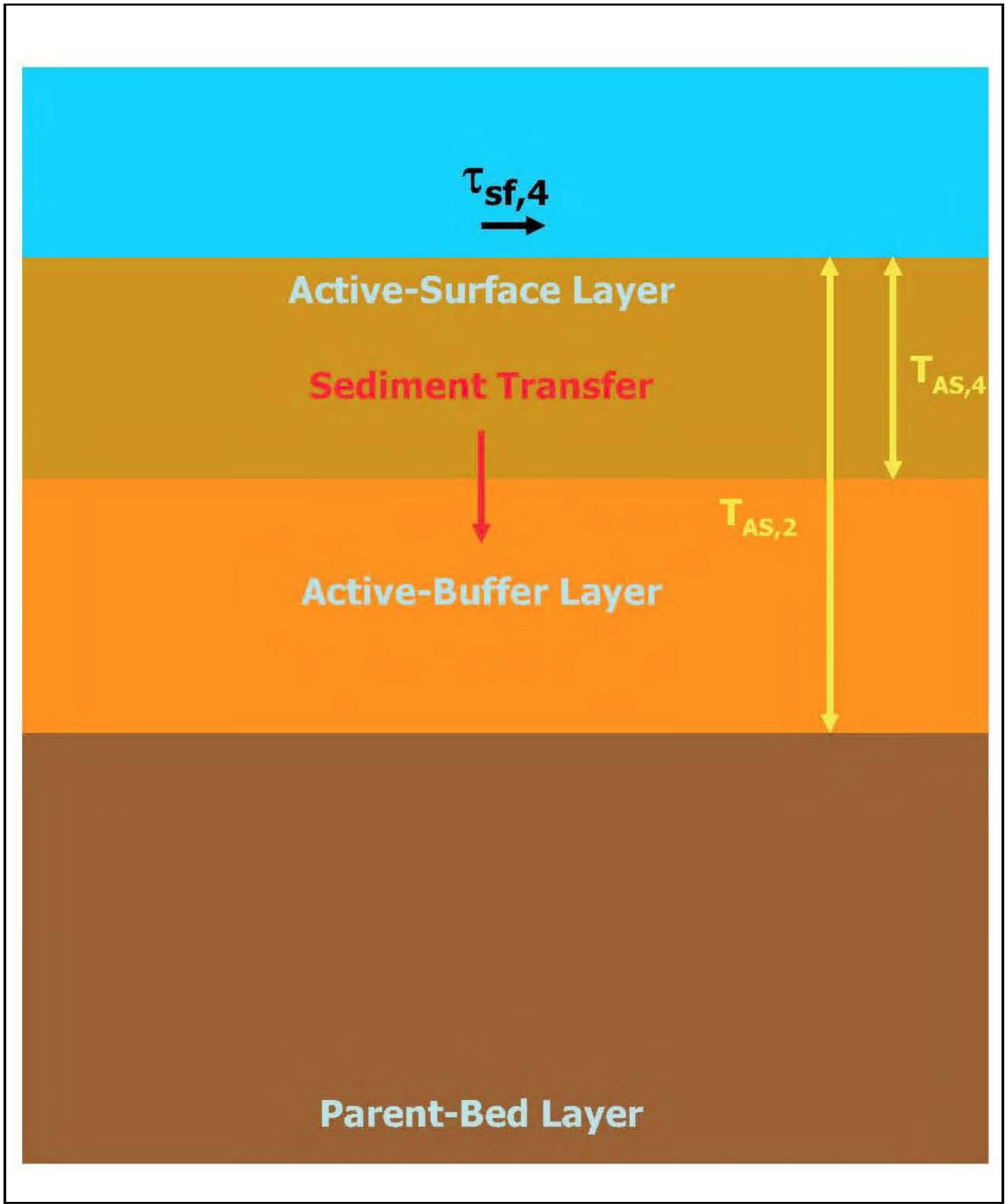


Figure A-11

Active-Surface Layer Thickness Decreases and Active-buffer Layer Thickness Increases as Shear Stress Continues to Decrease ($\tau_4 < \tau_3$) at time = t_4
Patrick Bayou Study Area

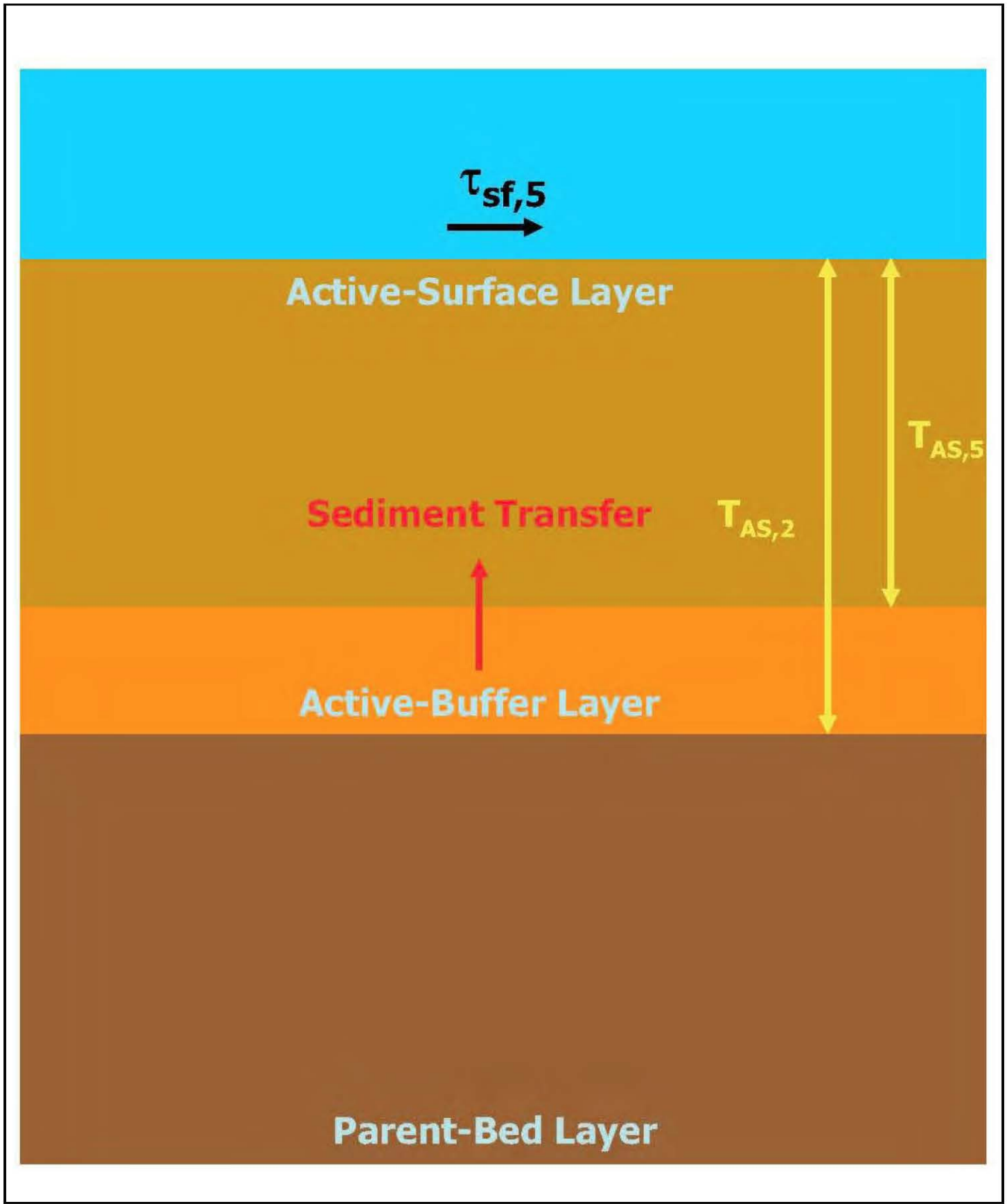


Figure A-12

Active-surface Layer Thickness Increases and Active-buffer Layer Thickness Decreases as Shear Stress Increases ($\tau_5 > \tau_4$) at Time = t_5
Patrick Bayou Study Area

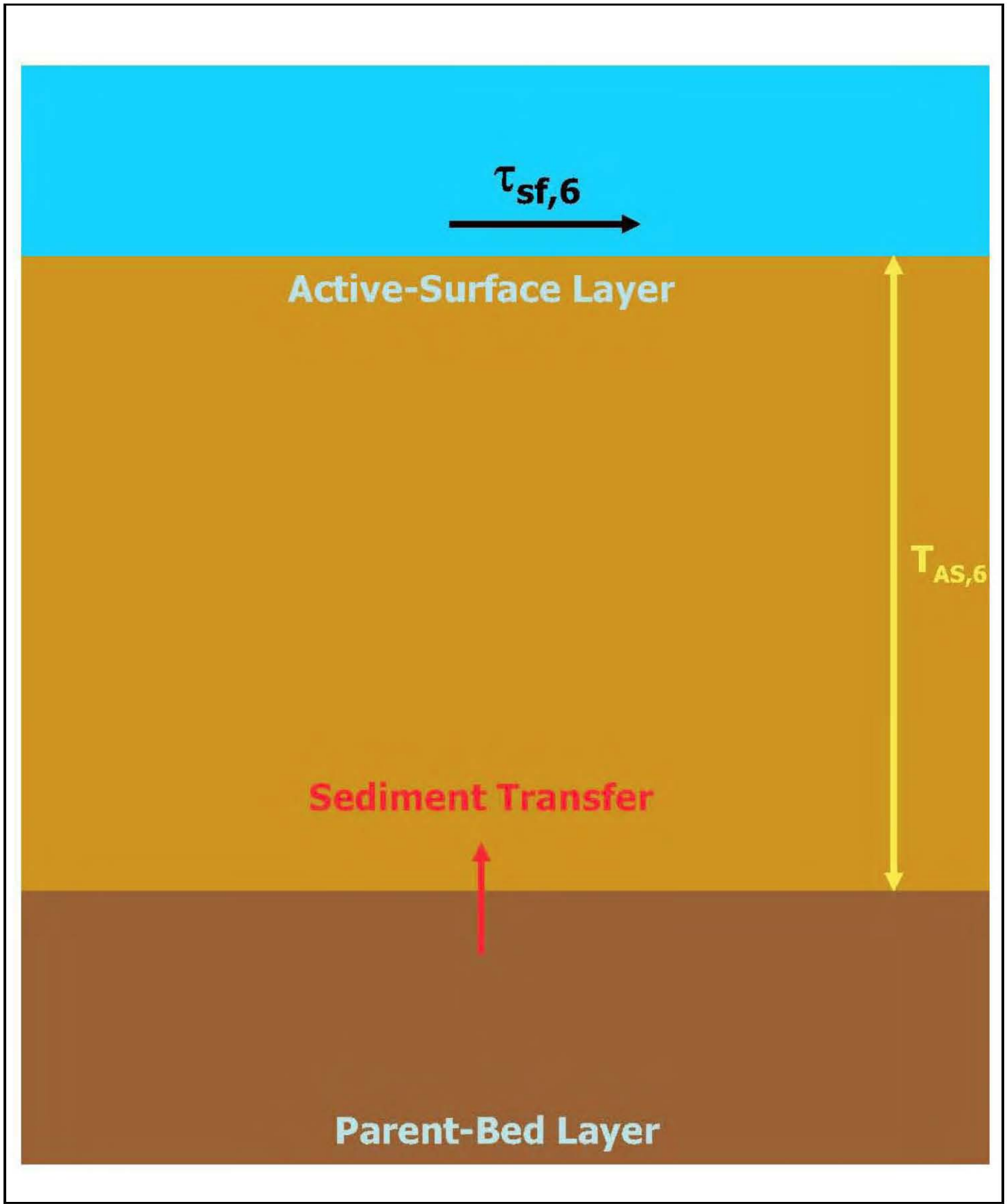


Figure A-13

Active-surface Layer Thickness Increases and Active-buffer Layer Is Destroyed as Shear Stress Increases ($\tau_6 > \tau_5, \tau_6 > \tau_2$) at Time = t_6
Patrick Bayou Study Area

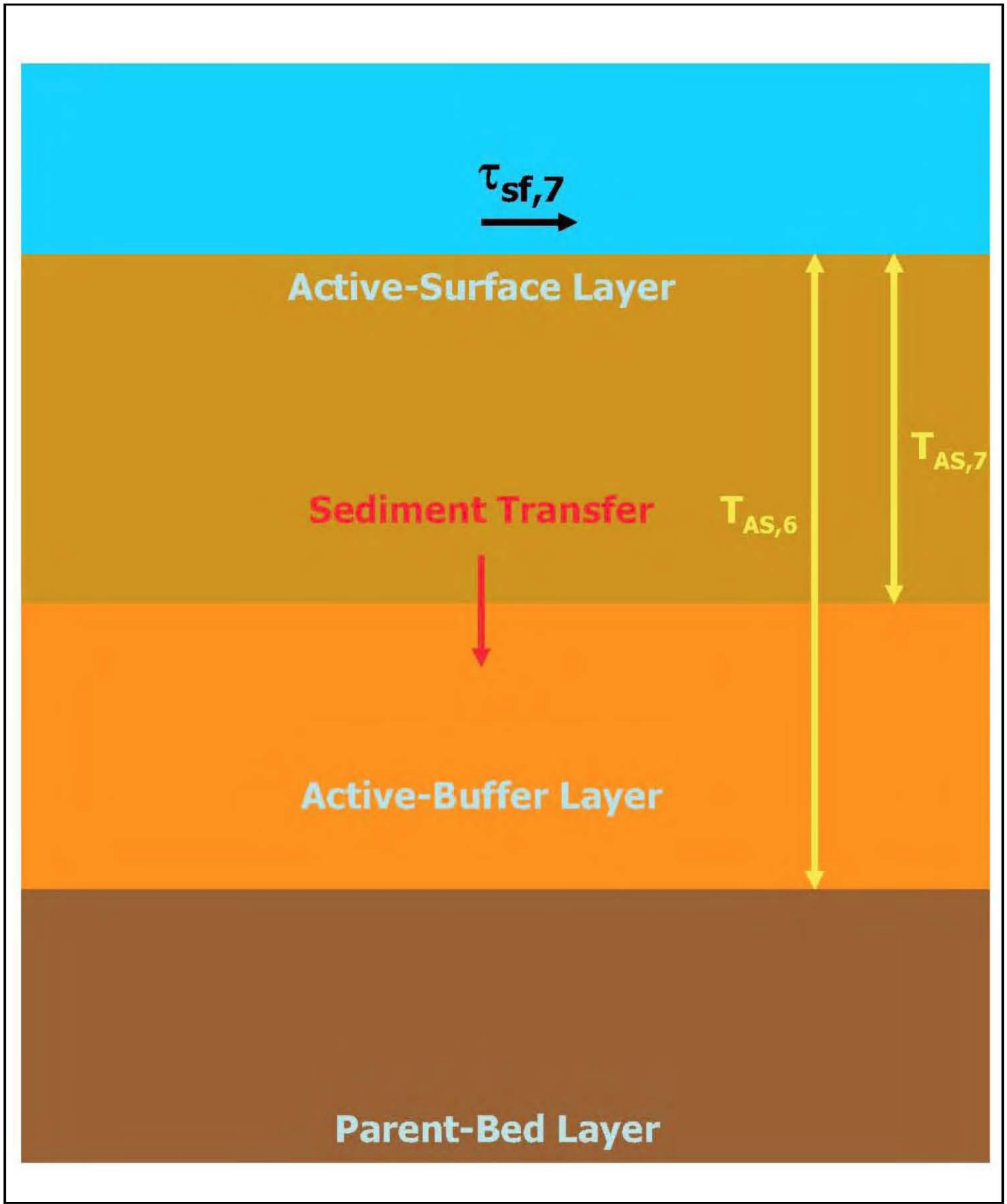


Figure A-14

Active-surface Layer Thickness Decreases and New Active-buffer Layer is Created as Shear Stress Decreases ($\tau_7 < \tau_6$) at Time = t_7
Patrick Bayou Study Area

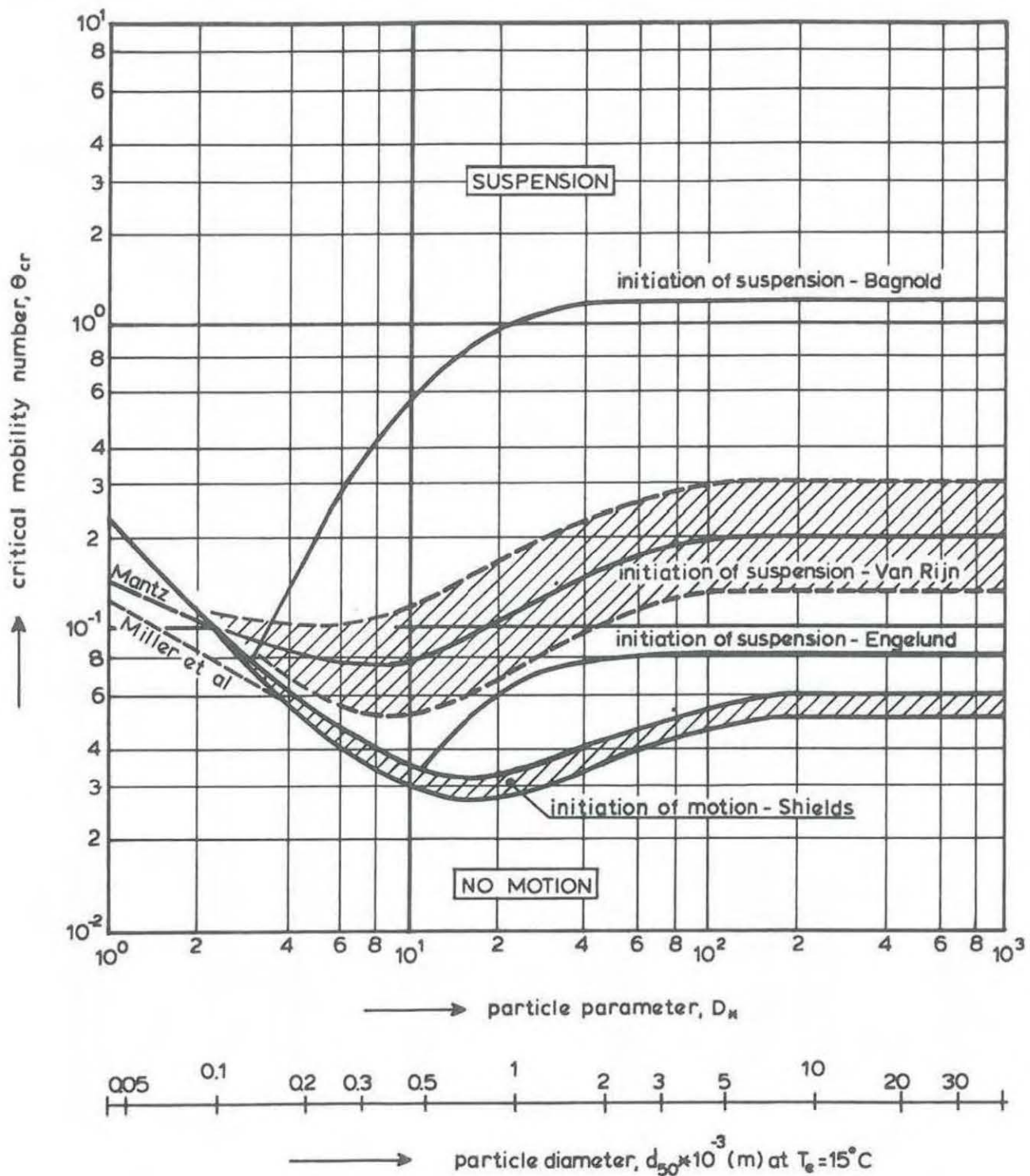


Figure A-15

Initiation of Motion and Suspension for a Current Over a Plane Bed, $\Theta=f(D^*)$, from Van Rijn (1989)

Patrick Bayou Study Area

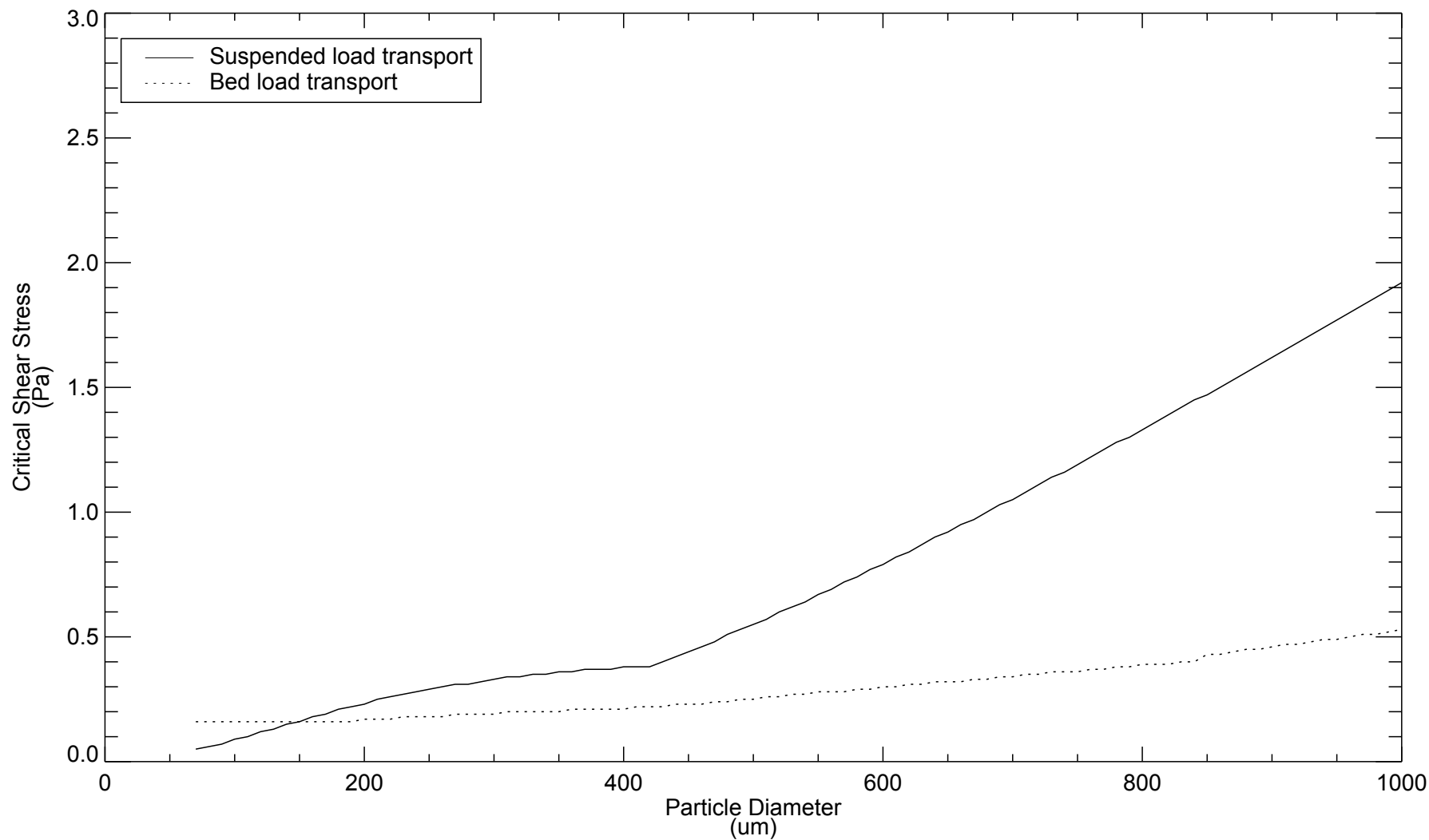


Figure A-16
Critical Shear Stress for Initiation of Suspended and Bed Load Transport as a Function of
Particle Diameter
Patrick Bayou Study Area

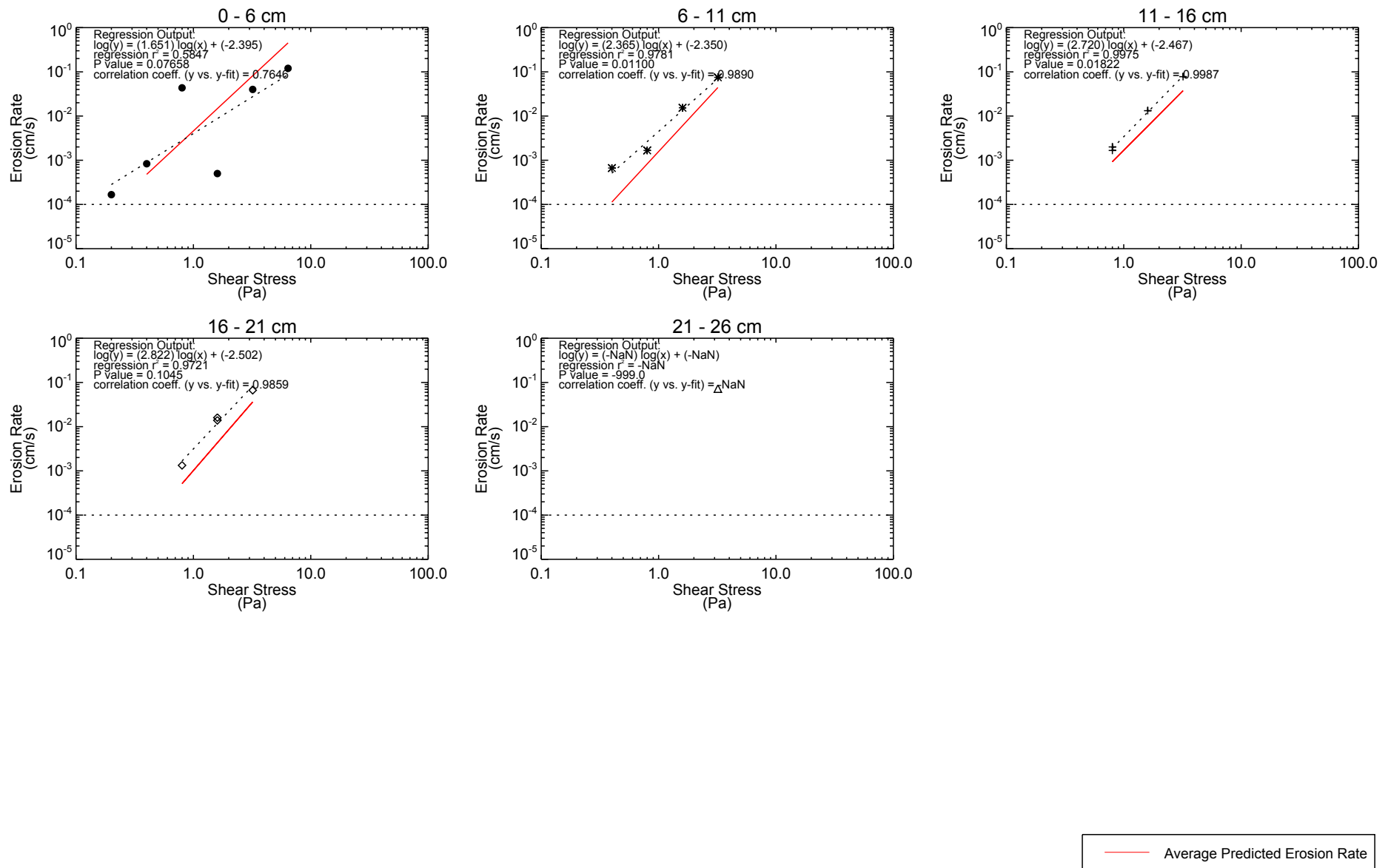


Figure B-1
 Comparison of Data (symbols) to Results of Log-linear Regression (dashed line) for Core SF-1
 Patrick Bayou Study Area

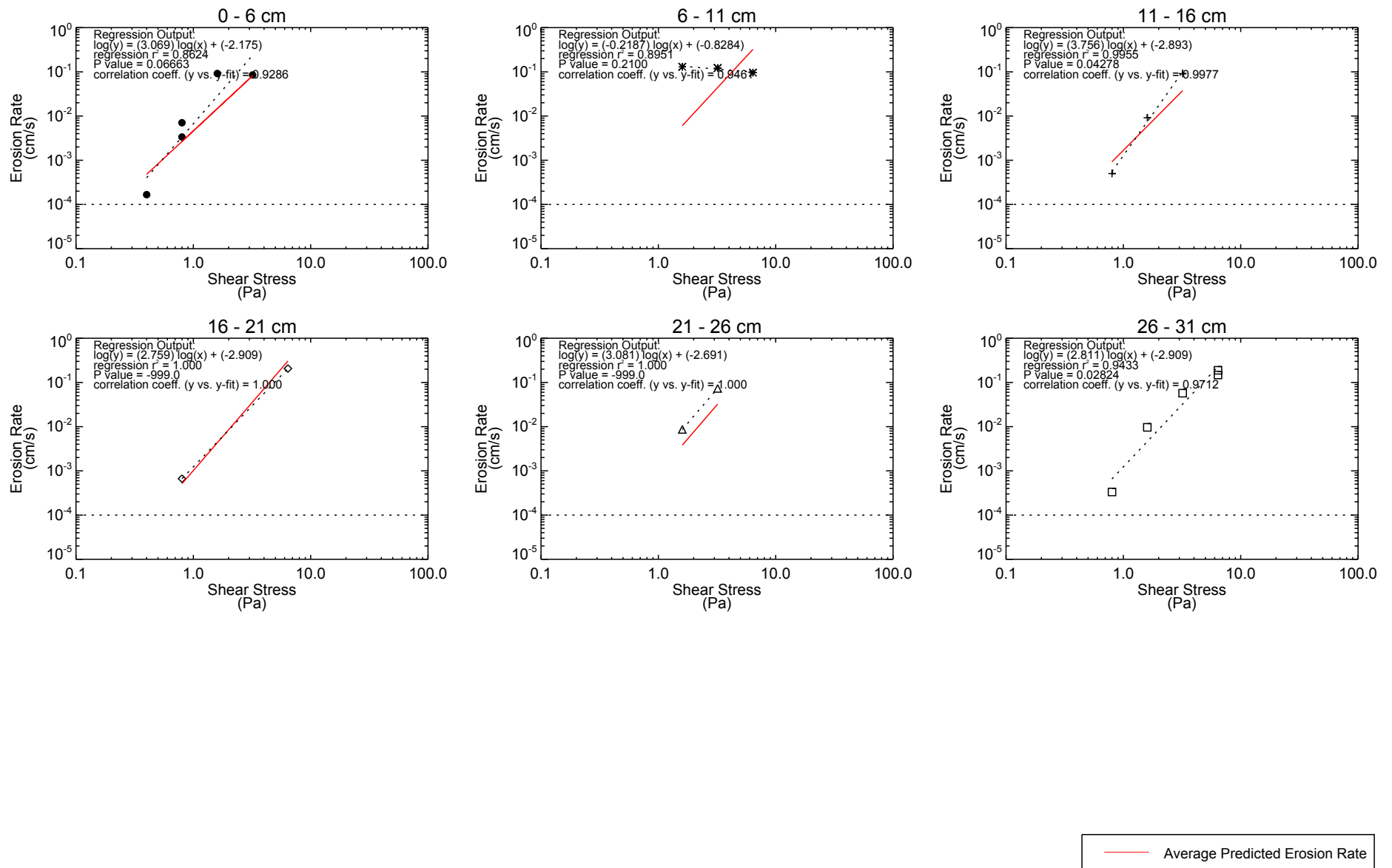


Figure B-2
Comparison of Data (symbols) to Results of Log-linear Regression (dashed line) for Core SF-2
Patrick Bayou Study Area

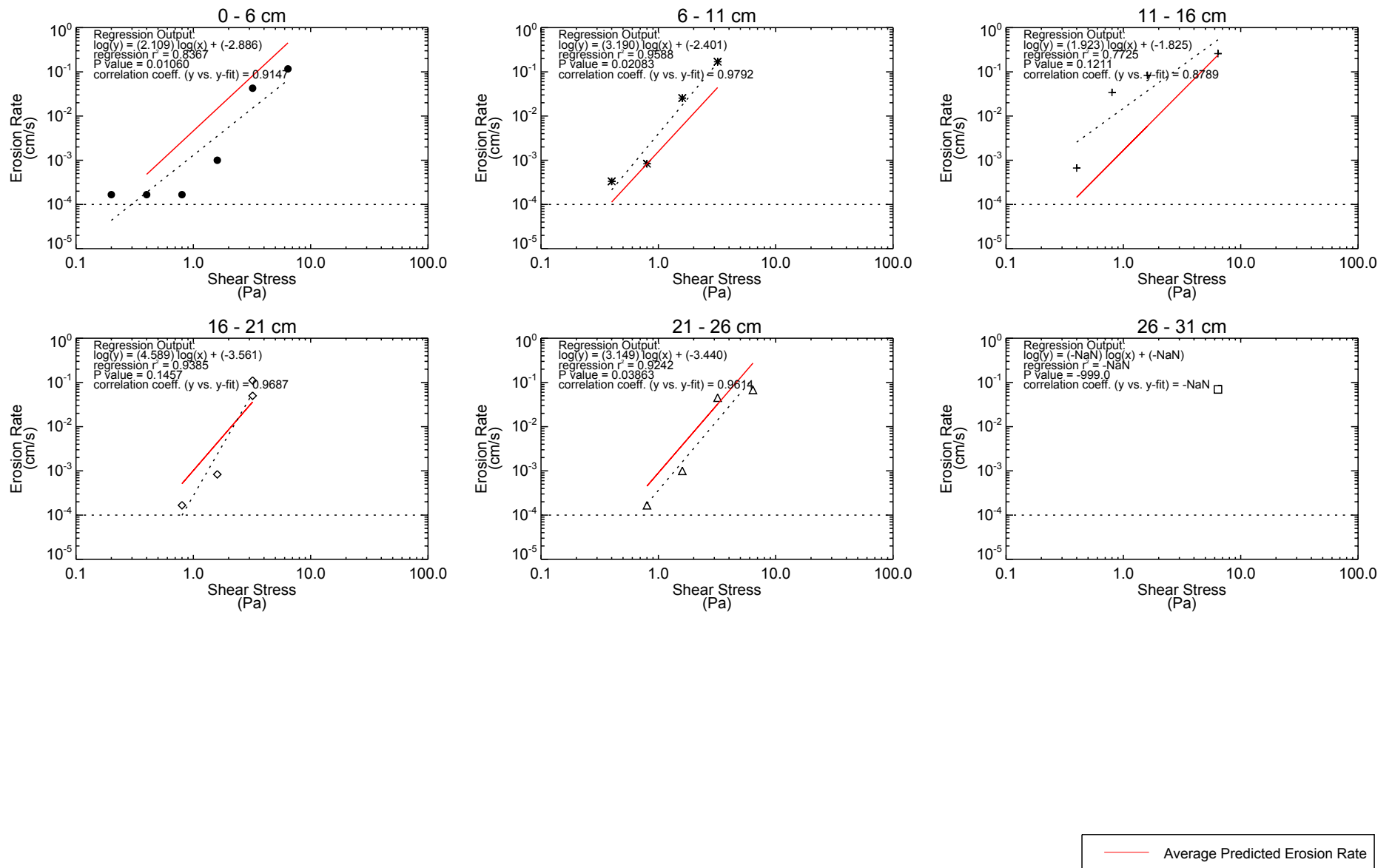


Figure B-3
 Comparison of Data (symbols) to Results of Log-linear Regression (dashed line) for Core SF-3
 Patrick Bayou Study Area

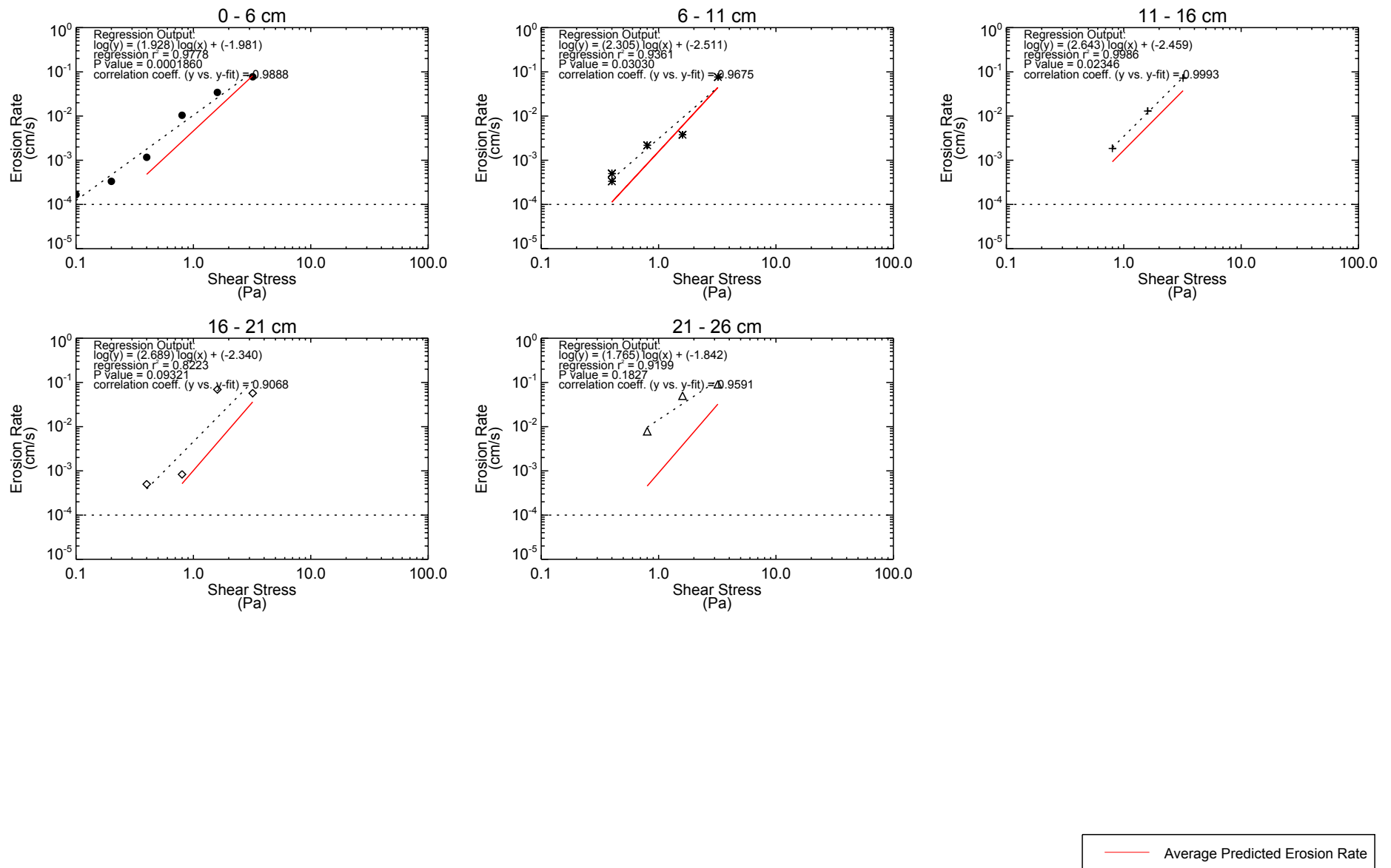


Figure B-4
 Comparison of Data (symbols) to Results of Log-linear Regression (dashed line) for Core SF-4
 Patrick Bayou Study Area

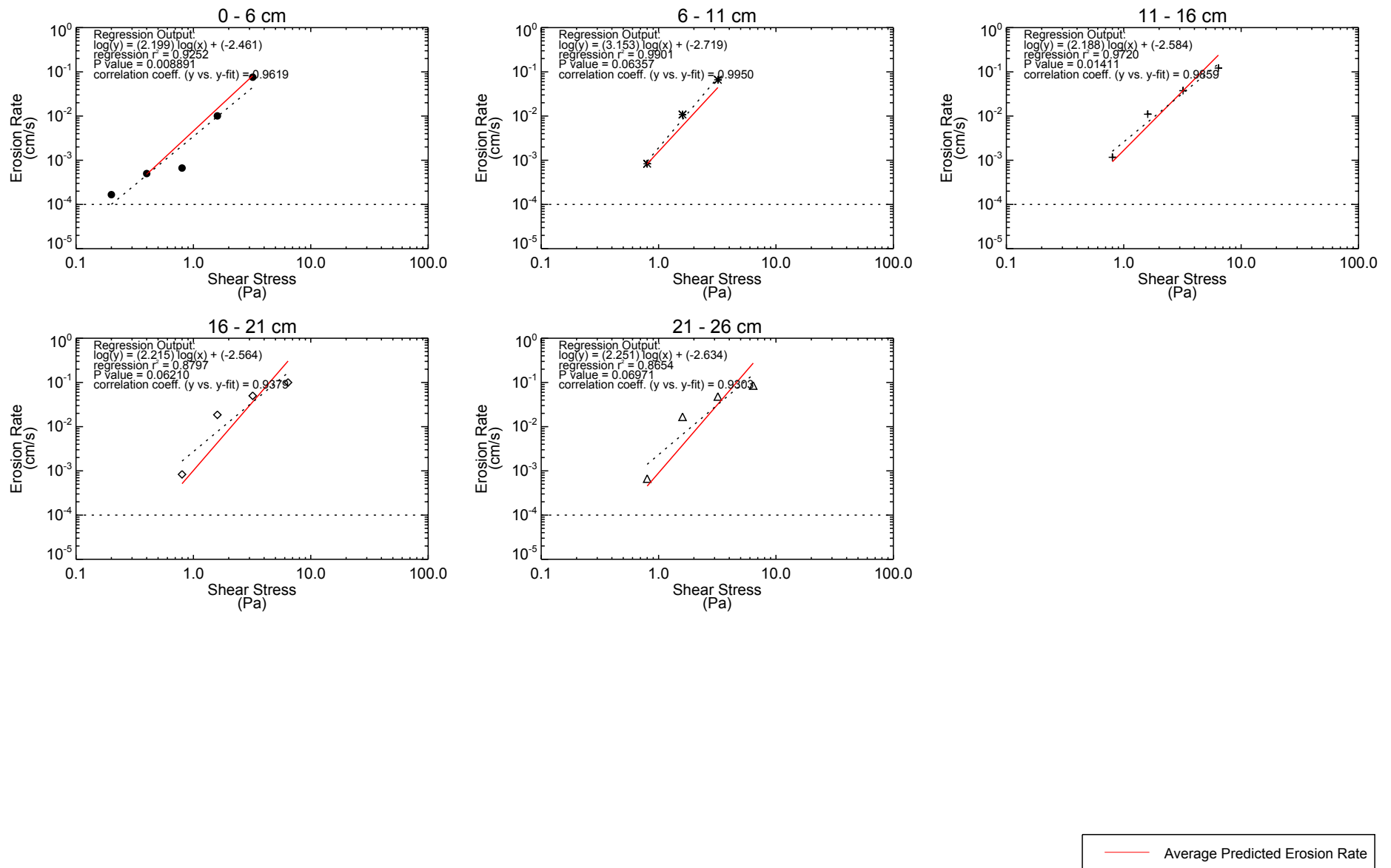


Figure B-5
 Comparison of Data (symbols) to Results of Log-linear Regression (dashed line) for Core SF-5
 Patrick Bayou Study Area

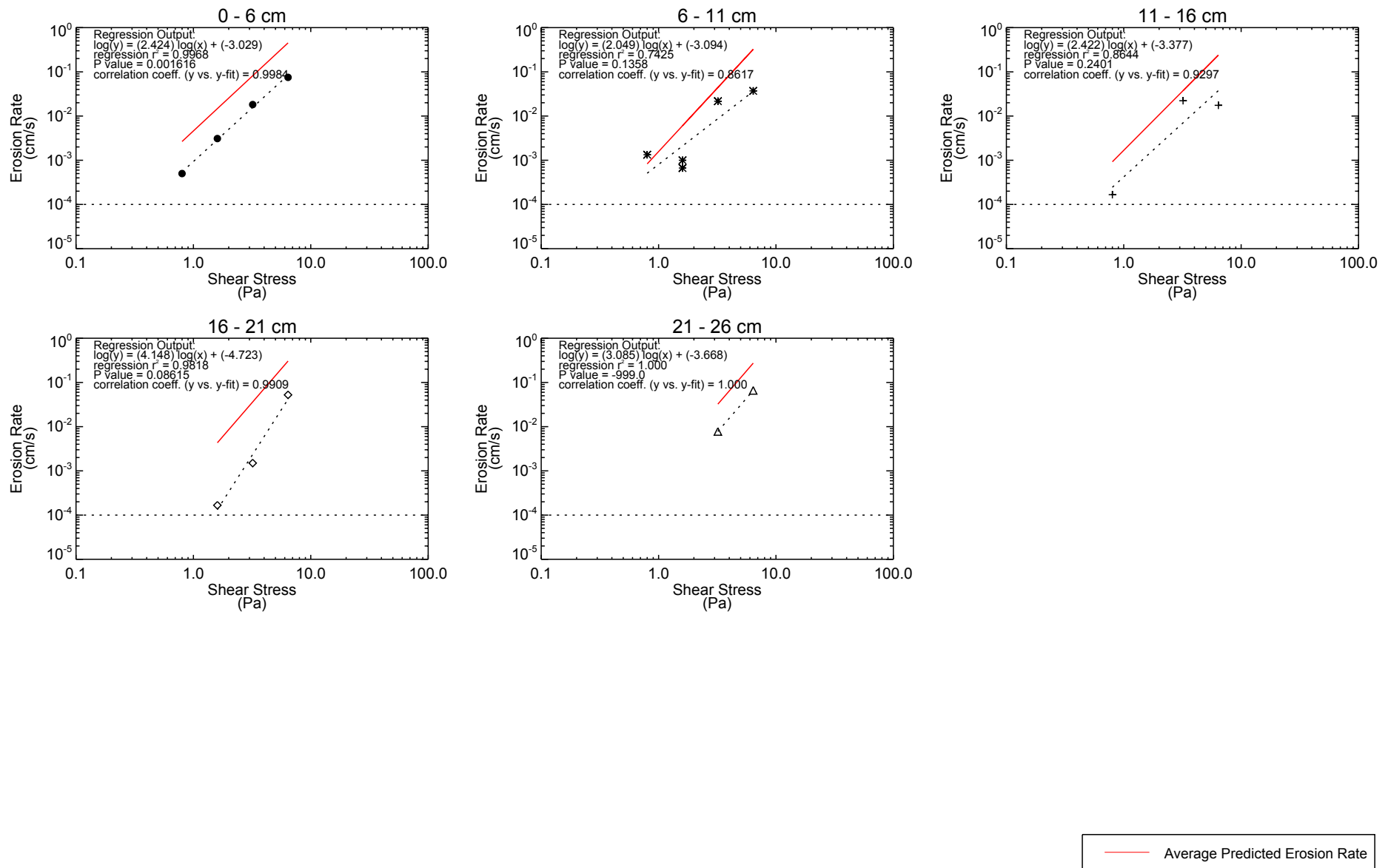


Figure B-6
 Comparison of Data (symbols) to Results of Log-linear Regression (dashed line) for Core SF-6
 Patrick Bayou Study Area

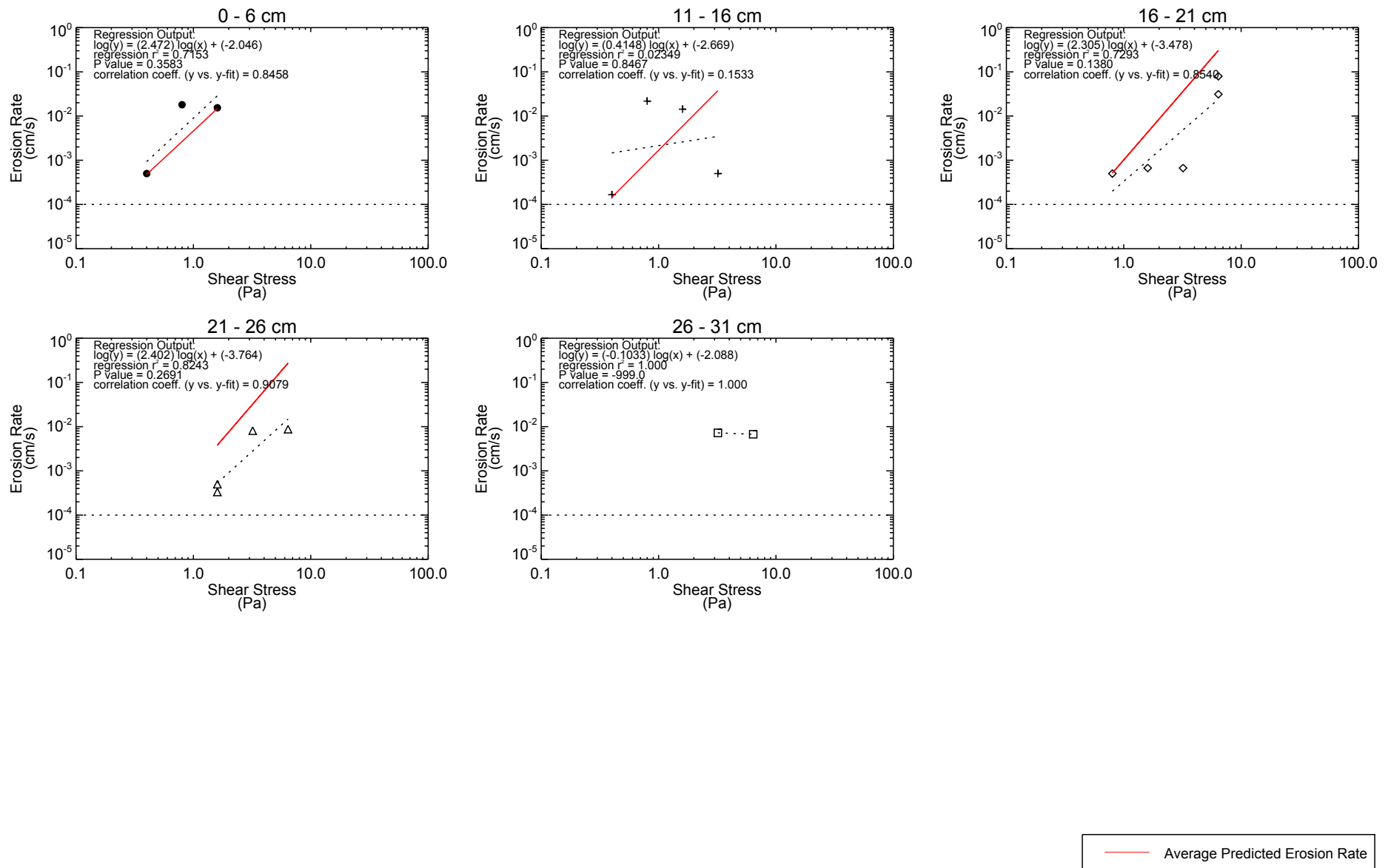


Figure B-7
 Comparison of Data (symbols) to Results of Log-linear Regression (dashed line) for Core SF-7
 Patrick Bayou Study Area

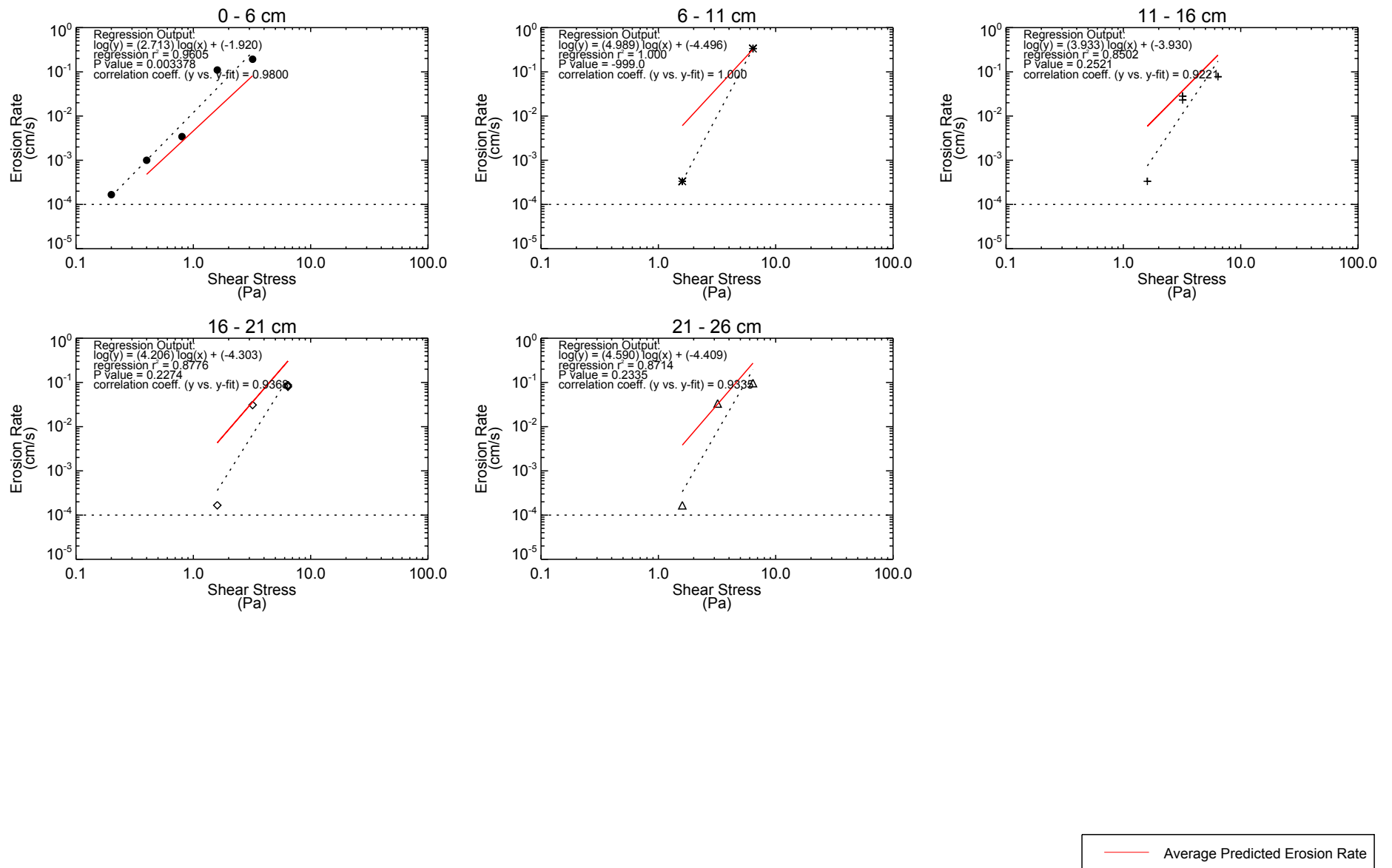


Figure B-8
 Comparison of Data (symbols) to Results of Log-linear Regression (dashed line) for Core SF-8
 Patrick Bayou Study Area

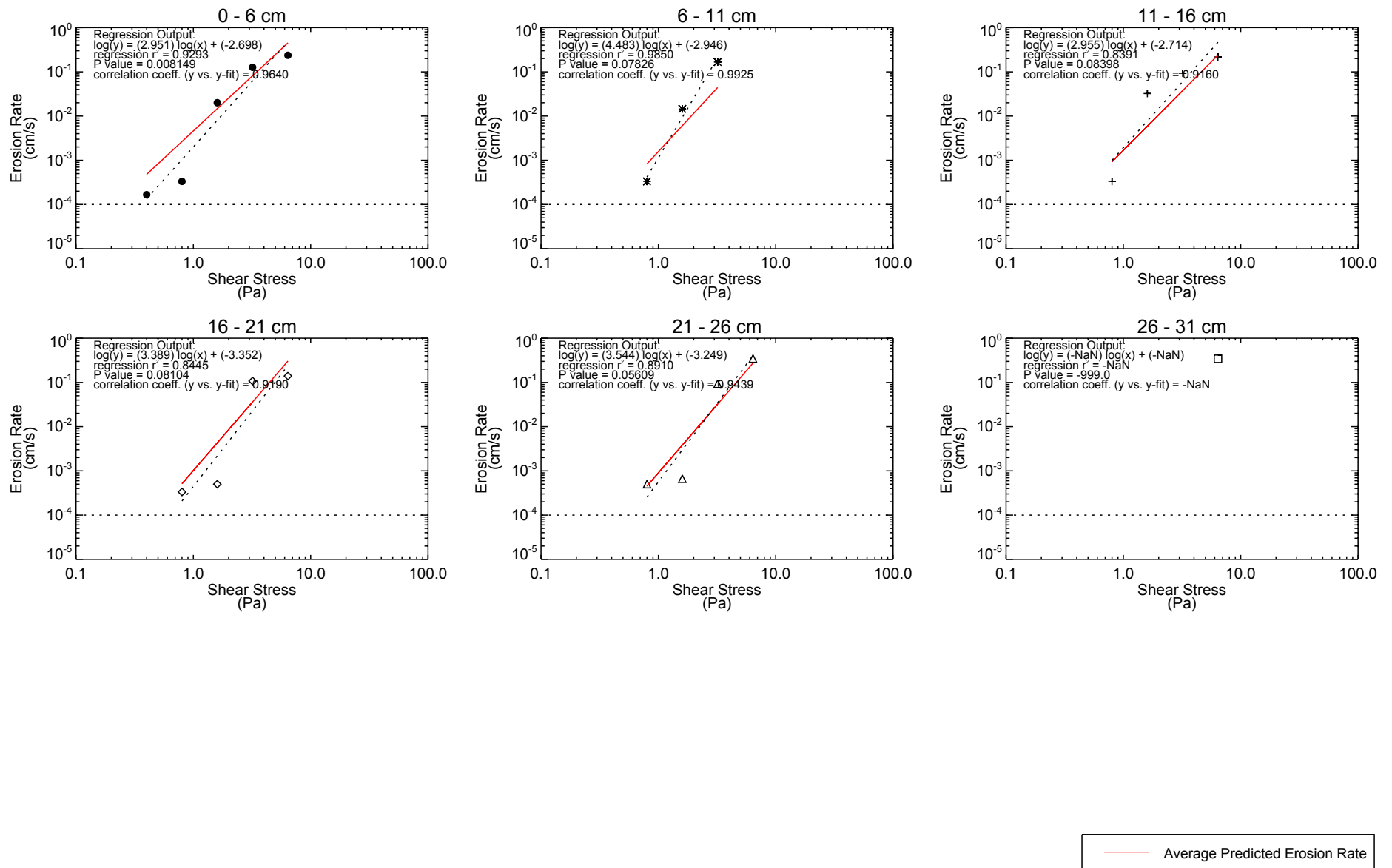


Figure B-9
 Comparison of Data (symbols) to Results of Log-linear Regression (dashed line) for Core SF-9
 Patrick Bayou Study Area

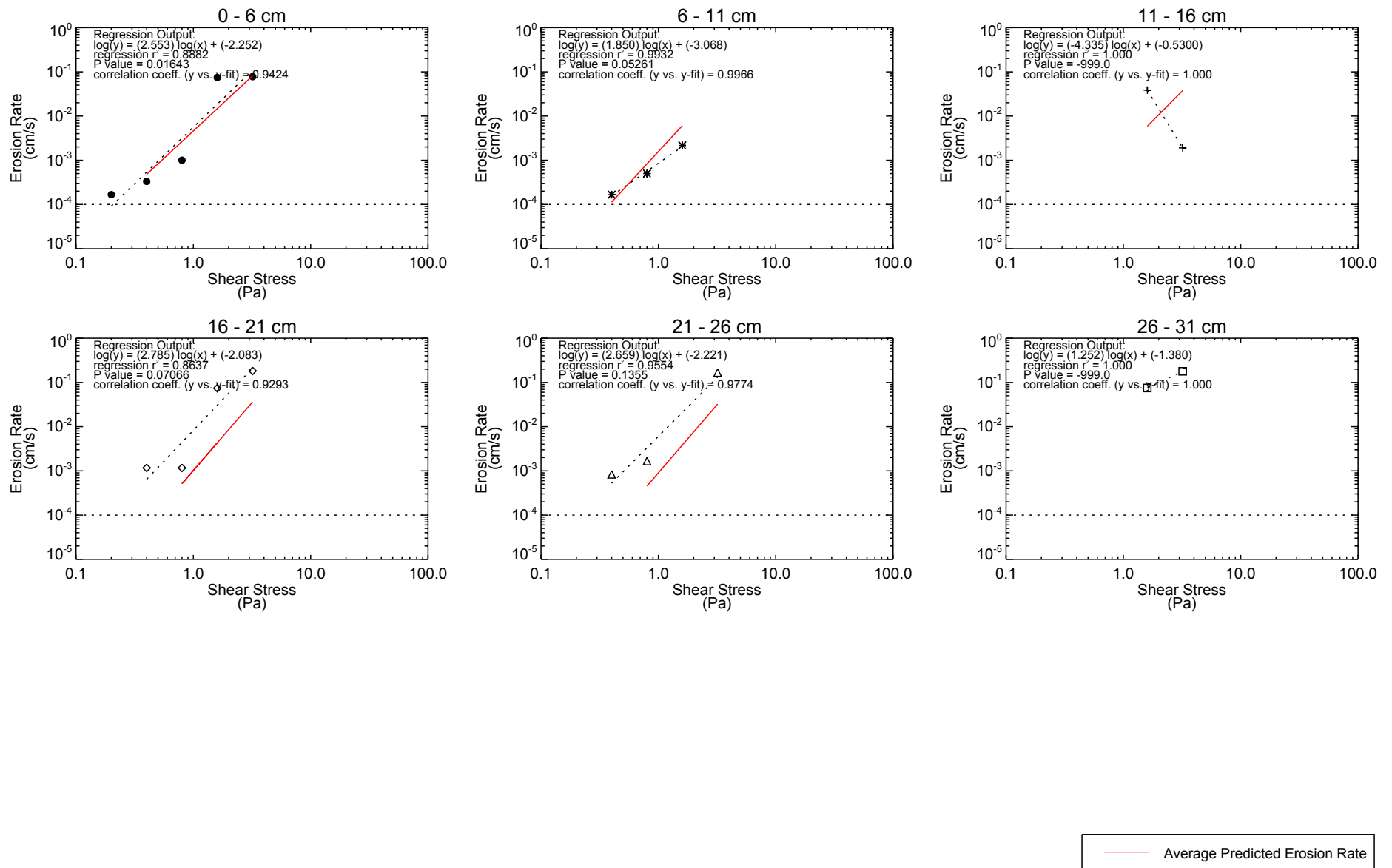


Figure B-10
 Comparison of Data (symbols) to Results of Log-linear Regression (dashed line) for Core SF-10
 Patrick Bayou Study Area

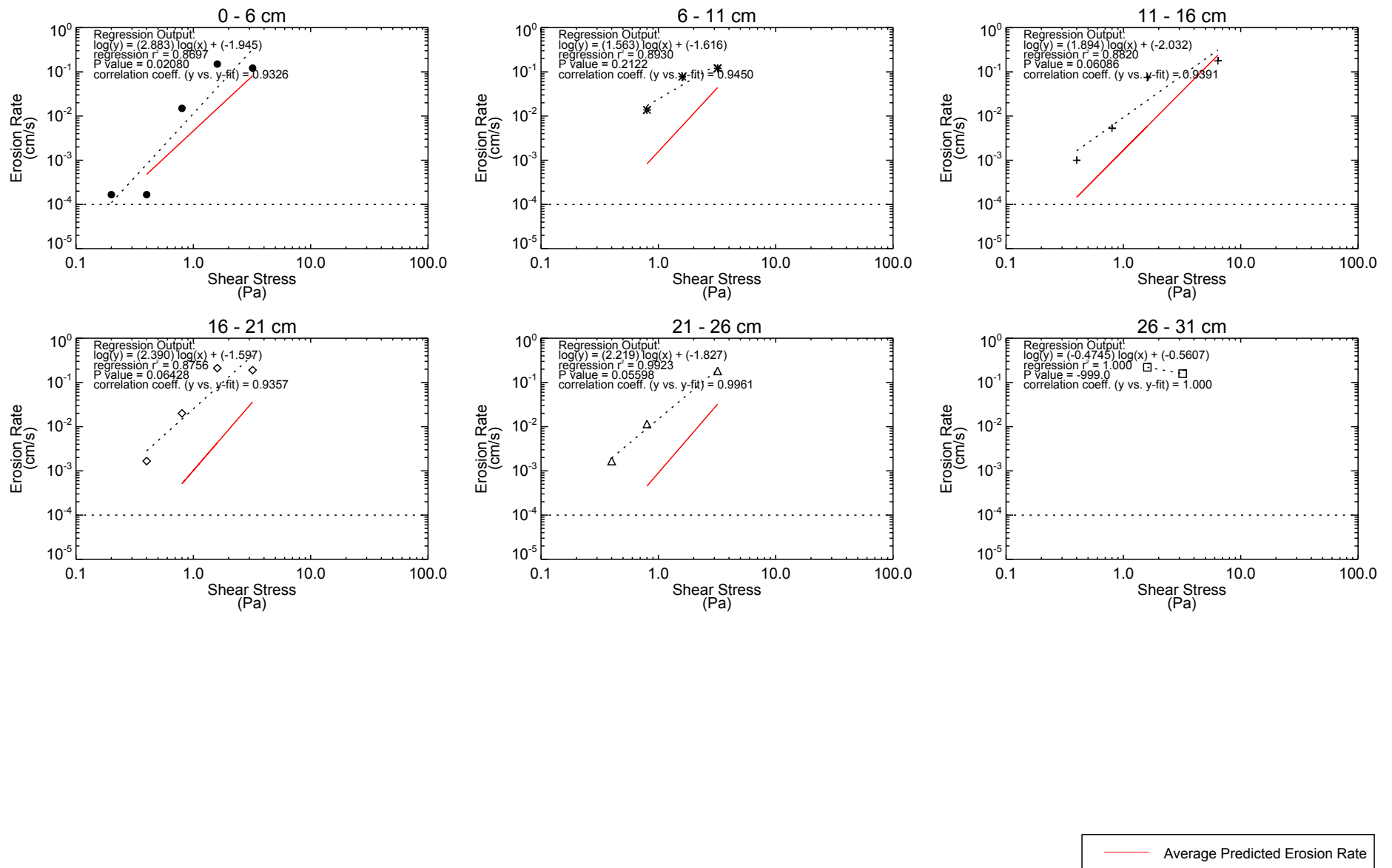


Figure B-11
 Comparison of Data (symbols) to Results of Log-linear Regression (dashed line) for Core SF-11
 Patrick Bayou Study Area

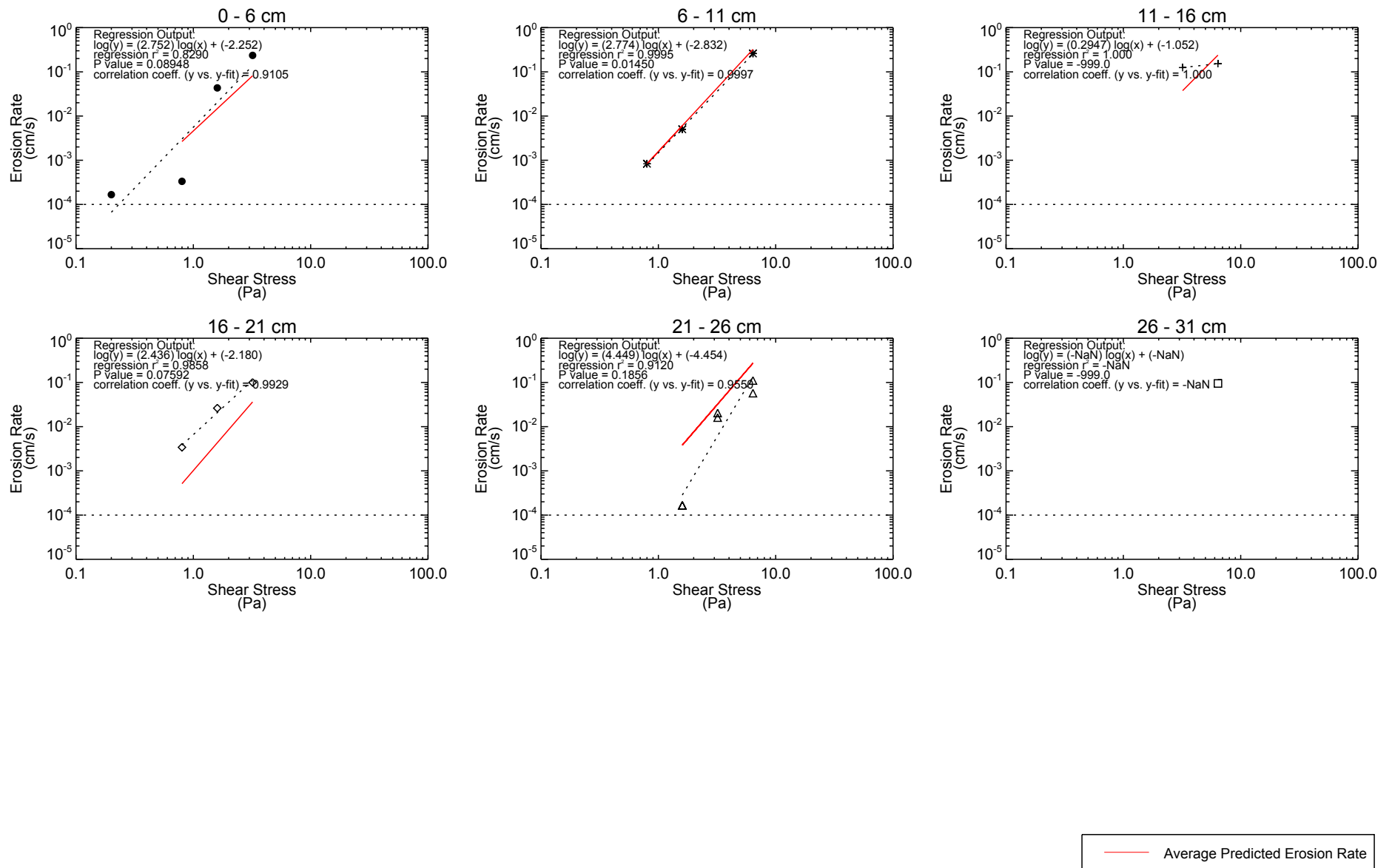


Figure B-12
 Comparison of Data (symbols) to Results of Log-linear Regression (dashed line) for Core SF-12
 Patrick Bayou Study Area

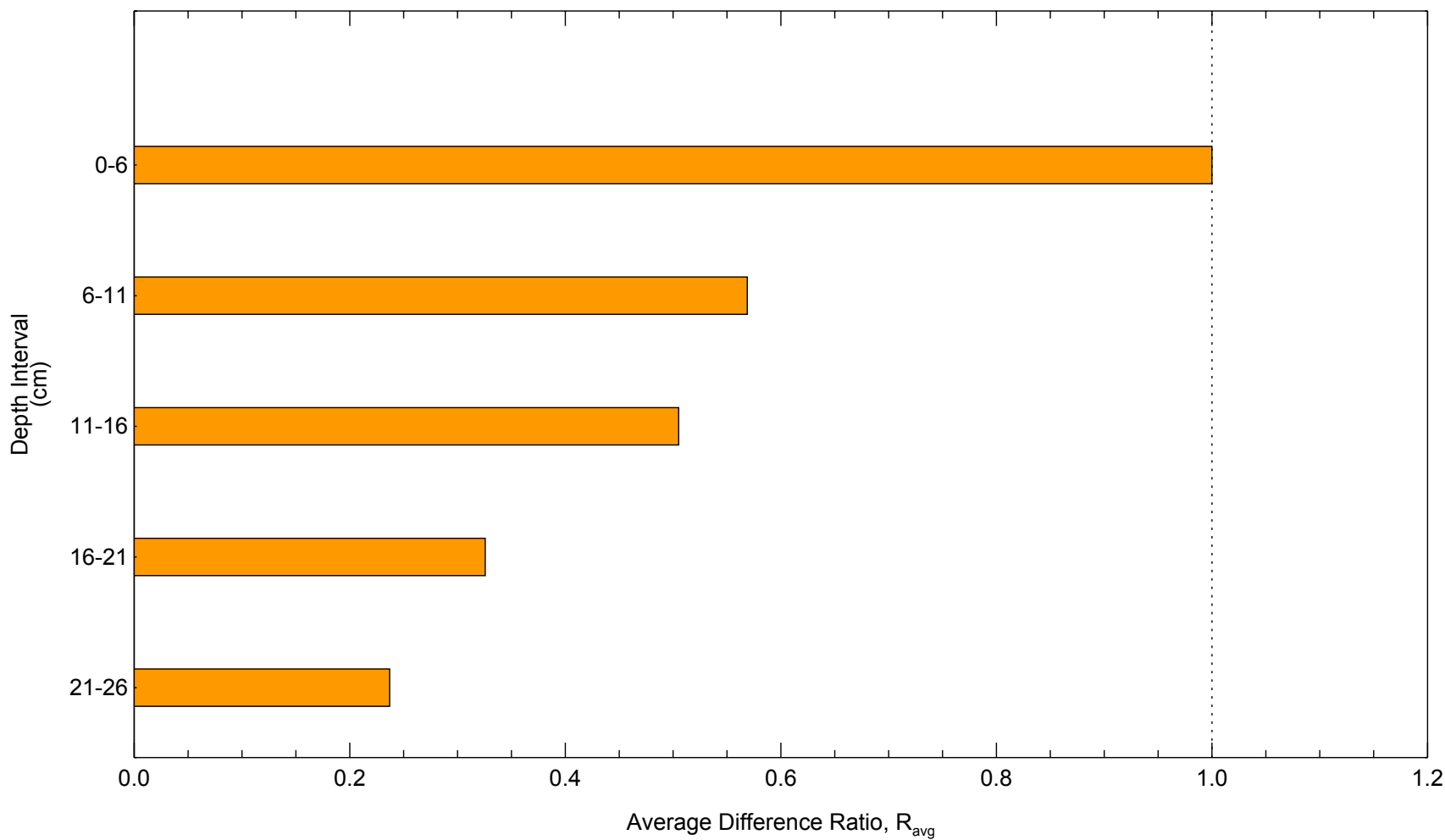


Figure B-13
Vertical Variation in Erodibility of Patrick Bayou Sediment
Patrick Bayou Study Area



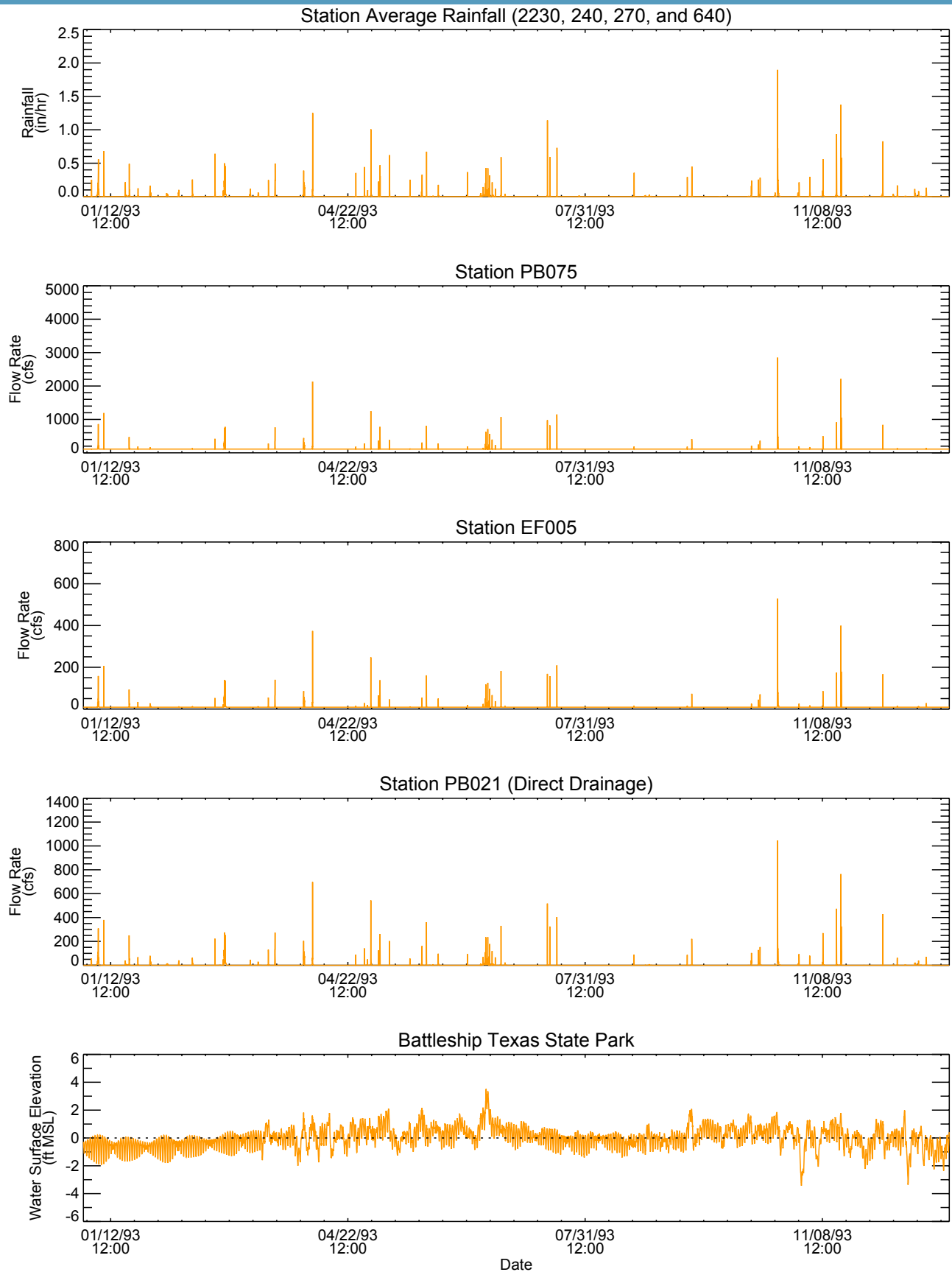


Figure C-1
Time History of Precipitation, Freshwater Inflow and Tidal Elevation Boundary
Conditions for 1993

Note: Rainfall data from Harris County Homeland Security and Emergency Management gauge stations. Flow rate predicted by watershed model. Water surface elevation from NOAA gauge station.

Patrick Bayou Study Area

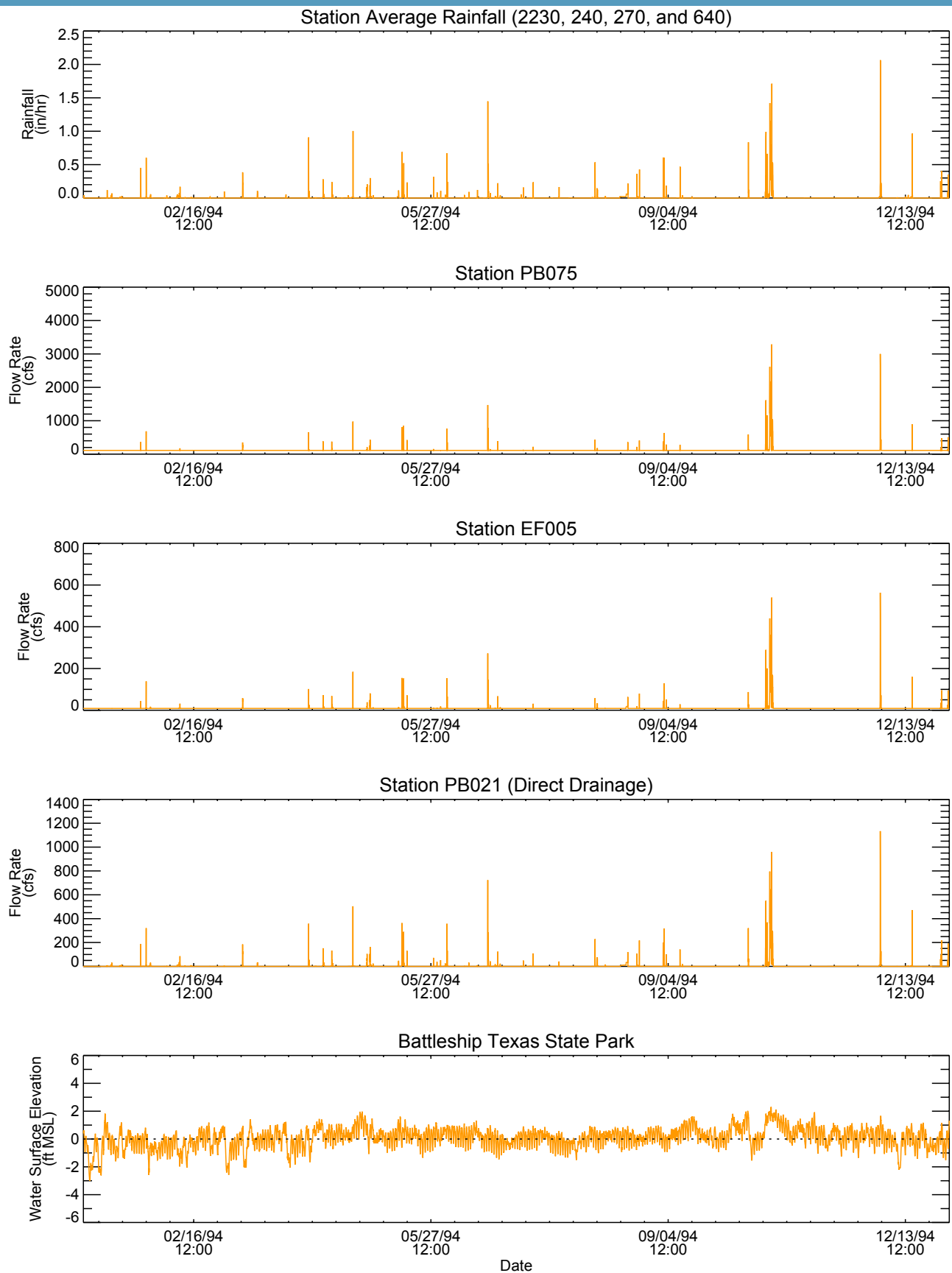


Figure C-2
Time History of Precipitation, Freshwater Inflow and Tidal Elevation Boundary Conditions for 1994

Note: Rainfall data from Harris County Homeland Security and Emergency Management gauge stations. Flow rate predicted by watershed model. Water surface elevation from NOAA gauge station.

Patrick Bayou Study Area



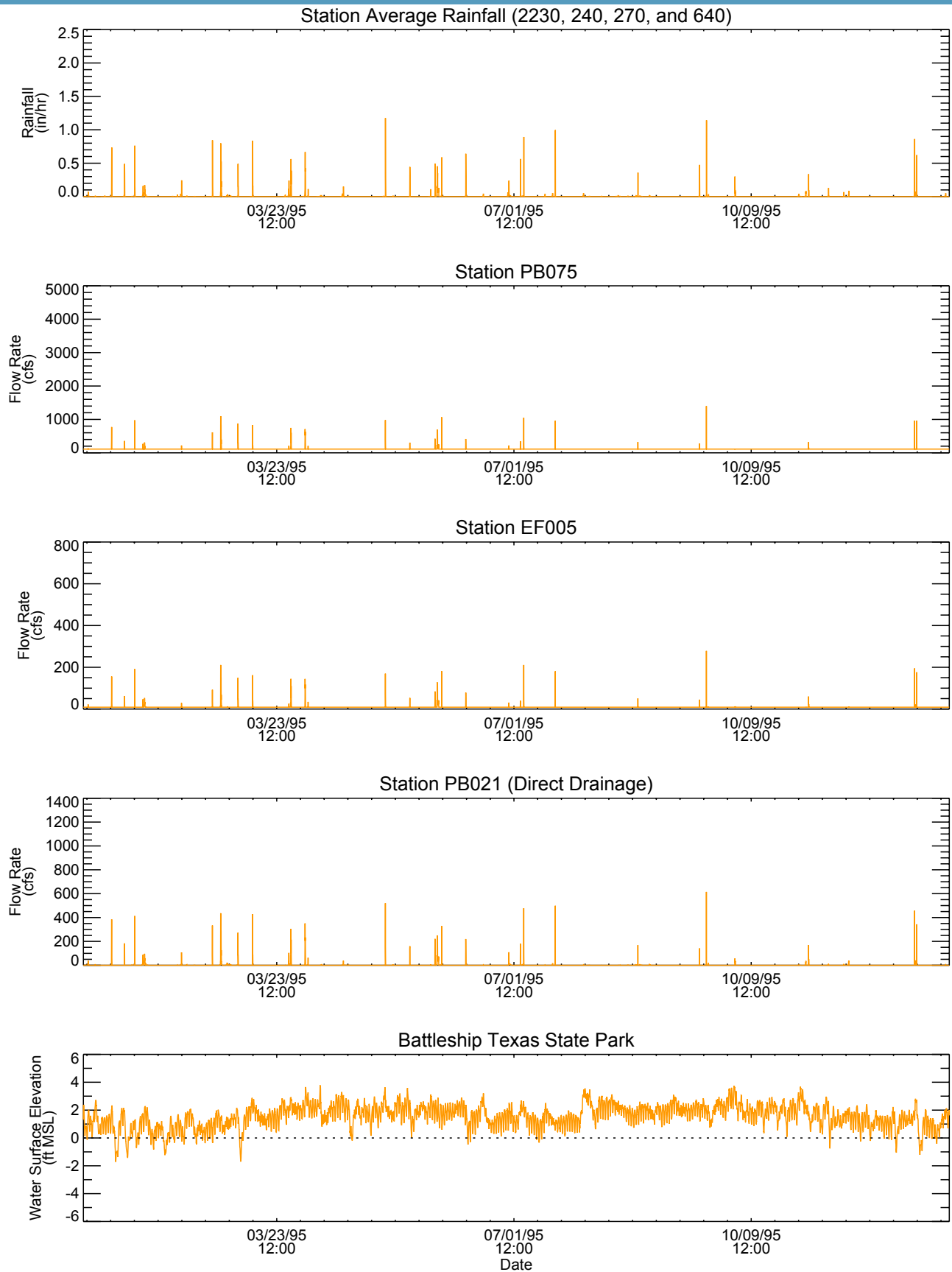


Figure C-3
Time History of Precipitation, Freshwater Inflow and Tidal Elevation Boundary
Conditions for 1995

Note: Rainfall data from Harris County Homeland Security and Emergency Management gauge stations. Flow rate predicted by watershed model. Water surface elevation from NOAA gauge station.

Patrick Bayou Study Area



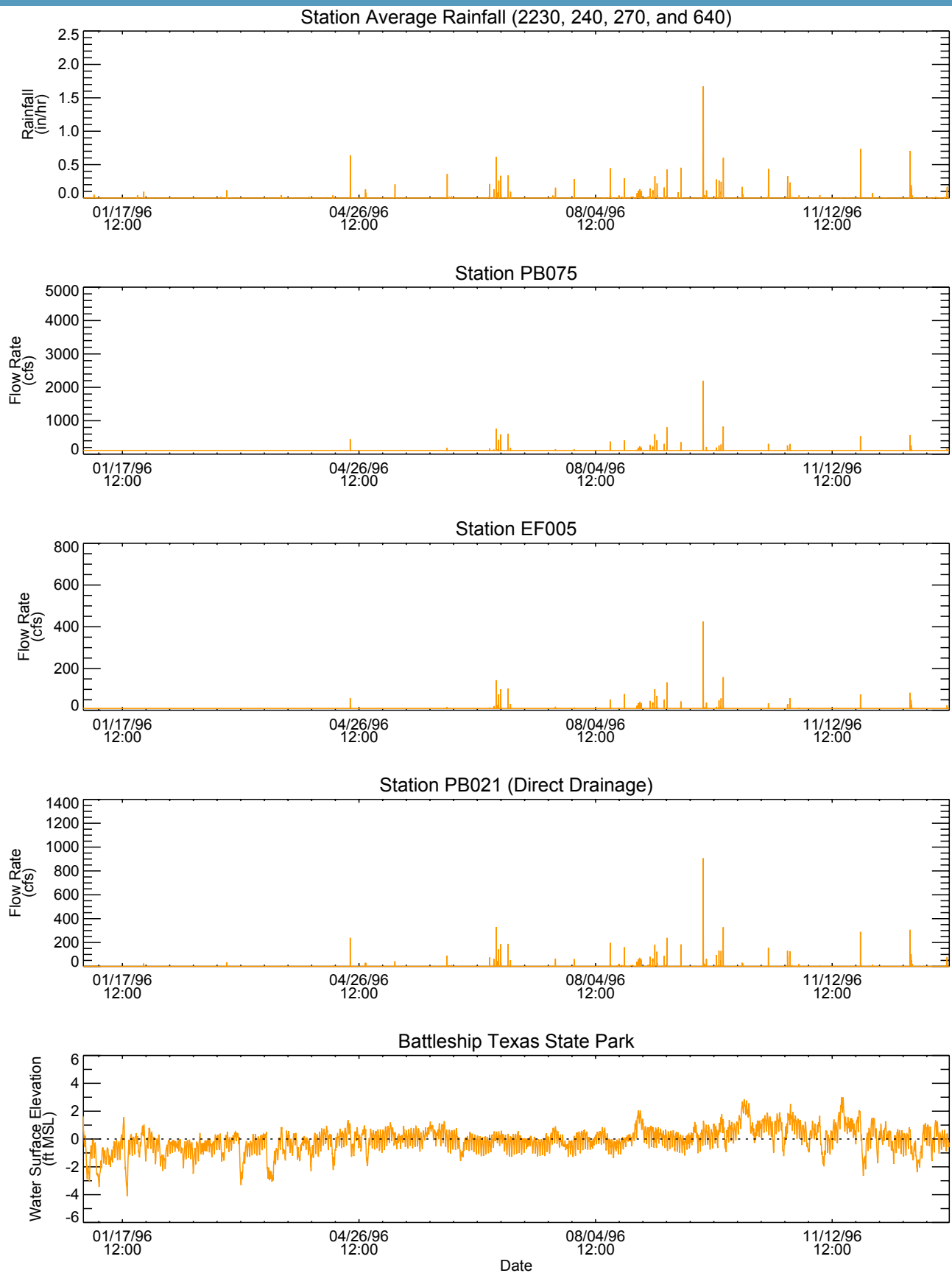


Figure C-4
Time History of Precipitation, Freshwater Inflow and Tidal Elevation Boundary Conditions for 1996

Note: Rainfall data from Harris County Homeland Security and Emergency Management gauge stations. Flow rate predicted by watershed model. Water surface elevation from NOAA gauge station.

Patrick Bayou Study Area



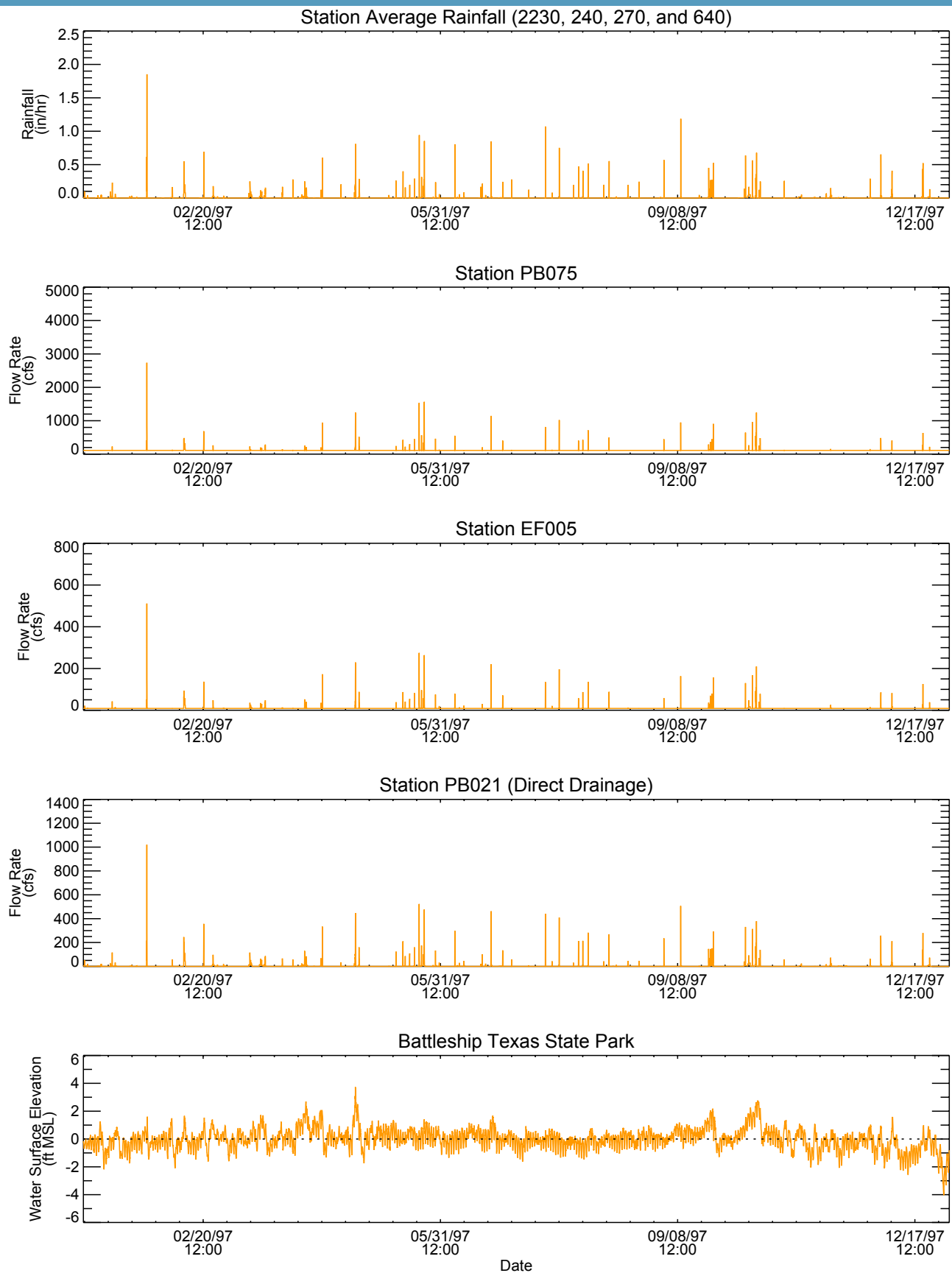


Figure C-5
Time History of Precipitation, Freshwater Inflow and Tidal Elevation Boundary
Conditions for 1997

Note: Rainfall data from Harris County Homeland Security and Emergency Management gauge stations. Flow rate predicted by watershed model. Water surface elevation from NOAA gauge station.

Patrick Bayou Study Area



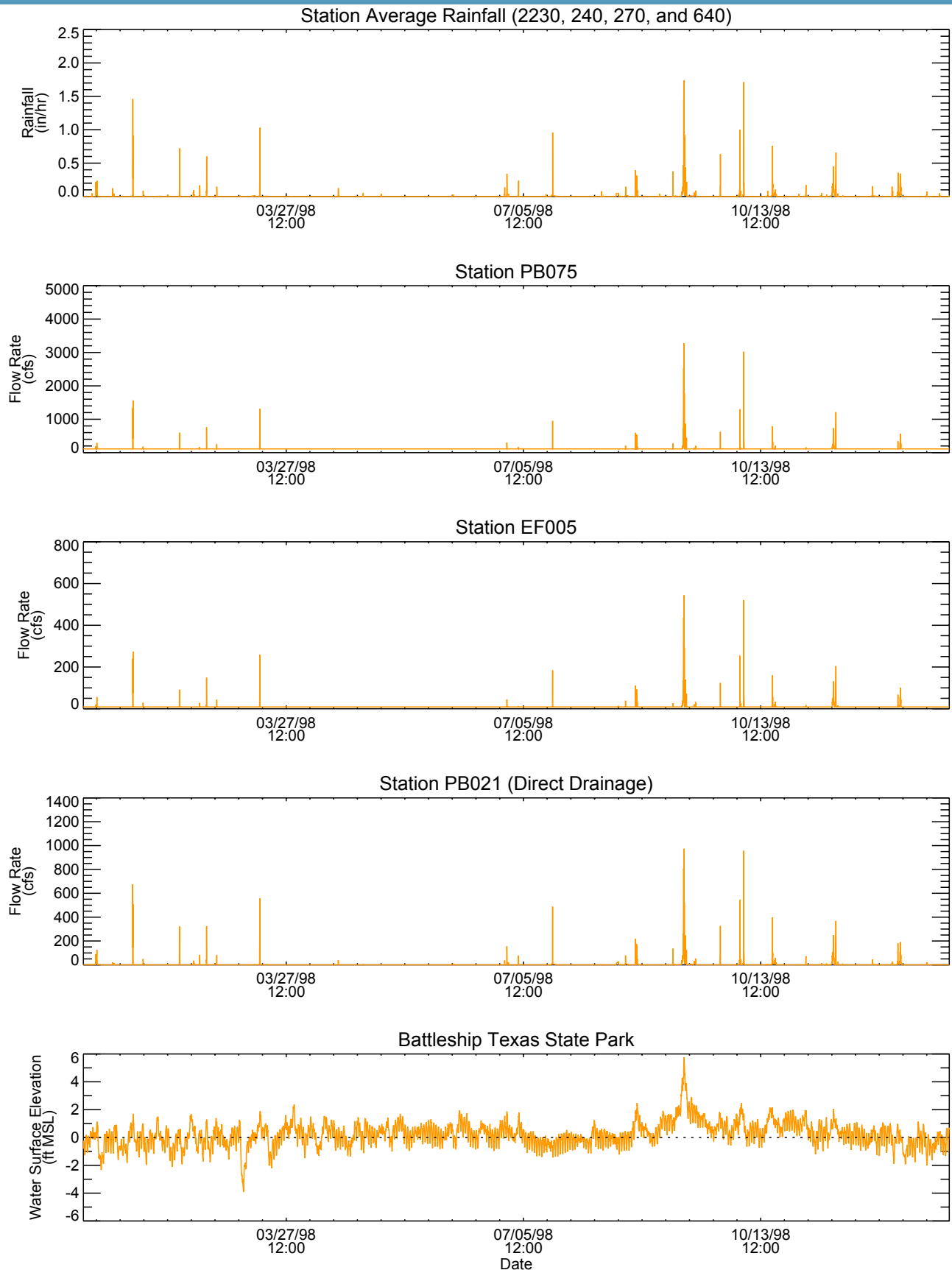


Figure C-6
Time History of Precipitation, Freshwater Inflow and Tidal Elevation Boundary Conditions for 1998

Note: Rainfall data from Harris County Homeland Security and Emergency Management gauge stations. Flow rate predicted by watershed model. Water surface elevation from NOAA gauge station.

Patrick Bayou Study Area



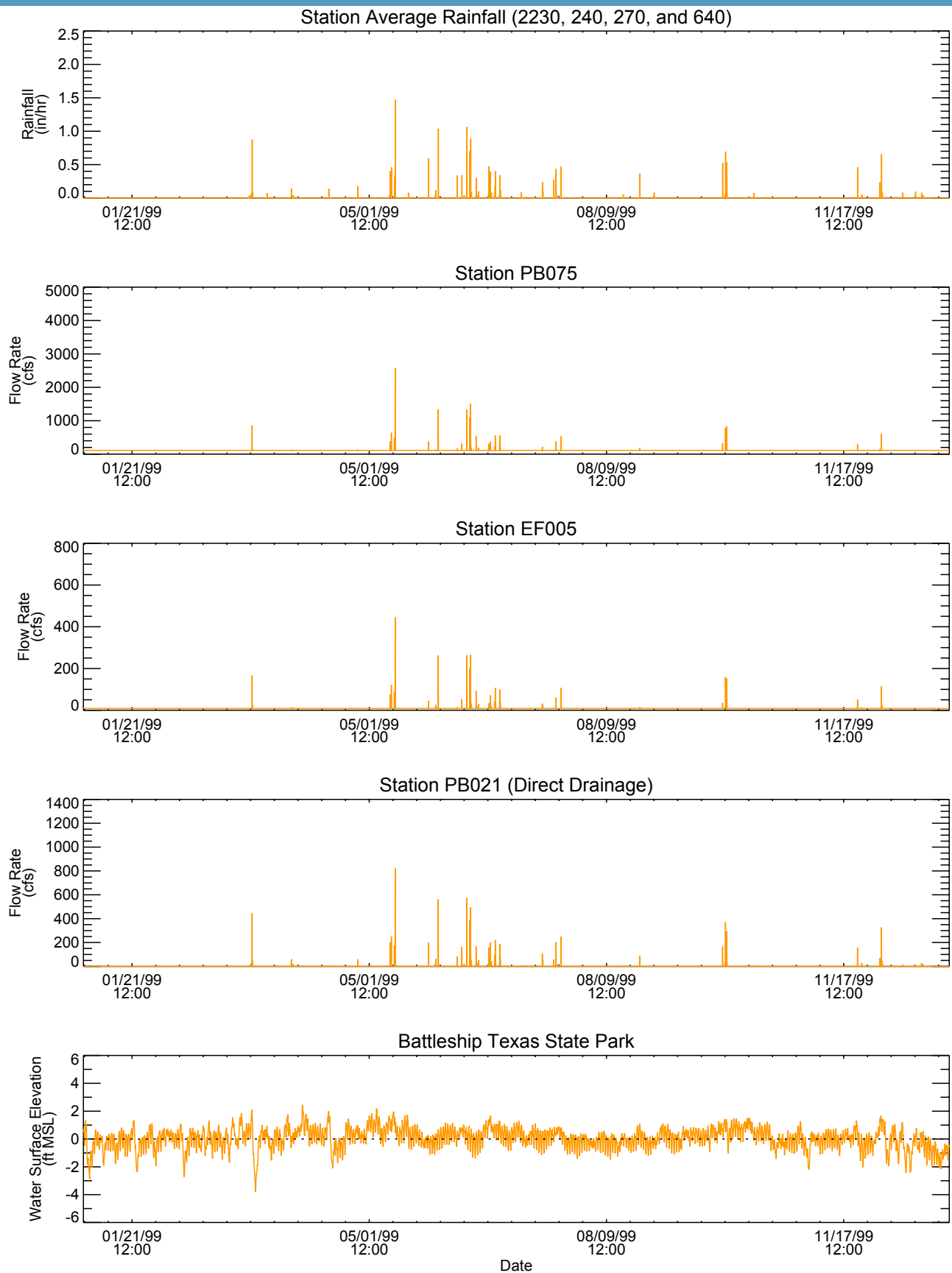


Figure C-7
Time History of Precipitation, Freshwater Inflow and Tidal Elevation Boundary Conditions for 1999

Note: Rainfall data from Harris County Homeland Security and Emergency Management gauge stations. Flow rate predicted by watershed model. Water surface elevation from NOAA gauge station.

Patrick Bayou Study Area



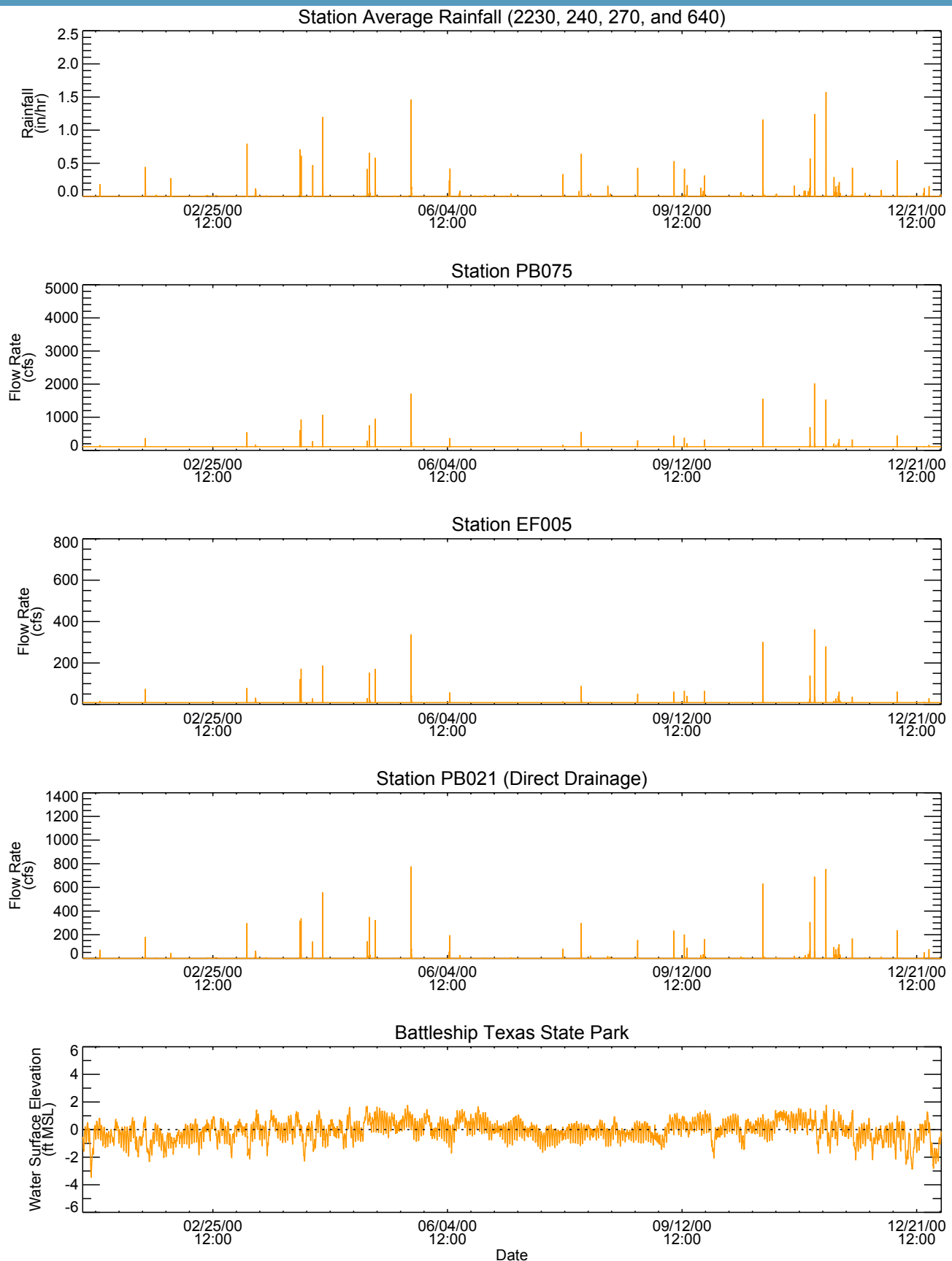


Figure C-8
Time History of Precipitation, Freshwater Inflow and Tidal Elevation Boundary
Conditions for 2000

Note: Rainfall data from Harris County Homeland Security and Emergency Management gauge stations. Flow rate predicted by watershed model. Water surface elevation from NOAA gauge station.

Patrick Bayou Study Area



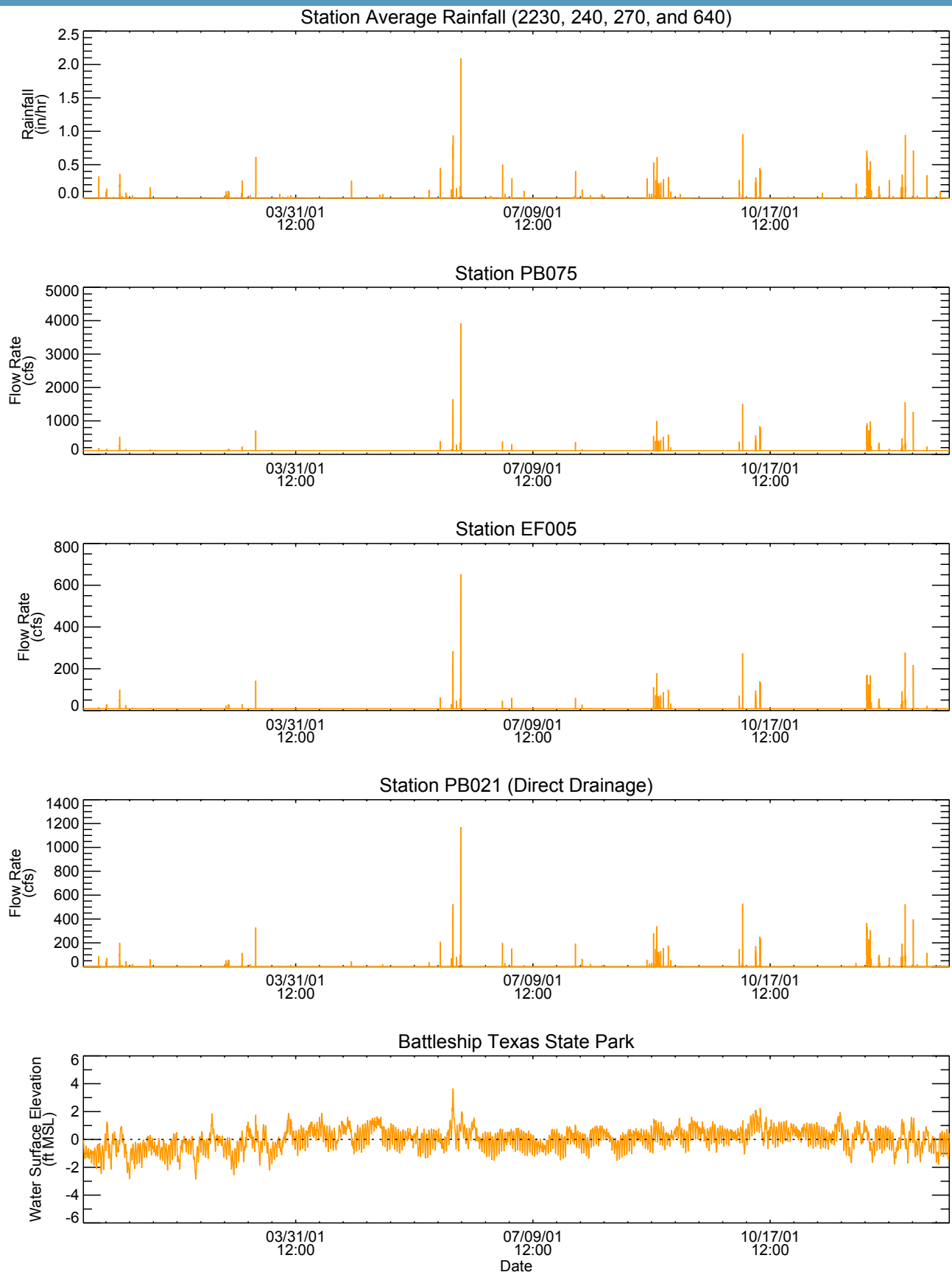


Figure C-9
Time History of Precipitation, Freshwater Inflow and Tidal Elevation Boundary Conditions for 2001

Note: Rainfall data from Harris County Homeland Security and Emergency Management gauge stations. Flow rate predicted by watershed model. Water surface elevation from NOAA gauge station.
Patrick Bayou Study Area



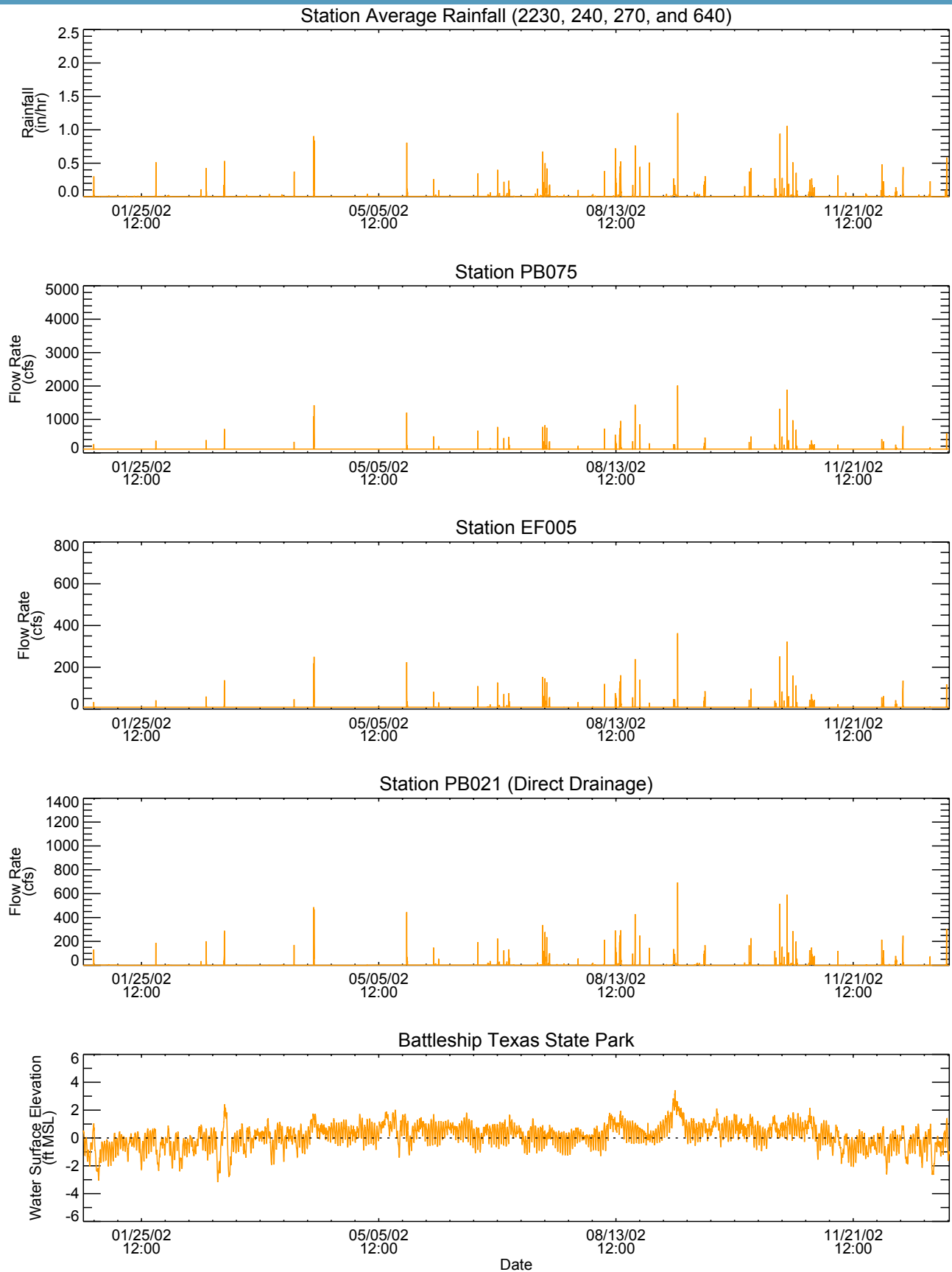


Figure C-10
Time History of Precipitation, Freshwater Inflow and Tidal Elevation Boundary
Conditions for 2002

Note: Rainfall data from Harris County Homeland Security and Emergency Management gauge stations. Flow rate predicted by watershed model. Water surface elevation from NOAA gauge station.

Patrick Bayou Study Area



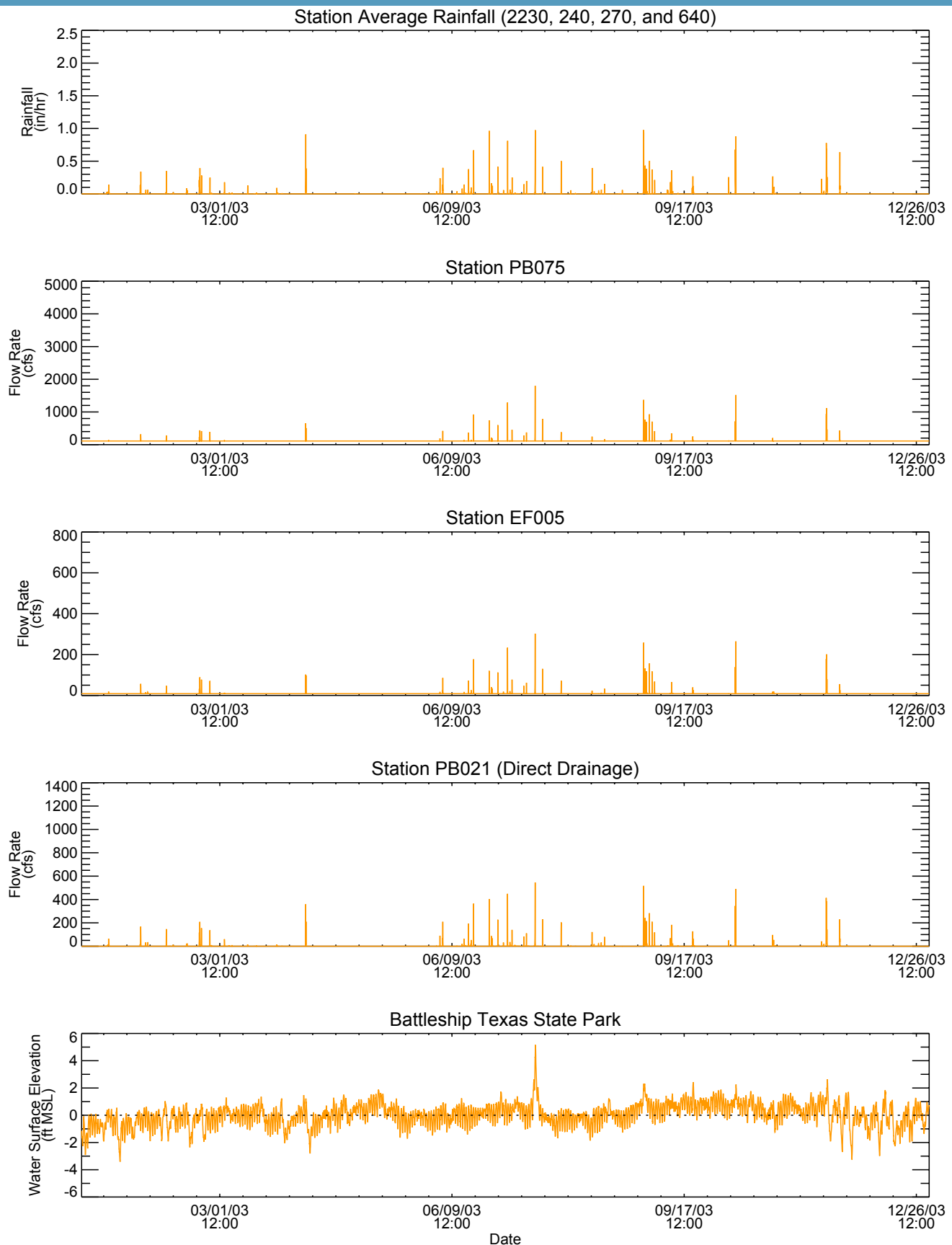


Figure C-11
Time History of Precipitation, Freshwater Inflow and Tidal Elevation Boundary
Conditions for 2003

Note: Rainfall data from Harris County Homeland Security and Emergency Management gauge stations. Flow rate predicted by watershed model. Water surface elevation from NOAA gauge station.

Patrick Bayou Study Area



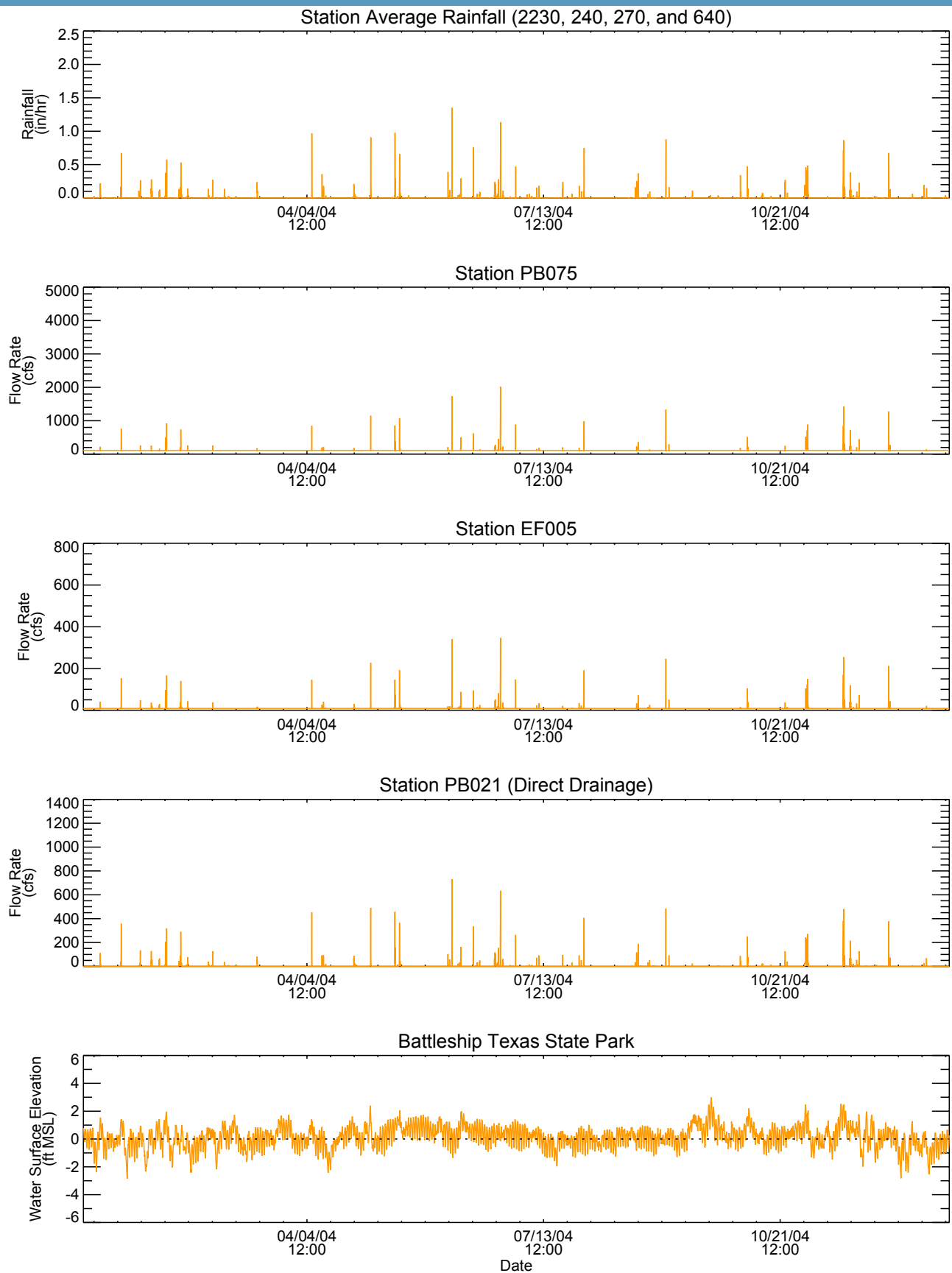


Figure C-12
Time History of Precipitation, Freshwater Inflow and Tidal Elevation Boundary Conditions for 2004

Note: Rainfall data from Harris County Homeland Security and Emergency Management gauge stations. Flow rate predicted by watershed model. Water surface elevation from NOAA gauge station.
Patrick Bayou Study Area



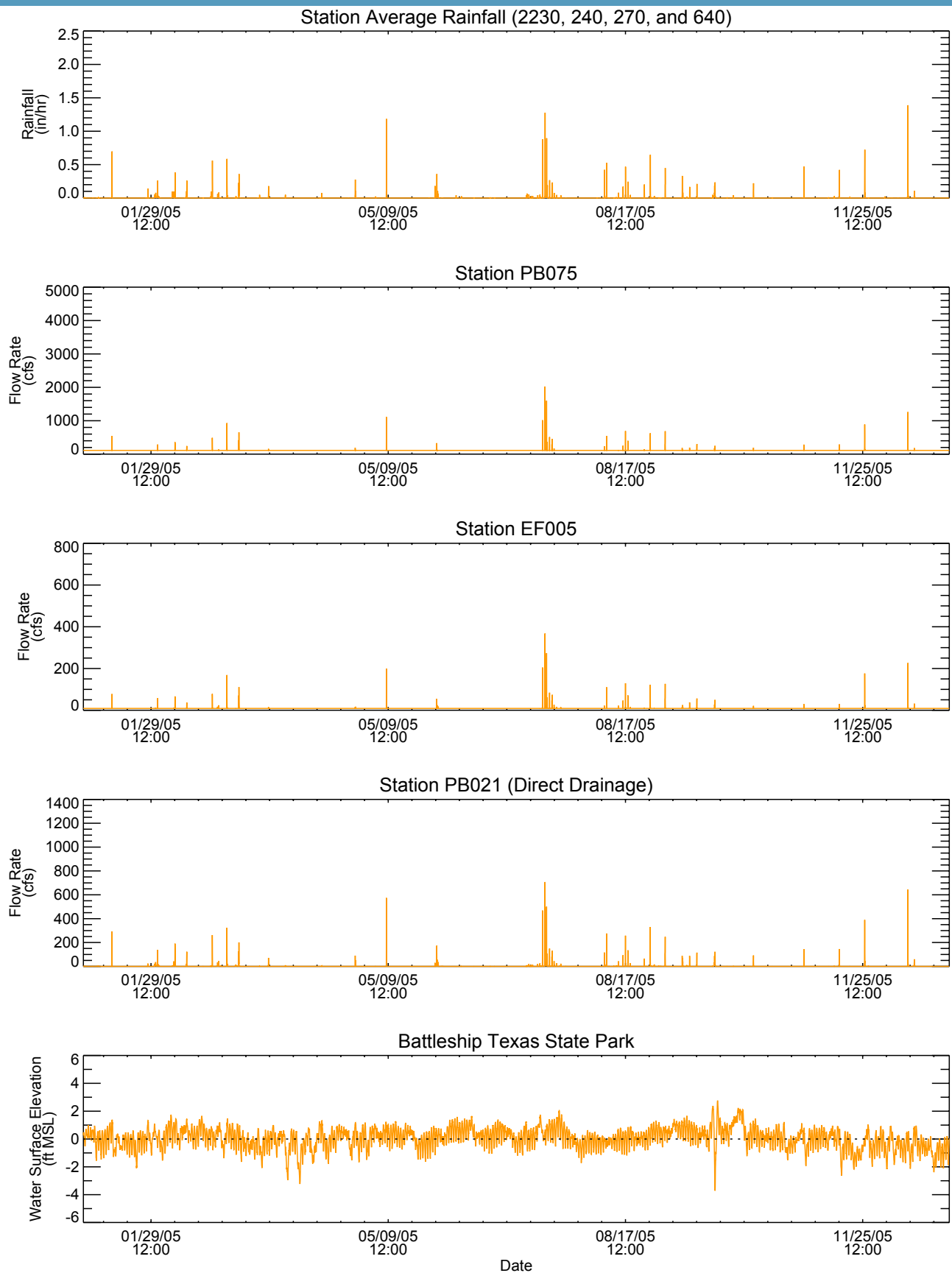


Figure C-13
Time History of Precipitation, Freshwater Inflow and Tidal Elevation Boundary Conditions for 2005

Note: Rainfall data from Harris County Homeland Security and Emergency Management gauge stations. Flow rate predicted by watershed model. Water surface elevation from NOAA gauge station.

Patrick Bayou Study Area



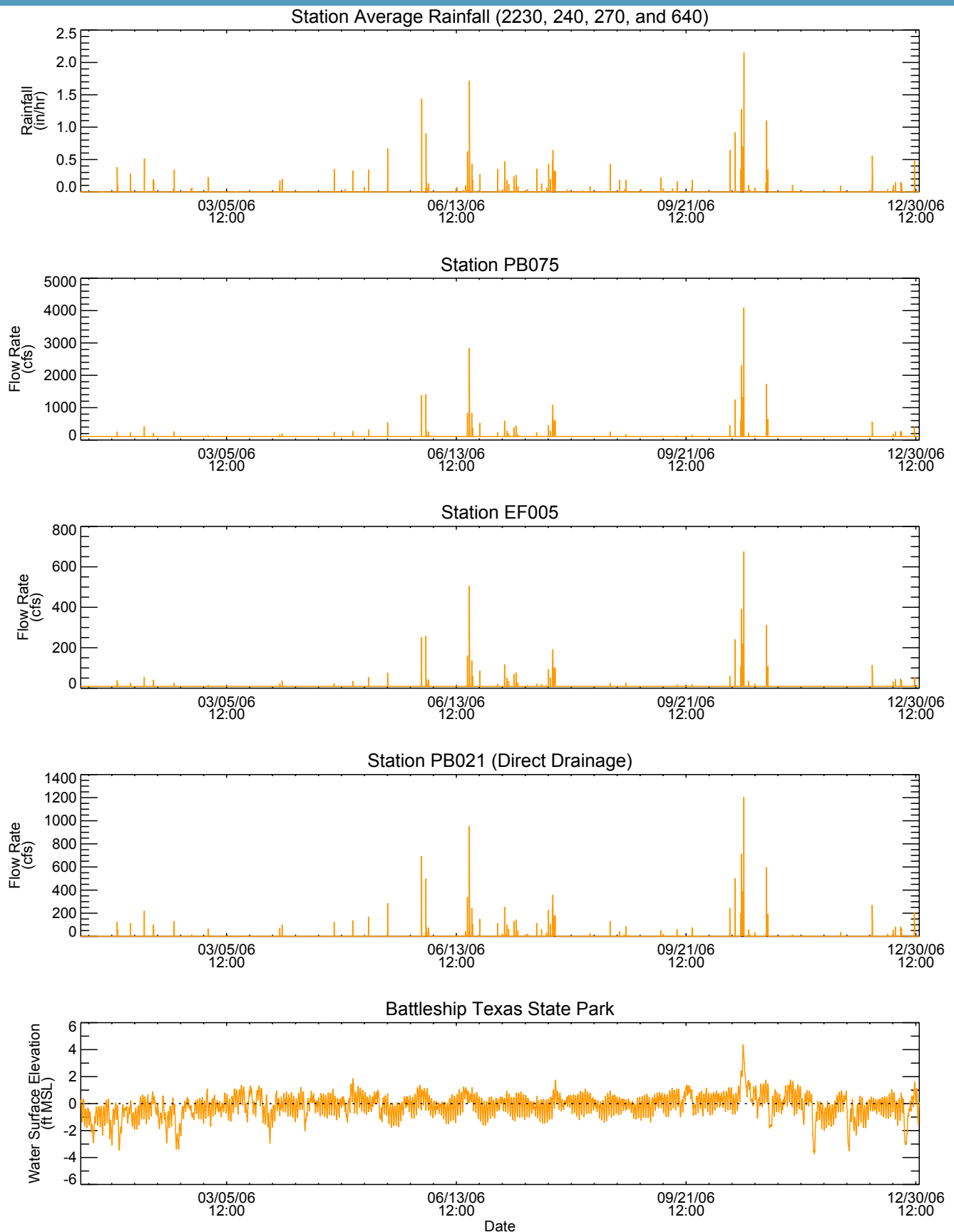


Figure C-14
Time History of Precipitation, Freshwater Inflow and Tidal Elevation Boundary
Conditions for 2006

Note: Rainfall data from Harris County Homeland Security and Emergency Management gauge stations. Flow rate predicted by watershed model. Water surface elevation from NOAA gauge station.

Patrick Bayou Study Area



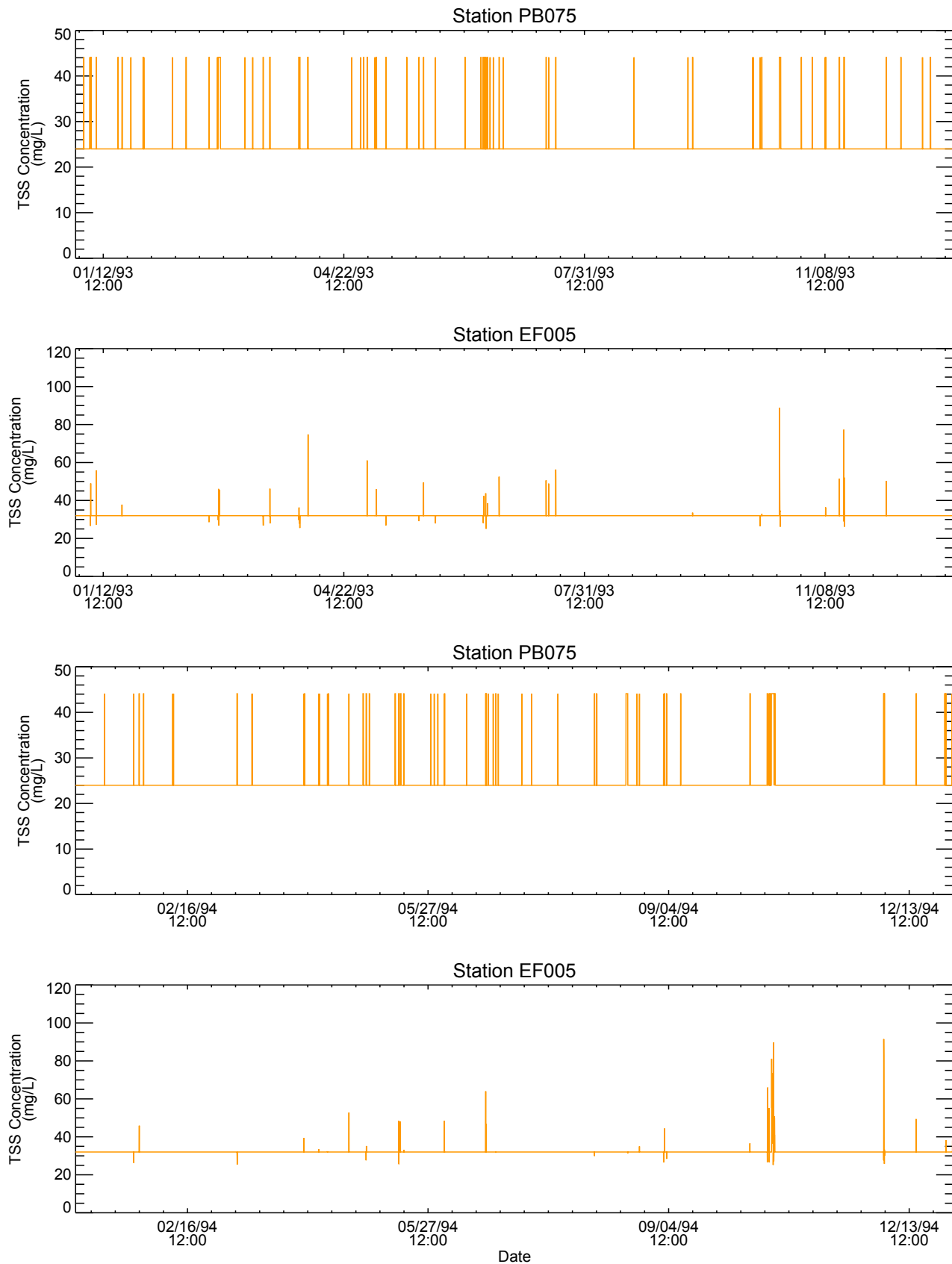


Figure C-15
Time History of TSS Concentration Boundary Conditions for 1993 and 1994
Note: TSS concentrations from rating curve.
Patrick Bayou Study Area

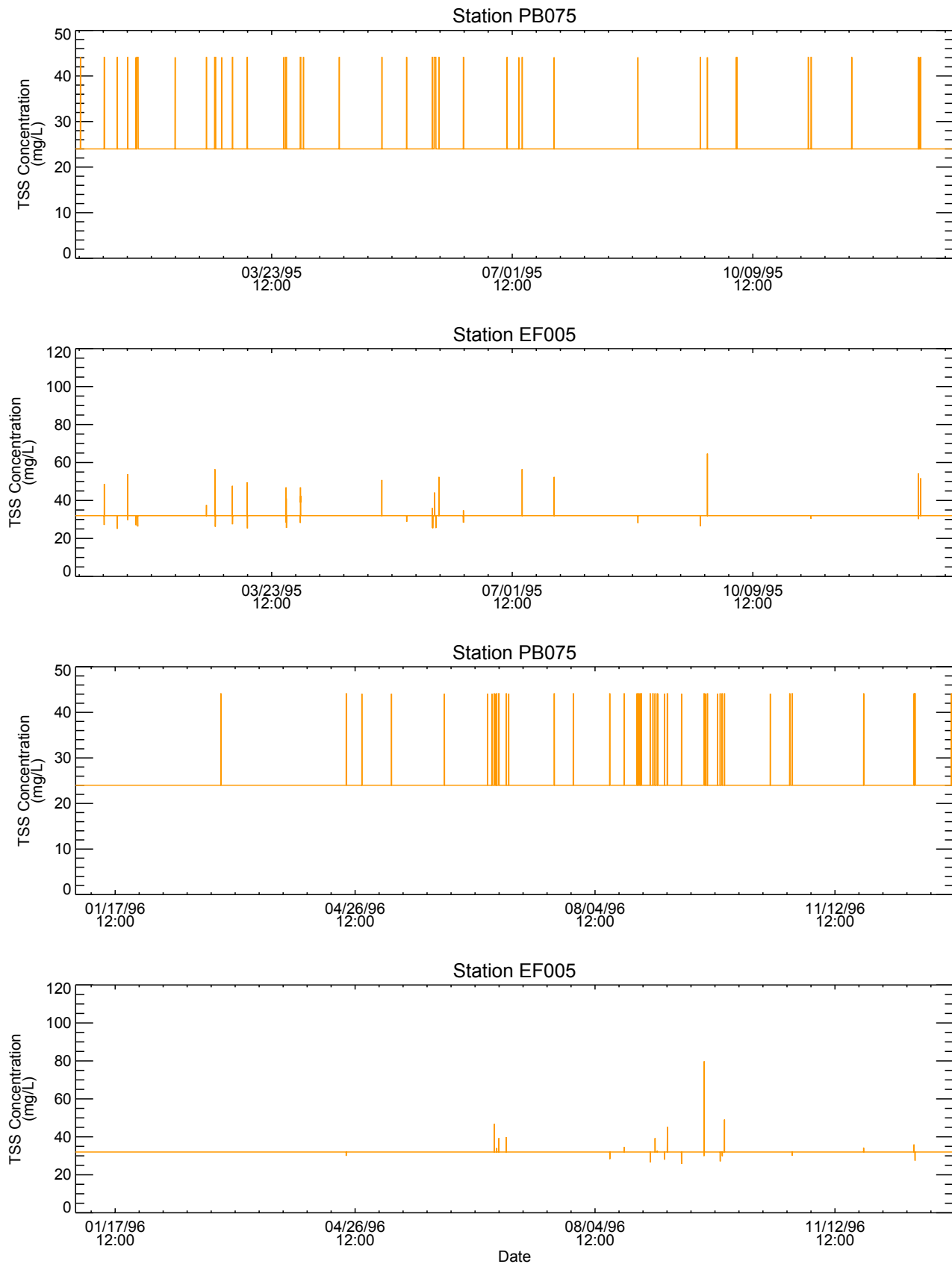


Figure C-16
Time History of TSS Concentration Boundary Conditions for 1995 and 1996

Note: TSS concentrations from rating curve.

Patrick Bayou Study Area



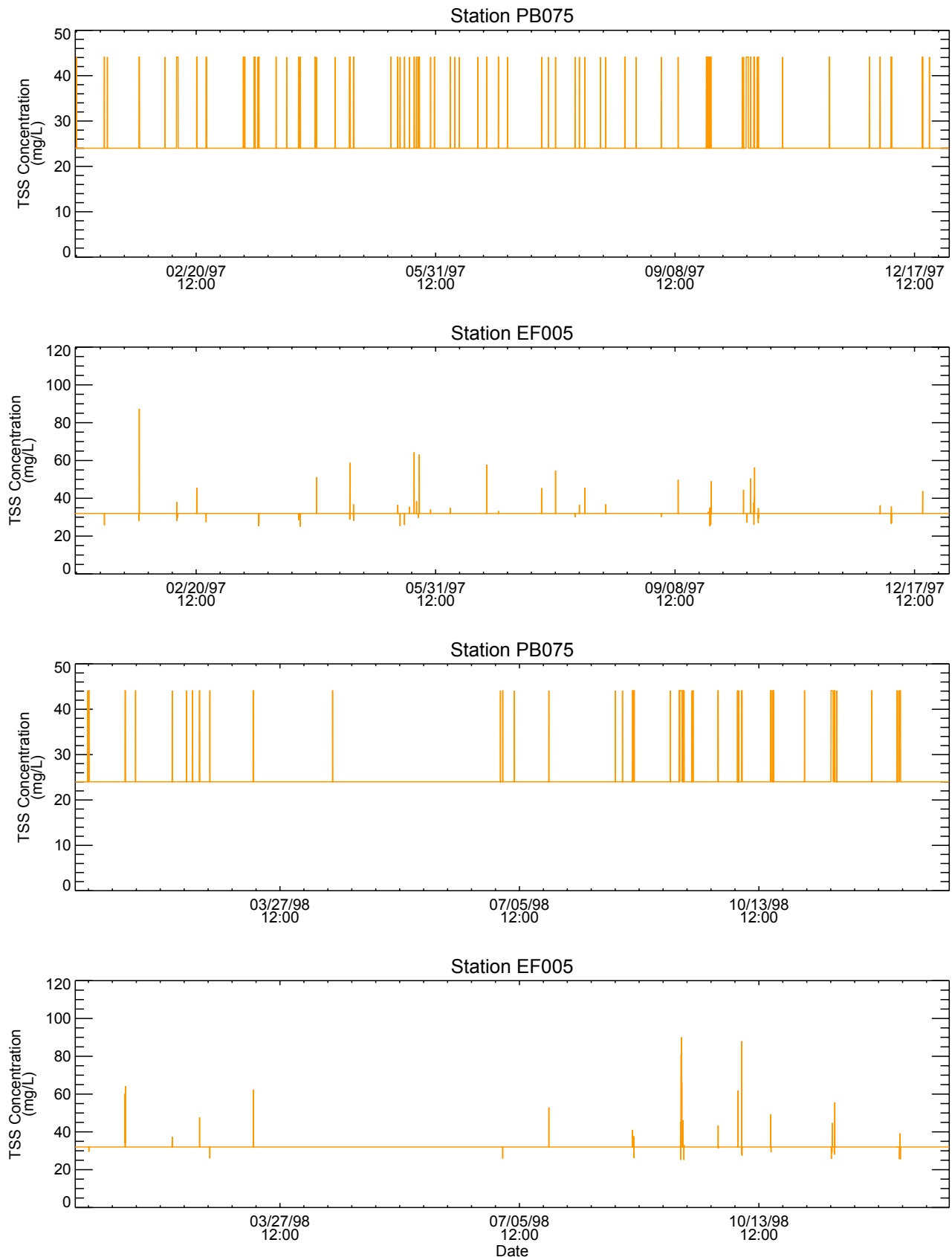


Figure C-17
Time History of TSS Concentration Boundary Conditions for 1997 and 1998

Note: TSS concentrations from rating curve.
Patrick Bayou Study Area



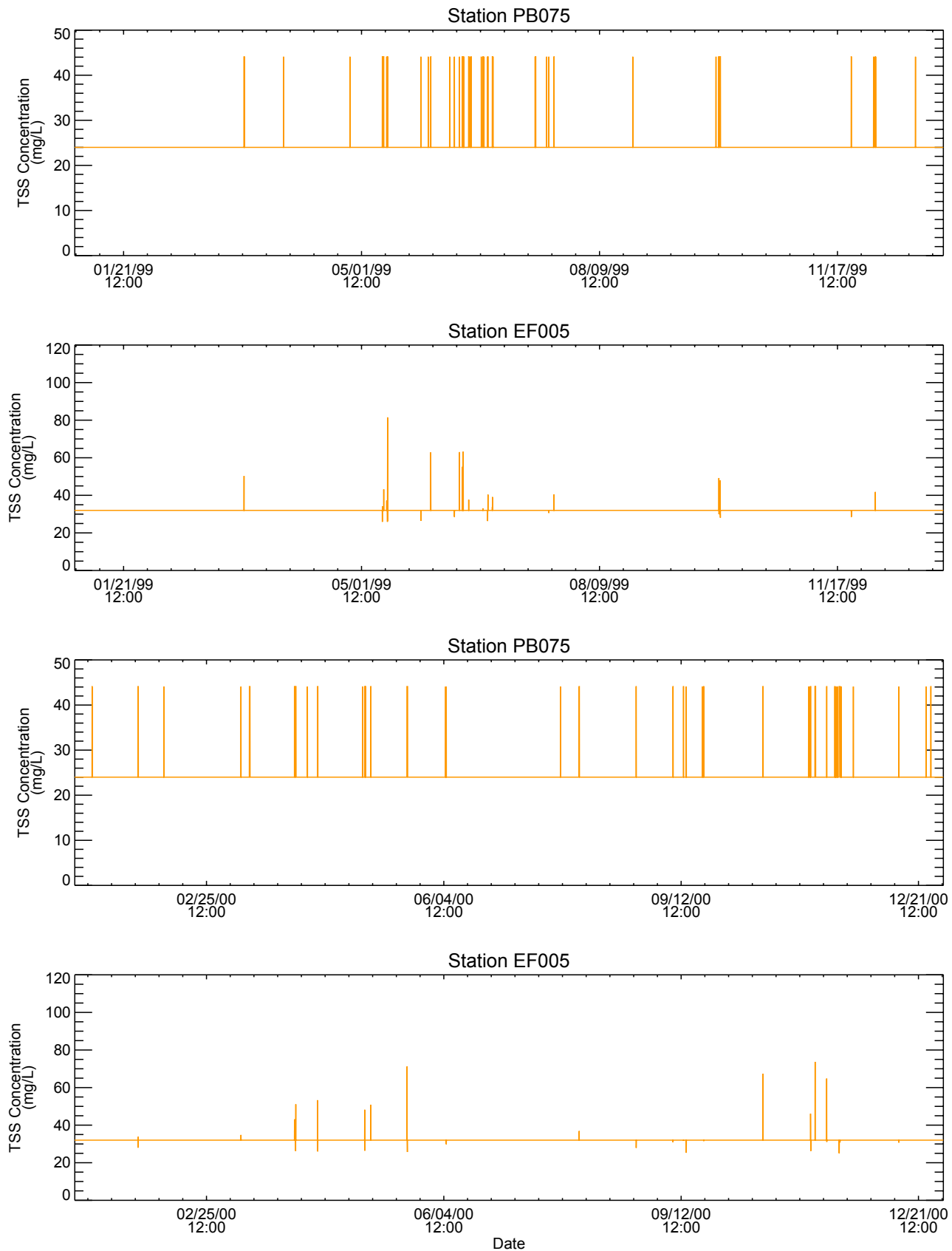


Figure C-18
Time History of TSS Concentration Boundary Conditions for 1999 and 2000

Note: TSS concentrations from rating curve.
Patrick Bayou Study Area



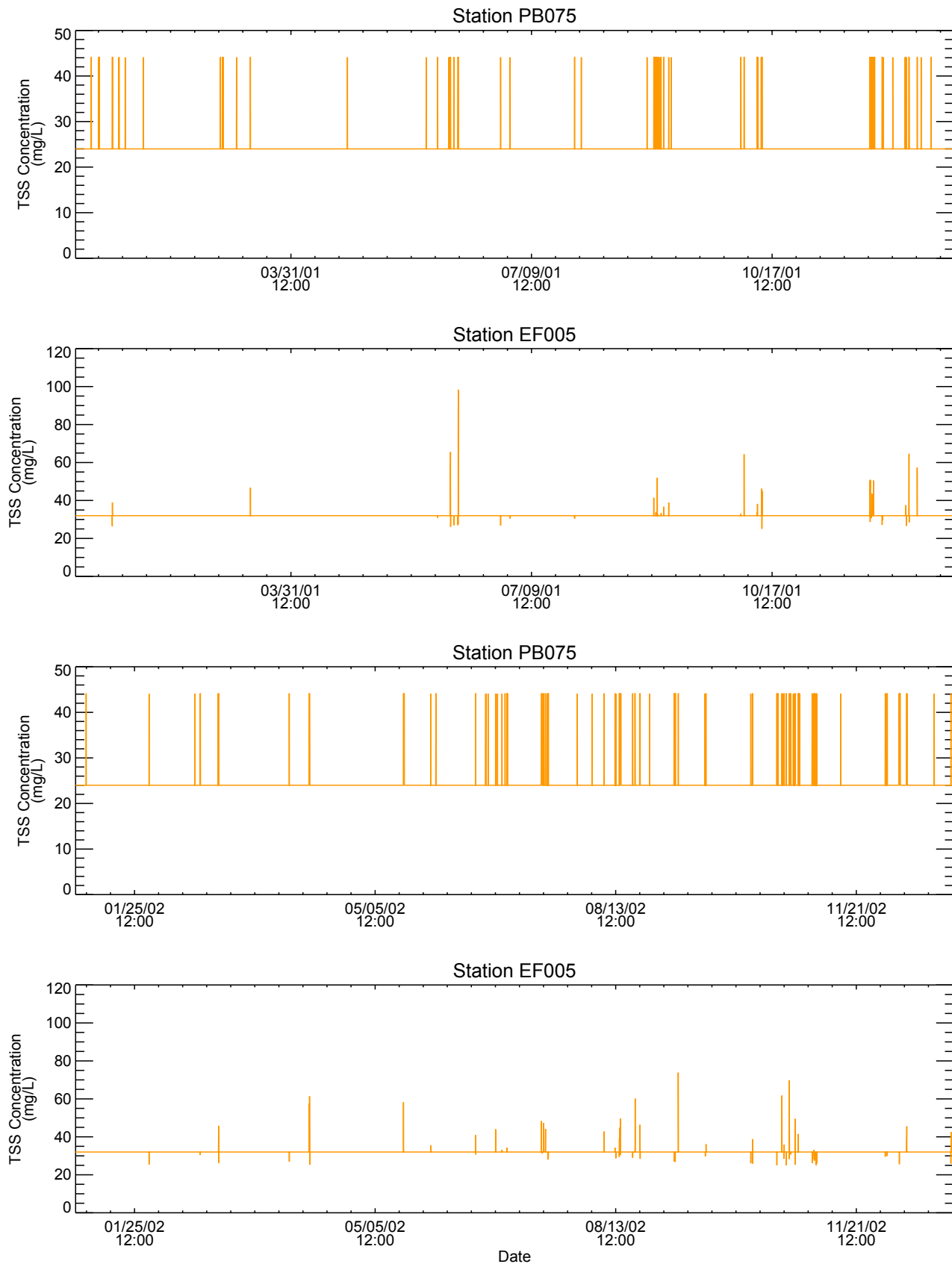


Figure C-19
Time History of TSS Concentration Boundary Conditions for 2001 and 2002

Note: TSS concentrations from rating curve.

Patrick Bayou Study Area



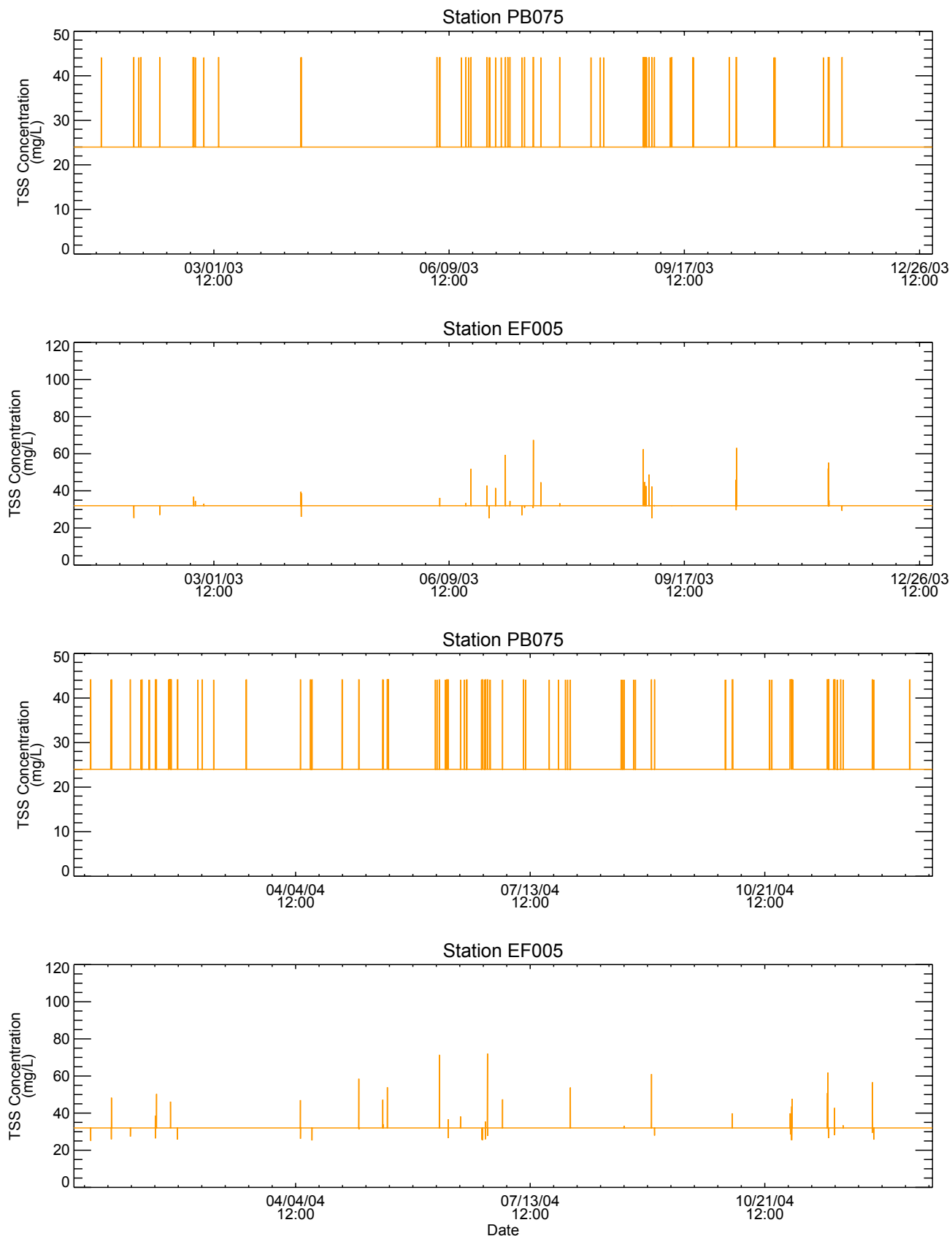


Figure C-20
Time History of TSS Concentration Boundary Conditions for 2003 and 2004

Note: TSS concentrations from rating curve.

Patrick Bayou Study Area



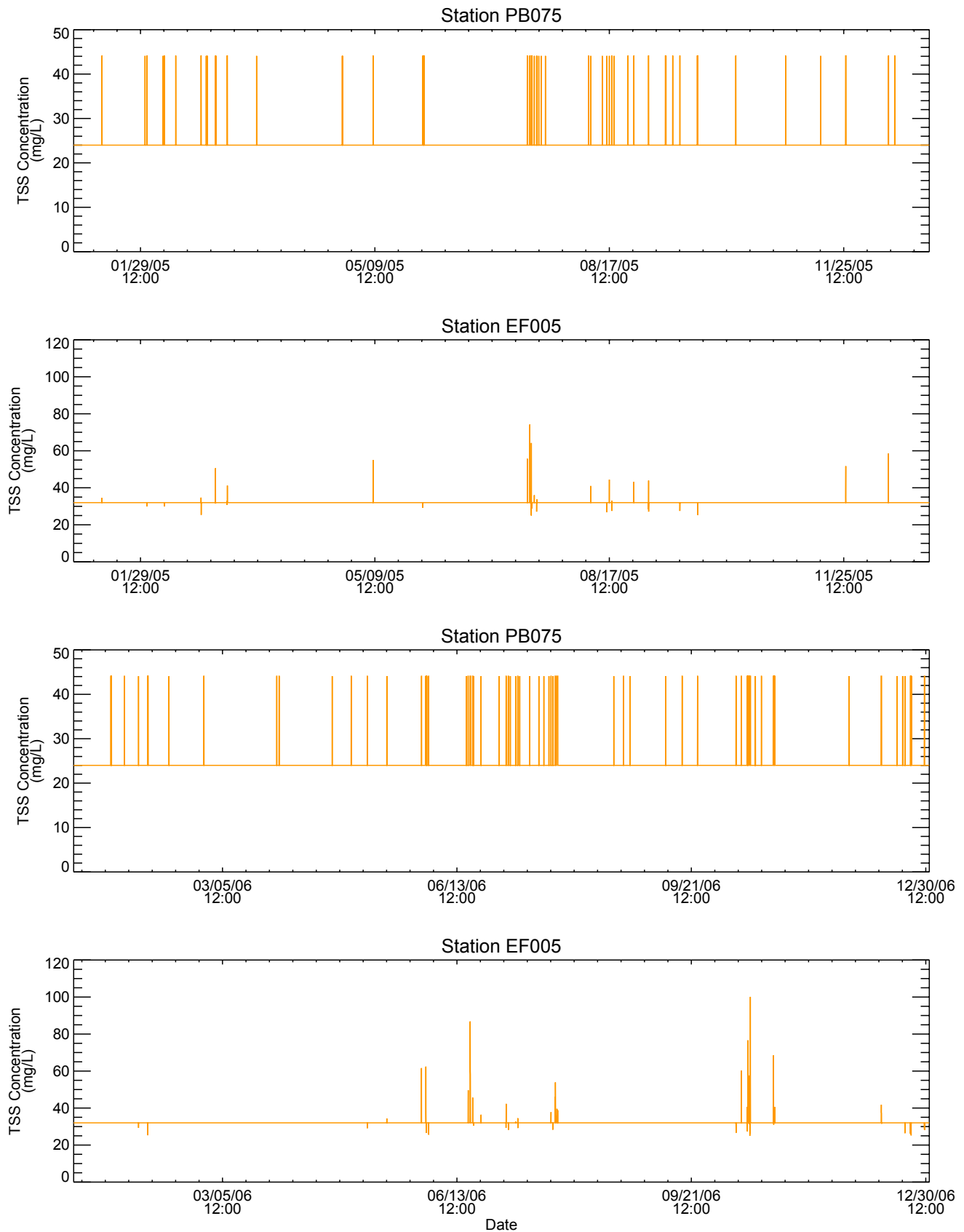


Figure C-21
Time History of TSS Concentration Boundary Conditions for 2005 and 2006

Note: TSS concentrations from rating curve.
Patrick Bayou Study Area



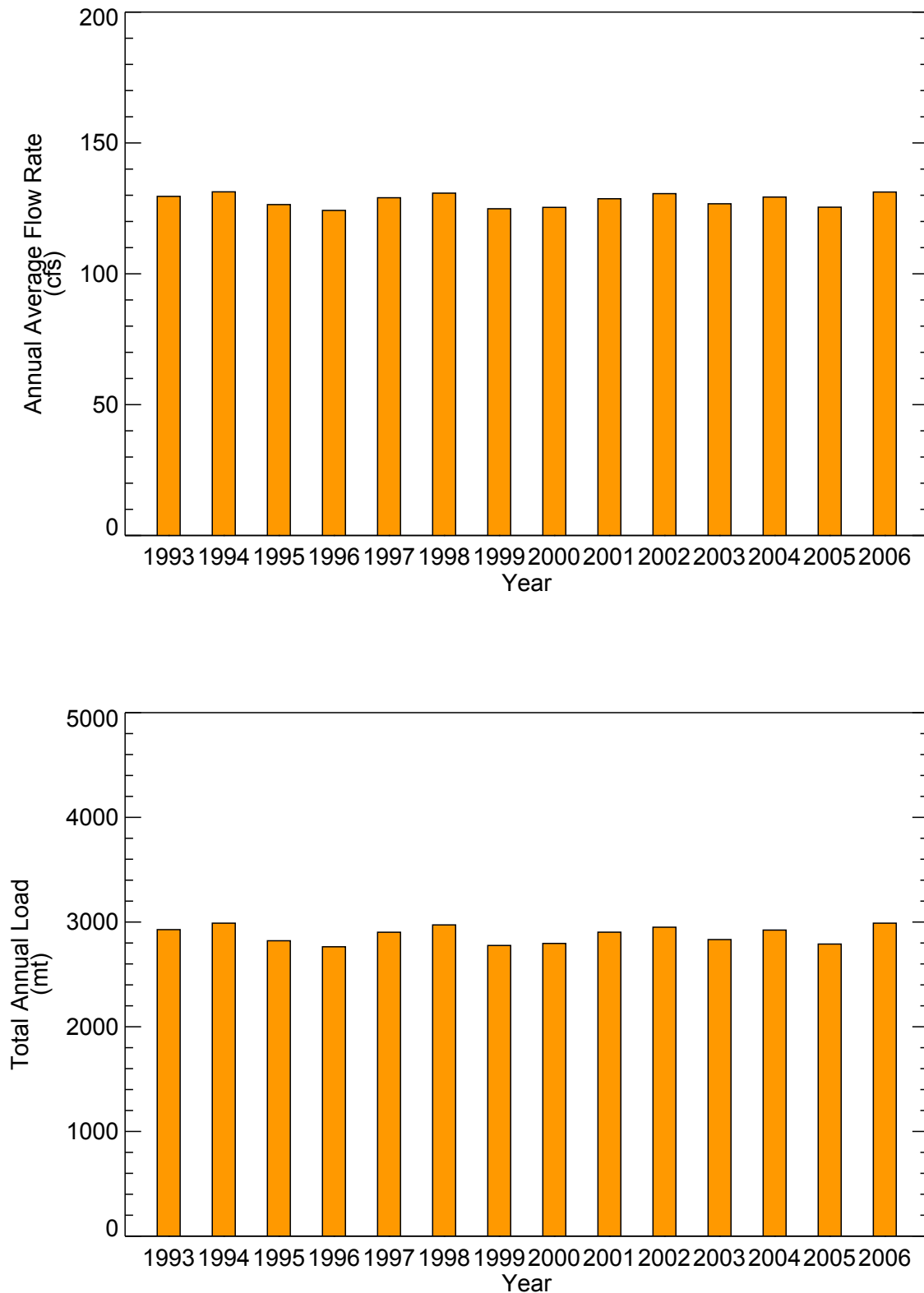


Figure C-22
Annual Variation in Average Total Inflow Rate and Total
Sediment Load During 14-year period
Patrick Bayou Study Area